Metal Powder Effects on Selective Laser Sintering

By

Radu Bogdan Eane

A Thesis submitted in accordance with the requirements for the degree of Doctor of Philosophy

The University of Leeds
School of Mechanical Engineering
Leeds UK

September 2002

The candidate confirms that the work submitted is his own and that appropriate credit has been given where reference has been made to the work of others.

With love for my supportive mother, Olga, my dad, Adrian
and my lovely wife, Mona
Thank you

"I do not know the key to success, but the key
to failure is trying to please everybody"
Bill Cosby

ACKNOWLEDGMENTS

First of all I wish to express my deepest gratitude to Professor T.H.C. Childs for his valuable supervision, advice, encouragement, patience and endless support throughout the research period and preparation of the thesis (Thanks Tom!).

I would like also to express my thanks to University of Leeds for the sponsorship of this research and financial support. I would like to thank the members of the Manufacturing, Strength of Materials and Measurement Laboratories for their support. In particular, Mr. Phillip Wood, Mr. Abbas Ismail and Mr. Tony Wiese.

I would like to thank Dr. Carl Hauser for his friendship and support during these years (cheers big boy!).

I would like to thank my friends that I have met at Leeds University. I will mention here only Dr. Alva Tontowi, Mr. Chris Taylor, Dr. Neri Valopato and Dr. M. Dewidar.

Last, but definitely not least, I would like to give very special thanks to my family and my wife Mona for their understanding, patience and emotional support throughout all these four long years.

Radu Bogdan Eane

Leeds, September 2002

ABSTRACT

Manufacturing functional prototypes and different tools using conventional methods usually is a time consuming process with multiple steps. The global economic pressure to get products to market faster has resulted in the development of several Rapid Prototyping (RP) techniques.

Layer manufacturing technologies are gaining increasing attention in the manufacturing sector. They have the potential to produce tooling either indirectly or directly, and powder metal based layer manufacture systems are considered to be an effective way of producing rapid tooling.

Selective Laser Sintering (SLS) is one of several available layer manufacture technologies. SLS is a sintering process in which designed parts are built up layer by layer from the bottom up using different powder materials. A laser beam scans the powder bed; filling in the outline of each layer's CAD-image by heating the selected powder pattern to fuse it.

This work reports on the results of an experimental study examining the potential of the selective laser sintering process to produce metallic parts using stainless steel powder. One material, a stainless steel powder and one sintering station research machine, which was constructed in Leeds, were used during the research. A step-by-step investigation was conducted. The research started with sintered tracks and finished with multiple layer sintering. The purpose was to find successful conditions and to establish the main problems that need to be overcome.

The main achievements of this thesis have been to develop laser power and scan speed sintering maps for a stainless steel powder. The maps have established conditions in which multiple layer blocks can be created, have established strategies to enable large areas to be sintered without warping and show that powder particle size has an important influence on sintering and on the position of the boundaries in the sintering maps. Although this investigation answered some questions, it also raised several more which are presented at the end of this thesis for future work.

Chapter 1. Introduction and Literature Review

Chapter 2. Experimental Equipment and Methods

Chapter 3. Stainless Steel Powder Preliminary Experimental Tests

Chapter 4. Layer and Multiple Layer Sintering of 314 HC Powder

Chapter 5. Discussion and Conclusions

LIST OF FIGURES

CHAPTER 1

CHAPTER 2

CHAPTER 3

CHAPTER 5

List of Tables

List of Notations

r	Scaling factor
f	Offset value
A_N	Andrew number (J/mm^2)
P	Laser power (W)
u	Scan speed mm/sec
s	Scan spacing mm
K	Thermal conductivity
E	Total Energy (J)
l	Length of the part (mm)
w	Width of the part (mm)
h	Height of the part (mm)
L_t	Layer thickness (mm)
L	Span length (mm)
b	Width of the sample (mm)
d	Depth of the sample (mm)
E	Modulus of Elasticity (GPa)
c	Depth of the sample/2 (mm)
y_{max}	Deflection at midspan (mm)
y_l	Deflection at any point of span (mm)
x	Distance from the support to the point at which the deflection is to be calculated when the specimen is straight (mm)
a	Distance from the support to the load applicator when the specimen is straight (mm)
T_s	Scanning time (sec)
T_o	Total time of one layer (sec)
N_n	Total number of layers
T_d	Delay time (sec)
N_l	Number of lines
T_t	Total time of building (sec)
T_c	Set-up time for each layer (sec)
ρ	Density (g/cm^3)
W	Weight (g)
V	Volume (cm^3)
W_{total}	Weight of the box plus the loose powder (g)
W_{box}	Weight of the box (g)
W_{powder}	Weight of the loose powder (g)
Vol	Volume of the box (cm^3)
R_a	Surface roughness (μm)
ρ_{Av}	Average density (g/cm^3)
W_b	Weight of the block (g)
T_m	Temperature at which maximum density is first obtained (K)
T_{opt}	Optimum sintering temperature (K)
T_{solid}	Sintering temperature (K)

Abbreviations

3D	Three-dimensional
3DP	Three-Dimensional Printing
CAD	Computer Aided Design
CAM	Computer Aided Manufacturing
CMM	Coordinate Measuring Machine
CNC	Computer Numerical Control
FDM	Fused Deposition Modelling
HSS	High-Speed Steel
LOM	Laminated Object Manufacturing
LPS	Liquid Phase Sintering
PM	Powder Metallurgy
RM	Rapid Manufacturing
RP	Rapid Prototyping
RT	Rapid Tooling
SEM	Scanning Electron Microscopy
SLA	Stereolithography
SLS	Selective Laser Sintering
STL	STereoLithography format

CHAPTER 1

INTRODUCTION AND LITERATURE REVIEW

1.1 Introduction

The first rapid prototyping technology was started over two decades ago. Rapid prototyping technologies have been growing rapidly since then. Rapid prototyping is a collection of processes in which physical prototypes are quickly created directly from computer generated 3D models. Today there are around 25 rapid prototyping technologies used around the world (Steen et al, 1998). One of these technologies is Selective Laser Sintering, known as SLS™. Selective Laser Sintering is one of the leading commercial Rapid Prototyping processes which produces fully functional parts directly from polymers and metallic powders without using any conventional tooling.

The very first sintering station was built at the University of Texas, Austin. The University of Texas holds the licence of the company DTM Corporation that has launched the commercial version of the Austin sintering station on the market. Over the last decade research has been focused on the uses of the technology for shortening product development times, verification and design, and reducing engineering costs. This research has mainly centred on polymer powder models. Current research in rapid prototyping area is becoming more focused on new materials, for example metallic powders for the production of tools and parts.

There are still many problems with metal selective laser sintering. A common one is part porosity. To gain a high density, the sintered parts need to be taken through a subsequent process, such as infiltration. Other problems include the balling phenomenon, layer warping and curling and layer oxidation. The main objectives of this research are to increases the understanding, using stainless steel powder, 314HC as an example, of how to reduce porosity in large sintered areas, aiming towards total elimination of post-processing. Further objectives are to create sintering maps and development a new scanning strategy to choose the best solution for diminishing the balling phenomenon, layer warping and layer curling.

1.2 Overview of Rapid Prototyping Technologies

The following section presents a brief account of the most used rapid prototyping technologies around the world. It also includes a short account of the software used during the entire process from CAD data to physical models. Figure 1.1 shows the most used rapid prototyping technologies today.

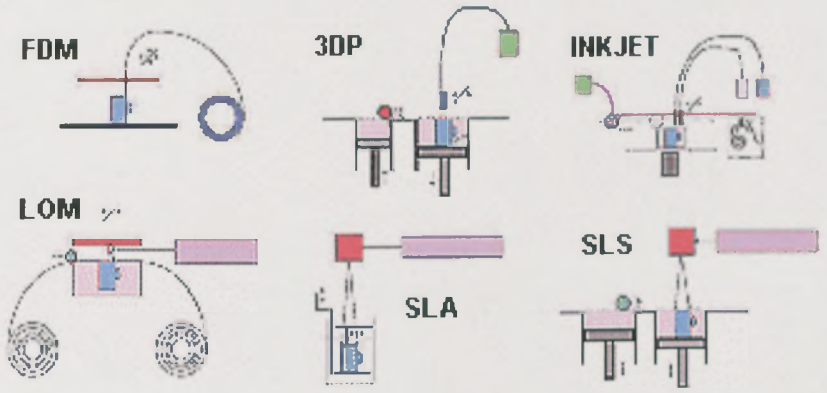

Figure. 1.1 The most used RP technologies in the world today
(www.manufacturingtalk.com/2002)

Fast and inexpensive production of three-dimensional structures from CAD data physical models has become already available in the early phase of the product development process. These models are a valuable assistance during the interpretation of complex designs and help the designer operate more efficiently. Rapid prototyping models are suitable for the verification of component form.

Rapid prototyping technologies can be divided into those needing the addition of material and those involving removal of material.

1.2.1 Stereolithography (SLA)

Stereolithography is the most widely used type of rapid prototyping technology. The process is commercialised by 3D Systems Ltd. The main characteristic of Stereolithography (SLA) is the ultra-violet laser, which is scanned over a photo curable liquid polymer system (figure 1.2).

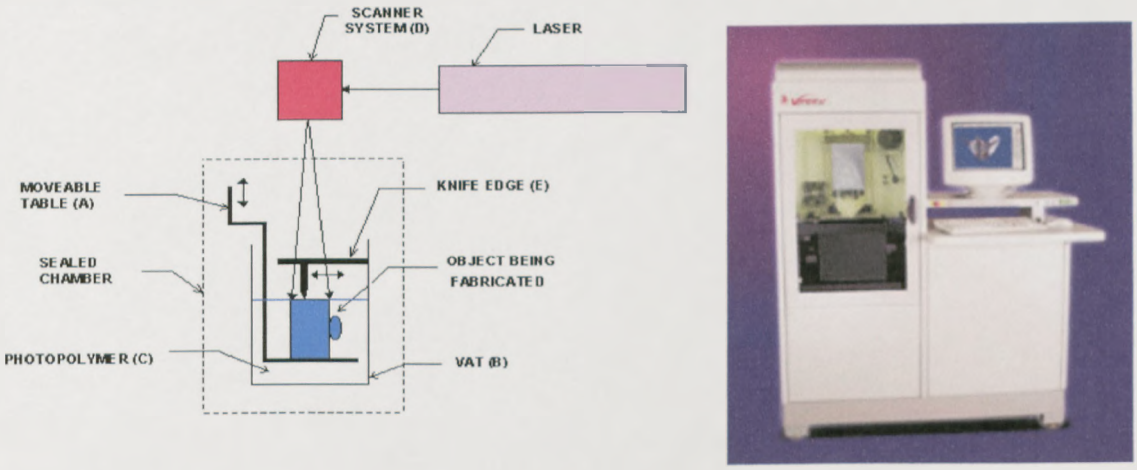

Figure. 1.2 Stereolithography scheme (www.manufacturingtalk.com/2002) and Vipersi2 SLA machine (3D Systems Inc/ 2002)

The ultra-violet laser causes the photo-curable liquid to polymerise, becoming solid. The solid parts are built inside a tank filled with resin on a submersible platform. At the beginning, the platform is raised allowing a very thin layer of polymer resin to be on top of it. The contour of the layer is scanned and the interior solidly filled. The platform is lowered into the vat by the distance of a layer thickness; the next layer is drawn and adhered to the previous layer. These steps are repeated, layer-by-layer, until the complete part is built up. There are some problems arising because of the viscosity of the resin and so called "trapped volume". A "trapped volume" is a volume of resin that cannot drain through the base of the part (Beaman *et* al., 1997).

The most common build styles used in SLA are ACES™, STARWEAVE™ and QuickCast™. Each of these styles has its own features and each is presented below:

a) ACES™ the laser almost wholly cures the interior of the part. This is achieved by using a hatch spacing that is equal to half the line width. This spacing is chosen such that all the photo-curable liquid receives the same UV exposure and hence the downward facing surfaces are flat (3D Systems ltd./2002).

b) STARWEAVE™ provides stability to the solid part by hatching the interior with a series of grids that are offset by half of the hatch spacing every other layer. The grids

are drawn such that the ends are not attached to the part border to reduce overall distortion (3D Systems ltd./2002).

c) QuickCast™ usually is adopted when the prototype is to be employed as a pattern for investment casting as it produces almost hollow parts (3D Systems ltd./2002).

The building styles used in Stereolithography are presented here to introduce some ideas which will be used in the work presented later in this thesis for the improvement of multiple layer sintering using stainless steel powder. Building styles described before are for guidance only and these were not used entirely for multiple layer sintering of stainless steel powder, 314HC, during multiple layer sintering tests presented later in this thesis.

1.2.2 Selective Laser Sintering (SLS)

Selective Laser Sintering is one of the most used rapid prototyping technologies in the world. One of the big advantages offered by Selective Laser Sintering over SLA is the easy way in which the parts can be handled and removed from the sintering area. The author wants to emphasise at this stage that figure 1.3 describes the DTM selective laser sintering process. There is also a German company, EOS GmbH, which produces its own sintering station. While both the DTM and EOS machines are based on the same underlying methodology, there are differences in machine implementations, including their respective material delivery approaches (Beaman *et.* al, 1997).

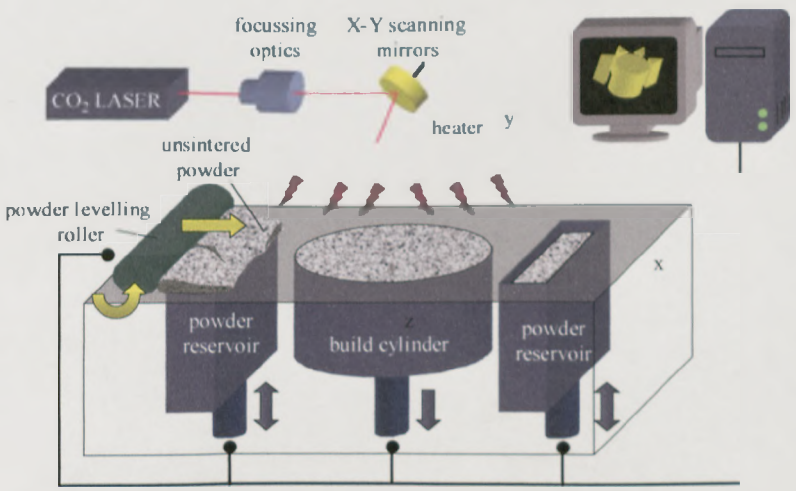

Figure 1.3 Schematic view of Selective Laser Sintering (E. Sachs *et al*, 1995)

A CO_2 or Nd:YAG laser controlled by a computer is used for heating, melting and fusing polymeric and metal powders over a short period of time in a back and forth cyclic manner sintering the powders into the shape of the required cross section.

The principle of Selective Laser Sintering is similar to SLA. A very thin layer of powder is spread over the sintering area; a CO_2 or Nd:YAG laser melts and fuses the powder. The process operates on the layer-by-layer principle. The sintering process uses the laser to raise the temperature of the powder to a point of fusing. As the process is repeated, layers of powder are deposited and sintered until the object is complete. The powder is transferred from the powder cartridge feeding system to the part cylinder (the working space container) via a counter-rotating cylinder, a scraper blade or a slot feeder. In the un-sintered areas, powder remains loose and serves as natural support for the next layer of powder and object under fabrication. No additional support structure is required. An SLS system normally contains an atmosphere control unit that houses the equipment to filter and re-circulate inert gas from the process chamber. It also maintains a set temperature of the gas flowing into the process chamber.

1.2.3 3D Printing

3D Printing is a process based, like SLS, on joining powder grains together. 3D printing uses a binder sprayed through a nozzle. This process starts with a level layer of ceramic or metal powder that is spread and levelled by a roller. An ink-jet printing head scans over the powder surface dropping a polymer binder material where the solid shape is required. As can be seen in Figure 1.4 the unbound powder acts as support material for future overhanging structure. In order to avoid the disturbance of the powder when the binder hits it, it is necessary to stabilise it first by misting with water droplets (D. T. Pham, 1997). Once the part is completed, it is heated to set the binder. Then the excess powder, which has been used as a support, is removed by immersion in water (E. Sachs et al, 1995).

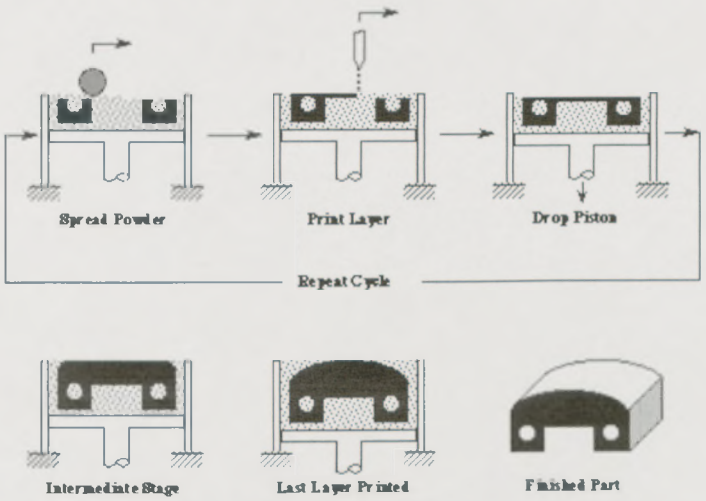

Figure 1.4 3D printing process (www.orbital.com/2002)

The part is next heated up at 900^0C for two hours in order to sinter it. After this treatment, the part may be dipped in binder and reheated so that its strength is improved.

1.2.4 Layer Object Manufacturing (LOM)

Layer Object Manufacturing process was developed by Helisys's Laminated Object Manufacturing Inc in 1985. The first commercial system was introduced on the market in 1991. The principle of this process is based on a laser beam that cuts the cross-section of the adhesive material. LOM is based on the layer-by-layer principle. Attached to two rollers, the adhesive material, usually pre-coated with adhesive, a heat sensitive polymer, is passed over the support platform. The laser cuts and cross hatches all the excess material and a boundary for removal later. The platform then moves down the thickness of the paper. A new layer is advanced from the feed roll and is bonded to the previously cut layer. This process uses a laser power of 25W to 50W to cut the material (D. T. Pham, 1997). Figure 1.5 shows a commercial machine built by Helisys Inc.

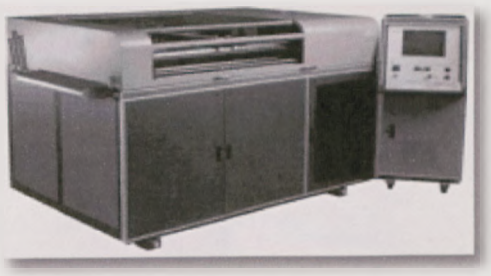

Figure 1.5 Layer Object Manufacturing system, Helisys Inc.

1.2.5 Other Free Form Fabrication processes

There are a few other methods used for creating 3D objects direct from a 3D CAD model. Free form fabrication processes include extrusion (voxel lines), ink-jets and 3D welding. The extrusion process, better known as Fused Deposition Modeling (FDM), was developed and is commercialised by Stratasys Inc. This process uses a continuous thermoplastic polymer or wax filament that is melted and deposited through a resistively heated nozzle. The material is heated to slightly above its flow point so that it solidifies relatively quickly after it exits the nozzle (J.J Beaman, 1997). This process allows building short overhanging features without the need for other support.

Ink-jet technologies use ink jets to directly deposit low-melting point target materials. Ballistic Particle Manufacturing uses a piezoelectric jetting system to deposit microscopic particles of molten thermoplastic. 3D Welding process builds 3D objects using an arc-welding robot to deposit successive layers of melted metal.

1.2.6 Summary

Rapid prototyping technologies can theoretically be used to build any complex shape at any size and with a sub-mm accuracy. The time to market is reduced significantly due to elimination of intermediary steps in the building process.

Although there is such a diversity of rapid prototyping technologies available and each of them tries to improve in the way they build up technology, there are still problems that arise which need to be solved. The reasons for this vary depending on the technique, ranging from inherently weak stock material in some techniques to insufficient density of structural stock material in others. Besides structural properties, the geometric

accuracy and surface finish of these techniques may be somewhat limited for certain applications.

Figure 1.6 presents a summary of the most used Rapid Prototyping technologies with their limitations and benefits.

Process	SLA	LOM	SLS	FDM
Manufacturer	3D Systems Inc.	Helisys Inc.	DTM Corp.	Stratasys Inc.
Materials	Epoxy resins Acrylate resins	Paper	Nylon Composite nylon Polycarbonate Rapid steel	ABS MABS Wax Elastomers
Results	Excellent accuracy and repeatability	Fast build time Good for large parts	No support needed Flexible parts Range of materials available	Small machine No post-processing No laser or liquids
Limitations	Support structures Post processing Expensive for large parts	Poor surface finish Fine detail can be lost	Expensive	Can not produce fine details
Applications	Design verification Low volume prototypes Tooling	Design verification Low volume prototypes Tooling	Design verification Low volume prototypes Tooling	Design verification Low volume prototypes

Figure1.6 Summary of rapid prototyping processes (M. Sarwar et al., 2002)

1.3 Software Issues

The manufacture of the parts begins with a computer generated three-dimensional model of the component. Generating 3D objects by layer-based manufacturing requires the conversion of the geometric description of the shape into a form suitable for processing by the Selective Laser Sintering process or by any rapid prototyping process.

Producing a part by SLS requires a complete, mathematical description of the part's geometry (Beaman *et.* al, 1997). There are three types of modellers used today by the designers to create the basic description: surface modellers, solid modellers and layer based format. Solid models are well known by their ability to determine explicitly whether a point lies inside, outside or on the surface of the part (Beaman *et.* al, 1997). Surface modellers are mainly used for designing the sculptured surfaces; this provides the ability to define a complex surface in terms of series of parametric surface patches "stitched" together such that continuity conditions are maintained at the patch boundaries (Beaman *et.* al, 1997). The layer-based format is the most used for larger manufacture and is derived

from a 3D CAD model, which is numerically sliced by planes, resulting in a pile of 2D sections of the part. Layers are generally 0.05 – 0.3 mm thick. The resulting geometry is transmitted in a standard file format, the "STL" file format, to the PC. "STL" file format is in fact a STereoLithography format. STL format was developed by 3D Systems to prevent losses of information like in International Graphics Exchange Specification (IGES) format and has become a standard input for all rapid prototyping techniques (Thummler *et* al, 1993).

These slicing approaches apply to all rapid prototyping technologies and to all kinds of powders or resins used in the processes presented in the previous sections.

STL format uses small planar triangles to approximate the surfaces building a faceted representation of the part geometry. Each triangle is described in STL format by X, Y and Z coordinates for the three vertices and a surface normal pointing to the outside of the triangle. Figure 1.7 shows the geometrical interpretation of a triangle in STL format.

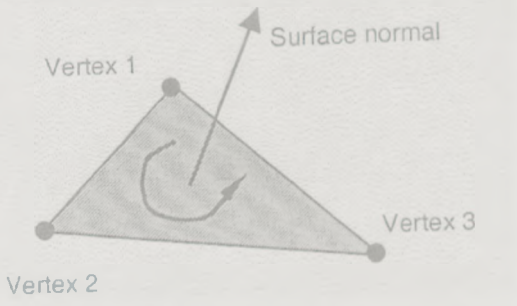

Figure 1.7 Interpretation of STL format

The approximation of the original geometry is linear so the number of triangles used to represent a surface dictates the level of accuracy on a non-planar surface. STL format can be accurate for highly curved surfaces but needs to employ a very large number of triangles (Beaman *et*. al, 1997 and Thummler *et* al, 1993) 2D contours produced during the slicing process will consist of line segments, which are only an approximate of the model geometry. Figure 1.8 shows model geometry approximated with the help of line segments.

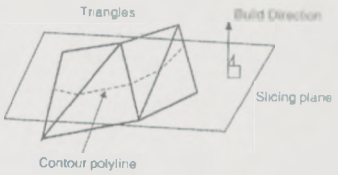

Figure 1.8 Line segments resulting from slicing a STL model

Slicing of the 3D shape plays an important role during the process. Slicing is done by intersecting the 3D CAD model with planes perpendicular to the direction of building (Figure 1.8). Errors called "stair-step" commence due to the layerwise manufacturing affecting the surface finish of the part. "Stair-step" error is caused by the approximation of the angled or curved surfaces with stacked layers of material (Beaman *et.* al, 1997). Figure 1.9 shows the "stair-step" effect and the effect of adaptive slice thickness on part accuracy.

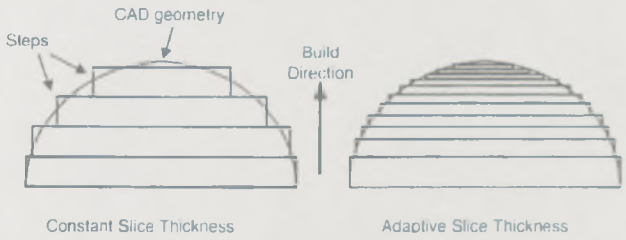

Figure 1.9 "Stair-step" and effects of adaptive slice thickness on part accuracy

This problem can be solved partially if an adaptive slice thickness is used. In many cases, adaptive slicing results in improving accuracy with fewer total slices, resulting in increased build speed (Beaman *et.* al, 1997). Once the geometric model being produced is sliced, the next step is the scanning pattern generation, with particular attention to laser – based rapid prototyping processes. The scanning of a cross section part area is executed using some pre-defined patterns, such as raster (uni or bi-directional), directional, contour or any combination of these patterns. Figure 1.10 shows raster and directional scanning.

Raster scanning is the easiest pattern to fill an area. The laser beam for this pattern is moving in a zigzag way along the x-axis, while increasing between each scan on the y-axis. Directional scanning is characterized by the laser beam following the geometry of the part. In contour scanning the laser follows the contour of the 2D geometry of the layer. Contour scanning is used usually when more accurate scanning is needed.

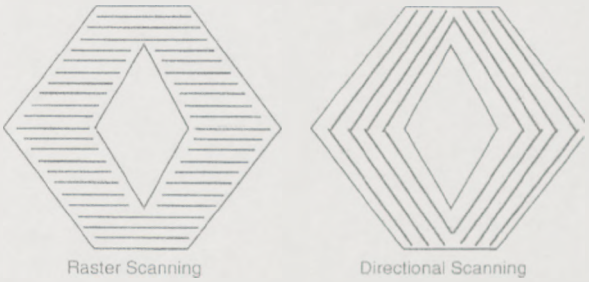

Figure 1.10 Directional scanning and raster scanning (J.J Beaman, 1997)

Beaman *et.* al, 1997 pointed out that for a given geometry, raster scanning generates a large number of short scan vectors and directional scanning creates a smaller number of long scan vectors. This observation is important because it can be concluded that the number and the size of the scanning vectors influence the accuracy and proprieties of the sintered part. The vector length also influences the density and the strength of the sintered part. It has been pointed out that shorter vectors in the raster scanning strategy improves the mechanical proprieties of the sintered part because of less delay between scans (Beaman *et.* al, 1997).

Furthermore, an important role is played during the sintering by the powder's physical properties. The common use of polymeric powders, in comparison to metal powders, is mainly a consequence of the ease of processing at temperatures below 400° C.

Polymers can be classified as being amorphous polymers, polymer chains in a disordered state, or crystalline polymers, polymers chains in a streamlined, regular chain morphology organised into small regions, called crystals. A glass transition temperature, T_g, is present for all polymers; below this temperature the material becomes brittle and rigid. Because of this, sintering of polymers is possible only at temperatures above the glass transition temperature. A polymer is still hard between T_g temperatures and the melting temperature T_m. Although amorphous regions are in a rubbery state its crystallites are still rigid. The polymer is solid below T_m and becomes liquid above T_m; at this state the polymer chain becomes chaotic like an amorphous polymer. Figure 1.11 shows volume change associated with melting of a crystalline polymer.

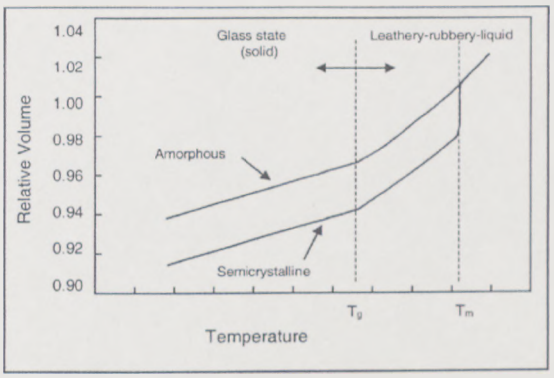

Figure 1.11 Volume vs. Temperature for crystalline and amorphous polymers (J.J Beaman, 1997)

Besides the powder properties, an important factor that affects the final accuracy of sintered polymeric parts, as well as metal parts, is the shrinkage phenomena. Sintered amorphous polymers present not such a big shrinkage compared to crystalline polymers, which have sharp melting transition behaviour and then exhibit high shrinkage (Beaman *et.* al, 1997). Shrinkage in polymers can be prevented by reducing the processing parameters in such way as to minimise sintering or by adding an inert binder to the system.

A further important set of parameters that need to be detailed is the thermal properties of the powder bed including thermal conductivity and absorptivity of the polymeric and metal powders. The importance of these parameters is very high during the sintering process regardless of using polymeric powders or metal powders. Part accuracy, part strength, sintering time and sintering basic requirements are all dependent on these parameters.

The relative density, ρ_r, and the porosity, ε, of the powder beds are very important information for the Selective Laser Sintering process. Apparent density of the powder bed is the density when the powder is in a loose state, the tap density is the highest density that can be achieved by different methods without applying any pressure over the powder bed. Usually, the powder beds have relative densities lying between 35-55% of fully dense, ρ_S, which is situated between the apparent densities and tap densities.

$$\rho_r = \frac{\rho}{\rho_s} \qquad (1.1)$$

$$\varepsilon = 1 - \rho_r \qquad (1.2)$$

Powder bed density, ρ_p, together with thermal conductivity, k, and specific heat, C, are important properties regarding the study of sintering process dynamics. Combining these three parameters, the result is the thermal diffusivity, κ, of the powder bed.

$$\kappa = \frac{k}{\rho C} \qquad (1.3)$$

Thermal conductivity, k, is a key factor during SLS as k states how the heat flows in the powder beds. Thermal conductivity of the powder beds is influenced by factors such as the powder bed temperature and the bed density. It has been observed that powder bed density increases with sintering, decreasing the porosity, and the thermal conductivity increases.

Calculations of thermal conductivity have used complex models, considering the contribution of many heat transfer mechanisms to powder conductivity. These models can predict well the thermal conductivity but a good agreement also could be found using a simple model such as used by Ryder [1998], Childs *et al* [1999] or Tontowi [2000]. The model calculates the thermal conductivity as a function of thermal conductivity of the solid material, k_s, and the porosity, ε (a and b variables are determined experimentally).

$$\frac{k}{k_s} = \left(1 - a\varepsilon - b\varepsilon^2\right) \qquad (1.4)$$

The absorbitivity of the powder bed is defined by the ratio of the absorbed radiation to the incident radiation. The result can be obtained experimentally by measuring the reflected radiation at the powder surface using an integrating sphere and assuming that the radiation reflected plus the absorbed radiation equals 1 (Nelson *et* al, 1993). The powder bed absorptivity varies with the type of laser used for sintering, Nd:YAG or CO_2 laser, due to the different behaviour of the powder according to the wavelengths of the laser radiation.

Attempts to process single-phase metallic powders and powder blends such as, mild steel, tungsten carbide, stainless steel, bronze-nickel and copper-tin have proven complex because of several factors that directly influence the mechanical and physical proprieties of the parts. The main dissimilarity between the sintering of metallic powders

and polymeric powders is the "balling" phenomena that occur during the sintering of metallic powders.

The surface tension is a property of a liquid film where by its magnitude is dependent on the energy of surface atoms per unit area. High surface tensions cause a material to reduce its free energy by forming spheres, balling, a shape that has the lowest area per unit volume. Viscous sintering has been described by Frenkel (1945) using a two-sphere model. The neck of radius x uniting two spheres of radius R grows according to

$$\left(\frac{x}{R}\right)^2 = \frac{3}{2}\left(\frac{\sigma t}{R\eta}\right) \qquad (1.5)$$

where σ is particle surface tension, ηis thermally activated particle viscosity, R is particle radius and t is the time (Beaman *et.* al,1997).

Liquid phase sintering (LPS) is defined as a heat treatment in which a liquid and a solid phase take part so that the sintering materials have more efficient interparticle bonds and higher strength. A first requirement for liquid phase sintering is the presence of wetting; the capillary pressure causes rapid densification of the powder without using external pressure. Liquid phase is present usually during the sintering of hard metals such as high-speed steel, stainless steel and ceramics. The specific surface energies are the main factors during the process. The decrease of the specific surface energies, Δ_γ, of the system as the driving forces results from the energies involved:

$$\Delta_\gamma = \Delta\gamma_S + \Delta\gamma_L + \Delta\gamma_{SL} \qquad (1.6)$$

$$\gamma_{SL} \leq \gamma_S + \gamma_L \qquad (1.7)$$

$$\cos\theta = \frac{\gamma_S - \gamma_{SL}}{\gamma_L} \qquad (1.8)$$

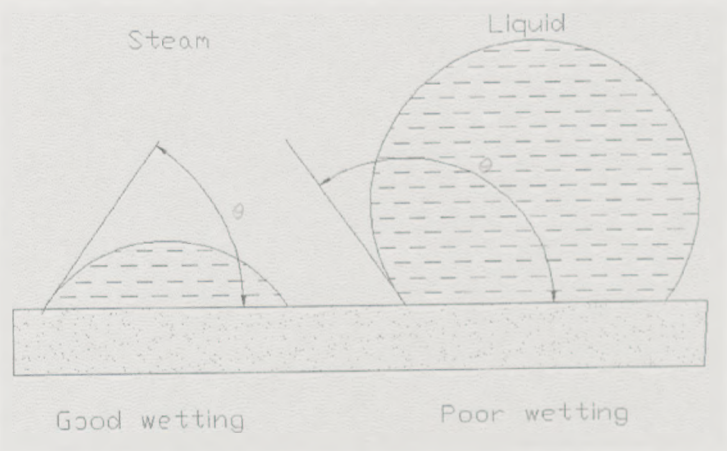

Figure 1.12 Particle-wetting angle

The superficial energy of the particles E is the main factor for starting the process.

The sintering process takes place in three stages:

a) Immediately after melting, rearrangement results in rapid densification of the powder. Particles slide on top of each other and inter-particle necks collapse under the effect of capillary pressure.

b) Densification by rearrangement, dissolution and re-precipitation starts to take place, if the solid particles are soluble to a certain extent in the liquid phase. Solubility in contact amongst the particles is higher than on other solid surfaces. This is reflected in the transfer of material from contact points, thus enabling approach over the centres of the particles and densification.

c) If during sintering the solid particles come into contact without intermediate melting, further densification can result only from material transfer in the solid state.

1.4 Powder bed interactions and effects on SLS

The relative density of the powder bed is directly related to three important factors, particle shape, size distribution and powder bed packing. These three factors establish the initial density of the powder bed, which in turn affects the sintered part density.

The first important factor that influences the powder bed density and also the sintering rate is the powder particle shape. Particle shapes can be classified in two general

categories. First is a circular or a spherical shape and the second is a non-spherical shape. Also the shapes can be outside these two categories and can be irregular shapes such as, angular, cubic, teardrop, sponge, acicular, ligametal, flake and aggregate. Figure 1.13 shows some of particle shapes.

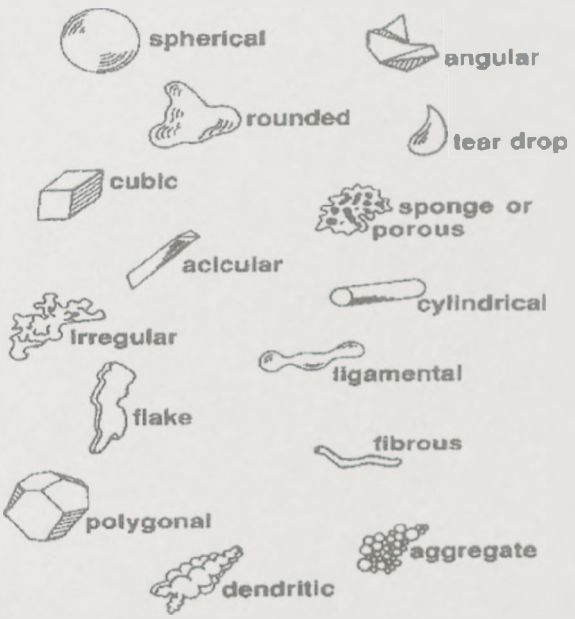

Figure 1.13 Particle shapes (German, 1994)

Experimental studies have shown that the porosity of the packing depends on both the particle size and shape. This is important information in the context of selective laser sintering relating the particle size and distribution to smoothness of the bed surface, bed density and powder flow. The powder's particle size affects the surface flatness and feature definition of the sintered part, the porosity of the powder bed before sintering and the rate of sintering during the process (Nelson, 1993) .

Figure 1.14 shows the four common types of particle size distribution.

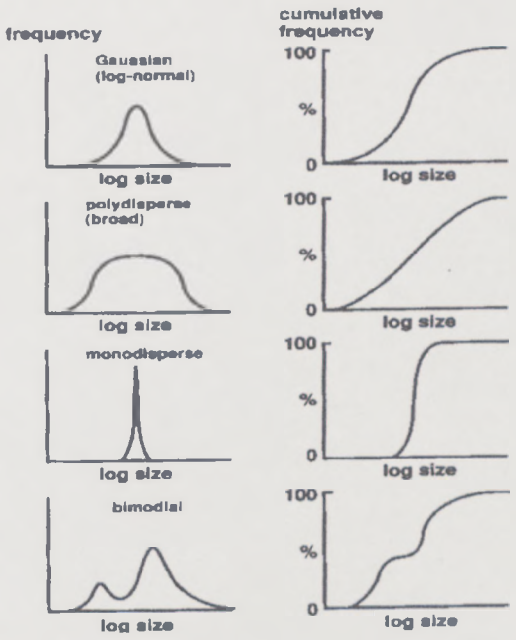

Figure 1.14 Types of particle size distribution

A monodisperse distribution of the spherical particles has a packing density of approximate 60% when assembled in an orthorhombic packing pattern (Beaman, 1997). Polydisperse gives more advantages in terms of packing density improvement because the small particles will pack within the pores of the large particles (McGeary, 1961) Polydisperse is an important type regarding the research undertaken and presented later in this thesis.

1.4.1 Powder bed packing

The apparent density of a bulk powder is defined as the powder mass divided by the bulk powder volume. The latter is related to particle packing. This is affected by the mode of filling, the container size and any external vibration during packing. These factors have to be kept constant. The variables that control powder packing are the particle characteristics of size distribution, shape, mass, resilience, interparticle friction, the container, deposition parameters and finally treatment after deposition (Salak, 1995 and Sontea, 1999).

By using monosize spherical particles, the maximum packing density theoretically achievable with face centred cubic packing is 74%. This value is much larger than the density value given by Beaman for a monodisperse orthorhombic distribution. The packing density can be increased by additions of much smaller spheres filling the interstices between the larger ones (A. Salak, 1995 and F. Thummler, 1993). The maximum packing density in close packing of binary mixures is 86%, with about 73% of coarse spheres in the mixture. The limiting densities can only be reached when all the particles fall into an ideal position. The packing efficiency decreases with increasing deviation from a spherical particle shape and decreasing particle size (A. Salak, 1995 and F. Thummler, 1993).

The relevant deposition parameters are the kinetic energy of the particles and the intensity of deposition. Packing density increases with kinetic energy, but decreases when the intensity of deposition exceeds a critical value (A. Salak, 1995).

The powders may be mixed to produce a powder of the required uniform particle size distribution from different selected fractions or to obtain, if possible, a statistical distribution of the particles for powders produced by different methods.

The aim of preparing a powder of specific size composition is to optimise the apparent density, flow rate and sinterability. If the mobility and density of the particles differ as a result of their form and size, the effect of external forces may cause segregation. The susceptibility of the powders to segregation differs and must be minimised. The quality of the mixture depends on the properties of the powder, such as density, particle form, mixing ratio, mean particle size, particle size distribution, surface structure and type of the mixer (Salak, 1995 and Thummler, 1993).

A non-spherical particle-packing model has been introduced by Buchalter and Bradley (1992). They said that orientation order strongly correlates with the density of the particles' packing. The property depends on the deposition rate. A higher density can be obtained by a lower deposition rate as this leads to a lower order. The irregularities of the particle surface also affect the packing density. Figure 1.15 shows that packing density increases as the particles become more rounded.

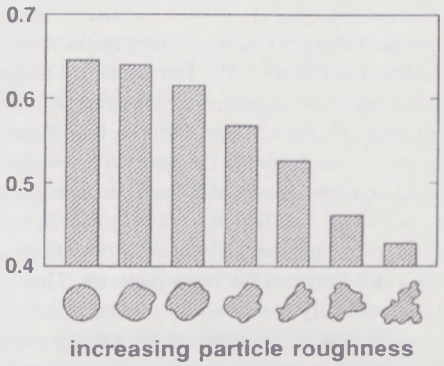

Fig. 1.15 Fractional density of monosize powder for varying particles roughness (German, 1994)

As far as selective laser sintering of metallic powders, especially the sintering of stainless steel powders is concerned, non-sphericity is not a problem as the gas-atomised powder is near spherical. Figure 1.16 shows the particle shape of stainless steel gas atomised powder. The round shape of the powder particles can be seen.

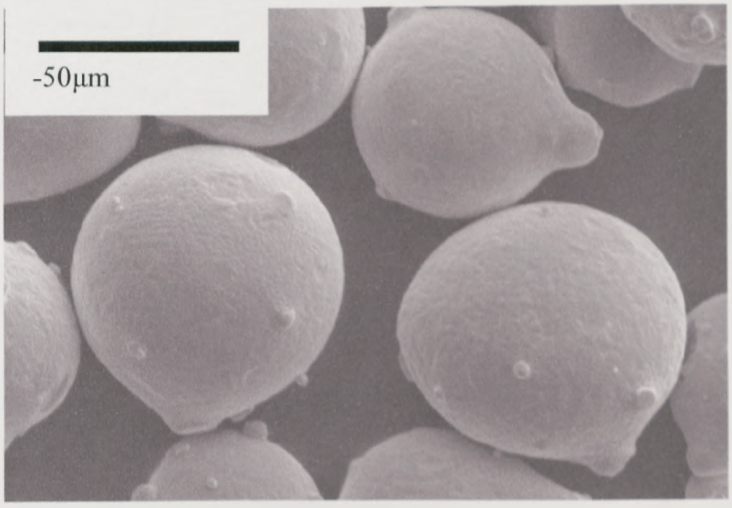

Figure 1.16 SEM image of stainless steel particles - gas atomised powder

1.4.2 Powder bed sintering mechanism

This section will explain the process of material transport during sintering in powder beds and present some models developed from material transport mechanisms.

The selective laser sintering process is one that can be identified by the rate of increase of contact area between the powder particles. The contact area depends on the

mechanism of material transport. Figure 1.17 shows the formation of the neck between two particles. This is the first stage during the mechanism transport.

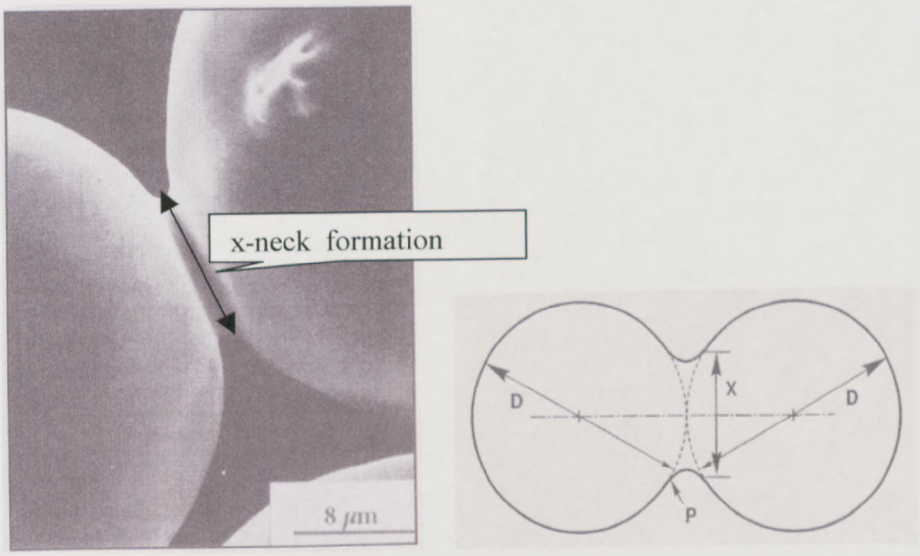

Figure 1.17 Neck formation schematic and real views between two powder particles – first stage (German, 1994)

The model for viscous sintering, already introduced in section 1.3.2, has been described using a two-sphere model (Beaman *et.* al, 1997). The neck joining two spherical particles of radius, R, grows according to:

$$\left(\frac{x}{R}\right)^2 = \frac{3}{2}\left(\frac{\sigma t}{R\eta}\right) \qquad (1.9)$$

$$R = \frac{D}{2} \qquad (1.10)$$

where σ is particle surface tension, η is thermally activated particle viscosity, t sintering time and R is particle radius (Beaman *et.* al,1997).

The model of viscous flow presented by equation 1.9 applies to an early sintering stage and is called the first stage. The second stage takes place later when the material is almost solid and the changing geometry results in modification of the equation above.

$$\left(\frac{x}{R}\right)^2 = \left(\frac{\sigma t}{R\eta}\right) \qquad (1.11)$$

where the notations have the same meaning as in equation (1.9)

The figure 1.18 shows the neck formation during the second stage of mechanism transport.

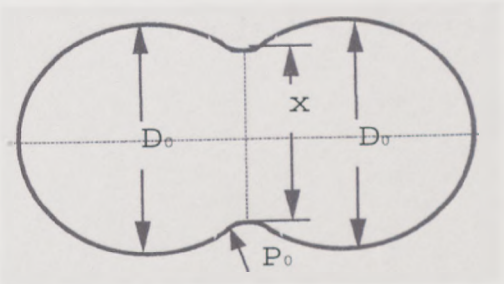

Figure 1.18 Second stage of transport mechanism

The model above is considering only the situation when the particles do not change their radius during the sintering process. An improved model has been considered in which the changing of the particle radius was considered (Beaman *et.* al,1997).

$$R(r) = R_0\left(\frac{4}{\{1+\cos[\theta(t)]\}^2\{2-\cos[\theta(t)]\}}\right)^{\frac{1}{3}} \qquad (1.12)$$

where R(t) is the particle radius at the time t and R_0 is the initial radius of the particle.

The sintering angle, θ, (referred to before as the wetting angle) is defined as $\sin(\theta)=\frac{x}{R}$ and changing with time becomes:

$$\frac{d\theta(t)}{dt} = \frac{\sigma}{\eta R_0}\frac{2^{-\frac{5}{3}}\cos(\theta)\sin(\theta)[2-\cos(\theta)]^{\frac{1}{3}}}{[1-\cos(\theta)][1+\cos(\theta)]^{\frac{1}{3}}} \qquad (1.13)$$

where all notations are the same as in equation 1.9.

1.4.3 Powder delivery systems

Three-powder spreading mechanisms in general use during selective laser sintering can be found in the literature. Figure 1.19 shows these three types of spreading mechanisms.

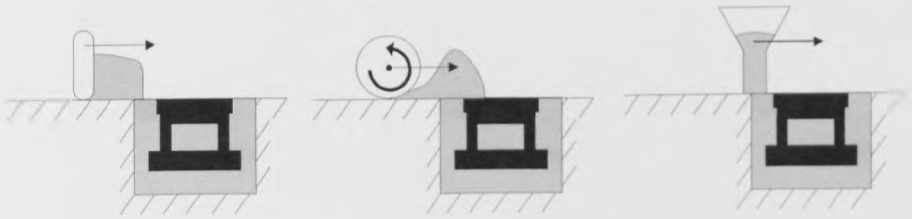

a b c

Figure 1.19 Different powder delivery systems

The first one (See figure 1.19 a) is based on the use of a scraper blade. This method is capable of spreading a uniform powder layer in one operation. This system gives rise to some basic problems; the quantity of powder required cannot be controlled during the spreading, the fixed line contact between the blade and the powder bed surface can cause irregularities in the powder, the powder cannot be compacted during the deposition process and the spare powder increases the weight of the powder shot causing an increase in friction between the moving powder heap and the underlying melted layer.

Alternatively, a solution that can avoid some of the problems associated with the blade system is the rotating roller (see figure 1.19 b). The rotary motion of this mechanism can cause turbulence at the contact line between the roller and the powder bed. This can break down particle agglomeration, smoothing the powder surface. After the roller leaves this contact line, only small disturbances will be visible on the surface of the powder bed. Moreover, the roller mechanism has the advantage that a vertical vibratory motion can be applied over the powder bed. This vibratory motion induces a 'beating' operation over the powder bed which should yield a higher powder density.

To decrease friction between the moving blade or roller and the previously sintered layer, a slot feed mechanism can be considered (see figure 1.19 c). This type of mechanism continually deposits powder during its movement over the sintering area rather than pushing a heap of powder across the building area. As a result, the contact between the sintered layer and the new layer of fresh powder is minimized. There is no 'beating' operation of the powder bed to increase the powder density but the slot feed mechanism has proven successful in reducing layer displacement.

Each of these three mechanisms can deliver the powder into the sintering zone, but none of them fulfils all the requirements imposed by the selective laser sintering technique. A solution has been proposed by combining two of these three mechanisms, a

slot feed mechanism and a rotating roller to create a four stage deposition cycle (C. Hauser, 2001): the cylinder piston is lowered just below the required layer thickness, the slot feed mechanism deposits a layer of uncompacted powder, the piston rises up to the required layer thickness and in the end, the roller crosses the powder bed and compacts the powder layer. Although it may be speculated that the powder bed density can be increased close to the powder tap density using the two deposition mechanisms presented before, it does seam apparent that the irregular distribution of the particles within the powder would make compaction difficult. Besides, the irregular distribution of the particles can also cause the previously melted layers to be displaced from their original position.

1.4.4 Summary

The author believes there are four main factors regarding the sinterability of powders. These four main factors, which influence the powder sintering, are powder packing, powder particle size, powder transport mechanism and powder flow-ability.

Powder packing, particle shape, particle size and size distribution are the important factors that influence powder density and the sintering rate. The initial powder bed density can be improved by compacting the powder. Methods to do this can include the compacting of the powder bed by the movement of the spreading roller mechanism, mixing the powder for some time to reduce the orientation order of the particles or shaking the powder bed.

An important issue that has also been described is the mass transport mechanisms during the sintering of the powders. The neck formation at the early stage has been presented and also the transformation that has taken place during the second stage. A mathematical model of these transformations has also been presented to help understand some very important factors that act during the process. These factors are particle surface tension, thermally activated particle viscosity, sintering time and particle radius. Considering the factors above and the mathematical model, it can be concluded that, based on equations 1.9 and 1.11, the material property, which determines the sintering rate, is the ratio of surface tension to viscosity, $\frac{\sigma}{\eta}$.

1.5 Thermal conductivity and absorptivity of the powder bed

Thermal conductivity is a physical property of the powder which plays an important role during the selective laser sintering process. It determines how the heat conducts into the powder bed. The powder bed used for selective laser sintering in these experiments is assumed to be packed; voids are still present even if the powder has been mixed. The voids are formed within the powder bed because of improper matching among the particles during the mixing process. Otherwise, heat transfer within the powder bed can be assumed to be controlled by a conduction heat transfer law.

It is well know that steady unidirectional heat transfer is described by the following Fourier equation:

$$Q = -kA\frac{dT}{dz} \qquad (1.14)$$

$$q = \frac{Q}{A} = -k\frac{T_0 - T}{dz} \qquad (1.15)$$

where Q and respectively q are the heat flux and heat-transfer rate per unit area, A respectively. $\frac{dT}{dz}$ is the temperature gradient and k is thermal conductivity. Figure 1.20 shows the unidirectional heat transfer representation through a layer of powder. (section 2.2.2 details a conductivity rig which works on this principle)

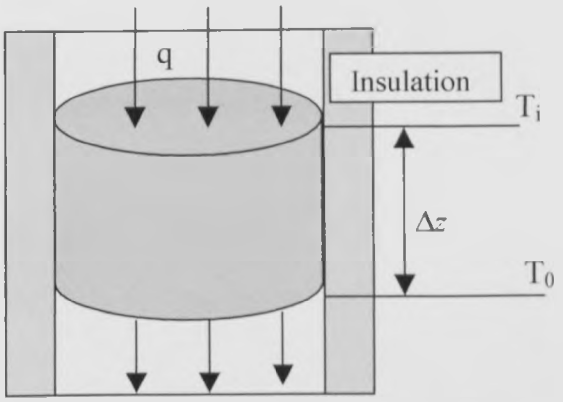

Figure 1.20 Unidirectional heat transfer

There are two main factors that have influences over the thermal conductivity of the packed powder bed. These factors are the void fraction within the powder bed, known as porosity, and the operation temperature. The major impact of the void fraction, ε,

over the thermal conductivity, is that at any operating temperature the thermal conductivity will always be lower than that of a solid part made of the same material. This happens because of the poor conductivity of the gas that fills the powder voids. Therefore, a decrease in the powder bed porosity will be followed by an increase in the thermal conductivity of the powder bed.

The laser energy is converted to heat energy at the surface of the powder bed during the sintering process. As the powder starts to melt and sinter due to the increasing temperature within the powder bed density begins to rise. At the same time the void fraction starts to decrease and a rise in thermal bed conductivity takes place. An important relationship for the sintering process, as the thermal conductivity is changing, associates the void fraction and operational temperatures with the thermal conductivity of the powder bed.

Consequently, some mathematical models of thermal conductivity with varying porosity fraction have been reported. Table 1.3 shows these models where k is the powder conductivity. Models such as Bruggeman-Bottcher, Missenard and Ryder-Childs are summarised in the table 1.1 according to the constants a, b, c and d:

$$k = a(1 - b\varepsilon^{c})^{d} k_{s} \qquad (1.15)$$

a	b	c	d	Investigators
1	1.5	1	1	Bruggeman-Bott
1	1	1	1.5	Bruggeman-Veinberg
0.3, 0.5, 1	1.5	1.5	1	Missenard
1	0.5	1	1	Ryder-Childs

Table 1.1 Mathematical models

A particular interest besides powder conductivity is represented by powder absorptivity during selective laser sintering process. A laser beam is a light source, hence, when it falls on an opaque powder bed, a part of its energy is dissipated and reflected into the surrounding atmosphere. The powder bed absorbs the remaining part of laser energy. The incident laser power (P) will be partially absorbed (P_A) and partially reflected (P_R) as follows:

$$P = P_A + P_R = \alpha P + \beta P \qquad (1.16)$$

where α is absorptivity ratio and β reflectivity ratio.

Dobranich and Dykhuizen (1998) calculated power absorbitivity for –300μm metal powder as being 0.35. On the other hand, C. M. Taylor et al. (2001) found that the values were below 0.25. Taylor also said that the quantity measured is heat retained by the powder bed. Further losses are accounted for compared to radiation-type measurements, i.e. heat convection and radiation from the bed surface. Figure 1.21 and table 1.2 show the experimental results obtained by C. M. Taylor et al. (2001) for stainless steel powder (314s).

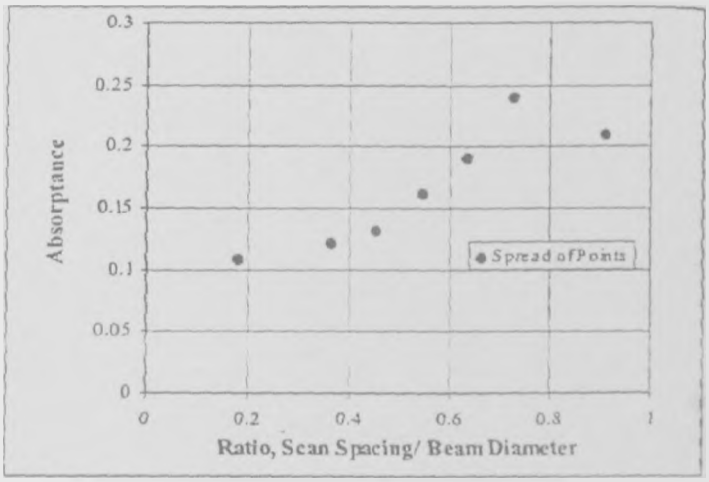

Figure 1.21 Powders absorbitivity variations C. M. Taylor et al. (2001)

Situation No.	Sintered Geometry	Atmosphere	Notes	α (0.0-1.0)	k (W/m.K)
1	60mm single line	Air	α example, Fig. 4.2	0.21	0.25
2	60mm re-scanned line	Argon	See Figure 4.3	0.05-0.13	0.16
3	40x20mm single layer	Argon	See Figure 4.4	0.11-0.24	0.19
4	60mm single line	Argon	DTM Rapid Steel 2. k example, Fig. 4.1	0.10	0.20

Table 1.2 C. M. Taylor et al. (2001) experimental results

Table 1.3 shows absorbitivity values of different powders and solid materials. Only a fraction of the incident laser power is absorbed by a singular metal particle surface. On the other hand, for a powder, which contains many particles, a large amount of the reflected energy will fall onto surrounding particles increasing the overall absorbitivity and allowing the radiation to interact with these particles (Tolochko et al, 2000). Figure 1.22 shows the absorbitivity rate for different solid materials using two kinds of laser.

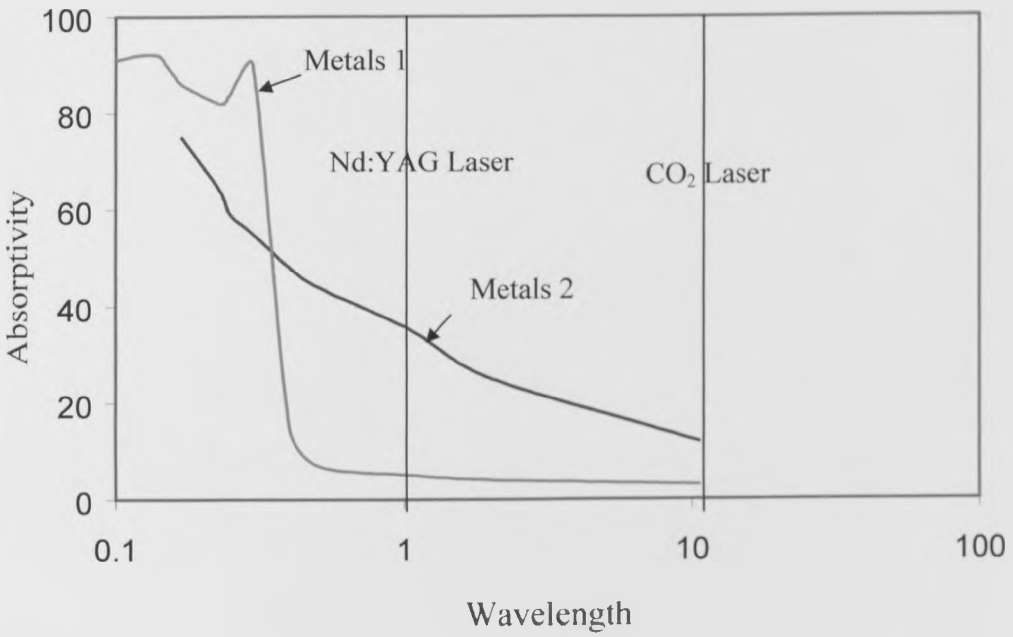

Figure 1.22 Absorbitivity as a function of wavelength for a solid, metals 1 (Au, Ag, Cu,) and metals 2 are transition metals (Fe, Ni, Cr, ...) (Hugel and Dausinger, 1996)

Table 1.3 Absorbitivity rate for some powder and solid materials (Tolochko et al., 2000; Nelson, 1993; Sih and Barlow, 1992)

Material	Nd:YAG Laser (λ =1.06 μm)	CO_2 Laser (λ= 10.6 μm)
Iron	0.46 (solid) 0.64 (powder)	0.45 (powder)
Tin	0.47 (solid) 0.66 (powder)	0.23 (powder)
Polycarbonate	-----	0.95 (powder)

1.6 Scanning parameters

The influences exerted on the final part by particle size, particle distribution, powder bed density, slicing methods, orientation of the part, are very important and affect the properties and accuracy of the sintered part. In addition to these parameters, there are other parameters which should be considered during selective laser sintering such as laser

spot diameter, laser power, scan speed, layer thickness and scan spacing. These parameters play an important role during the process and each can influence the accuracy of the final part.

1.6.1 Spot diameter

Spot diameter plays a crucial role during the sintering process (Steen, 1998). A decrease in the spot size will increase the power density that increases energy concentration and also a decrease will lead to a reduction in exposure area. A smaller spot size allows for increased sintered part definition but will also increse the build time during area sintering.

1.6.2 Laser power and scan speed

The main effect caused by increasing the laser power is to allow melting at faster speeds and a greater depth of heat penetration. The increased scan speed will shorten the time for heating giving less time for the heat to diffuse sideways causing a narrowing of the melt region and heat affected zone.

There is a strong association between laser power and speed. A suitable way of expressing the interaction time as a function of the power density is in the form of a compound variable, which may be referred to as the energy density, Eρ, (Deckard, 1995).

$$E\rho = \frac{P}{2R \cdot u} \qquad (1.17)$$

It can be observed from equation (1.17) that the energy density delivered to the powder bed will increase with increasing also laser power or decreasing spot size and scan speed. The equation above can also be used to compare the interaction parameters found in it with changes in melt pool size and density, which are almost linear (Gedda, 2000). Equation (1.17) gives us only a limited image of the melting response (Gedda, 2000). This is because a number of assumptions have been made in order to get this expression. The physical and chemical properties of the material have been considered to be fixed, the optical properties of the powder bed and melted area are assumed to be identical and fixed throughout the build cycle, changes in layer geometry and vector length have no influence on the melting response and there are no heat losses.

However, despite these negative aspects, variations in laser power and scan speed are used in accordance with to equation 1.12 to observe and compare experimental data. The next part in this section will be the discussion of two issues and some considerations regard the behaviour of a single track melt bed. Melting of pre-placed powder on top of an underlying substrate and melting of pre-placed powder without an underlying substrate are also considered.

The first aspect that will be discussed is when the melt track is supported by surrounding powder. It has been reported that surface tension forces and surface tension drive fluid flow dictate melt pool geometry and stability (Niu et al., 1999 and Abe et. al., 1995). Thus, because the surface tensions are strong in liquid metals, the melt track will try to gain a form such that its surface area will be a minimum and its volume will be a maximum. Hence, the melted track has the tendency to form a cylindrical shape with an area cross-section equal to that of a circle or an ellipse. Moreover, it has been found that a large number of powder particles will sinter to the core of the track and deform the final shape of it (Niu *et* al, 1998). It has also been observed also that surface tension forces try to minimise the surface area by breaking the track into a series of balls. This phenomenon can be controlled partially by using a low scan speed.

The above problems change when an underlying substrate is used to build a track on top it. First, if it is necessary for rastering to be achieved without porosity between tracks, the wetting angle, θ, should be lower than 90^0 (see Figure 1.12). A more detailed presentation regarding the wetting angle can be found in section 1.3.2. If the laser power is high, so that the absorbed energy is high, we can expect a strong bond between even for a large layer thickness (Steen, 1998). Moreover, it is known that the strength of the fusion bond is dependant on Marangoni convection and heat penetration (Steen, 1998). An increased melt penetration is followed by an increase in melt aspect ratio (Steen, 1998).

If the boundary between two fluids is exposed to a temperature gradient, its surface tension will vary from point to point. These surface tension gradients will induce shear stress that result in fluid motion. The effect will cause the fluid to be flowing from regions of low surface tensions to regions with high surface tensions. The fluids, which are viscous, are pulled along causing a volume motion and local stirring of the melt pool. It is this phenomenon that is better known as Marangoni convection.

1.6.3 Scan spacing and layer thickness during SLS

If a sintered layer is to be achieved, overlapping of melt pool tracks will have to take place. Research concerning the optimisation of the scan spacing ratio to achieve uniform density and track layer thickness has been well documented and some of this research will be presented here.

It has been reported that a high level of porosity within a single layer occurs at conditions where single tracks were found to ball such as high scan speed (H.J. Niu et al., 1998). It has also been reported that using some pre-defined patterns such as a rastered or unrastered spot influence the behaviour of the melt in much the same way (H.J. Niu et al., 1998). A process map has been made which summarises the changes in surface morphology of a sintered single layer for a scan spacing of 0.15mm and using a range of CO_2 laser powers and scan speeds (H.J. Niu et al., 1998). Figure 1.22 shows a process map for variations in single layer porosity in experiments with a tool steel powder.

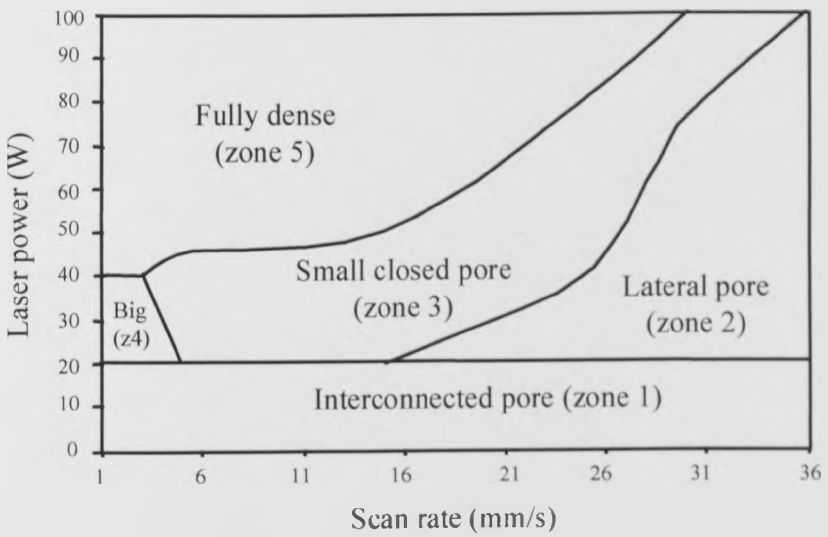

Figure 1.22 Variation within single layers porosity (Niu et al., 1998)

The map contains five zones, each one representing a different mode of solidification. Zone 1, represents the interconnected porosity which occurs at temperatures below the melting point of the powder. Zone 2 represents the inter-run porosity and zone 3 is where a highly dense structure can be obtained but with small areas of porosity. In zone 4 the parts obtained were highly dense but with large areas of porosity and zone 5 is where parts can be made to full density. To conclude, in this example the balling effect can be

controlled at speeds below 30mm/s and laser powers over 40W (H.J. Niu et al., 1998). This is an important observation regarding the research undertaken and presented in this thesis.

The powder sintering process is also influenced by the layer thickness. A thin layer of powder during the process is an important requirement because the bond required to fuse consecutive layers is often difficult to achieve (W.M. Steen, 1998). The reason for this is because the underlying solidified layer needs to be remelted in order to obtain a strong fusion bond. The solidified layer is not directly irradiated during the process; the degree of remelting will depend on the transmitted energy through the fresh powder layer.

As the molten front of the current layer continues through the powder to the layer beneath, it will refreeze at the point of contact due to the additional thermal load caused by the high thermal conductivity of the lower layer; to ensure a strong bond the current layer must be remelted before the substrate melts (Steen, 1998). It has also been ascertained that if the lower layer remains cold, then the current layer will not wet the substrate and the 'balling' phenomena can occur.

It has been also found that the melt depth of the melt front changes depending on the value of the scan spacing. An increase in scan overlap can cause a reduction in melt depth and a decrease in scan overlap can lead to an opposite effect. This phenomenon occurs because of the changes in the absorptivity since the surface and porosity of the powder layer change when it is melted. Hence, a solution for controlling the laser penetration within the powder bed includes increasing the scan spacing or reducing the layer thickness.

It has also been reported that the melt depth can continually increase at the start of a layer only reaching a steady state conditions after 10 consecutive scans.

The total energy E (J) induced into a block with a length l, a width w and a height h and built with a layer thickness L_t is calculated using the following formula (Laoui et al., 2000):

$$E = \frac{P}{v} * \left[l * \left(\text{int}\left(\frac{w}{s} \right) + 1 \right) * \left(\text{int}\left(\frac{h}{L_t} \right) + 1 \right) \right] \tag{2.4}$$

where P is the laser power (in Watts), v is the scan speed (in mm/s), s is the scan spacing (in mm) and "int" refers to integer.

Laoui [2000] reported that for various combinations of layer thickness and scan spacing the density increased with increasing energy. The influence of layer thickness

on density is more pronounced at lower values of supplied energy. With a smaller layer thickness, more energy is transferred to the underlying sintered layers improving further densification. Layers are often barely distinguishable indicating that a high temperature bed and a higher laser power help in improving interlayer bonding.

1.7 Selective laser sintering of metallic powders

A particular issue that will be followed and discussed throughout this thesis is concerned with direct selective laser sintering of stainless steel powders. In the last few years researchers have made advances in the understanding of polymer powder sintering. Conversely, the research involving metallic powders is not very advanced. Because of the high demand for metal tooling, rapid metal tooling development has a position of central importance in rapid manufacturing research. DTM introduced its first metal materials (RapidSteel 1.0) in 1996. This material was primarily used to create steel/copper mould inserts from which large quantities of plastic parts and prototype quantities of pressure die cast parts could be produced. In 1998, DTM introduced its next generation of metal material (RapidSteel 2.0), which offered improvements in processing time, finishing time, and accuracy. Laserform ST-100 is the latest version of the DTM RapidTool process. Laserform ST-100 is a stainless steel 420 based powder coated with a plastic binder that is sintered and infiltrated in one furnace cycle.

There are two approaches regarding selective laser sintering of metal powders, indirect and direct selective laser sintering. Indirect SLS work by melting the polymer coating on each metal particle. This "green" part can then be handled with subsequent de-binding, sintering and low melting point infiltration stages which are necessary to produce a full density part (Beaman et al., 1997). Direct SLS aims to melt and consolidate the chosen metal during the SLS process directly to form a desired shape having full density, eliminating the need for debinding and infiltration.

Direct laser sintering is the main concern of this thesis. Direct SLS is a process in which a high energy laser beam directly consolidates a binderless metal powder, to high density, preferably with minimal or no post-processing requirements. Early attempts to use SLS to process single phase metals such as tin or zinc were unsuccessful due to the quick consolidation of molten powder into a sense of balls with diameter approximately equal to

the laser beam diameter (Beaman et al., 1997). To overcome the tendency to form balls, a low and high melting temperature powder mixture approach was developed (Bunnell et al., 1994; Das et al, 2000). The laser power heats the powder bed inducing melting in only the low melting point material. The disadvantage of this processing route was that the components produced exhibited mechanical properties and characteristics of their weakest composite phase, thus lacking the full mechanical functionality required for heavy-duty tasks. Klocke et al. (1995) and Kruth et al. (1996) reported that due to the brief heat interaction time in SLS processing, the only means of building parts consisting of high melting point metal is via Liquid Phase Sintering (LPS). The liquid wets the high melting point powder and binds it together. Using this two-phase powder approach, it becomes possible to induce melting without balling by adjustment of the volume fraction of the high melting point phase. This approach has been used successfully in SLS processing of metals and ceramics such as Cu-Sn bronze-Ni, Ni-Sn, WC-Co and alumina-boron oxide (Gopalakrishna and Bourell, 1993; Beaman et al., 1997).

There have been other successful attempts to use direct SLS processing for metal and metal-ceramic materials (Deckard et al., 1993). These material systems include binary and ternary mixtures such as bronze-nickel and tungsten carbide-cobalt-nickel. The nickel is the high temperature component and bronze forms the liquid phase during SLS processing. With this material system densities up to 80% of theoretical density were attained. To increase the density of bronze-nickel parts to 95% of theoretical density, traditional liquid phase sintering at elevated temperatures was used (Agarwala et al., 1993).

Carter et al (1993) sintered iron powder using direct laser sintering, but the final density was very low (35% of theoretical density). Carter explains that due to the greater thermal contraction on the upper surface of each layer the sintered powder tends to warp upwards. They built an anchor of thin sintered layers onto which the actual structure was constructed to overcome this problem. Other ways to avoid warping and distortion of layers include; heating the powder bed (Carter et al, 1993; Klocke et al., 1995) and bonding the part to a rigid sample of the same material during the first stages of the sintering process. Simchi et al (2001) investigated laser sintering of steel based powder mix. They noted that careful consideration of shape, size and distribution of the particles and the chemical constitution of the powder system can increase the powder bed density for laser processing. They reported densities of 90-97% theoretical for the laser sintered

material without shrinkage, and 99% of theoretical density after a post processing step. Another material approach was a cermet composite used for the production turbine sealing components. This cermet composite is composed of two different types of titanium coated ceramic abrasive grit, a nickel alloy matrix, and a lower melting point cobalt based braze material (Fuesting et al, 1996). They reported that energy densities of 2000 to 4000 J/cm^2 were required to eliminate porosity. Energy densities of 1900 to 2200 J/cm^2 produced a very fine-grained equiaxed fully dense super-alloy microstructure which may exhibit super-plastic properties at elevated temperature, and energy densities in the range of 2500 to 3500 J/cm^2 produced a fully dendritic microstructure. They also reported that mechanical testing results indicated that direct SLS can produce properties equivalent to or better than conventional labour intensive processing.

Wilkening (1996) has been successful in sintering a mixture of Ni, Cu, Sn and P using direct laser sintering. The porosity of parts produced by this process is approximately 25%, which requires a secondary process to fill the pores improving the mechanical characteristics of the part and creating a much smoother surface. This process is commercialised by EOS GmbH with the name of EOSINT M. The EOSINT M builds tools for plastic injection moulding and metal die-casting. The system offers a high performance layer manufacturing technique where even complex shapes can be built with ease, including geometric shapes and internal cooling channels which are impossible to make with conventional tools This sinter station machine can build metallic parts up to 250 × 250 × 185 mm^3 using a Nd:YAG laser. The laser scan speed reached 3000 mm/s. Although in some studies, as reported above, it is possible to obtain parts with high density using direct metal sintering (Klocke and Wirtz, 1996; Das et al., 1997) the materials are limited, and the accuracy and surface finishing is poor.

Moreover regarding other aspects of direct laser sintering, Niu and Chang (1999 a) discuss surface tension effects and conclude that surface tension driven fluid flow dictates the melt pool shape. The strong surface tension forces will act to minimise the surface area further by breaking up the liquid bead into a series of balls. This phenomenon was found to be a major concern during early direct metal laser sintering research.

Niu and Chang (1999) further discussed that the balling problem for M2 high-speed steel could be controlled at scan speeds lower than 20 mm/s. They also demonstrated that at high laser powers (80W-150W) and scan speeds of 10-20mm/s balling became more

widespread. Hence a balance between power and speed had to be found. This could be achieved by decreasing the scan speed further (<10 mm/s). Niu and Chang (1999) attempted to use Raleigh instability to explain the phenomena of melt balling, which describes the break up kinetics of a column of liquid, and could be used to help explain melt pool balling during selective laser melting.

O'Neill (2002) using an Nd:YAG laser sintered a 316 L stainless steel powder batch. O'Neill and concluded that the scan spacing and scan length have a high impact over the sintered coupons. O'Neill also discussed that scan spacing had a significant effect on the total energy delivered to the powder layer. He added that a small scan spacing resulted in an increase in overlap of the scan lines and hence an increase in the total energy imparted on the powder layer. Also, a low scan spacing was shown to produce strong fusion bonds at high speeds and relatively low powers.

Figures 1.23, 1.24 show some coupons obtained by O'Neill using a Nd:YAG laser.

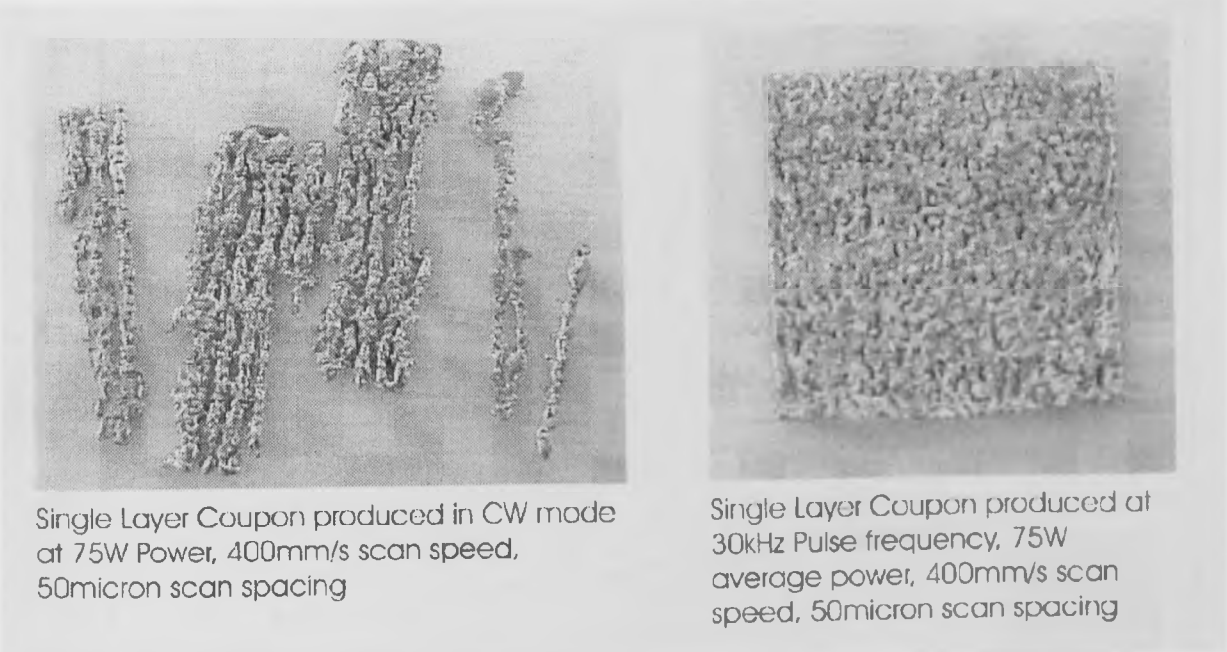

Figure 1.23 Layers scanned using 75W laser power O'Neill (2001)

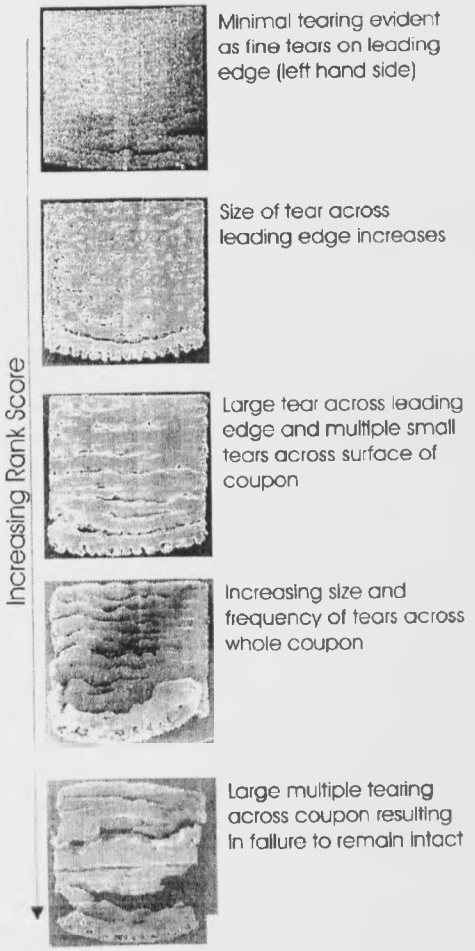

Figure 1.24 Coupons scanned at different scan speeds and laser settings using a Nd:YAG Laser, O'Neill (2002)

O'Neill also observed the formation of a first scan line. He said that as the first line is created the temperature distribution is uniform across its cross-section. As further lines are scanned a steep thermal gradient is generated and differential thermal expansion occurs. At smaller scan spacing, more scan tracks are required to make the layer and the cumulative compressive stress is increased and therefore several tears may appear across the layer. Regarding the scan length, O'Neill added that the time between scans is a significant factor. As the scan tracks increases in length, the time taken to complete a single track is increased, resulting in a longer exposure to the heat source. In this case, the bending effect appears due to the thermal gradients. Figures 1.25 shows the coupons scanned at different scanning conditions (O'Neill 2001).

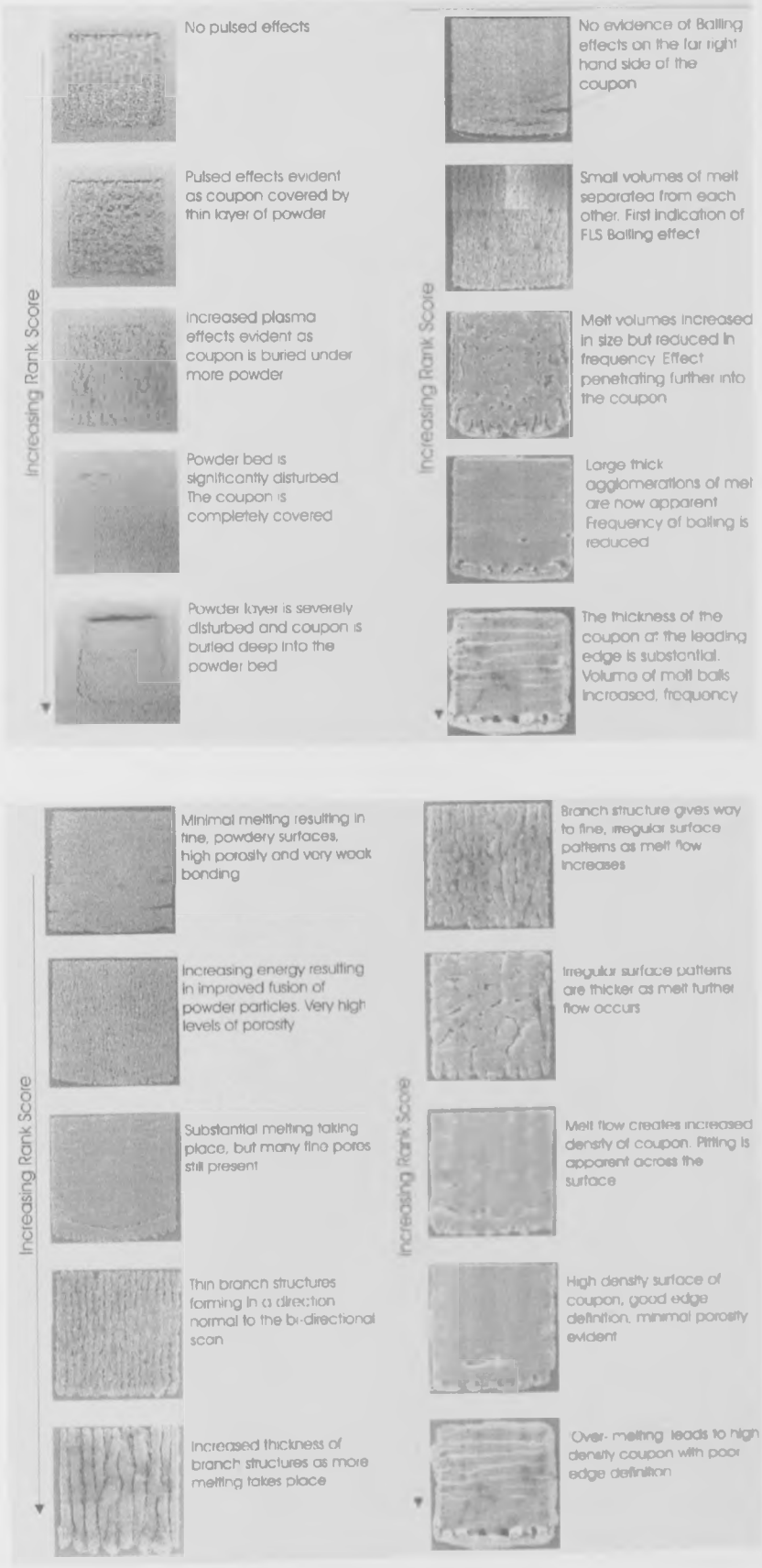

Figure 1.25 Coupons scanned using a Nd:YAG laser (O'Neill 2001)

In addition, Hauser et al. (1999 a) carried out research using a CO_2 laser on stainless steel powder. The research proved that the presence of oxygen within the sintering atmosphere and powder bed allows surface oxides and slags to form as the powder is heated and melted by the scanning laser beam. They added that the elimination of all oxygen is required in order to reduce the melt volume allowing surface tension forces to become less dominant. In addition, Hauser et al. (1999 a) found out that in order to obtain a good sintered layer the length of scan should be short. They carried out their research using direct laser sintering for powder beds at room temperature. Hauser further said that the thermal gradients that exist during sintering caused severe warping and stress cracking when the scan length was long. Figure 1.26 and 1.27 show the result obtained by Hauser et al. (1999 a) using 316s HC powder.

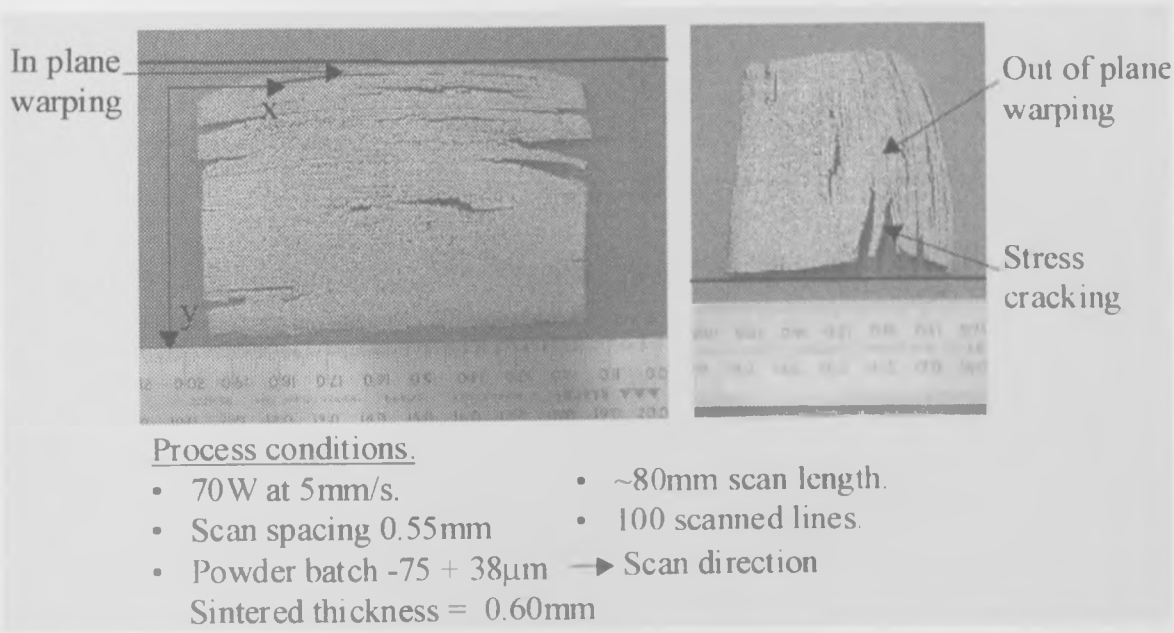

Figure 1.26 Warping coupons with scanned using a CO_2 laser (Hauser et al. 1999 a)

Hauser et al. (1999 b) further said that the range of conditions for successful multiple layer sintering were similar to conditions for single layer sintering. They also found that higher energy densities (>1.5J/mm^2) were needed in order to improve the layer bonding.

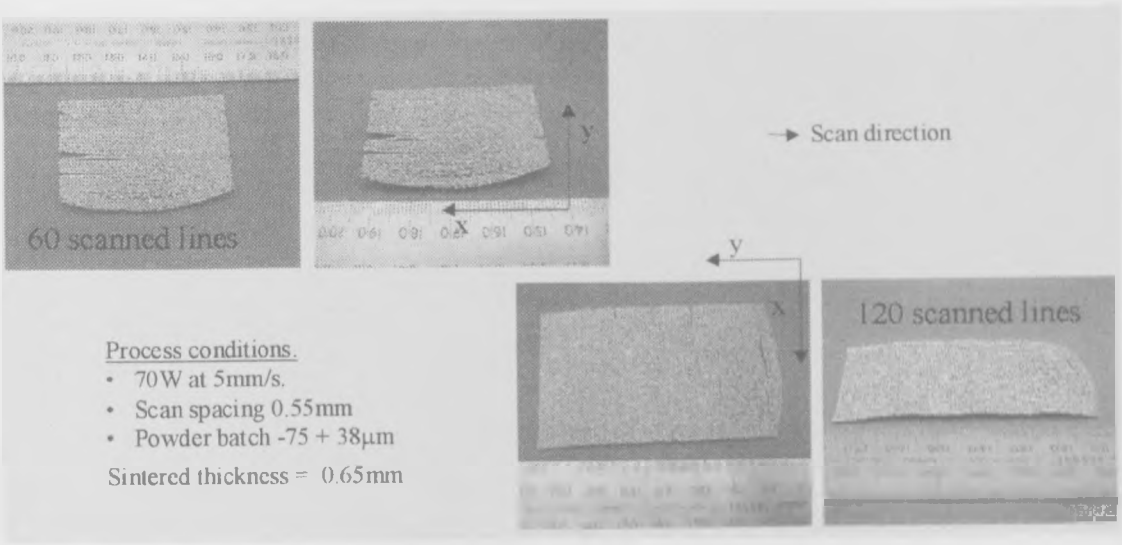

Figure 1.27 Influence of scan length on coupons scanned using a CO_2 laser (Hauser et al. 1999 a)

Dewidar (2002) carried out research using a High Speed Steel powder. The laser used during this research was a CO_2 laser. Dewidar also added, like all the researchers before him, that the length of each scanned line within a raster scan set is a major contributor affecting the degree of warping of a single layer. As the scan length increases the probability of warping also increases resulting in dramatic upwards movements of single layers. He also noticed that the monolayers built at low laser powers were fragile. Figures 1.28 and 1.29 shows some of the coupons scanned using an argon atmosphere by Dewidar (2002).

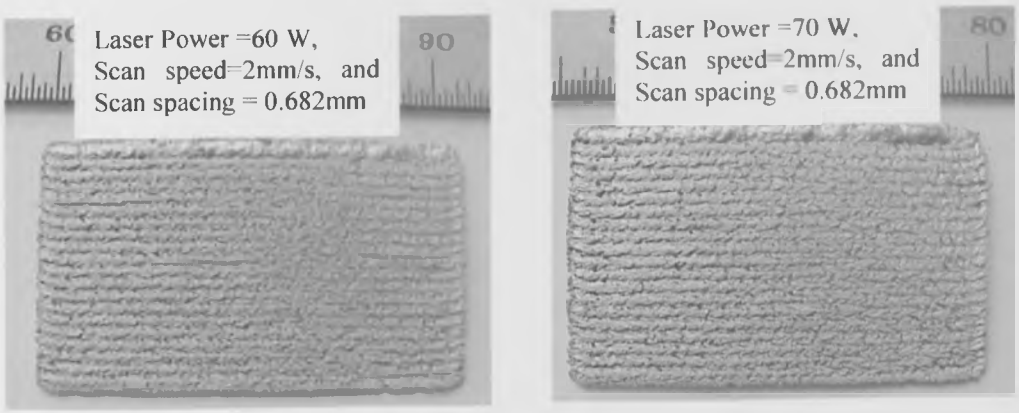

Figure 1.28 Coupons scanned using a CO_2 laser in an argon atmosphere (Dewidar 2002)

Dewidar also found that the best conditions to build a good monolayer (high quality, uniformity, good density, and repeatability) are: laser power=50 W, scan speed=1mm/s, and scan spacing=0.682 mm using a CO_2 laser beam with a diameter of 1.1 mm. He added that even in this case there are possibilities of cracks to appear on the layer surface. Dewidar tried different strategies of rastering but each proved to be unsuccessful. Figure 1.29 shows some of his attempts.

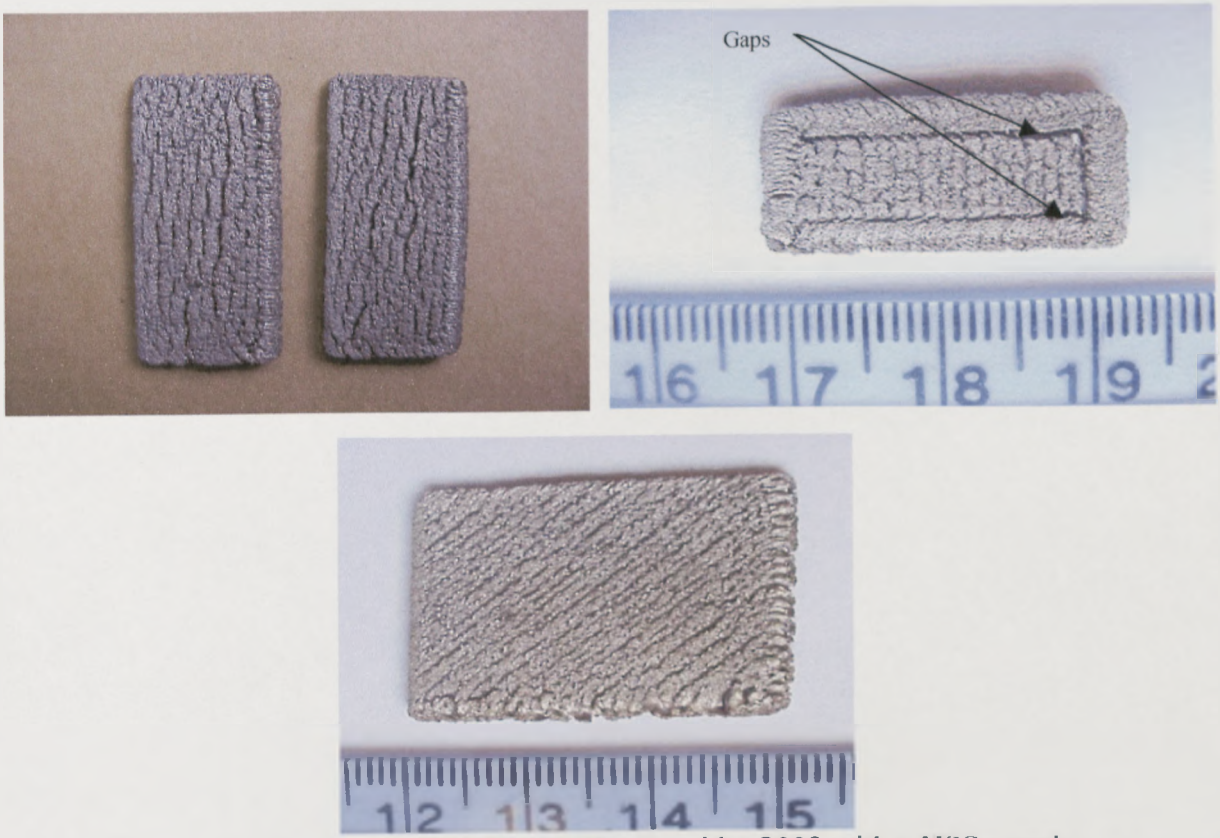

Figure 1.29 Rastering strategies used by Dewidar 2002 with a HSS powder

Although in some studies, as reported above, it is possible to obtain parts with high density using direct metal sintering (Klocke and Wirtz, 1996; Das et al., 1997, Hauser et al. 2001, O'Neill 2001, Dewidar 2002) the accuracy and surface finish are poor. More research is needed to be able to improve the properties and accuracy of parts that are produced by direct laser sintering.

1.8 Present work

In this chapter previous work has been examined regarding various rapid prototyping techniques and in particular selective laser sintering. The present work aims to gain a better understanding of direct selective laser sintering of stainless steel powder without using any binder. The differences between the sintering of polymer powders and metallic powders are represented mainly by their properties and how the metallic powders act during the sintering process.

1.9 Goals and objectives of the thesis

The main objective of the research presented in this thesis is the improvement of the direct selective laser sintering stainless steel, 314HC, powder and to improve the powder delivery system in the Leeds High Power Sintering Station. The goal is to develop the understanding of the effects of laser scanning parameters, laser power, scan speed and scan spacing on processing. Further aims are to understand powder bed properties, to develop new overlapping strategies for improving part density, to design a new delivery powder mechanism for the sintering area and automation of the entire process. Results of this work will then be used to build suspended single layers typically found at the start of a build or overhanging features. The results of this research will be used to produce multiple layers and to analyse the importance of the layer thickness during the build process.

1.10 Management of the Thesis

This thesis is comprised of five chapters. Chapter 1 contains an introduction and literature review of existing knowledge regarding rapid prototyping and in particular, the selective laser sintering technique. Chapter two describes the techniques used in powder preparation and discusses the apparatus used to measure the powder flowability and powder thermal conductivity. The Leeds High Power Sintering Station (LHPSS) and the slot feed mechanism design for use with the LHPSS are also discussed. Chapter three contains the preliminary experimental tests carried on the stainless steel powder followed by sintering tests results for single tracks using different apparatus settings and two different atmospheres. Chapter four contains the research results for single layers and

multiple-layers created using different conditions. Chapter five contains the discussions and conclusions.

CHAPTER 2

EXPERIMENTAL EQUIPMENT AND METHODS

2.1 Introduction

Chapter two of the thesis explains and presents all the equipment and research methods used during the research undertaken involving direct selective laser sintering of stainless steel powders. Additionally, a part of this chapter presents the design process of the new slot feeder mechanism used in the Leeds High Power Sintering Station.

Before entering into details, a brief survey of the three main parts of the thesis- the sintering of single tracks, the sintering of layers and multiple-layers and the development of powder mixing and spreading procedures and equipment – is presented, to give a context to the remainder of the chapter. The first task of single track melting experiments was performed under different conditions using powders from a single size range and from a mixed size range. Four batches of powder have been used, each having a different particle size, and melted using different laser powers, scan speeds and scan lengths for manufacturing a series of line scans. The chamber atmosphere used during the experiments was controlled and argon gas was pumped into the chamber continually. The experiments include depth, width and mass measurements of the sintered tracks, comparative observations between the different powders and microscopy studies monitoring the changes in the tracks microstructure. The research regarding line scans has been conducted especially to determine the effects of the powder, scanning and chamber conditions on melt pool shape. Furthermore, observations were carried out specifically to collect information about the differences that took place when mixed powders were used compared with single batches of powder. As a result, all the information obtained was compared and mapped.

The second task of this research was developed from the information obtained from the first task with emphasis on morphological changes, surface roughness and porosity during single and multiple layer production.

Finally, since it was important at the beginning of this study to create a level of uniformity in the deposited powder layer, it was also thought useful to use powder-

mixing equipment to control particle distribution homogeneity in the powder before powder spreading over the sintering area. In addition, the necessity of building multi layers has required the development and design of a new spreading mechanism trying to replace the previous one, which did not meet expectations.

Chapter two is organized in three sections which summarize the materials, experimental procedures and equipments, calibration procedures and software used during the entire process. Section 2.2 describes the experimental powder, including considerations regarding powder mixing, powder flow rate, powder density and powder thermal conductivity; section 2.3 describes the experimental sintering station, the Leeds High Power Sintering Station (LHPSS). Besides, section 2.3 describes the design process of the slot feed mechanism (SFM), which is in use in the LHPSS. Also, this section explains the software used for controlling the SFM and the HPGL code used to control the laser beam. Section 2.4 describes the experimental conditions and the calibration procedures. Section 2.5 is the chapter summary.

2.2 Powder composition, size range and storage

The four batches of powder used in this research were argon atomised austenitic stainless steel alloy of type 314S HC. The acronym HC signifies the high content of carbon that existed within the stainless steel alloy powder. Osprey Metals Ltd. supplied the powder and each batch is separated by particle size distribution as follows: -300+150μm, -150+75μm, -75+38μm and -38μm. The table 2.1 shows the main components which are present in 314S HC powder.

Table 2.1 Composition of 314S HC powder

Elements	C	Fe	Ni	Si	Cr
Wt %	0.4	53.6	20	1	25

The gas atomised production method has been chosen because the particles obtained are spherical in shape, show low surface oxidation and smooth surfaces. It was considered that these characteristics permit a more accurate evaluation of flow properties between the four types of powders and diminish the problems of powder contamination.

Osprey Metals Ltd delivered the powder in self-sealing containers (figure 2.1) of five kilograms each. These containers were used also for powder storing. The experimental powder has been filtered to remove the larger bits of melted metal after use in the sintering station and stored separately in different containers (figure 2.2).

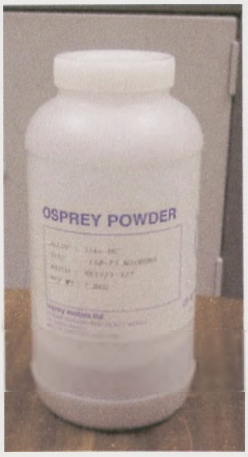

Figure 2.1 Self-sealing containers
Osprey Metals Ltd (5 kg each)

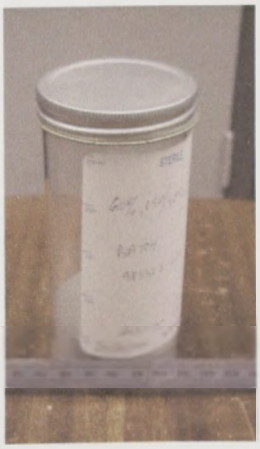

Figure 2.2 Containers used for storage of the used powder

The experimental powder was used in its initial state without attempting to change its state by warming it up. But in some experiments the powder was degassed by infiltrating argon gas throughout the powder bed during the sintering process.

Throughout the duration of this research the powder handling was kept to a minimum. Two reasons were considered for this approach. Firstly, to keep the reproducibility of data by preventing particle segregation and exposure during handling. Secondly, to reduce the adsorption of contaminants from the atmosphere.

2.2.1 Powder mixing

Powder mixing tests were carried out using five v-cone mixers. The design allowed for several different powder samples to be mixed simultaneously. Each v-cone (figure 2.3) consisted of two stainless steel tubes welded together to form a 60^0 V form. Powder was placed in the mixer through the tube open ends prior to being sealed using two

threaded caps. Each cap was fitted with a rubber o-ring to ensure the sealing of the v-cone.

Figure 2.3 V-cone

The mixing was carried out using rotation provided by a lathe (figure 2.4). The procedures were as follows. All five v-cones were fitted to a central shaft, displaced by 72^0 rotation to reduce the vibration during use. The mixer assembly was placed between centres of the lathe and turned for the amount of time required. Figure 2.4 shows the mixer assembly fitted between the lathe's centres.

Figure 2.4 V-cones mixer assembly used for powder mixing

2.2.2 Powder flow rate, density and thermal conductivity

Powder flow rate

Flowability rate of the powders was characterised by two main methods. Either the Hall flowmeter test or the Carney flowmeter test was used. Two methods were needed due to the poor flow rate encountered for the very fine particle size powders, as will be

seen in Chapter 3. A flowmeter was designed, manufactured and supported using a laboratory clamp stand. The experiments were carried out in accordance with the standard tests for Carney and Hall flow meters. Figure 2.5 shows the Hall funnel built for this study. The required specifications and engineering drawings can be found in Appendix A. Figure 2.6 shows the Hall funnel assembly.

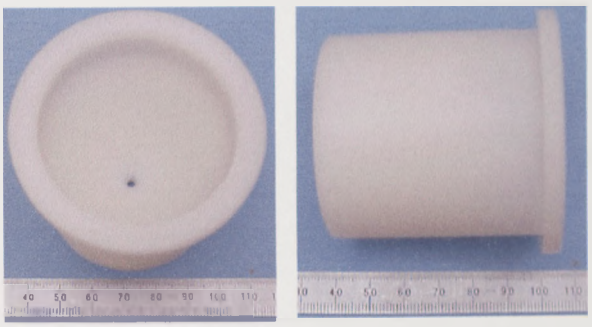

Figure 2.5 Hall's funnel build

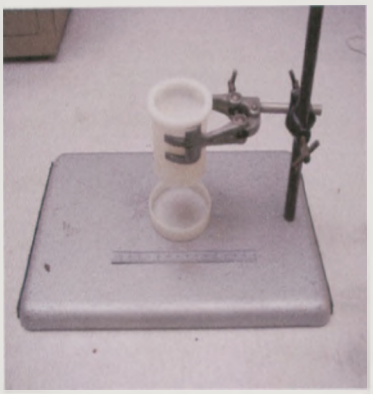

Figure 2.6 Hall's funnel assembly

The flowability is measured by the time required for 50g of a powder to flow through the flowmeter under the influence of gravity. The flow time of a 50g powder sample is determined in seconds. The flow time is dependent in a complex manner on the internal friction between the powder particles and the funnel geometry. Flowability is greatly affected by the particle size and shape. Very fine powders flow poorly or not at all because of the forces which appear at the surface of the powder.

The Carney funnel has the same dimensions as those of Hall's, except for a larger orifice diameter of 5mm compared with Hall's of only 2.5mm (figure 2.7).

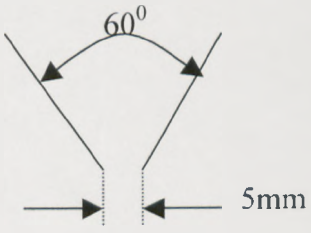

Figure 2.7 Schematic view of Carney flowmeter

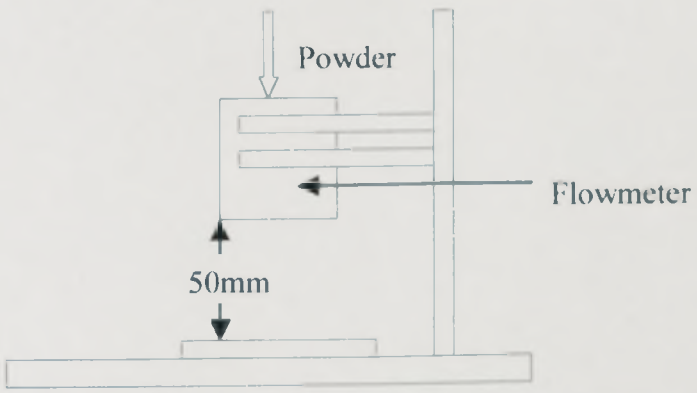

Figure 2.8 Schematic view of Carney flowmeter assembly

Figure 2.8 shows the standard clearance from the flowmeter lower base to the collecting container.

In order to determine the influence of the powder flow on direct laser sintering, powder flowability rate was measured. Besides mono size powders, mixed powders were also used and a comparison between the two types of powders was considered.

Table 2.2 summarises the experimental tests carried out.

Test number	Powder mix (μm)	Powder mixing times (min.)
1 1.1	-38μm	15,30,45,60
1.1.2	-75/38 μm	15,30,45,60
1.1.3	-150/75μm	15,30,45,60
1.1.4	-300/150μm	15,30,45,60
1.1.5	-300/150 with addition of 0 to 100 %, -38μm	15,30,45,60
1.1.6	-150/75 with addition 0 to 100 % of -38μm	15,30,45,60
1.17	-75/38 with addition of - 0 to 100 % of 38μm	15,30,45,60
1.1.8	-300/150 with addition of 0 to 100 % of – 75/38μm	15,30,45,60

Table 2.2 Flow rate experimental tests number

Powder density

The powders may be mixed to produce a powder of the required uniform particle size distribution from different selected fractions or to obtain, if possible, a statistical distribution of the particles for powders produced by different methods.

The aim of preparing a powder of specific size composition is to optimise the apparent density of the powder, flow rate and powder sinterability. The quality of the mixture depends on the properties of the powder such as density, particle form, mixing ratio, mean particle size, particle size distribution and surface structure.

If the mobility and density of the particles differ as a result of their forms and sizes, the effect of external forces may cause segregation. The susceptibility of the powders

to segregation was minimised during this research by eliminating the powder storage time between mixing and use.

V-cone mixers are used most extensively and are suitable for dust fractions and fine-grained materials. The powder mixing experiments were carried out using the V-cone mixer. The stainless steel powder was transferred from its sealed plastic container into a small plastic tray. The V-cones were filled to 30% of their capacity each. Also, when only a small amount of powder was required, only one V-cone was used for mixing, keeping the others empty. It was suggested that a powder volume of 25-40% used with the V-cones would be optimal for powder mixing process.

The powder mixing times chosen during the experiments were 15min, 30min, 45min and 60 min. The chuck-selected speed during the mixing process was chosen to be a fixed value of 77 rpm. These values were kept constant during the experiments.

In addition, based on results from single powder experiments the batches of powder were coupled and mixed together in different size fractions. The measurements of different size fractions were carried out using a machined nylon cup.

Figure 2.9 shows the nylon cup of known volume used during powder density calculation. The plastic cup physical parameters are as follows:

- weight – 4.88 g
- inside height – 10 mm
- inside diameter – 35mm

Figure 2.9 Machined nylon cup

The powder density was measured before and after mixing. The density of each shot was calculated according to equation 2.1:

$$e = \frac{M - M_C}{V} \qquad (2.1)$$

where M is the weight of the powder, M_C is the weight of the cup and V is the volume of the cup.

Table 2.3 summarises the powder density experimental tests carried out for all four batches of powder

Table 2.3 Powder density experimental tests

Test Number	Powder mix (μm)	Powder mixing times (min.)
1.2.1	-38μm	15,30,45,60
1.2.2	-75/38 μm	15,30,45,60
1.2.3	-150/75μm	15,30,45,60
1.2.4	-300/150μm	15,30,45,60
1.2.5	-300/150 with addition 0 to 100 % of -38μm	15,30,45,60
1.2.6	-150/75 with addition 0 to 100 % of -38μm	15,30,45,60

Powder thermal conductivity

In selective laser sintering (SLS), thermal conductivity of the powder bed plays a key role in conducting the heat of the laser beam within the powder bed. Measurements regarding the powder thermal conductivity were carried out using a conductivity rig. Figure 2.10 shows the schematic view of the conductivity rig, its connectors and PC and table 2.4 summarises the thermal experiments carried out.

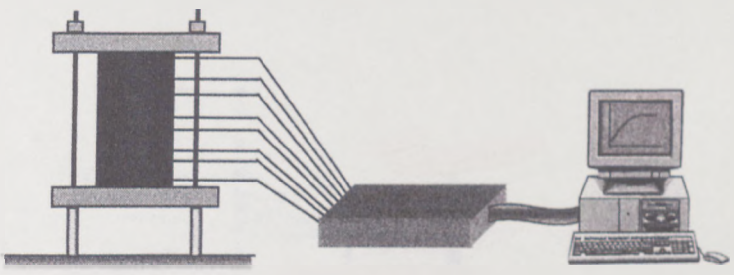

Figure 2.10 Schematic view of thermal conductivity rig connectors and PC

Table 2.4 Thermal conductivity experimental tests

Test number	Powder mix (μm)	Heating time (min)
1.3.1	-38μm	75,100,125,150
1.3.2	-75/38 μm	75,100,125,150
1.3.3	-150/75μm	75,100,125,150
1.3.4	-300/150μm	75,100,125,150

Figure 2.11 Thermal conductivity rig

Figure 2.11 shows the thermal conductivity rig used during the experimental tests.

A comparative experimental method was used (A. Tontowi, T.H.C.Childs, 2001). The heat conduction through a reference disk was compared with that through the powder specimens. A heat source situated on top of the rig, was heated up (for a schematic view see figure 2.12). The heat was transmitted through the powder specimens and reference disk. A one-dimensional flow was created by insulating the stack of disks, firstly placing the disks in a plastic isolator tube and then filling the tube with glass wool. A new tube is placed over and locks the whole system.

The temperature variation along the whole assembly is measured by eight thermocouples. There are two thermocouples allocated for each reference disk (T1 to T8 in figure 2.12). The reference disks are disks made of a material with a known thermal conductivity. The reference disks were made of austenitic stainless steel 316 with a thermal conductivity of 15.3 W/mK. The thermocouples enable the temperature gradient in each of

the four reference disks to be obtained. By extrapolating the temperatures in the reference disks to the top surface and bottom surface of each specimen, the unknown conductivity of the powder can be estimated. Comparing the temperature gradient in the powder specimens with the temperature gradient of the reference disks permits the powder specimens' conductivity to be calculated.

Data collection has been made using the six thermocouples, which were connected to an Analogue to Digital Converter PCL818HG and then linked to a PC 386 computer. The computer program recorded the temperature gradients of all thermocouples over a period of time. The thermocouples used during the experiments were K-type able to measure temperatures up to 400^0C.

The powders used during the experiment were prepared by loading them directly in the thermal conductivity rig. The empty containers each have the same diameter as the comparator of 68 mm but the thickness of the containers are different. One has a thickness of 3mm and the other one of 6mm. The powder volume in each container can be calculated as follows:

- 3mm container $V_3 = 3\pi (68.14)^2/4$ mm^3
- 6mm container $V_6 = 6\pi (68.14)^2/4$ mm^3

Then, the powder density can be calculated by dividing the weighed powder mass by the powder volume.

Figure 2.12 shows the conductivity rig. If there is no heat loss through the side walls:

$$K_c\left(\frac{dT}{dz}\right)_{comparator} = K_s\left(\frac{dT}{dz}\right)_{sample} \qquad (2.2)$$

where K is the thermal conductivity and $\left(\frac{dT}{dz}\right)$ is temperature gradient along the stack.

Subscripts c and s stands for comparator and sample respectively. Equation 2.2 holds for all four comparators and both samples.

The total temperature drop ΔT_{sample} across a sample has two terms, one, ΔT_0, due to contact resistance at the comparator/sample interfaces, the other due to conduction:

$$\Delta T_{sample} = \Delta T_0 + \left(\frac{dT}{dz}\right)_S \Delta z_s \qquad (2.3)$$

Substituting from equation 2.3

$$\Delta T_{sample} = \Delta T_0 + \frac{K_c}{K_S}\left(\frac{dT}{dz}\right)_{comparator} \Delta z_S \qquad (2.4)$$

Thus a graph of ΔT_{sample} against $\Delta z_S \left(\frac{dT}{dz}\right)_C$ should be a straight line with gradient (K_c/K_S).

If K_C is assumed, K_S can be obtained. This is the procedure adopted in this thesis, with checks on the validity of equation 2.2.

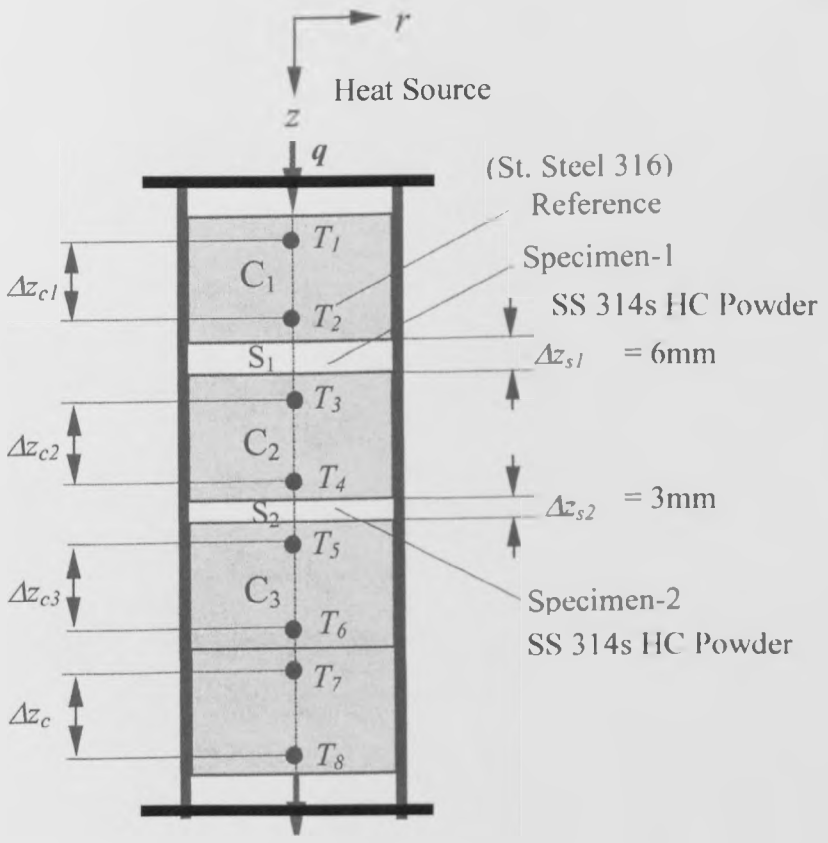

Figure 2.12 Schematic cross section view of the conductivity rig

2.3. The sintering station (LHPSS)

All sintered parts presented later in this thesis have been made using the Leeds High Power Sintering Station, which has a maximum laser power of 250W using a continuous wave CO_2 laser.

The sintering station is formed of six main sub-systems: 1) the laser system and optics system, 2) the X-Y scan head, 3) the chamber, 4) the powder spreading mechanism, 5) the z-motion control table and 6) the PC which controls all the major operations during the experiments. Control of the system is centred mainly on the PC which runs the X-Y scan head, and the calibration software, PC-Mark and Postgrid. Additionally, the PC runs the motion control program for positioning the table and the hopper, DMC motion program, and the software, L-Scan, which generates HPGL data files.

2.3.1 The original selective laser sintering station

Figure 2.13 shows the LHPSS. The figure shows all six main sub-systems, which make up the sintering station.

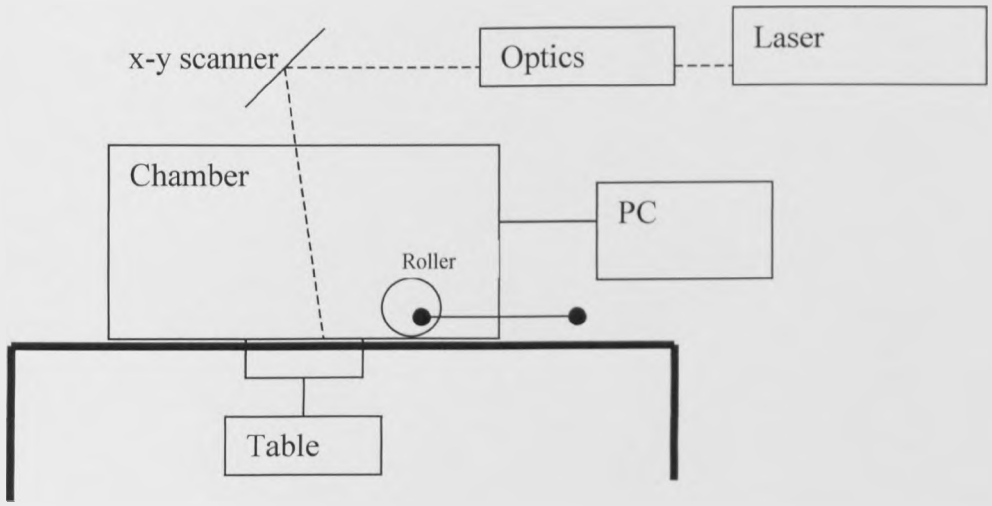

Figure 2.13 Schematic view of the Leeds High Power Sintering Station

The laser used during this research was a SYNRAD 240 Watt "Duo-Laser®" CO_2 Laser firing an infrared beam. The wavelength of the infrared beam is 10.6 μm.

Two 60-1 series tubes, each of them with an output of 125W, make up the laser head. These tubes are mounted one next to the other and each of them is controlled by a water-cooled solid-state RF power supply. An optical beam combiner within the laser head combines the output from the two tubes. The combiner is almost 100% efficient in merging the two linearly polarised beams, providing a maximum laser power output of 250 W.

Furthermore, the as-supplied output beam diameter at the laser head system was 4.4 mm. V&S Scientific Ltd. supplied a BEZ-10 beam expander. This was positioned at 350mm from the laser head and was used to focus the infrared beam onto the powder bed. The spot diameter obtained at the surface of the powder bed was 1.1mm and this setting was used throughout the duration of this research.

The laser power was controlled either manually or by computer. The manual control was realized by using a Synrad UC-1000 universal laser controller that was adapted to house a potentiometer with a 1000 division numerical counter. The potentiometer was used to manage the laser output power and the accuracy obtained with this was higher than when the supplied potentiometer was used (UC-100). Computer control allowed for faster processing sequence times but only eight different laser powers could be defined for a scanning routine. In conclusion, both control methods have been used during the research.

General Scanning Inc. (Banbury, UK) supplied the type G325DT scan head, used to raster the laser beam over the sintering area. The mirrors (figure 2.14) composing the scan head are placed perpendicular to each other and each has a scan angle of 40^0 to the highest point. The lower mirror is used for the X scan and the upper mirror is used to reflect the X-axis in the Y direction. The Y direction is perpendicular to the powder bed and, as a result of the reflection, the laser beam is redirected through 90^0 onto the powder bed surface. Limited rotation closed loop galvanometers control the mirrors' movements through a Digital Scanner Controller (Hauser, 2001).

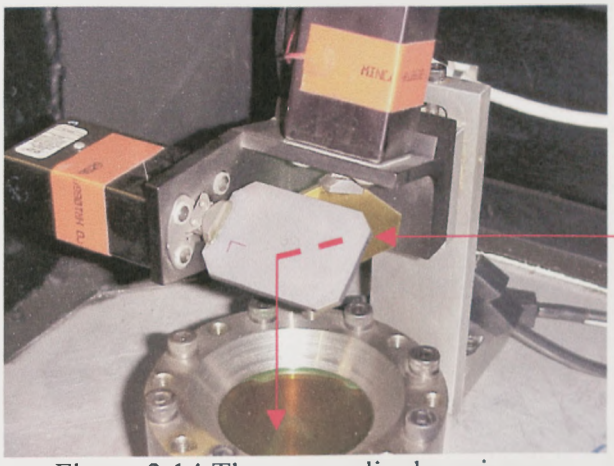

Figure 2.14 The perpendicular mirrors

The chamber, used for ensuring that sintering atmospheric conditions are met, is described in this part of the thesis. Figure 2.15 shows the build chamber. The chamber's walls and roof were built using 10mm thick stainless steel (AISI 304L) plates, which were welded together and finally attached to a stainless steel base plate, 25mm thick. The cavity formed in this way was 460mm long, 260mm high and 250mm deep. Moreover, one of the walls was machined and a doorway 250mm long and 150mm high was built in the middle of the wall. The doorway gives access to the powder spreading mechanism and to the sintering area for removing the sintered parts as well. The doorway is fitted with an access plate, which is equipped with a polycarbonate-viewing window.

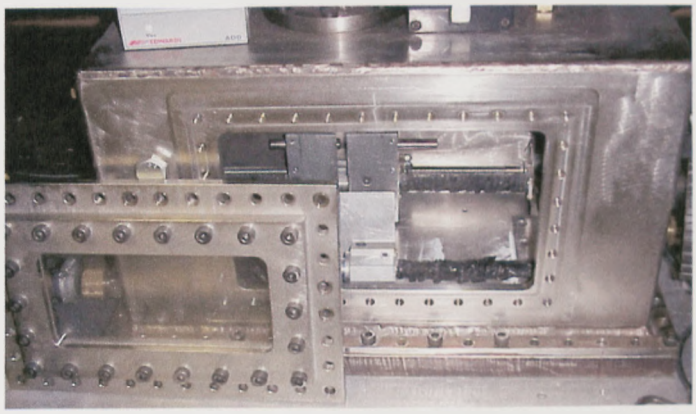

Figure 2.15 The build chamber

Two holes were machined, one into the base of the chamber to give access to the build cylinder and the piston unit and the second one into the chamber roof to clear the

access of the laser beam to the sintering area. Both holes were centred on the same Y-axis line and both have the same diameter of 75mm.

On top of the chamber, on the same centre line, was attached a cylinder, 180mm long, 6mm wall thickness and the same diameter as the hole. The cylinder was sealed to the chamber ceiling with 12 M8 cap head bolts. Also, the upper end of the cylinder was capped by a flanged collar which housed a Zinc-Selenium laser window, through which the laser beam entered the sintering area.

In addition, other small holes were drilled into the chamber walls, which were used to house evacuation pipes and the sealed passage used by the stepper motor to move the slot feeder mechanism, situated inside the chamber.

The build cylinder is attached to the chamber floor on the same centre line as the hole made in the chamber floor. The hole has two main functions, firstly to contain the deposited powder and the sintered parts and secondly to house the piston. The cylinder dimensions are 150 mm length, 75 mm hole diameter and 0.6 mm wall thickness. A stainless steel flange was welded to one end of the cylinder. The other end of the cylinder was sealed with a threaded cap and a vacuum seal. A gas outlet pipe was fitted at the end and connected through an Edwards fine leak control valve to the vacuum pump. Moreover, the end housed a linear bearing, which is the connection and motion transmitter between the motion control table and the piston head.

In addition, the piston head houses a 3065/15M-sintered disc, with porosity of 5 μm, inserted between two perforated stainless steel plates. The sintered disc allows the inert gas to be evacuated from the chamber through the piston head and powder, while preventing exit of the powder into the piston head.

All this section has described the sintering machine as developed by others. In the next section original improvements of this thesis are described.

2.3.2 Powder spreading development

In order to start the process of building multiple layers it was necessary to develop and to implement a new spreading mechanism. The requirements for the new system were to spread layers of powder with less then 0.5mm thickness, while creating as

little disturbance within the already deposited powder bed as possible. A new spreading mechanism was required due to the poor quality of the powder bed flatness obtained with the old spreading mechanism.

The previous spreading mechanism, used in the LHPSS pushed the powder over the sintering area. This process of moving powder by pushing induces a movement of the powder particles in the powder bed. The movement of the powder particles affects the layers below the sintering surface and can cause a movement of the sintered layers. The new spreading mechanism tries to eliminate these problems by dropping powder over the sintering area from a slot feed mechanism (SFM).

During the design process other possibilities were considered but proved to be not successful. The major problem which had to be overcome was the small volume inside the chamber. Besides, this was a need to limit the drilling of new holes into the chamber walls because more holes in the chamber walls would have meant more problems regarding the sealing of these holes and it would have been more difficult to keep a constant atmosphere inside the chamber.

With the aim of building multiple layers in mind, the design process started by building an exact replica of the chamber floor outside the chamber. A piece of wood was used in which were drilled holes; each one of the holes represents those in the real chamber floor. The SFM mechanism was constructed and bench tested offline. The wooden bed was also built to fix and align the ball screw, rods and motor.

Engineering drawings of the slot feeder mechanism and a list of necessary materials were made. Figure 2.16 show the engineering drawing of the slot feed mechanism assembly (at the end of this chapter can be found more drawings of SFM parts). The author wants to draw attention to the fact that the figure 2.16 was made at an early stage of the design process and that not all the assembly components appear in the drawing. Figure 2.16 also shows the frame that initially was intended to support the V-hopper. This solution was abandoned later.

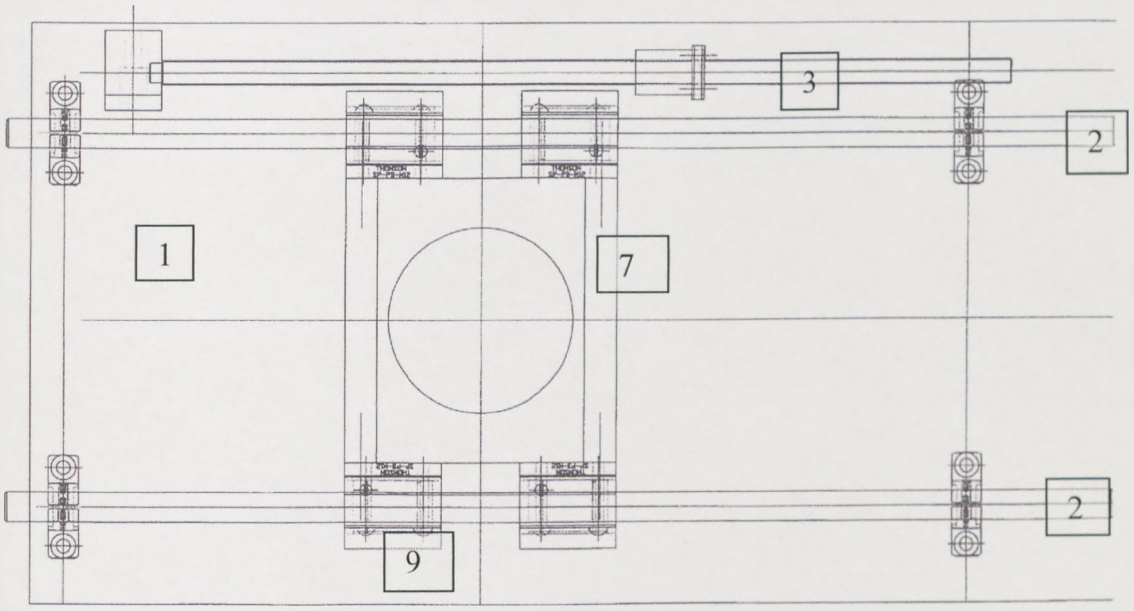

Figure 2.16 Slot feed mechanism assembly

Assembly components used for creating the slot feed mechanism are:

1. Base plate, wood plate;
2. Guide rods;
3. Ball lead screw;
4. Pillow blocks;
5. Hopper end block;
6. Hopper guide plates;
7. Hopper side walls;
8. Pillow blocks spacer;
9. Linear bearings;
10. Clamps;
11. Block spacer;
12. Universal ball joint;
13. Switches;
14. Castellated socket-headed cap screws;
15. Plastic cover;
16. Stepper motor

The slot feed mechanism for powder deposition works as follow:

1. The hopper is filled up with metal powder.
2. A stepper motor moves the lead screw at a predefined speed.
3. The rotary motion of the ball screw is converted to a linear motion by the pillow block, which moves the hopper assembly.
4. As the hopper traverses the build area powder is dropped over the slot.

The slot feed mechanism consists of four principal subsystems: V-hopper, linear bearings and hopper guide plates; ball lead screw and the rods; the stepper motor and the electronic stepper controller (ESC). Figure 2.17 shows a schematic view of SLF assembly.

The main control unit was centred on a Pentium PC. For security reasons, it could be overridden by a manually activated electronic stepper controller. The control unit, CU, was used during the research to move the V-hopper in the X direction back and forward and to modulate the V-hopper velocity.

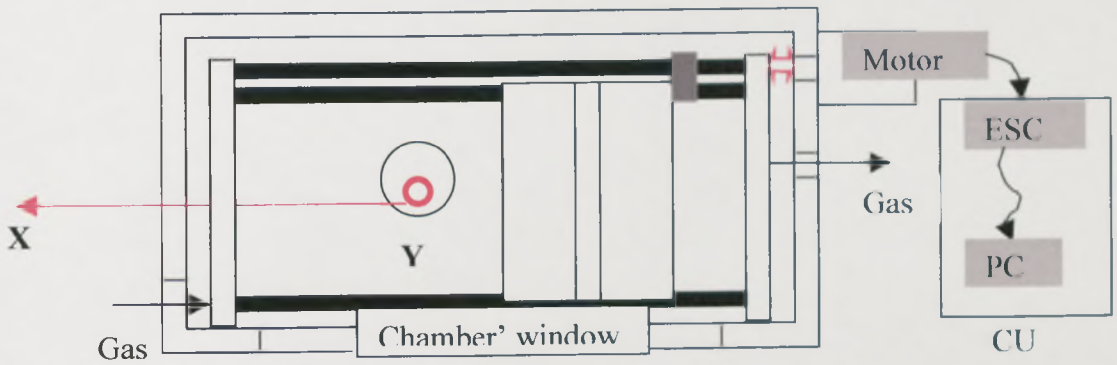

Figure 2.17 Schematic top view of the chamber including assembly compounds

The stepper motor and the electronic stepper controller

Figure 2.18 shows the electronic stepper controller used during the experiments.

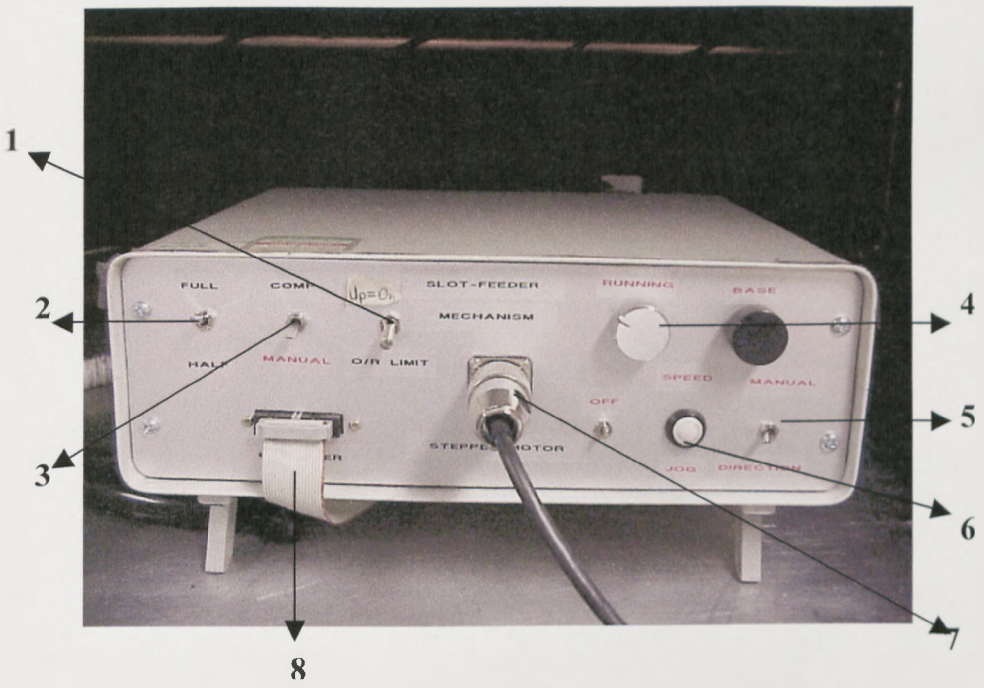

Figure 2.18 Stepper motor controller

The stepper motor controller was built both as a connecting system between the stepper motor and the PC Pentium 386 and as a safety system. Figure 2.18 shows the principal functions of the controller. 1 (figure 2.18) represents the limiter button. It is used to switch on or off the power of the two switches situated at the end of the two rods. Electrical switches were placed as a safety measure in case the V-hopper continues to move after the PC inputs the switch off command (figure 2.19 security switches – next page).

2 is the button that allows change of the stepper motor's step sequence. It can be used to run the motor on full steps or on half steps. Button number 3 (figure 2.18) is used for changing the control from manual to automatic.

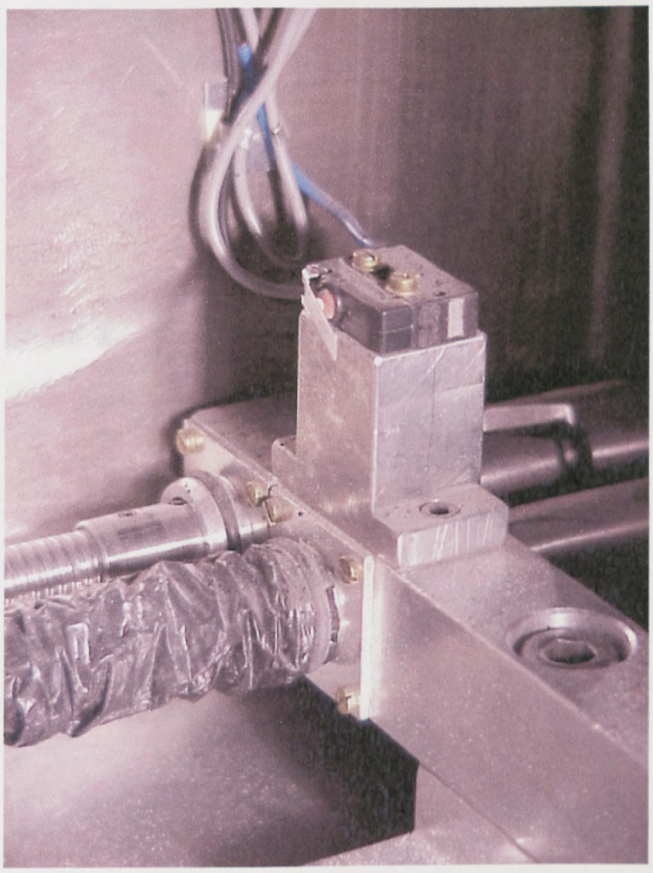

Figure 2.19 Security switches – turns the power off

4 is used to vary (increasing or decreasing) the motor's number of steps. 5 is used to change manually the direction of the V-hopper. 6 is used for manual movement of the V-hopper, number 7 is the feeder and finally, number 8 is the 25-pin ribbon connector with the PC. Alternatively, for easier use of the stepper motor controller an external manual switch connected to the SMC using a spiral cable was considered and implemented. The external manual switch replaced the button number 6 especially during the more delicate positioning manoeuvres of the hopper.

The stepper motor used for moving the ball lead screw was a 5V motor. Figure 2.20 shows the stepper motor assembly. Trying to avoid drilling more holes into the chamber walls, a compromise solution was considered. The pump evacuation pipe was moved to the hole in the middle of the chamber wall that was used before by the old manual spreading mechanism and the motor shaft was fitted into the old evacuation pipe hole.

Furthermore, a complicated solution for holding the stepping motor in place was avoided by use of a metal housing block, as shown.

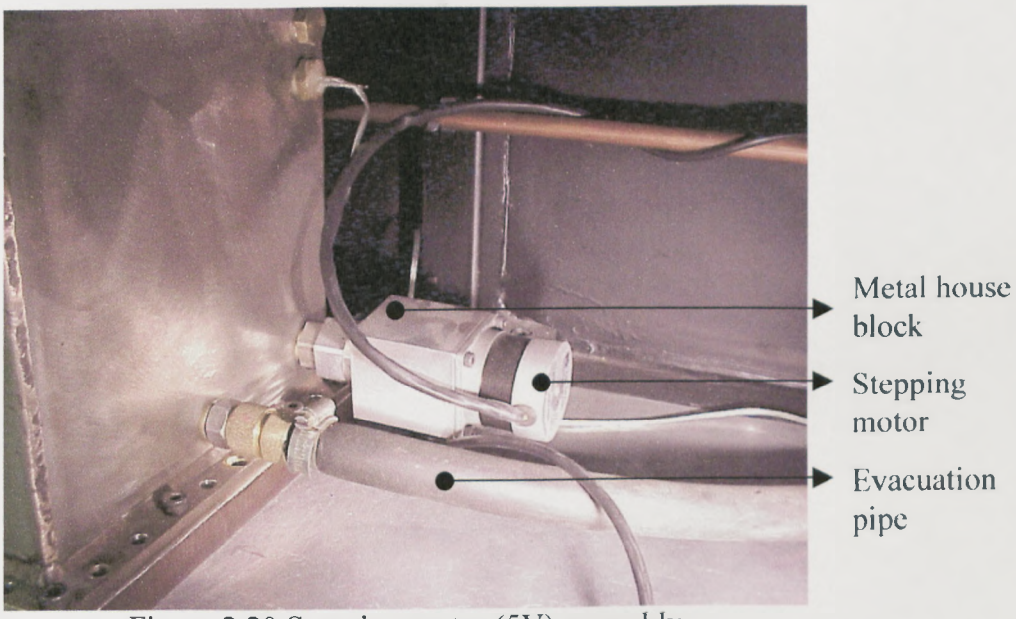

Figure 2.20 Stepping motor (5V) assembly

V-hopper assembly

The V-hopper design was based on the results obtained during the powder flowability experimental tests. An association between the V-hopper and Carney flowmeter has been kept. For instance, the distance between the two blades of the hopper is 5mm the same as the Carney flowmeter gap; the angle formed by the blades and flowmeter sidewalls is the same.

The V-hopper assembly has two main functions; firstly to sustain the powder weight (6-7 kg of powder) and secondly, to ensure a smooth movement of the assembly during the powder spreading process.

The V-hopper was made of two stainless steel plates of 1.5mm thickness, 112mm high and 130mm wide; and two stainless steel sliding bases of 5mm thickness, 98.4mm high and 107mm wide. The 5mm thick sliding bases were machined to a trapezoidal shape (figure 2.21).

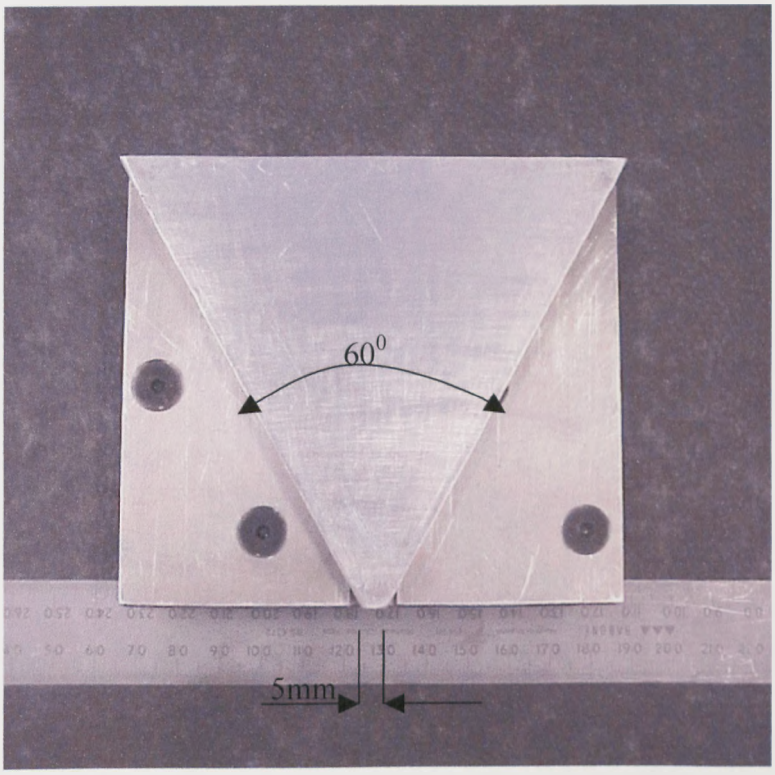

Figure 2.21 The end plate wall of the V-hopper

One face of each sliding base was milled off and a guide supporting rib was made (10mm wide and 98.4mm high). The longitudinal ribs were used as a connector and sliding system between the V-hopper and the metal plates. Moreover, the distance between the hopper and the chamber floor could be adjusted easily using the clamps (figure 2.22) situated at the back of the hopper. The clamps are attached by the sliding ribs, described before, using an M4 cap head bolt.

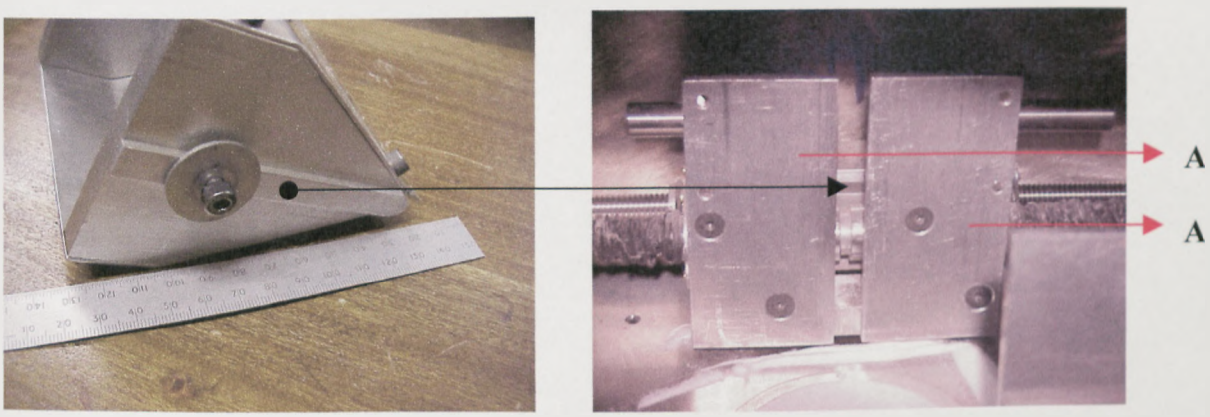

Figure 2.22 Side view of the V-hopper (with emphasis on the sliding ribs)

Furthermore, each linear bearing (C) was attached to a metal plate (A). Two linear bearings were used for each side of the V-hopper. A metal shred (D) was used to connect the linear bearings and to ensure a constant distance between them as well as to keep a constant distance between the two metal plates attached to the bearings (figure 2.22 and 2.23). Besides, as a safety measure a block spacer was used to keep the distance constant (B). Figures 2.22 and 2.23 show different views of the V-hopper assembly. In the end, the block spacer (B) was replaced by a female screw not-thread. This variant was considered more advantageous, especially during the adjusting of the distance between the powder bed and the V-hopper, compared with the previous alternative.

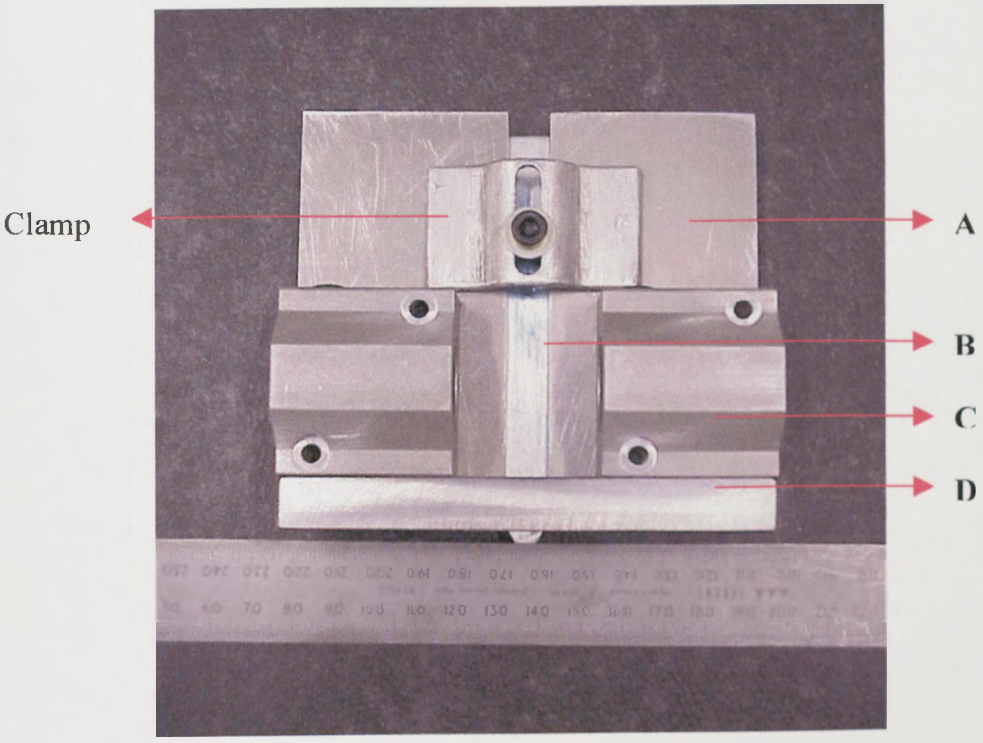

Figure 2.23 Back view of the V-hopper including the clamp and linear bearings

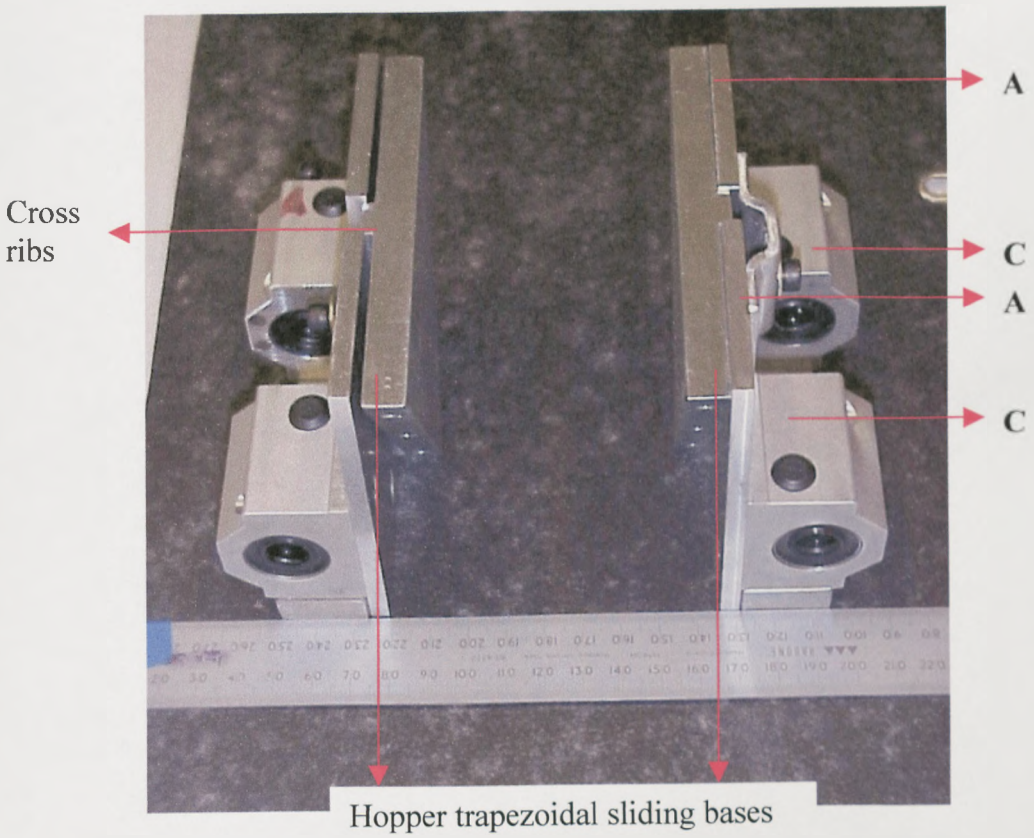

Figure 2.24 Top view of V-hopper assembly but the side-walls of the hopper

The ball lead screw and the connecting tie rods

The ball lead screw plays an important role during the spreading process. The precision of the spreading and the flatness of the powder bed depend on the precision and smooth movement of the lead screw.

The precision lead screw, was a trapezoidal rolled stainless steel shaft of 12mm diameter and the trapezoidal-flanged nut was bronze. They were provided by Ondrives (Derbyshire, England). The rods have 14 ϕmm shaft diameter and are 390mm long. Figure 2.25 shows the lead screw and the connecting tie rods placed on the wood replica of the chamber floor.

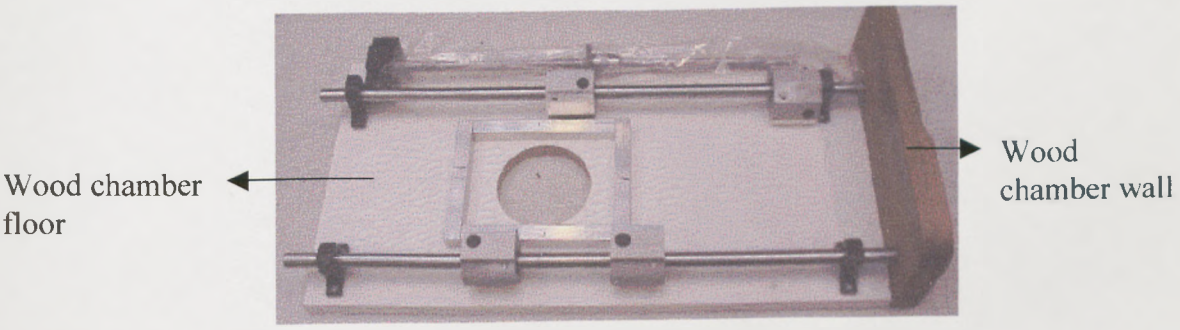

Figure 2.25 The lead ball screw and the connecting tie rods

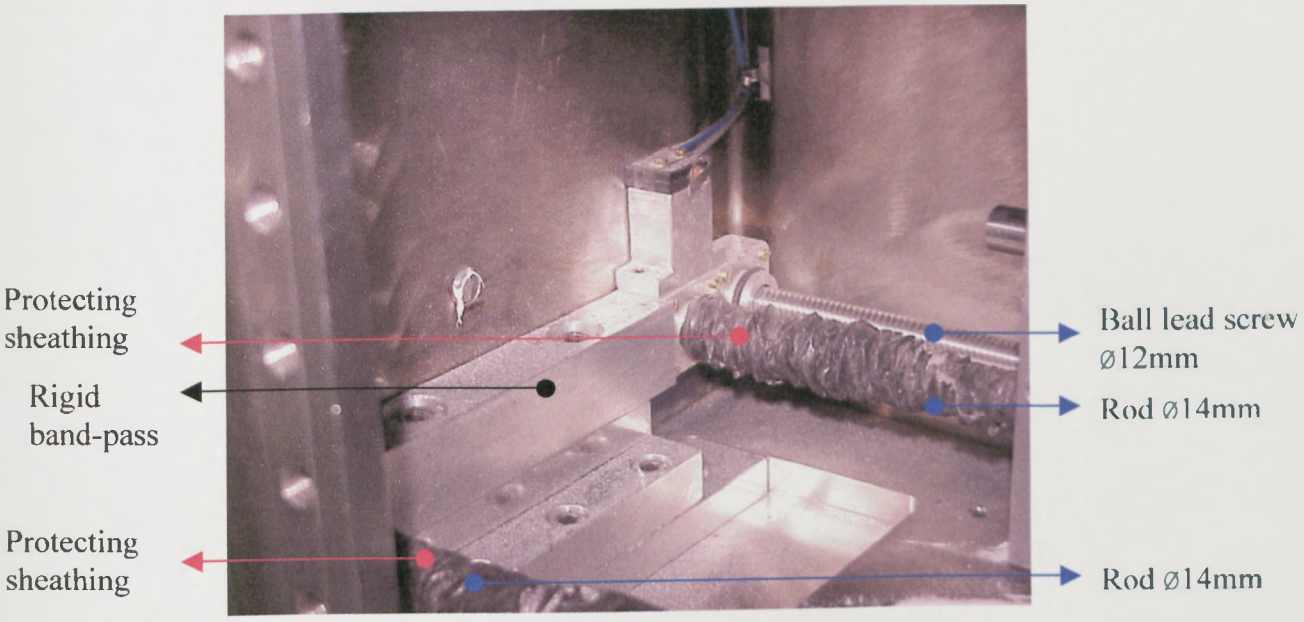

Figure 2.26 Inside view of the chamber, the spacer

Moreover, a rigid band-pass (figure 2.25 and 2.26) was designed especially for this project. The band-pass was used to ensure parallel alignment of the rods and the ball screw. In addition, it was used for increasing the height ensuring that the lead screw axis is collinear with the stepper motor shaft axis (figure 2.26).

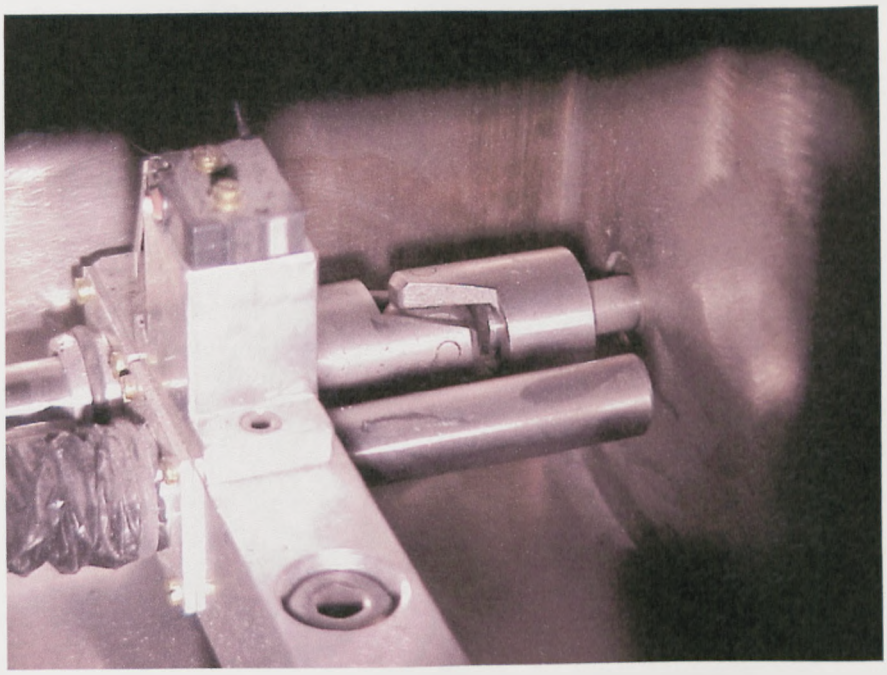

Figure 2.27 The rigid band-pass and the universal ball joint

The connection between the lead screw and the stepping motor was made using a universal ball joint (figure 2.27).

Due to the severe conditions inside the chamber, for example powder infiltration, the lead screw and the connecting tie rods were protected using a plastic sheet. The plastic sheet was wrapped around the rods and sealed at each end using a rubber ring fastener. The author wants to emphasise that the protective cover seen in figures 2.26, 2.27 and 2.28 wrap only the connecting tie rods. Due to the intense use of the V-hopper, the lead screw protective cover was torn off and removed.

In the end, the V-hopper feeder mechanism was fitted into the chamber (figure 2.28). As a result, the thickness of the spread powder layers was reduced from 1mm thickness down to 0.3mm.

In addition, the powder bed flatness was improved and disturbance within the powder bed during the spreading process eliminated. Further, the V hopper's side-walls have been protected from contact directly with the chamber steel floor and also protected from wear by attaching an attrition-resistant plastic sheet. The attrition-resistant plastic was attached (glued) to each of the hopper sidewalls and the solution proved to be viable during the research carried out on the sintering station. The powder bed flatness was not affected by the using of the attrition-resistant plastic at the bottom of the V-hopper (figure 2.29).

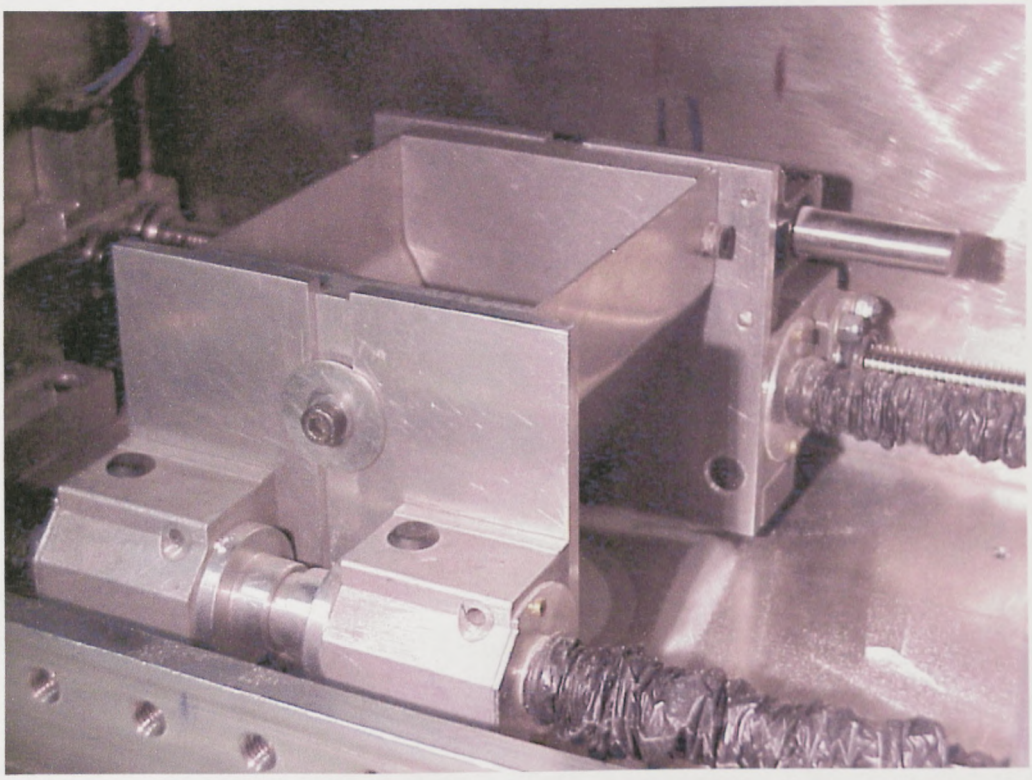

Figure 2.28 Slot feeder mechanism

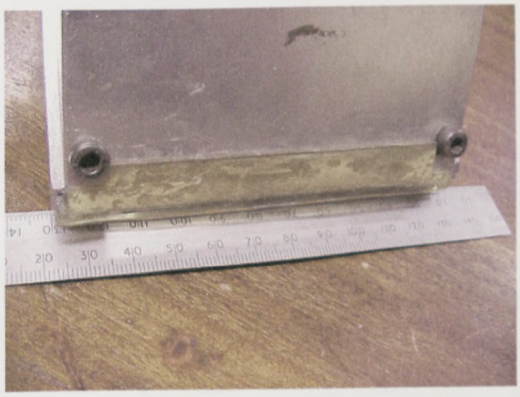

Figure 2.29 Attrition-resistant plastic attached (glued) by the V-hopper sidewalls

2.4 Software's and automation of the process

One of the main goals, besides the improvement of the powder spreading, was the automation of the entire process. The automation of the entire process involves the movement of the piston-table and the V-hopper.

Initially, a Pascal software program was written for controlling the V-hopper spreading process (Appendix B). Later, the Pascal software program implementation was discarded because of difficulties in controlling both the V-hopper and the piston-table at the same time. Instead, a Galil DMC controller card was adopted. A DMC 1040-control card was acquired. 1040 represents a card that can control four moving axes at the same time. One axis was used to control the Y-axis, the motion table, another one was used to control the X-axis, the V-hopper, and the last two were left empty for future development of the system. A computer software program using a DMC controller program was written. The software program could control and modulate all the parameters regarding the movement of the motion table and the V-hopper.

A second program was used to create input from the DMC controller. The L-scan is a computer program which has two tasks to perform within the LHPSS sintering station. In the first place, the L-scan program compiled and output HPGL graphic files. HPGL (Hewlett Packard Graphics Language) describes 2D graphic files, raster patterns, inputted by the user. Secondly, the program had the role of generating a system parameters file for switching the system settings for recalibration of the X-Y scan head when the laser is focused from the top of the V-hopper to the powder bed (chamber floor). HPGL codes were designed to be used with Hewlett Packard pen plotters. HPGL is an easy to use computer program. Each point that is wished to be "plotted" is defined using X-Y coordinate system (PRx,y). The points' coordinates and the commands can be easily decoded by PC-Mark MT and transmitted to the mirrors. PC-Mark MT is also used to control the laser head output and to mark out eight different laser power settings using one HPGL file.

2.5 Experimental approaches

All the research presented in this thesis was carried out using four batches of stainless steel powder; two different chamber atmospheric conditions and a range of scan speeds, scan powers and laser scanning condition.

2.5.1 Laser power calibration

The laser power output calibration was performed using two laser power probes with a ± 6% accuracy over 600W. The probes were supplied by L.G. Products Ltd (Slough, UK). The power of the laser was measured by placing the heat sink of the power probe in the path of the laser beam at a position approximately 160mm above the build zone. This position was not critical provided it was at a location sufficiently away from the focal point of the laser. At the focal point the high heat intensities could damage the surface coating on the heat sink, compromising the accuracy of the probe.

The probe was exposed to the stationary beam for a period of 20 seconds, removed, then left for a further 16 seconds before taking the reading. The reading was then multiplied by a factory set laser calibration factor of 1.032 to ensure a ± 6% accuracy. Between all measurements, the UC-1000 controller was left in 'standby' mode. This mode supplied a tickle or pulse (every 1μ sec) below the lasing threshold to maintain the plasma in the lasing tubes in an ionised state, allowing positive laser switching therefore eliminating the need for a warm up period.

Figure 2.30 shows the calibration curve for manual laser power modulation. These data were used through out all the experimental research carried out on the sintering station. It is necessary to mention here that laser re-calibration was performed typically 4 or 5 times per year. The data differences were minimum so that it was considered only one chart to be presented in this thesis (see figure 2.30).

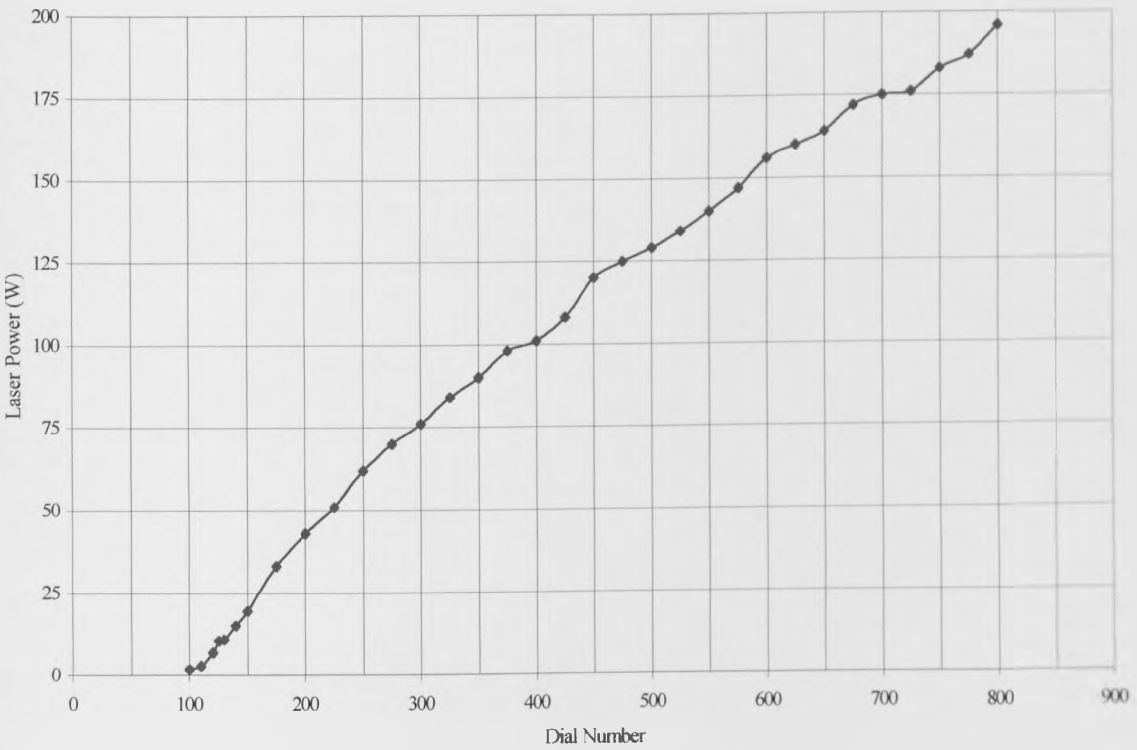

Figure 2.30 Calibration graph for manual laser power modulation

2.5.2 Chamber conditions

The process chamber used during the experimental work contained either an air atmosphere or an argon atmosphere. The argon rich atmosphere was achieved by a combination of build chamber evacuation (to approximately 50mbar gauge pressure) followed by an argon gas purge until local atmospheric pressure was re-established. This procedure was repeated twice before balancing the flow rate of argon through the build chamber at a slight overpressure (50mbar). Because no flow gauges were available, to maintain consistency the flow rate was balanced at the maximum pumping speed of the vacuum pump. The inlet flow from the gas bottle was regulated using the LV10K flow control valve connected to the outlet flow of the build chamber. Flow from the build cylinder remained closed at all times.

Once the flow rate through the build chamber was balanced the build chamber was left for at least a 15 minute settling period before laser exposure. These conditions were maintained throughout the duration of each experimental test. The total cycle time for build chamber conditioning prior to laser exposure was about 20 minutes. The argon was

supplied by BOC and was bottled with a 99.9 % purity. Trace elements of other gases, particularly oxygen, are still likely to reside within the powder bed and build chamber.

2.5.3 Scanning conditions and procedures

A unidirectional single scan was used to sinter a series of single tracks in the powder layer (series 1.1 – 30.8). An experimental tray was filled up with stainless steel powder and placed on top of the V-hopper. The powder placed in the tray was levelled using a metallic ruler. The scan speed used during the experiments was varied between 25W and 170W. The detailed scan conditions can be found in Appendix E. Table 2.5 summarises the powder sintering test conditions.

Table 2.5 Selective laser sintering experimental tests

Test serial numbers	Powder size	Type of sintering	Laser power range (W)	Scan speed range (mm/s)
Series 1.1 ~ 5.8	-300	Track	25~170	1~17
Series 6.1 ~ 10.8	-38	Track	25~170	1~17
Series 11.1 ~ 15.8	-150	Track	25~170	1~17
Series 16.1 ~ 20.8	-75	Track	25~170	1~17
Series 21.1 ~ 25.8	300 add 38	Track	25~170	1~17
Series 26.1 ~ 30.8	150 add 38	Track	25~170	1~17
Series 31.1 ~ 35.8	-300	Layer	25~130	1~10
Series 36.1 ~ 40.8	-150	Layer	25~130	1~10
Series 41.1 ~ 45.8	300 add 38	Layer	25~130	1~10
Series 46.1 ~ 50.8	150 add 38	Layer	25~130	1~10
Series 51.1	300 add 38	Multiple	60~110	1~8
Series 56.1	150 add 38	Multiple	60~110	1~8
Series 57.1	150	Multiple	60~100	1~8

The length of the scan track was kept constant, 20mm, during the experiments regarding the single tracks. The influence of track length was not important at this stage. The separation between the sintered tracks in the tray was 8mm. An 8mm gap was considered sufficient to avoid the thermal influences from one track to another during the sintering process.

All experiments regarding single layers were based on the information obtained from the single track experiments (series 31.1 – 50.8). The layers were sintered using the tray. The main advantage of using the tray was that a large number of layers could be sintered using the same environmental chamber conditions. In contrast to this,

sintering directly on the powder bed enabled the obtaining of only one layer at the time. The main reason for using both, the tray and the powder bed, was the impossibility of building multiple layers on the tray. Using the tray at this stage just helped to sinter more metallic coupons at one time.

Multiple-layer experiments were carried out using the results collected from the previous experiments when were sintered metallic tracks and single layers (series 51.1 – 57.1). All the experiments regarding the multi-layers building process were carried out using the V-hopper. In addition to the optimal scanning conditions obtained from previous experiments, several values of layer thickness were chosen, 1mm, 0.75mm, 0.5mm and these remained fixed during the experiments.

2.5.5 Test conditions

During the entire research program, the powder was protected from contamination using sealed plastic containers. Also, it was tried to prevent the segregation of the powder during the storage period. The caps were removed only when powder was needed for experiments. The mixed powder used during the experiments has been sintered only in a "fresh" state and after use it has been stored in different containers. Furthermore, the unused mixed powder that was not sintered during the experiments has been stored separately for future use. Moreover, the "old" mixed powder has been mixed again before being used in the sintering station, trying to avoid in this way the segregation of the powder.

2.5.6 Repeatability and reproducibility of results

The repeatability of results is defined in this work as the consistency of the melted tracks for any given powder deposition and at any given point in time within the purge cycle. The data repeatability from testing is important especially when comparisons between different tests are required. Therefore, it was important at the onset of this research to establish and maintain a sufficient level of consistency in the melting results.

To tests the data repeatability, two tracks and two layers were scanned on the same powder sample using the same scanning conditions and over a five minute time frame within the purge cycle. Each track or layer was then measured, weighed and the

most pronounced surface irregularities recorded. However, not all conditions displayed in the sintering maps created tracks available for measurement. The range of conditions available for measurement fluctuated depending on the powder batch being used. These tests were repeated for all six batches of powder and all two atmospheric conditions.

The reproducibility of the data is defined in this work as the consistency of the melted tracks produced using different powder deposit from the same batch of powder and after prolonged atmospheric conditioning. The importance of data reproducibility is based on the following considerations:

- testing was carried out over many atmospheric conditioning cycles;
- gas purging was often continuous for up to 3-4 hours when using the build plate;
- many powder samples were used;
- experimental tests were carried out over a long period of time.

2.5.7 Microscopy and Measurement equipment

All sintered metal parts were prepared for microscopic inspection. First, the samples were cut using a Struers Actum 5 circular cutting machine provided with a 356CA circular cutting wheel (HV 500 grit). Second, the metal bits obtained after the cutting operation were mounted using a hot automatic mounting press. The melted plastic powder used for mounting was Bakelite moulding powder. In addition, a cold method of mounting was used because it has been observed that the hot automatic mounting press induced a displacement force within the sintered part which affected the accuracy of the final parts. Third, the polishing processes were carried out in four steps. The sintered parts were lapped using a Metaserve 2000 grinding wheel using grinding paper (P800 and P1200) and Metalo polishing wheels with encloses of 6μm diamond compounds and finally, 1μm wheel diamond compounds. In the end, each sample was etched using Marble's Reagent acid. Etching the samples enabled an easier approach during the microscopic search.

The optical microscope used during the research has a digital vernier calliper, which was used for dimensional measurement. Mass measurements were performed using an electronic balance with 0.001g accuracy.

All dimensional measurements were carried out in the x, y and z directions of single tracks, single layers, and multiple layers, produced at different scanning parameter

settings. The equipment used for dimensional measurement was a digital vernier calliper with accuracy 0.01 mm and an optical microscope. Dimensional measurements of melted tracks, layers, and multiple layers using the electronic calliper were carried out in three steps. The first step was measurement of scan length in the x direction for single tracks, X_1 X_2 X_3 and an average was recorded (figure 2.31). The same method was applied for layers and multiple layers. Measurement was then continued by measuring the depth in the y direction. Three measurements from each side were taken, Y_1, Y_2 and Y_3, and an average value was obtained. The final step was measurement of the track width, layer width, and multiple layer width in the z direction. The positions of each are numbered Z_1, Z_2, to Z_3. The average width was then obtained and recorded by summing up these values then dividing by three. The same procedure was used to measure single layers and multiple layer samples (figure 2.32).

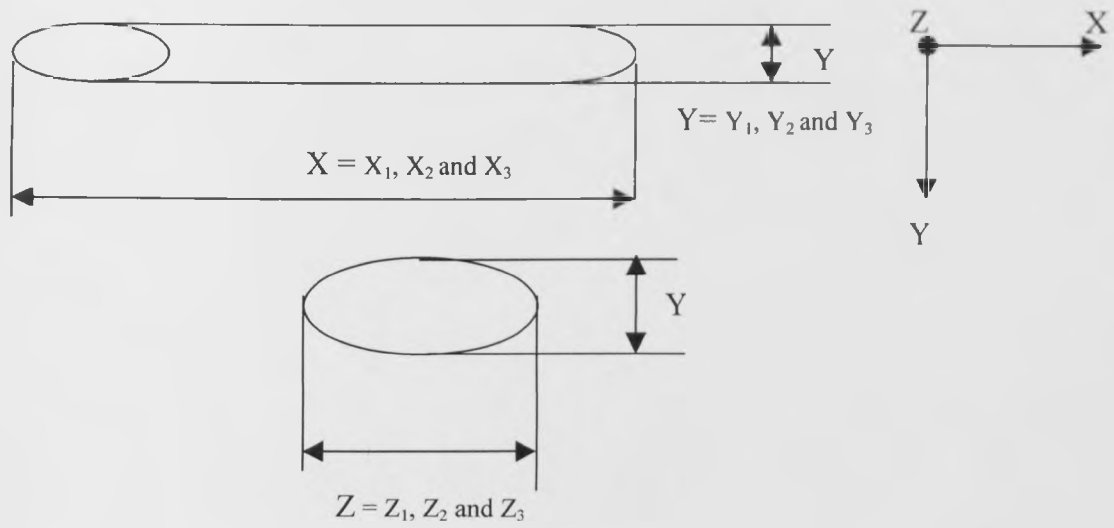

Figure 2.31 Track measuring procedure

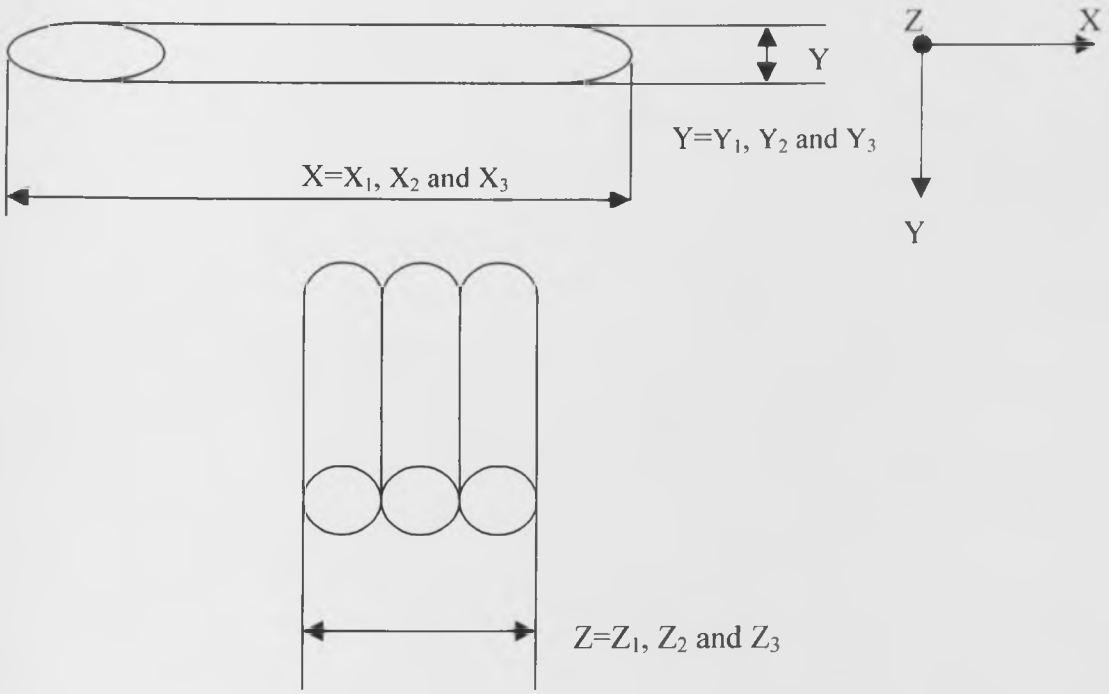

Figure 2.32 Layer measuring procedure

The sintered part density proved to be difficult to calculate accurately due to the complex shape and open porosity. As an alternative assessment, the approximate mass per unit length was calculated.

2.6 Summary

This chapter has outlined the experimental procedures, which will be used to investigate the direct laser sintering of stainless steel powder using a high power CO_2 laser sintering station. The results obtained from the application of these procedures are presented in the following chapters.

Engineering drawings used during design process of slot feeder mechanism:

Schematic side views of SFM system

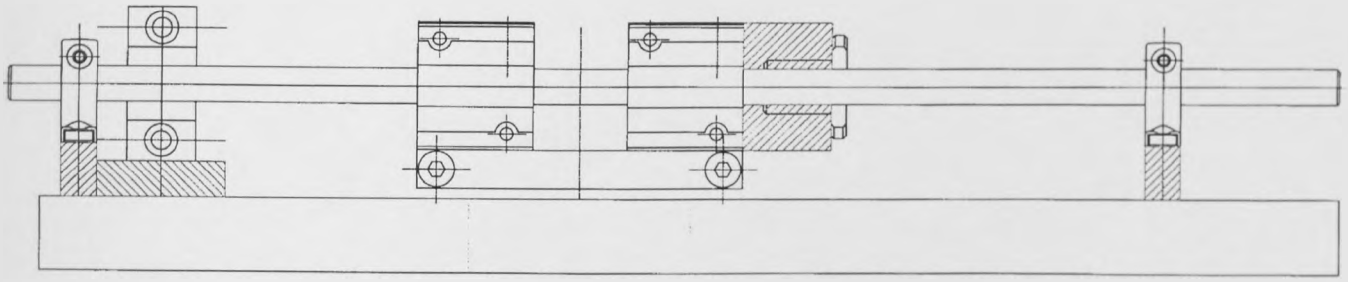

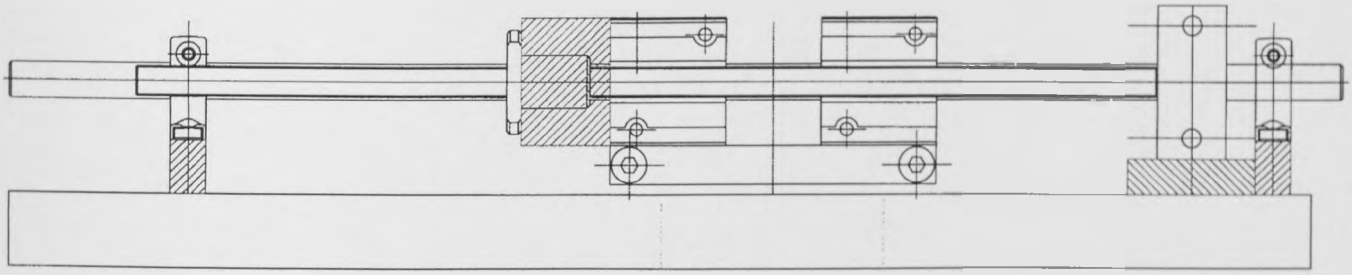

Rigid support

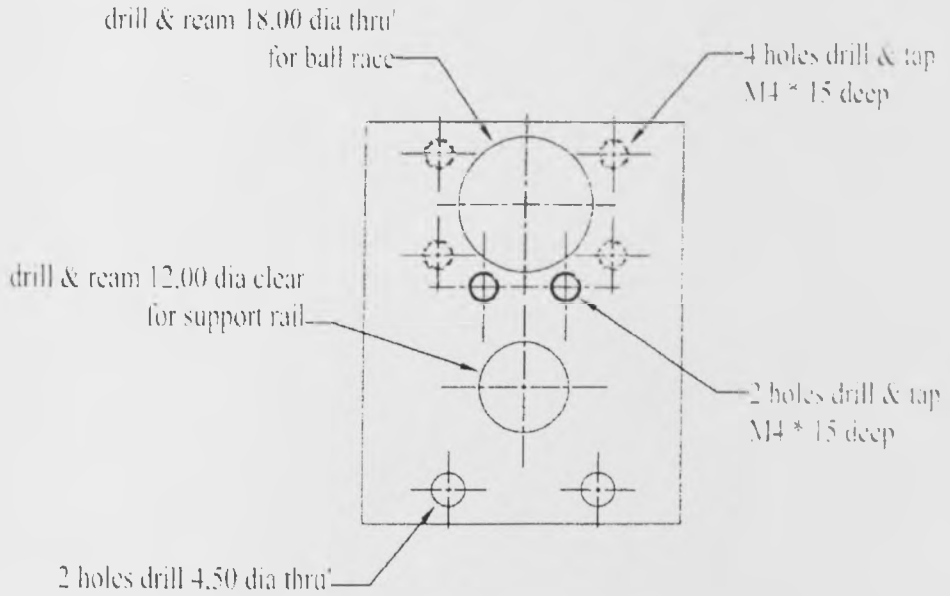

Super plus pillow bloc – series SP PB M12

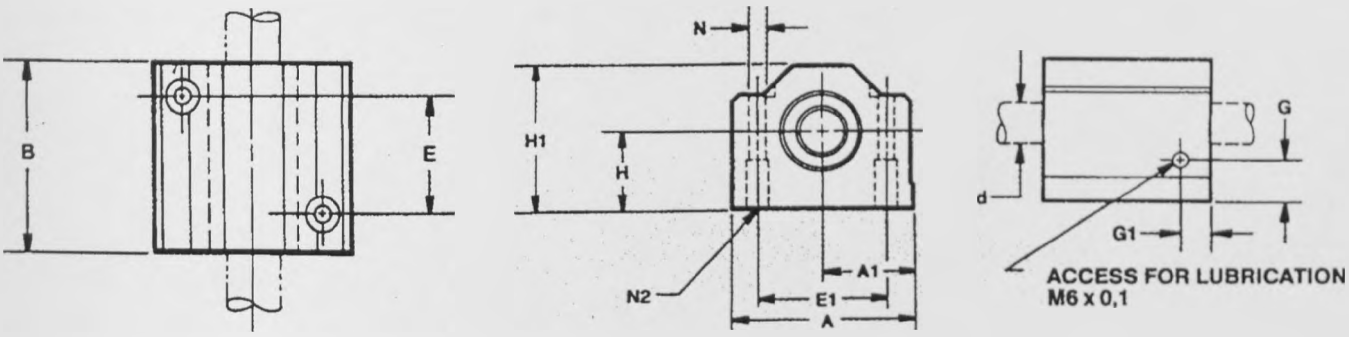

H_1 = 35mm, H = 18mm, B = 39mm, A= 43 mm

Single needle roller joint – series MN25

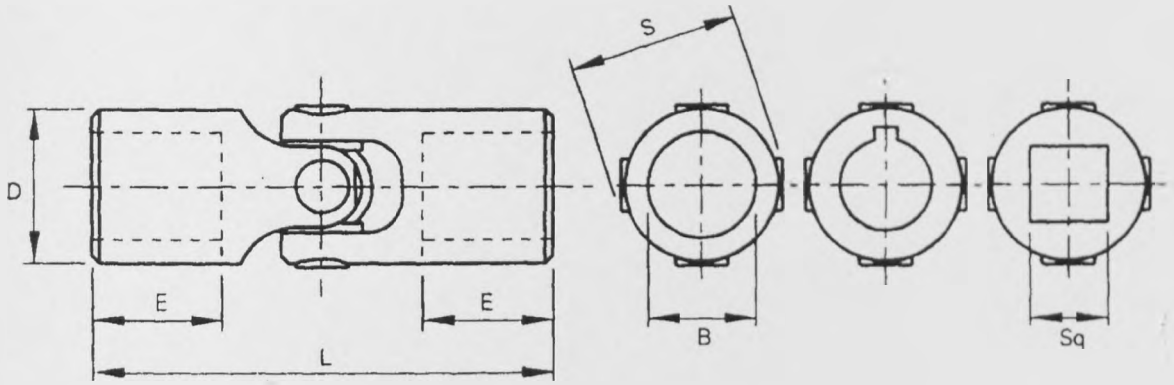

Precision rolling ball screw – series RMS 1202 C75 -350

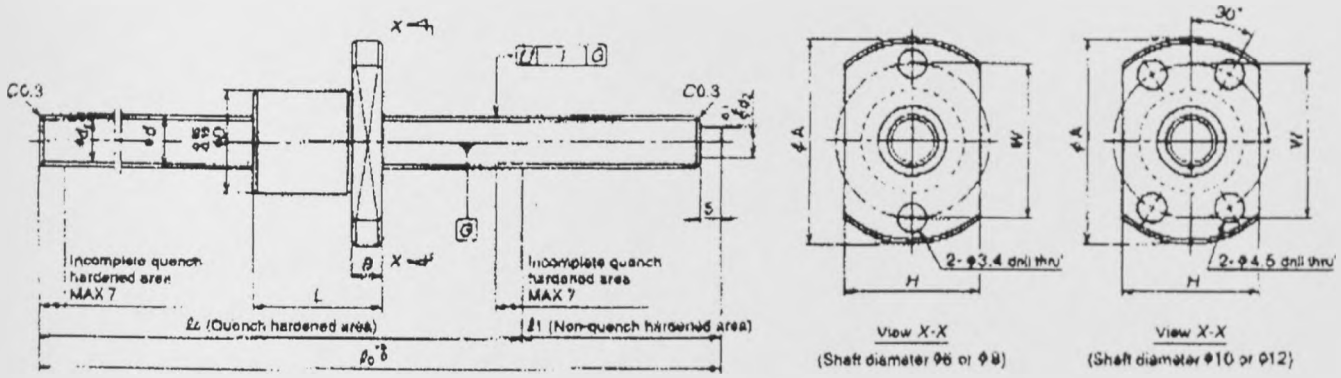

Shaft diameter – 12mm, Lead =2, Root diameter = 11mm

CHAPTER 3
STAINLESS STEEL POWDER PRELIMINARY EXPERIMENTAL TESTS

3.1 Introduction

In order to complete the objectives set out in this research several different tasks had to be accomplished besides the tasks related to improving the sintering station which were detailed in chapter two of this thesis. The first tasks presented in the first part of this chapter are focussed on powder bed properties. These tasks comprised experimental tests regarding the powder densities, powder flow rates and powder thermal conductivity.

The second part of this chapter (see sections 3.5 and 3.6) sets out the results obtained for melted tracks using selective laser sintering. Stainless steel 314HC powder was melted using a CO_2 laser at various scan speeds and laser powers in an oxygen and argon atmosphere as outlined in Table 2.5.

The result obtained during these experiments will help to understand and improve the selective laser sintering of 314HC stainless steel powder as well as accomplishing the main goal of this thesis, the building of multi layers.

3.2 Powder mixing test results

Different powders may be mixed together to produce a powder of the required uniform particle size distribution from different selected fractions or to obtain, if possible, a statistical distribution of the particles for powders produced by different methods.

Preparing a powder in this way allows control over the apparent density, flow rate and sinterability. The quality of the mixture depends on the properties of the powder such as density, particle form, mixing ratio, mean particle size, particle size distribution and surface structure.

If the mobility and density of the particles differ as a result of their form and size, the effect of external forces may cause segregation. The susceptibility of the powders to segregation were minimised during this research by eliminating the powder storage time.

V-cone mixers were used to mix the powder and were suitable for dust fractions and fine-grained materials. This is the reason why V-cone mixers were chosen for this research. V-cone mixers are described in chapter 2, section 2.3.2.

Using monosize spherical particles the maximum theoretical packing density achievable is 74%. The packing density can be increased by the addition of much smaller spheres filling the interstices between the larger ones. The limiting densities can only be reached when all the particles fall into an ideal position.

The research carried out and presented in this thesis regarding the powder mixing was performed in two steps. Firstly, single powders were mixed for 7.5, 15, 30, 45, and 60 minutes. Secondly, the powders were mixed together in different percentages using V-cones (section 2.2.2).

3.2.1 Single powders

Table 3.1 summarises the conditions of the tests and the collected data for all four batches of single powder.

Test Number	Mass (g)	Mass (g)	Mass (g)	Avg. mass (g)	Powder Density Kg/m	Mixing time (min)
	43.5074	43.9657	43.0097	43.4942	4499.549	0
-150	43.9846	43.958	43.762	43.9015	4547.873	7.5
microns	44.1302	44.3725	44.393	44.2985	4594.976	15
powder	43.5112	43.7738	44.0639	43.7829	4533.802	30
	43.9343	43.9837	43.9244	43.9474	4553.319	45
	43.3237	43.7251	43.8409	43.6299	4515.649	60
	42.286	42.4677	42.4152	42.3896	4368.492	0
-75	43.0138	44.1314	43.2395	43.4615	4495.669	7.5
microns	43.9875	43.896	43.932	43.9385	4552.263	15
powder	43.8051	43.2594	43.5204	43.5283	4503.594	30
	43.0002	43.8661	43.8285	43.5649	4507.937	45
	43.0617	43.4958	44.8822	43.8132	4537.397	60
	41.065	41.9693	41.5535	41.5292	4266.408	0
-38	42.2804	42.8518	42.1408	42.4243	4372.609	7.5
microns	42.9341	42.5486	42.0828	42.5218	4384.177	15
powder	42.0737	42.2433	42.0285	42.7817	4415.013	30
	41.3612	41.2213	42.1655	41.5826	4272.744	45
	40.6154	41.8317	41.6472	41.364	4246.808	60
	44.5068	44.5456	44.8958	44.6494	4636.609	0
-300	44.4339	45.1733	44.4822	44.6964	4642.185	7.5
microns	45.7089	45.8846	44.8979	45.4971	4737.186	15
powder	44.6153	44.5463	44.6769	44.6128	4632.267	30
	44.5498	44.1331	44.7729	44.4852	4617.127	45
	44.7921	45.8395	44.4623	45.0313	4681.92	60

Table 3.1 Single powder tests

These results are plotted in figure 3.1.

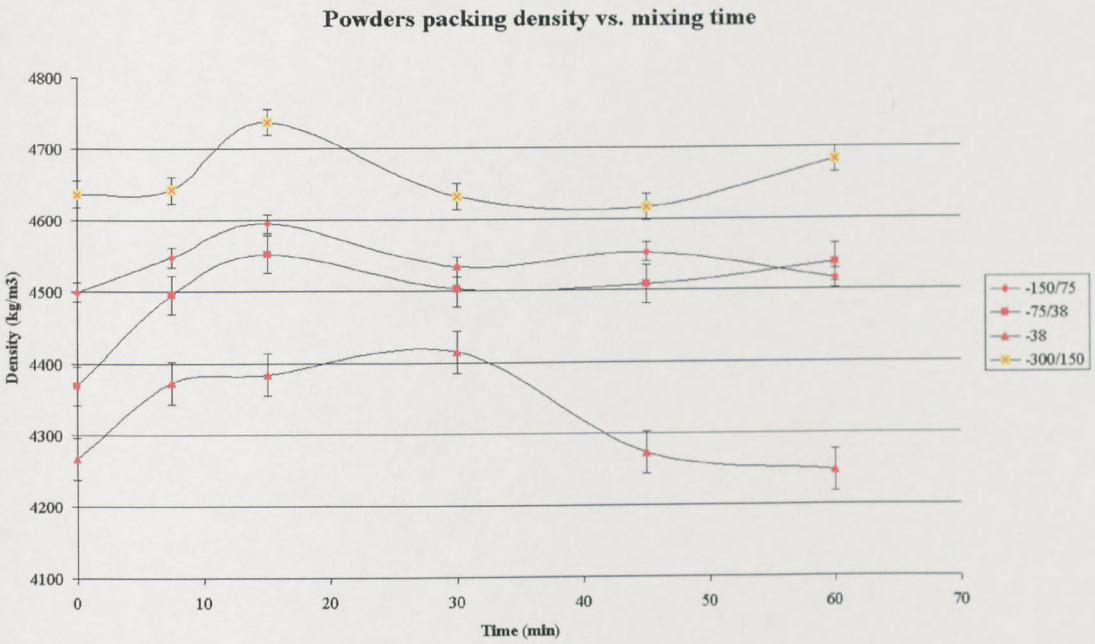

Figure 3.1 Powders packing densities measured

Figure 3.1 emphasises the importance of powder mixing for the attainment of higher powder packing densities. It is also clear from the graph that mixing time affects the powder density, which peaks after 15 minutes. However, the particle size distribution of –38μm followed a slightly different relationship showing a peak in packing density after 30 minutes of mixing. Furthermore, the –38μm powder could be over mixed. It started to re-segregate after 60 minutes of mixing. The –38μm powder density after 60 minutes was lower then the initial (0 minutes) measured density. The –300/150μm, –150/75μm and –75/38μm powders did not show big changes of the powder densities for the mixing time above 15 minutes.

3.2.2 Mixed batches of powders

The last section showed that a mixing time of 15 minutes optimised the maximum achievable packing density for all the powder batches except for the -38μm powder distribution. Although, a 15 minutes mixing time appeared to be the optimal time for reaching the highest powder density, it was decided to begin inter-mixing the four mixed batches of powder for all four time period; 15, 30, 45 and 60 minutes. It was considered that data values obtained would give a full picture of the phenomena that may occur.

It is known from the literature that the packing density increases with the particle size ratio (large diameter/ small diameter). The optimal ratio for obtaining a high packing density, with one small particle filling the triangular pores between the large particles, is known to be 7/1-ratio. In our particular case the size average ratio was 5.8/1. The minimum size ratio used was 3.9/1.

Figure 3.2 shows the data obtained during the mixing tests for -38μm powder with addition of –300/150 μm powder while table 3.2 gives the numerical results. The graph shows a mixing time of 15 minutes.

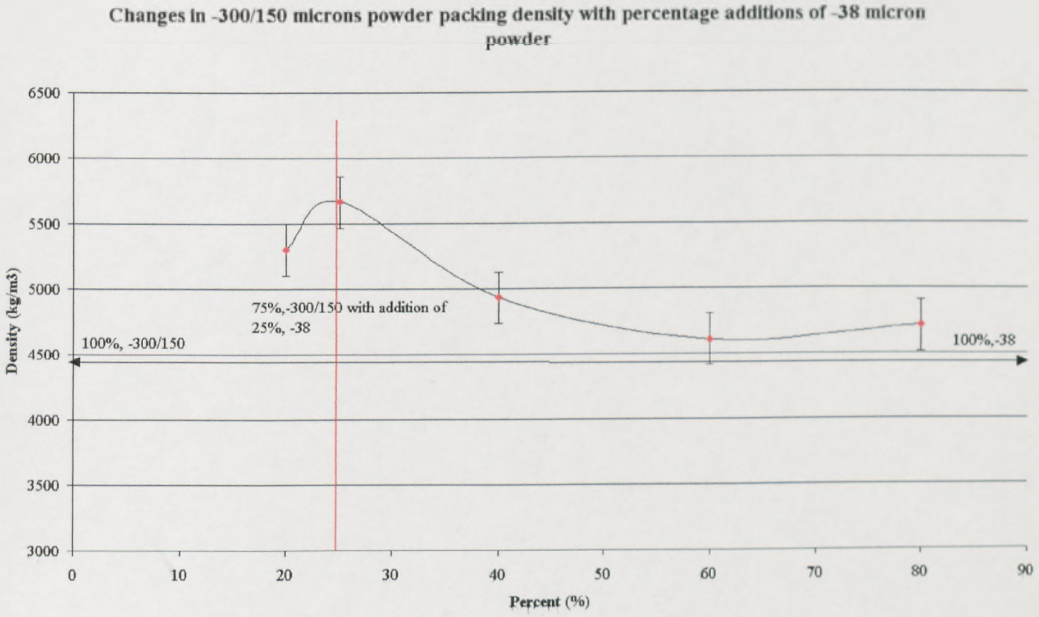

Figure 3.2 -38μm powder packing density with additions of –300/150μm powder

Test Number	Mass (g)	Mass (g)	Mass (g)	Avg. mass (g)	Powder Density Kg/m3	Mixing time (min)
80%,300 + 20%,38	49.9213	50.019	50.8235	50.2546	5301.658	15
75%,300 + 25%,38	52.9871	53.1059	53.8718	53.3216	5665.254	15
60%,300 + 40%,38	46.9531	47.1391	47.2837	47.1253	4930.378	15
40%,300 + 60%,38	48.3923	48.7102	48.2481	48.4502	4609.254	15
20%,300 + 80%,38	44.1121	45.0123	44.7192	45.2812	4711.582	15

Table 3.2 Values recorded for –300/150μm powder with additions of -38μm powder

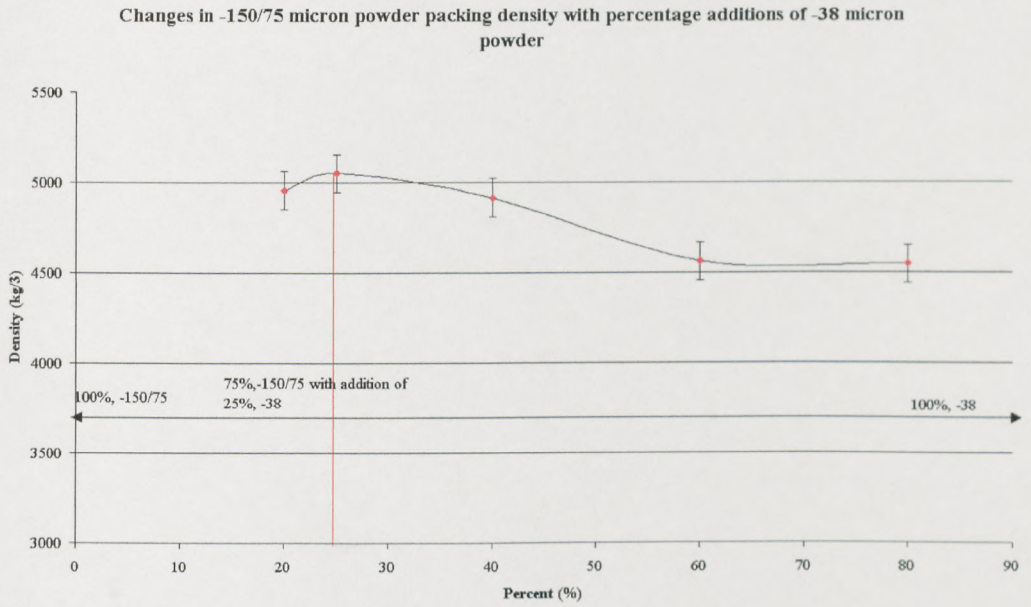

Figure 3.3 -38μm powder packing density with additions of –150/75μm powder

Test Number	Mass (g)	Mass (g)	Mass (g)	Avg. mass (g)	Powder Density Kg/m3	Mixing time (min)
80%,150 + 20%,38	47.5891	46.9128	47.5874	47.3631	4958.58	15
75%,150 + 25%,38	48.2114	48.1911	48.0442	48.1489	5051.181	15
60%,150 + 40%,38	47.1137	46.9193	46.9925	47.0095	4916.508	15
40%,150 + 60%,38	45.1913	45.2108	45.1541	45.1854	4563	15
20%,150 + 80%,38	45.1121	44.9917	45.1692	45.091	4549	15

Table 3.3 Values recorded for –150/75μm powder with additions of -38μm powder

In this instance the maximum attainable density for a time of 15 minutes mixing was achieved with a percentage of 25% -38μm powder and 75% -300+150μm powder. This density was found to be approximately 20% and 12% higher than that of the densities of -38μm powder and –300+150μm powder respectfully.

Figure 3.3 and table 3.3 show the data obtained during the mixing tests for -38μm powder with addition of –150+75μm powder. In this case the maximum attainable density for a time of 15 minutes mixing was reached with a percentage of 25% -38μm

density for a time of 15 minutes mixing was reached with a percentage of 25% -38μm powder and 75% -150+75μm as well as 20% -38μm powder and 80% -300+150μm. A small improvement in powder densities after mixing can be observed but it is not significant. The density was found to be around 10% higher than that of the two mixed powder initial densities.

Appendix C (a) shows the data obtained during the mixing experimental tests for –75/38 μm powder with addition of –150/75μm powder. The maximum attainable density was reached for a mixing time of 15 minutes. The percentage used for attaining the highest density with these two batches of powder was 40% of –75/38 μm and 60% of-150/75μm. The powder density obtained by mixing these two batches of powder did not show a significant powder density improvement. The powder density obtained was 7% higher than the initial density measured for each batch of powder.

Appendix C (b) shows the data obtained during the mixing tests for -38μm powder with addition of –75+38μm powder. The peak in packing density was reached after a mixing time of 15 minutes. Also, a high density was also obtained for a mixing time of 30 minutes. The packed densities obtained for these batches showed an increase but it was only 8% compared with pre-packed powder densities.

Finally, these results show that the mixing of the four individual particle batches increases the powder packing density by an average of 10%. And the mixing together of two powders produces a packing density higher than mixed individual powders but not significantly higher except for mixing powders of -38μm powder size with –300+150μm powder.

It is thought that the influence of the spreading mechanism and the vibration within the system will alter the powder densities obtained. It is estimated based on some trial tests that a drop of at least 5% would be expected.

It has also come to light that the size of the powder sample used alters the calculations for the density. In general, a larger powder sample resulted in a larger calculated density. The results presented here are for samples larger than susceptible to this effect.

3.3 Powder flowability tests

Flowability of the powders can be measured using the two main methods which were described in the previous chapter (chapter 2, section 2.2.3). Hall's flowmeter was initially chosen for the testing here. However, preliminary trials showed that the finer powders did not flow through its ϕ 2.5mm orifice. Therefore Carney's funnel which had a larger orifice diameter of ϕ 5.0mm was used for the finer powders (-38μm for example).

A flowmeter was designed, manufactured and supported using a laboratory clamp stand. The experiments were carried out in accordance with the standards tests described in section 2.2.3 for Carney and Hall's flow meters.

The powder flowability tests were carried out in three stages. Firstly, the flowability of raw powders was measured using both flow meters available. Secondly, the powders were mixed together for 1 minute in different percentages and the flow rates measured. Finally, the powders were mixed together for pre-defined times, 15, 30, 45 and 60 minutes, and then the flow rates were measured. Numerical results are gathered in Appendix D.

3.3.1 Powder flowability for raw powders

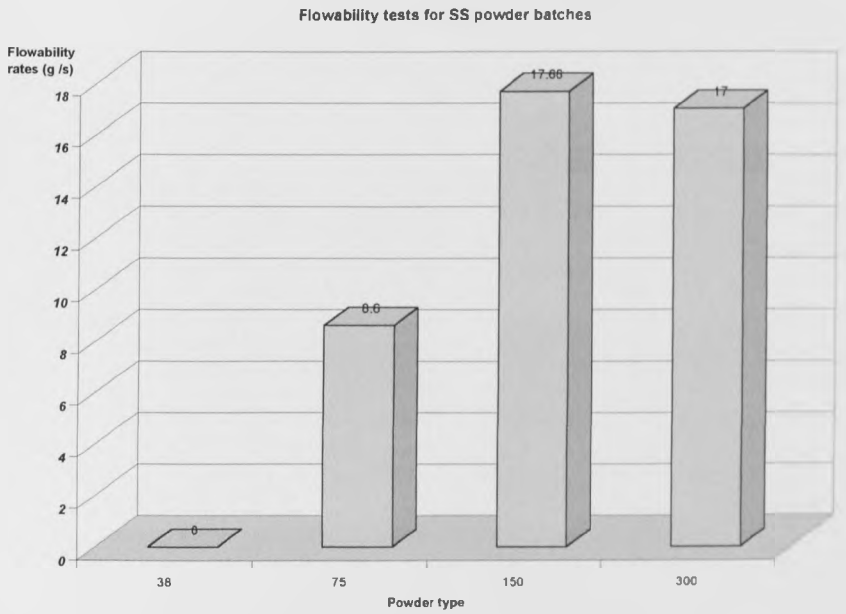

Figure 3.4 Flow rates of the as received state powders

Figure 3.4 shows the results collected for the measurements of the raw powders. The figure presents the results for the Carney's funnel because when Hall's funnel was used only the 150μm and 300μm powders flowed through it.

These observations may be compared with observations of flow from the V-hopper mechanism (section 2.4) during powder bed spreading. These tests showed that it is very difficult to obtain a flat powder bed by spreading the -38μm powder using the V-hopper mechanism. The powder bed obtained was not regular and it had big gaps within the powder bed.

Moreover, the -38μm powder flowed through the V-hopper 5mm gap only because of the system vibrations during spreading. In addition, the 300μm and 150μm powder flowed very easily during the spreading tests. The amount of powder used during the spreading experiment needed to be increased because of "mountains" of loose powder at the bottom of the V-hopper spreading mechanism. Furthermore, during the multi-layer sintering tests it was observed an influence of the powder flowability proprieties over the sintered parts. The powder flowed through the V-hopper gap under the gravity force and continuously pushed into the powder bed causing a displacement of the sintered layer.

3.3.2 Powder flowability for mixed powders

The tests for measuring the flowability rates of mixed powders were carried out at the same mixing times as those for the powder packing tests. The powders were mixed for 15, 30, 45 and 60 minutes. The flowability tests were carried out immediately after the mixing process, to avoid the segregation of the powders due to storage.

Figure 3.5 shows the Carney's flowability experimental test results obtained for –300 +150 μm powder with additions of –75+38 μm powder mixed for the time periods of 15, 30, 45 and 60 minutes.

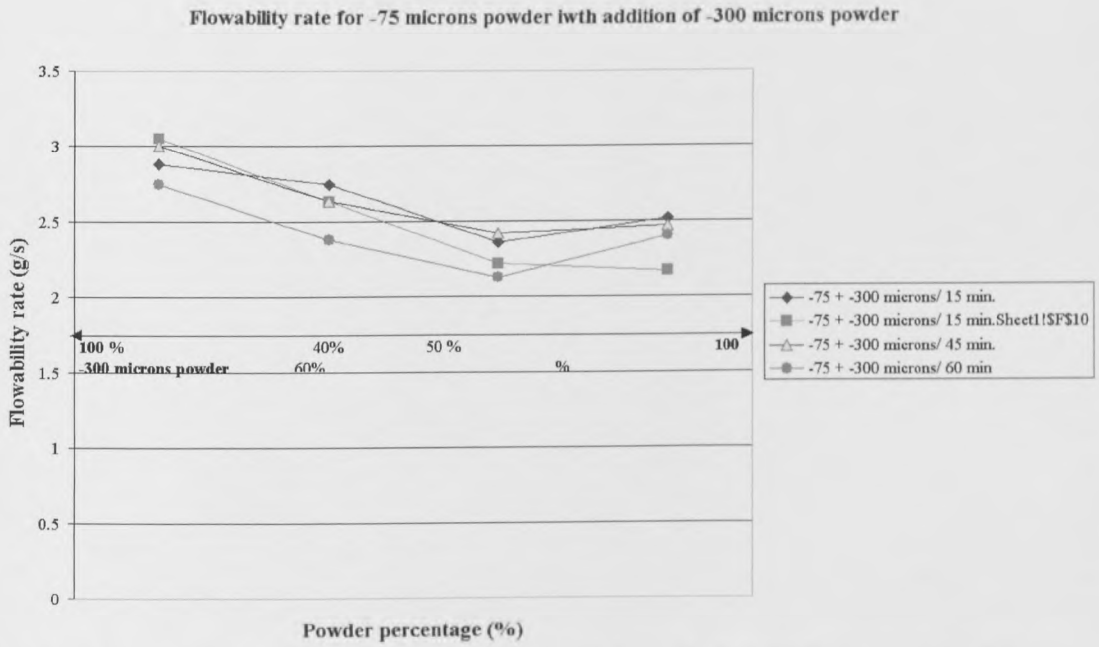

Figure 3.5 Flow rates for –75+38μm powder with addition of –300/150μm powder for different mixing times

The flowability of the packed powder tends to increase again when one of the powders has a bigger percentage than 80% in the mix. In general, this mixed powder did not showed big differences of powder flowability data when the percent of each powder in the mix was lower then 80%. The spreading experimental tests with this mixed powder showed that the powder bed obtained had a fairly good flatness.

Figure 3.6 shows the flowability rates from the experimental tests for -38μm powder with addition of –300+150 μm powder. A sharp decrease of the flow rate was recorded after 15 minutes of powder mixing compared to the raw powder flow tests. It was also recorded that a percent of -38μm powder bigger a 40% in the mix it made the mixed powder to not flow at all. The spreading tests showed a very good quality of the powder bed surface when the -38μm powder was less then 40% in the mix.

Figure 3.5 shows the Carney's flowability experimental test results obtained for –300 +150 μm powder with additions of –75+38 μm powder mixed for the time periods of 15, 30, 45 and 60 minutes.

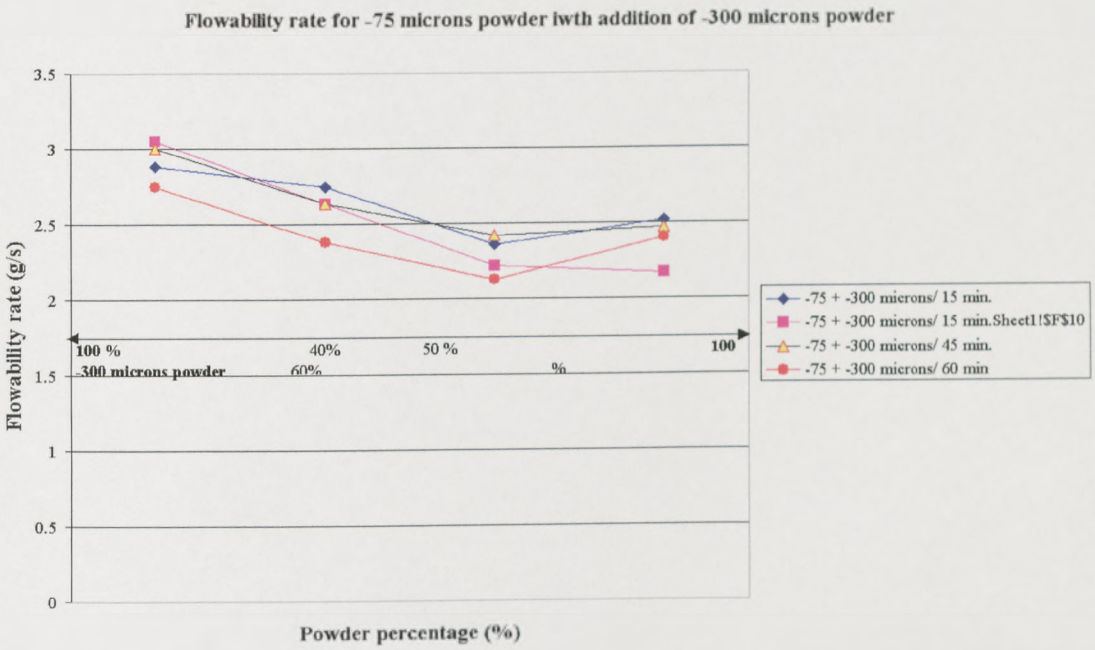

Figure 3.5 Flow rates for –75+38μm powder with addition of –300/150μm powder for different mixing times

The flowability of the packed powder tends to increase again when one of the powders has a bigger percentage than 80% in the mix. In general, this mixed powder did not showed big differences of powder flowability data when the percent of each powder in the mix was lower then 80%. The spreading experimental tests with this mixed powder showed that the powder bed obtained had a fairly good flatness.

Figure 3.6 shows the flowability rates from the experimental tests for -38μm powder with addition of –300+150 μm powder. A sharp decrease of the flow rate was recorded after 15 minutes of powder mixing compared to the raw powder flow tests. It was also recorded that a percent of -38μm powder bigger a 40% in the mix it made the mixed powder to not flow at all. The spreading tests showed a very good quality of the powder bed surface when the -38μm powder was less then 40% in the mix.

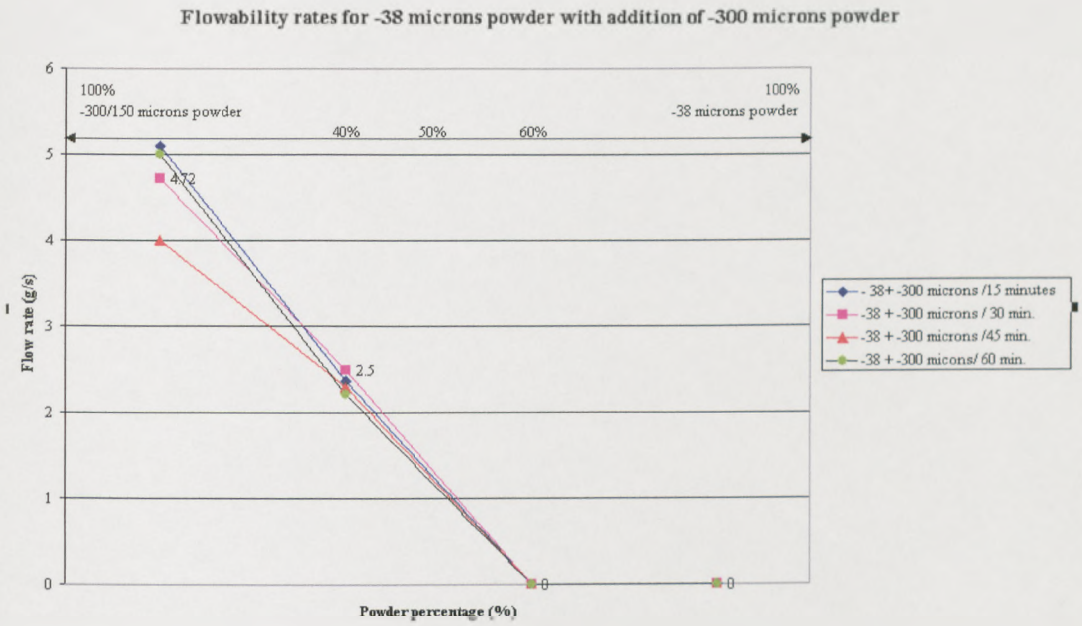

Figure 3.6 Flow rates for -38μm powder with addition of -300μm powder for different mixing times

Figure 3.7 shows the flowability rates measured during the experimental tests for –150+75 μm powder with addition of –300+150 μm powder. This also showed a sharp decrease of the powder flowability rate after 15 minutes of mixing.

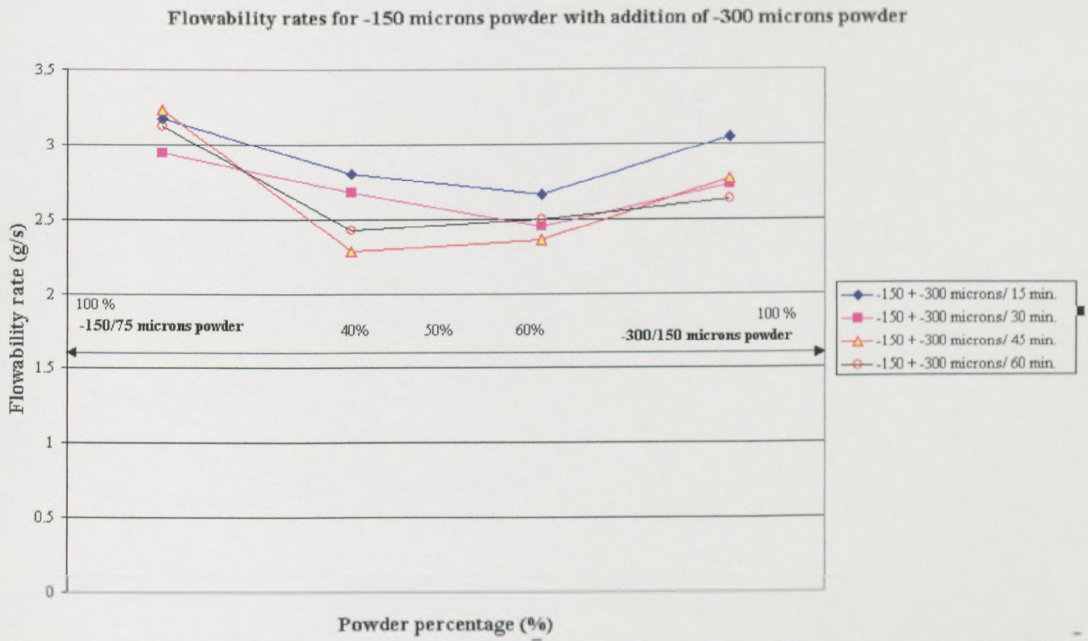

Figure 3.7 Flow rates for - 75μm powder with addition of –300 μm powder for different mixing time

The effect of the powder mixing over the powder flow rate had a significant impact but the influences of the surface superficial forces over the small particle flow was still predominant.

3.4 Stainless steel powder thermal conductivity tests

The thermal conductivity experimental tests are listed in Table 2.4. In all of them, the heated top plate of the rig was held at 150 degrees Celsius.

Figure 3.8 shows a typical variation of the thermocouple temperatures R1 to R6 with time. R6 was always noisy and may have been damaged.

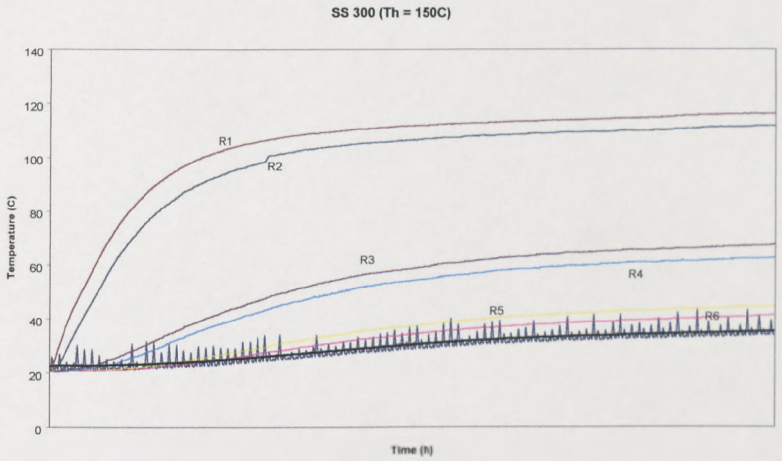

Figure 3.8 Temperature vs. time for –300+150μm powder heated at 150^{0}C

Figure 3.9 is a single example extended to 24 hours. It ca be seen that a steady state is achieved after a time interval from 4 to 5 hours.

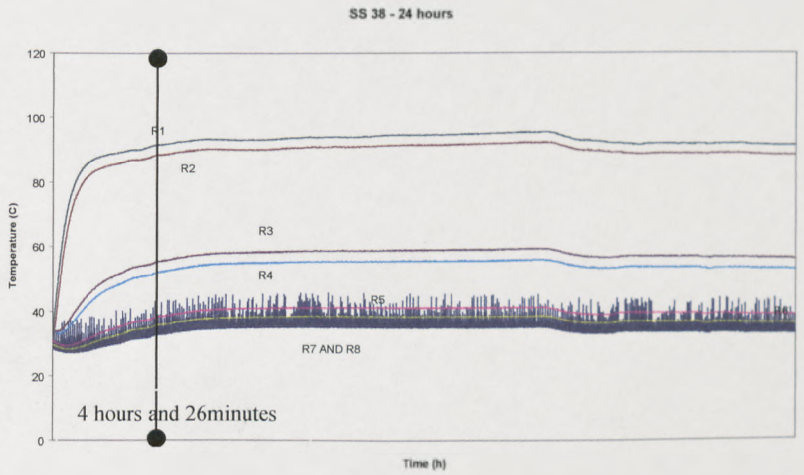

Figure 3.9 Temperature vs. time for -38μm powder heated at 150^{0}C for 24 hours

Figure 3.10 shows how the temperature differences across a comparator vary with time. In the steady state (T_2-T_1) and (T_4-T_3) became equal. This supports the assumption of no heat loss from the sides of the rig. (T_6-T_5) is less then (T_2-T_1). This fact suggests either a heat loss from the lower part of the rig or an error in (T_6-T_5). It is believed there may be errors in T_6, indicated by the variation shown in figures 3.9 and 3.9.

In calculations according to the theory of Chapter 2, equation 2.4, (dT/dz) for the comparator will be taken from the average of (T_2-T_1) and (T_4-T_3) for sample 1 and from the average of (T_4-T_3) and (T_6-T_5) for sample 2.

Appendix E contains steady state numerical results. These have been used to populate Table 3.5. Figure 3.11 is a plot after equation 2.4. From its slopes, the conductivity values in Table 3.5 have been deducted.

Figure 3.12 shows the variation of conductivity with powder size. There is no significant difference. An average value of 0.31 W/mK is obtained.

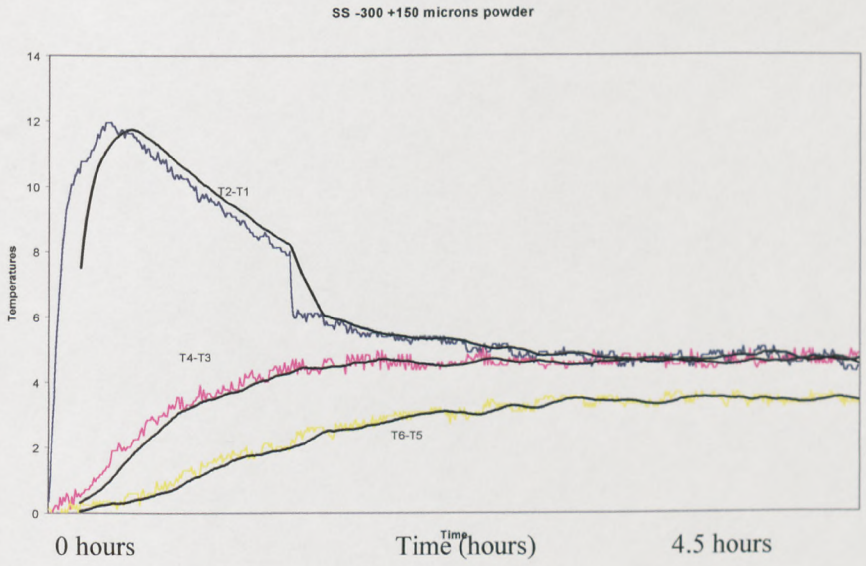

Figure 3.10 Temperature difference within the reference disk for -300+150 microns powder

Table 3.5 Analysis of thermal conductivity data

Powder size	ΔTs_1	ΔTs_2	$\Delta z\left(\frac{\Delta T}{\Delta z}\right)_{comp\ 1}$	$\Delta z\left(\frac{\Delta T}{\Delta z}\right)_{comp\ 2}$	Thermal conductivity k (W/mK)
-38μm	38.5	15	0.80	0.36	0.28±0.05
-75/38μm	27.6	13.8	0.62	0.28	0.32±0.02
-150/75μm	15.2	14.5	0.47	0.50	0.33±0.06
-300/150μm	45.2	15.3	0.91	0.40	0.25±0.05

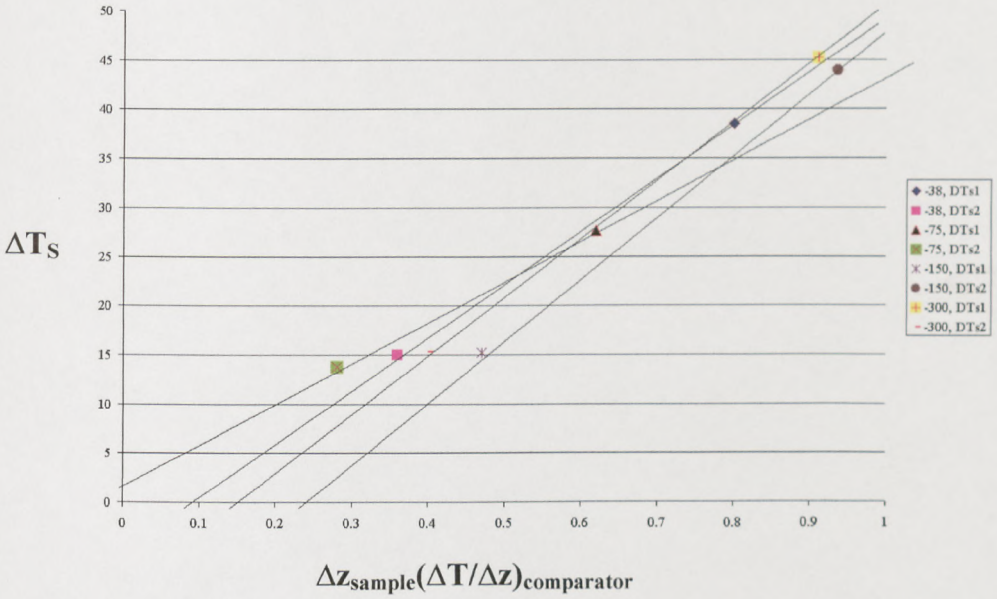

Figure 3.11 ΔT_{sample} vs. $\Delta z_{sample}(\Delta T/\Delta z)_{comparator}$

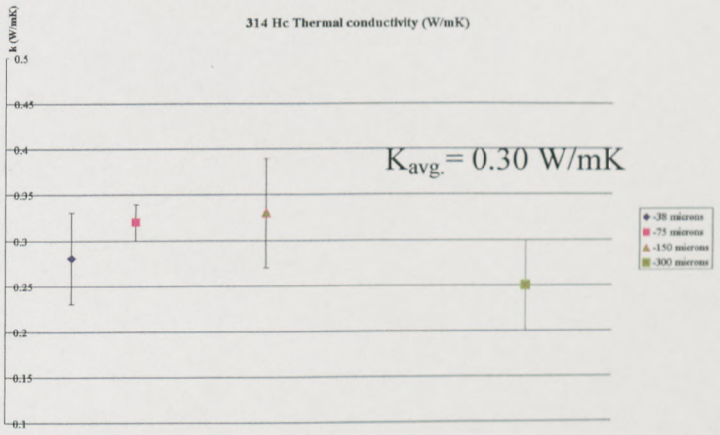

Figure 3.12 Thermal conductivity for all batches of powder

3.5 Selective laser sintering of SS 314 HC powder tracks

This section reports the formation of single tracks in powder beds. Six different powder batches have been used during the sintering experimental tests. Four single size fractions: -300/150μm, -150/75μm, -75/38μm and -38μm powder, and two mixed fractions: 75%, -300/150μm with addition of 25%, -38μm powder and 75%, -150/75μm with addition of 25%, -38μm powder. In every case, tracks of 20mm length were formed by the scanning laser beam, with powers from 25W up to 170W and scan speeds from 1mm/s up to 17 mm/s (except in a few cases where the scan speed was reduced down to 0.5mm/s). The sintering test results are presented like sintering maps. Due to difficulty of classifying the melt pool behaviour, each of the maps was created individually using the melt pool growth and shape observed during the experimental tests.

3.5.1 Qualitative observations for tracks scanned in oxygen atmosphere

The experimental tests in an argon atmosphere were done intending to clarify the effects and the requirements of the selective laser sintering atmosphere. Particular attention in this section of the thesis has focused on the significance of oxygen during the formation and growth of the stainless steel melt pool. This includes all four batches of un-mixed powder as the CO_2 laser scans the powder bed surface over a range of scanning speeds and laser powers.

The oxygen atmosphere was achieved by exposing the stainless steel powder bed to laboratory air during the sintering process. The powder was in its as received state. No powder pre-heating was carried out prior to the start of the sintering process. However, the powder used during the experiments was collected from unbroken sealed containers. Prolonged atmospheric exposure caused powder agglomeration because of the moisture absorption in the -38μm powder batch and an increased chance of further oxidation from all powder during the sintering process.

Conditions for sintering single tracks using an air atmosphere were found to be very limiting and this is the reason why the results for single tracks and layers will be presented together. Furthermore, the main focus of this thesis is to build multi-layers so particular attention was paid to those sintering atmospheres, which help to reach this goal.

The air atmosphere is not helpful for sintering. From the beginning of the tests it became obvious that the oxygen atmosphere was more helpful in understanding the sintering phenomenon than using it to build multi-layers.

Figure 3.13 shows the stages of oxidation behaviour observed during the experimental tests. Furthermore, information regarding particle bonding and melt pool growth and quality during single line scanning had been taken into consideration when the sintering maps were made. During sintering, temper coloration following classical oxidation theory could be observed on the surfaces of individual 314 HC particles as the powder bed was heated by the laser beam. Moreover, as the net energy density increased, small droplets of molten metal liquid began to form, covered by a dark surface oxide scale and seated within a trail of oxidised powder.

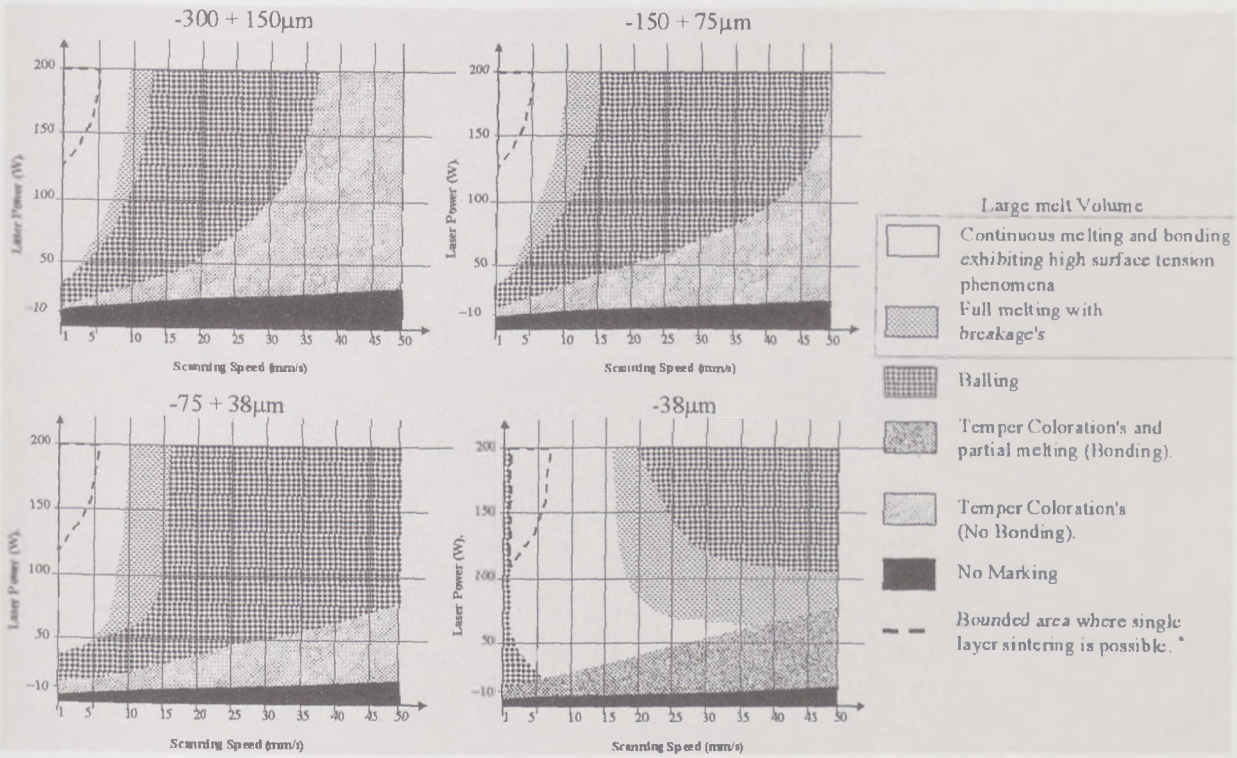

Figure 3.13 Sintering maps for tracks scanned using a oxygen atmosphere
(C. Hauser, T.H.C. Childs, K Dalgarno and R.B Eane, 1999)

The phenomenon of melt pool balling and breakage was widespread during oxygen sintering because of the liquid surface tension forces which were allowed to dominate due to large melt volumes and the influence of the surface dark scale. If the scanning speed was low, below 8 mm/s, and the laser power was high, it was found out

that surface tensions became less dominant and the melt pool began to flow more freely. The result of this behaviour was a continuous melt pool that solidified into a tubular shape, circular or semi-circular in cross section. Still, such high sintering temperatures dramatically increased the melt pool volume and a slag believed to be rich in chromium (Cr_2O_3) was observed on the sintered part surface.

Single layer scanning was carried out over a range of conditions where single line scanning was successful. It was found out that single layer scanning could only be achieved at very high laser energy densities. Furthermore, experimentation showed that if the scan spacing was larger then 0.6 mm then the bonding was limited and if the scan spacing was lower the 0.4mm balling occurred. Consequently, the next experimental sintering tests for single layers were performed using an average of 0.5mm scan spacing.

The presence of oxygen within the sintering atmosphere and powder bed allows surface oxides and slags to form as the powder is heated and melted by the laser beam. Moreover, the next experimental tests carried out using argon atmosphere showed, together with the results obtained during the air experiments, that the elimination of the oxygen is required in order to reduce the melt volume, allowing surface tension forces to become less dominant.

3.5.2 Qualitative observations for tracks scanned in argon atmosphere

Figures 3.14 to 3.19 shows photographs of single tracks scanned in an argon atmosphere. Four types of melt pool growth were observed. These all can be seen in figure 3.21, for –75/38μm powder. At the lower laser powers and higher scan speeds, for example at 75W laser power and 15 and 17 mm/s scan speed, tracks were hardly formed at all. Their edges were irregular. Perhaps they were only partially melted and the liquid that formed hardly had time to flow at all. This type of track will be called *partially melted.*

At the opposite extreme (high powers and low scan speeds), for example 130W and speeds below 5 mm/s, the tracks were fully melted but were broken into discrete lengths. The irregular, bulbous thickness of parts of the tracks is caused by surface tension attempting to reduce track surface areas. These tracks will be called *fully melted and broken.*

At low powers and low scan speeds (for example 25W and 50W and 1 mm/s scan speed) tracks were fully melted but were not bulbous in cross-section. Instead their surfaces were concave. These will be called fully melted, crescent or half-moon shaped.

Finally, at laser power of 15W and less, the laser beam was not powerful enough at any scan speeds to cause any marking on the powder bed surface.

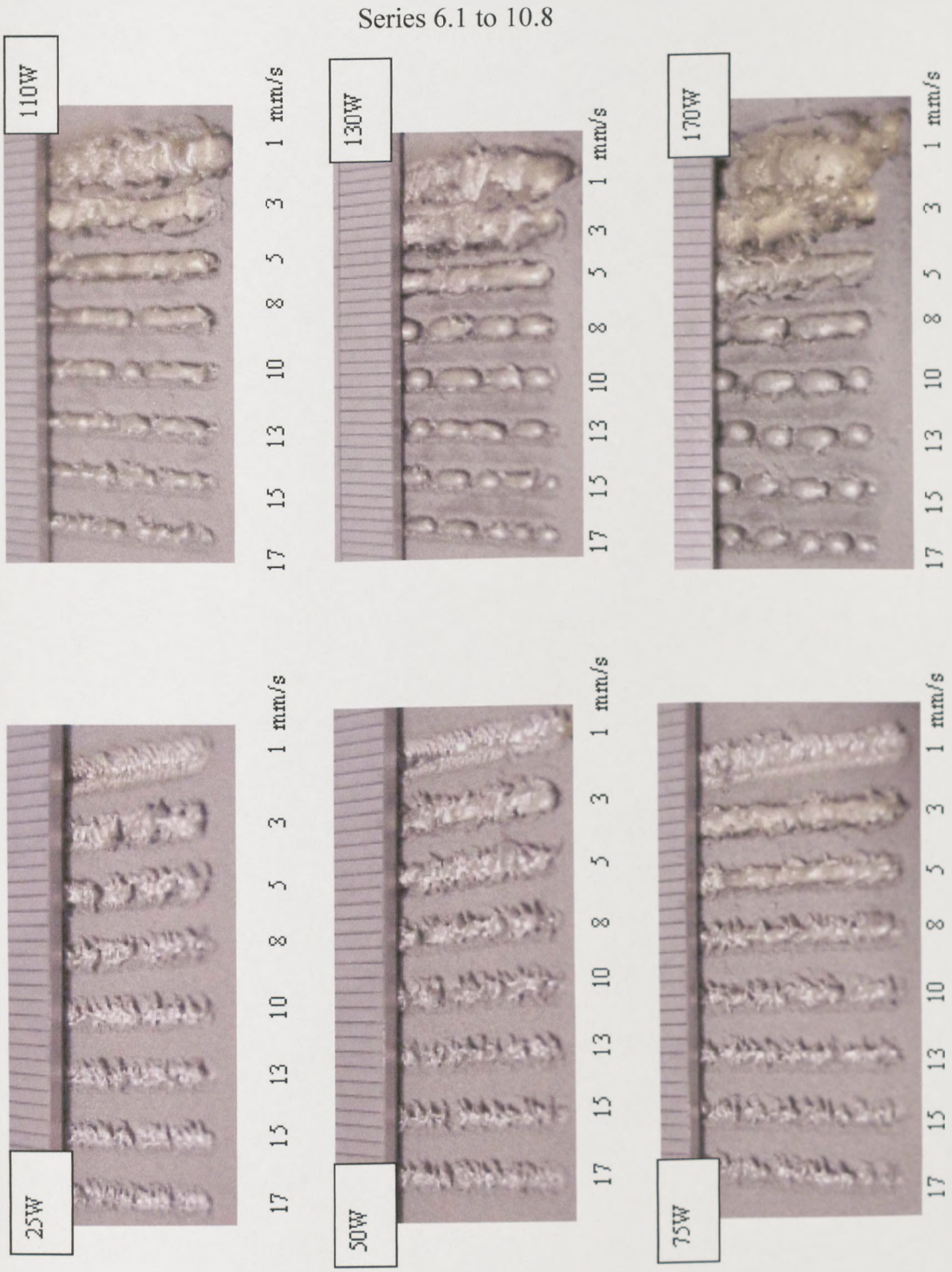

Figure 3.14 Tracks sintered in argon atmosphere
using **-38μm** powder batch at different scanning conditions

Series 16.1 to 20.8

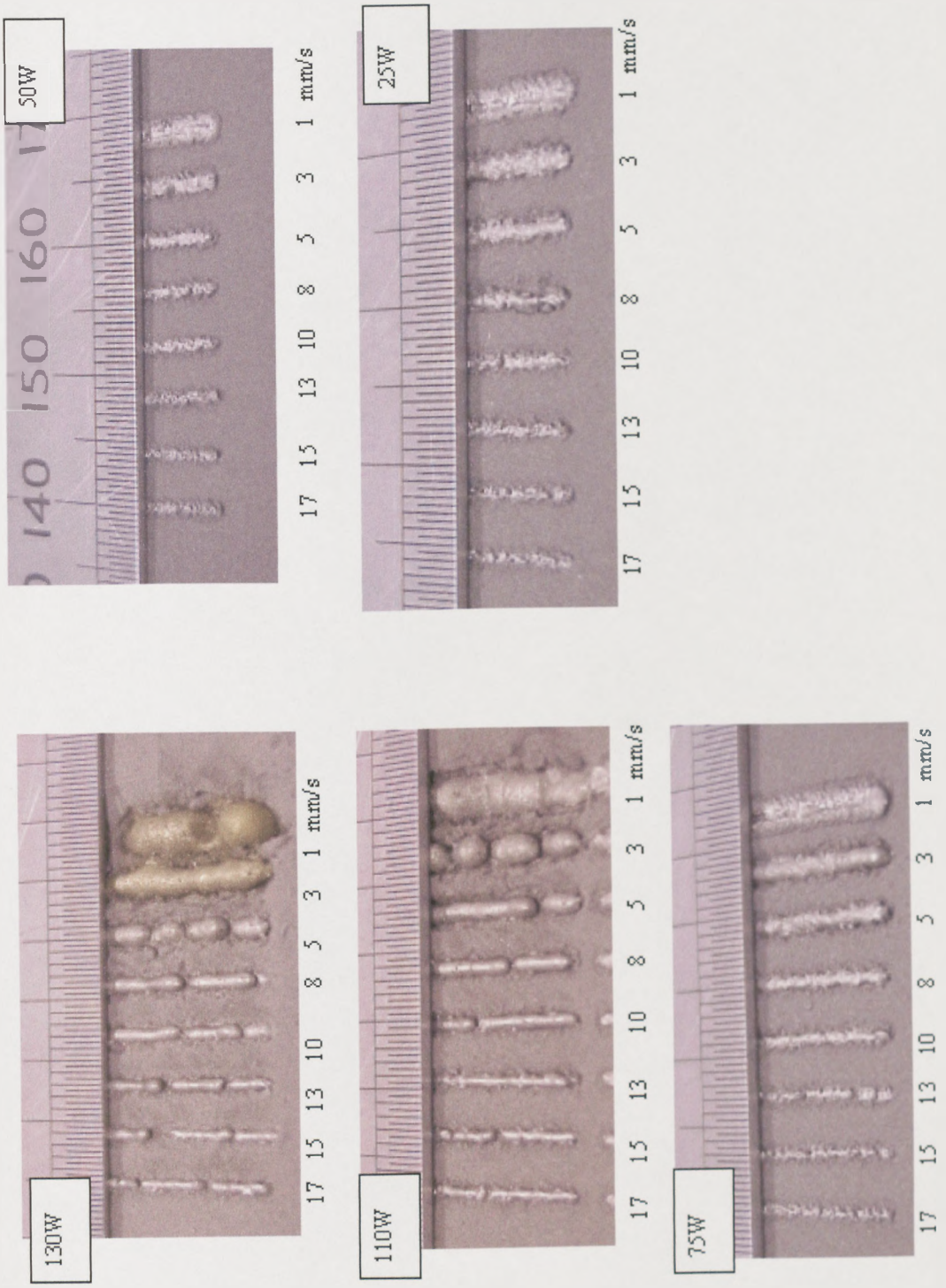

Figure 3.15 Tracks sintered in argon atmosphere

using **–75/38μm** powder batch at different scanning conditions

Series 11.1 to 15.8

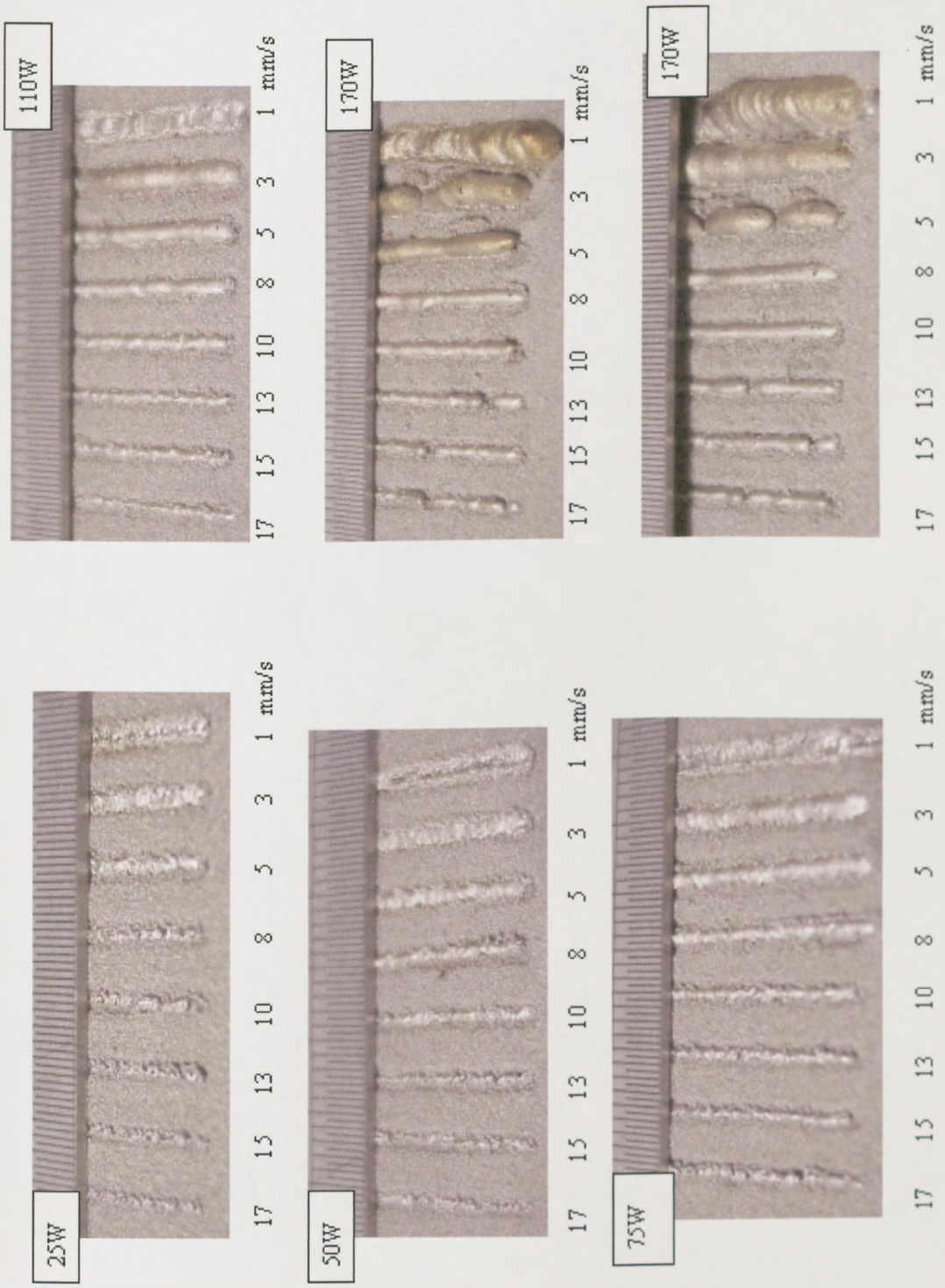

Figure 3.16 Tracks sintered in argon atmosphere using **–150/75µm** powder batch at different scanning conditions

Series 1.1 to 5.8

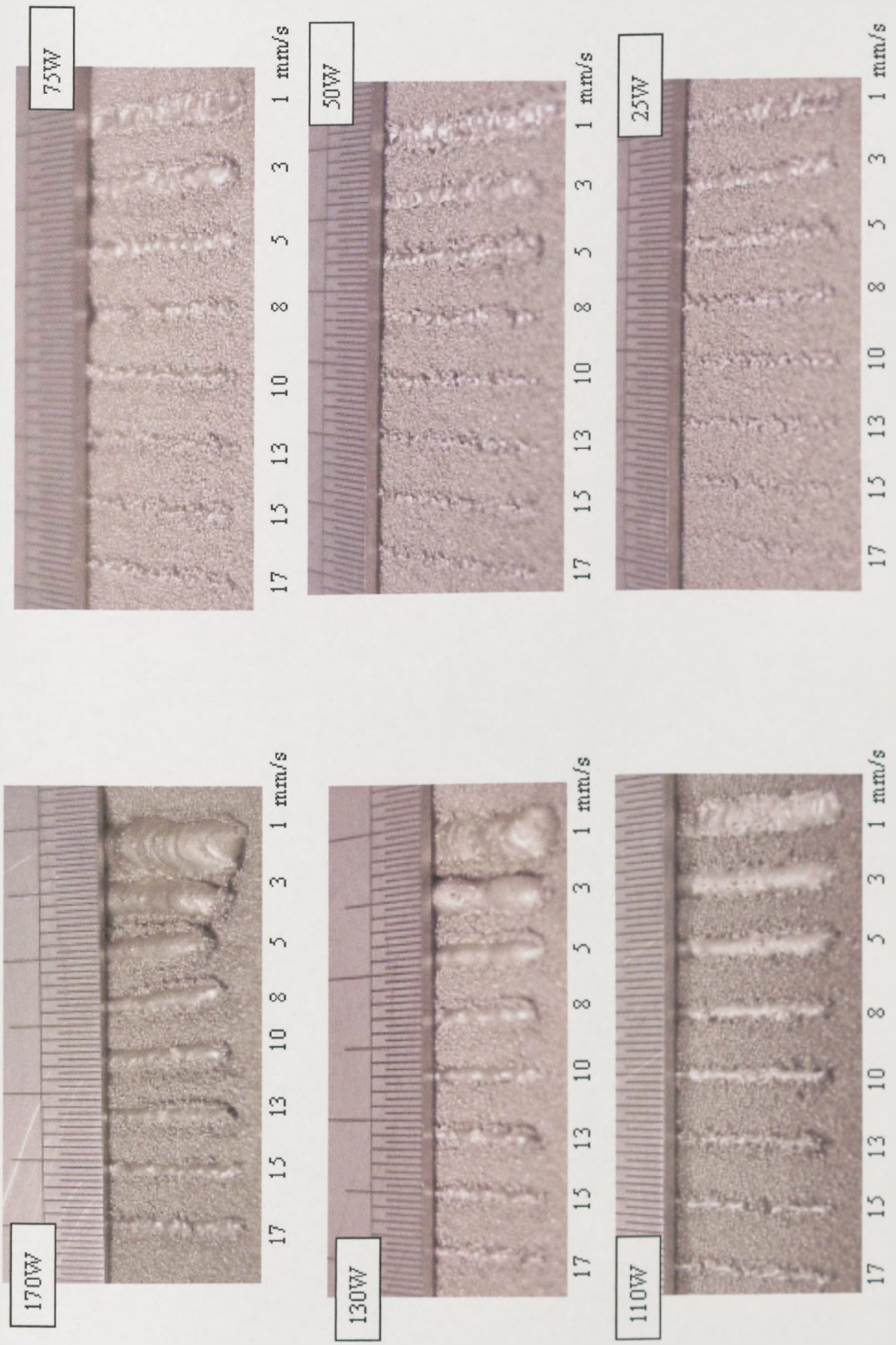

Figure 3.17 Tracks sintered in argon atmosphere
using **–300/150μm** powder batch at different scanning conditions

Series 26.1 to 30.8

Figure 3.18 Tracks sintered in argon atmosphere
using **–150/75μm** powder with addition
of 25%, -38μm powder at different scanning conditions

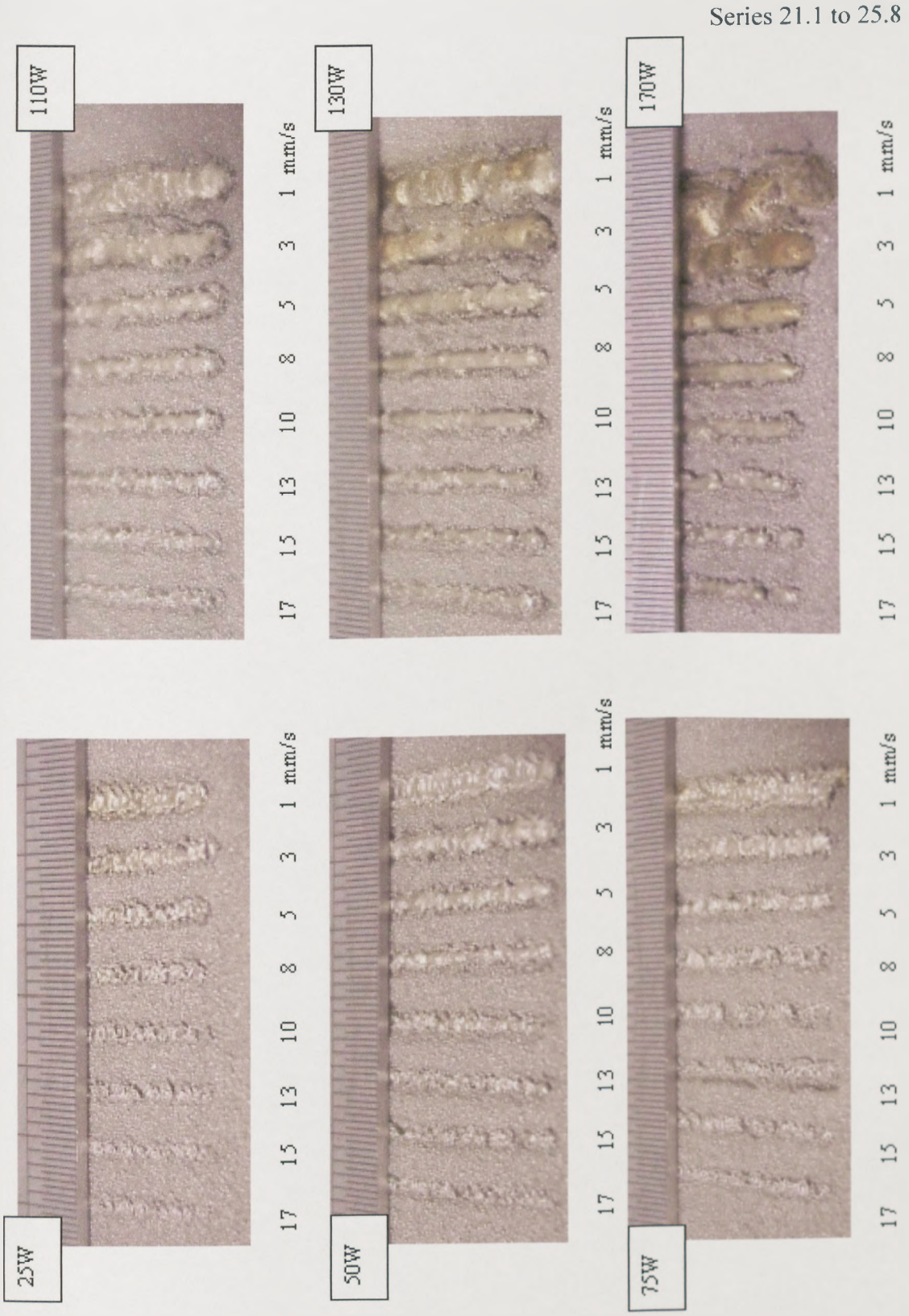

Figure 3.19 Tracks sintered in argon atmosphere
using **–300/150μm** powder with addition
of 25%, -38μm powder at different scanning conditions

Sintering maps were plotted, showing what type of track was formed at the different laser powers and scan speeds. Figure 3.20 to 3.23 shows the four maps for the four single size fraction powders, obtained from figures 3.14 to 3.19. They all have similar regions (regions described above). A diagonal line a-b separates *full melted* tracks to the left from *partially melted* tracks to the right. A line a-d separates the half-moon sectioned *fully melted* tracks to the left from bulbous tracks to the right. Between lines a-b and a-d, a line c-b separates *fully melted* continuous tracks to the left from *fully melted and breakage* track to the right.

In some cases, it was difficult to decide exactly where a boundary was, for example lines a-b and a-b' in figure 3.20. And indeed in the region between a-b and

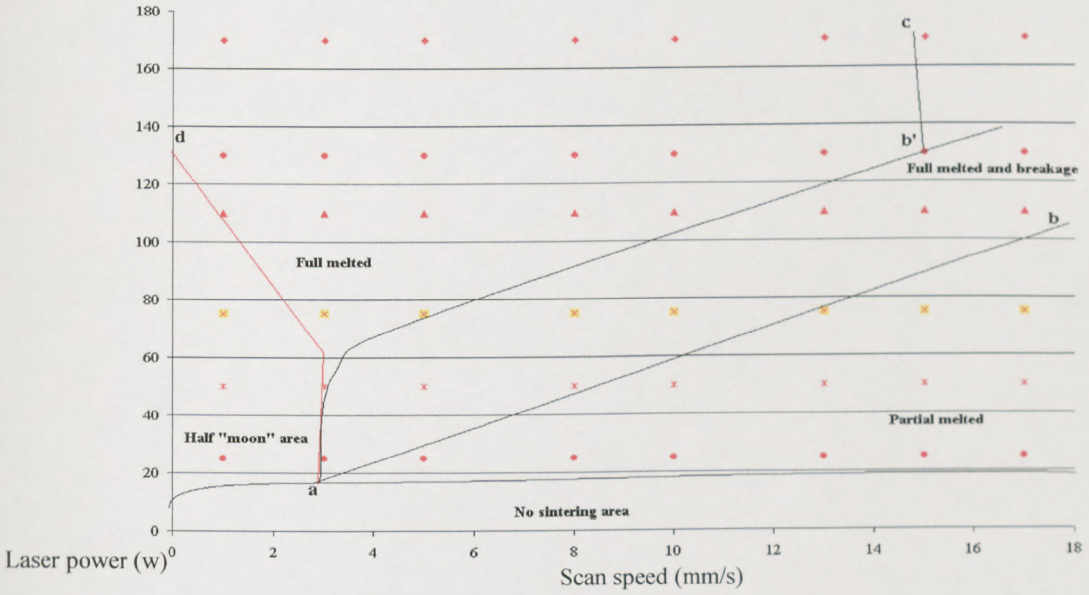

Figure 3.20 Process map of melting regime for –300/150 microns powder irradiated in argon (series 1.1 – 5.8)

a-b', maybe the tracks are showing signs of being irregularly broken, as is certainly the case above to the right of c-b.

The main difference between the four figures is that as powder size decreases, the line c-b moves to the left, to lower (power, speed) combinations. Also, for the -38μm powder (figure 3.21), the half-moon section track region is smaller than for the other batches of powder.

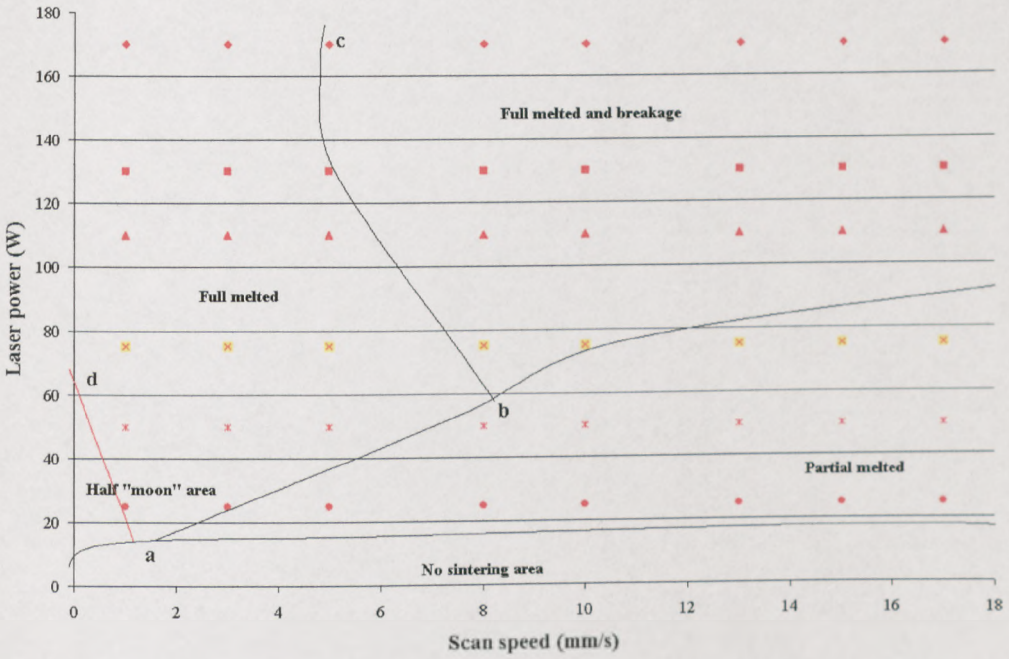

Figure 3.21 Process map of melting regime for –38 microns powder irradiated in argon

Another difference can be seen, by referring back to figure 3.20. The partially melted tracks for the -38μm powder have much more irregular edges then those for other powders.

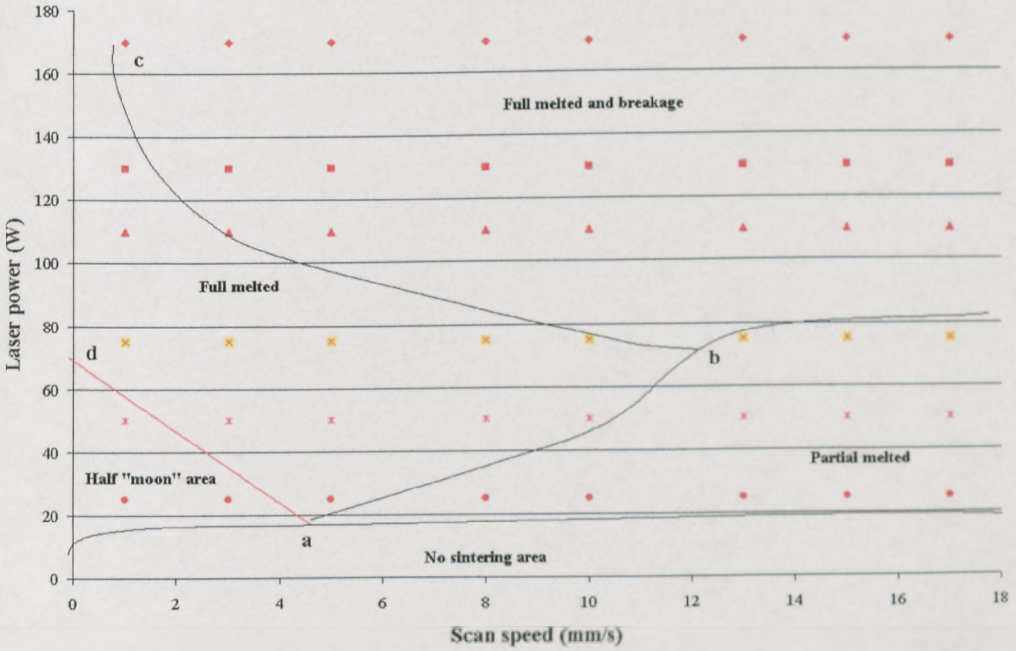

Figure 3.22 Process map of melting regime for –75/38 microns powder irradiated in argon

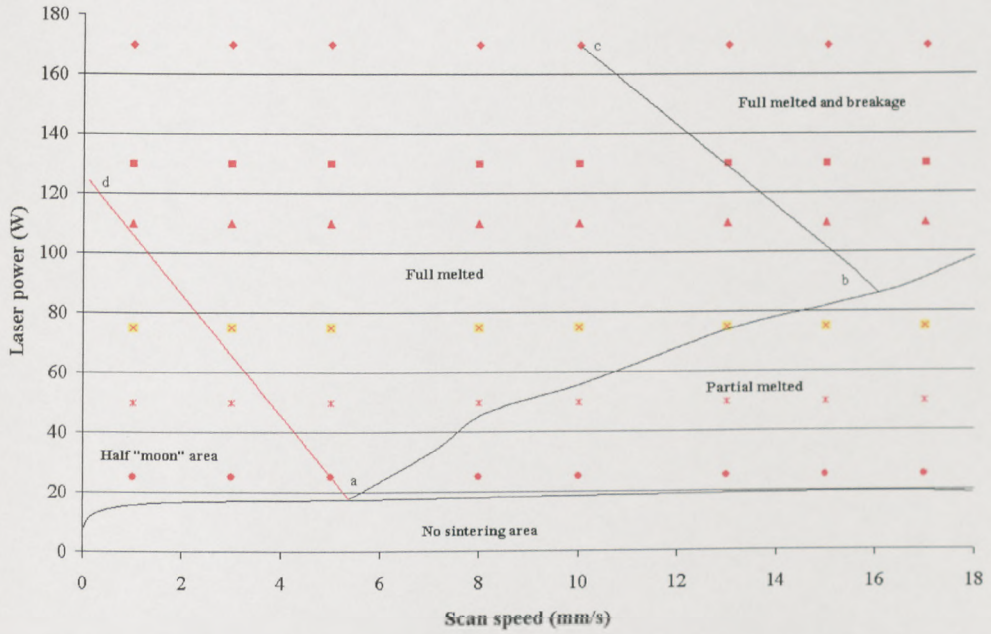

Figure 3.23 Process map of melting regime for –150/75 microns powder irradiated in argon

Figure 3.24 and 3.25 shows similar maps for mixed powder size fractions. Comparing figures 3.24 and 3.25 with figures 3.20 and 3.23 the main difference is the movement of the boundary c-b to lower power/speeds in figures 3.24 and 3.25 compared to

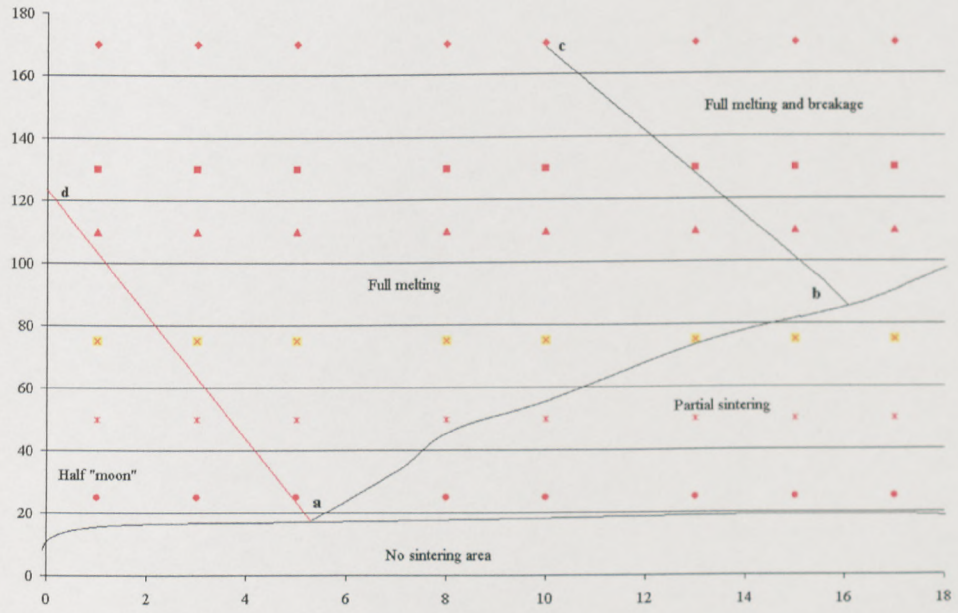

Figure 3.24 Process map of melting regime for –300/150 with addition of 25%, -38μm powder irradiated in argon

figure 3.20 to 3.23. And also, in figure 3.24, the boundary a-b is more strongly demonstrated.

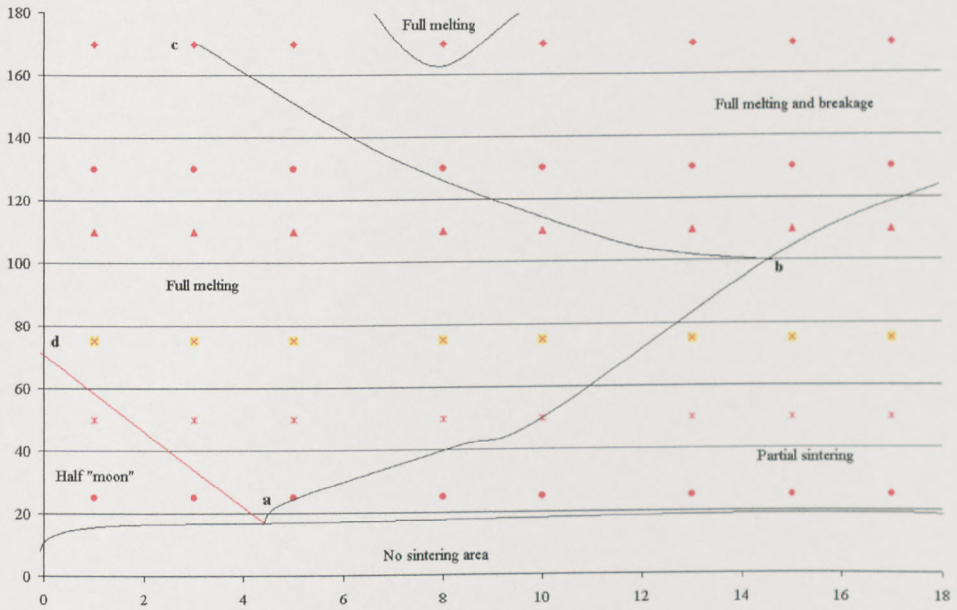

Figure 3.25 Process map of melting regime for –150/75 with addition of 25%, -38μm powder irradiated in argon

Finally, a strong similarity was noticed between the sintering map of –150/75μm powder (figure 3.23) with the sintering map for the mixed powder –300/150μm with addition of 25%, –38μm powder (figure 3.24).

3.5.2 Track dimensional measurements

The single tracks described in section 3.5.1 were lifted, where possible, from their beds. A micrometer was used to measure the average widths and depths. The mass of the 20mm lengths were also measured to obtain their weights per unit length. All the measurements are collected in Appendix G. Not all weights per length were measured as indicated by the gaps in the appendix Tables. Zero entries indicate where it was not possible to lift the tracks without destroying them because they were too fragile.

Typical results for the single size powders are shown in figures 3.26 to 3.28. In each case, part (a) is for the –300/150 μm powder and part (b) is for -75/38 μm powder. These represent examples with small and large regions of fully melted and breakage tracks (see figure 3.26 a and c), respectively.

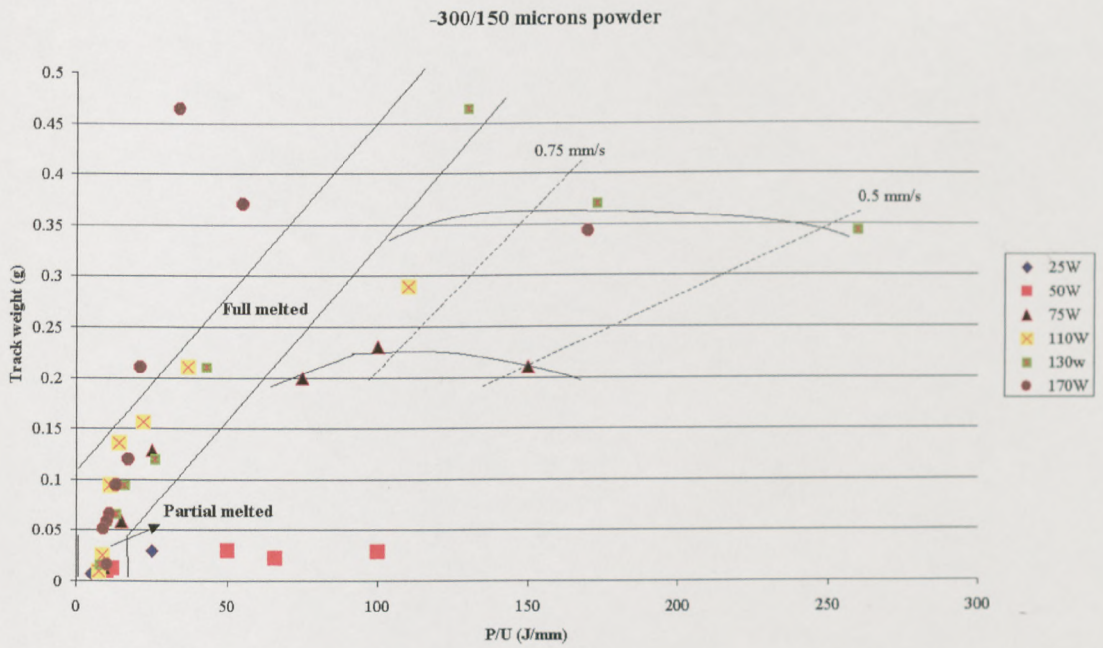

3.26 (a) Track weight vs. laser energy for –300/150 μm powder

Figure 3.26 (a) and 3.26 (b) plot measured track masses per unit length against P/U, on a linear scale. P/U is the laser energy per unit length directed on to the track. Most of the results fall within two straight-line regions, labelled "full-melting" and "partial melting". The full melting region has a slope of unity. The melted track mass is proportional to the laser energy used during the sintering experimental tests. It exists for P/U > 10 J/mm. Referring to figure 3.26 (a), this coincides with the line a-b' in that plot. For lower P/U values, figure 3.26 (a) shows partially melted tracks, with less mass per unit length then for the fully melted tracks. The region marked "fully-melted" contains all the data for P/U > 10 J/mm except for the results where the scan speed was less the 1 mm/s (a few tests were carried out at 0.75 mm/s and 0.5 mm/s) A progressive reduction in mass per length, at a given energy per length, is seen as scan speed is reduced. Also, there are there data points, for P=25W, that lie above the rest of the data.

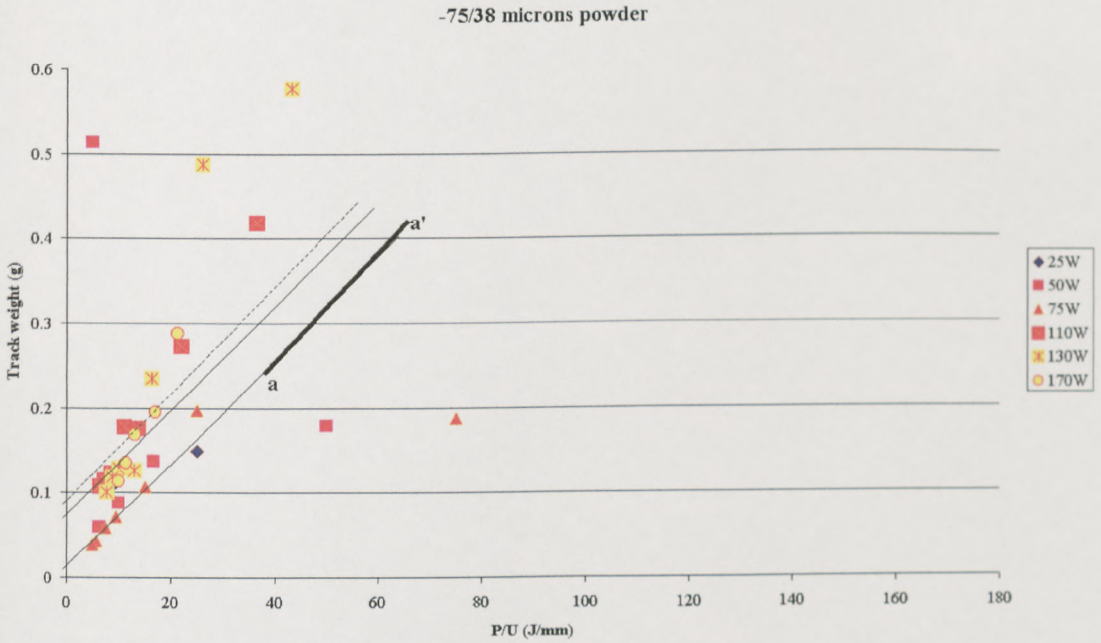

3.26 (b) Linear scale graph, Track weight vs. laser energy for –75/38 μm powder

Figure 3.26 (b) is a similar plot, but for –75/38μm powder batch. A line marked a-a' represents the non-fully melted data line from part (a). Most of the data in figure 3.26 (b) is a band, of slope unity, above the line a-a', with about twice the mass per unit length at a given P/U as in part (a). There is no *partial-melting* region. The tracks were either *fully*

melted, or not coherent enough to be lifted from the powder bed. Fully melted tracks for P/U> 5 J/mm corresponds to the boundary a-b in figure 3.22.

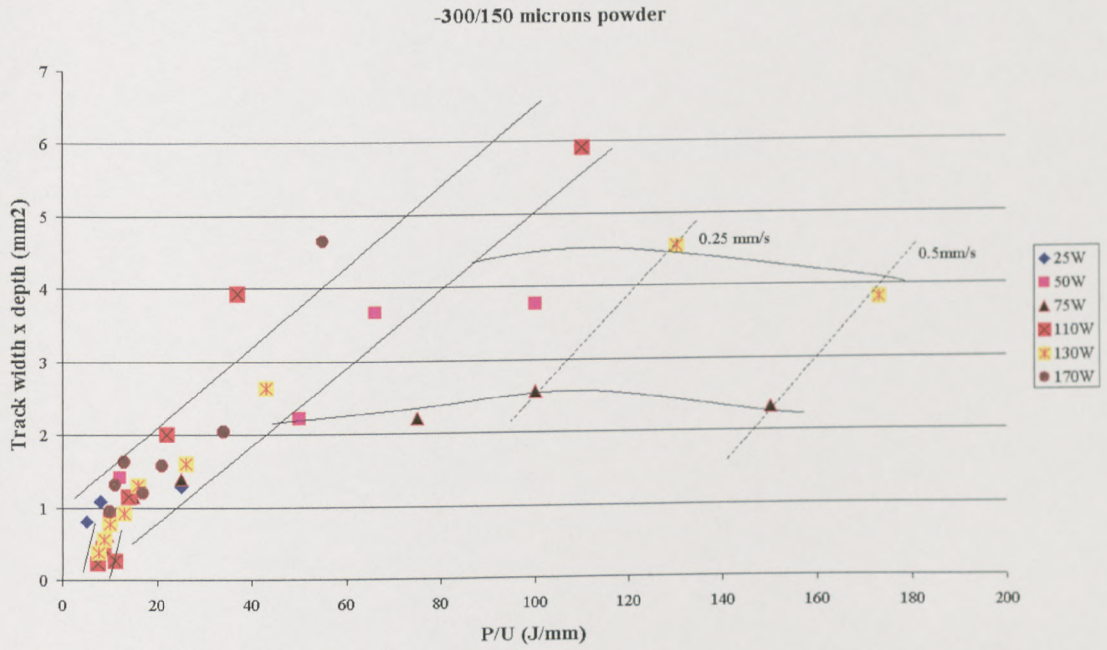

3.27 (a) Track w x d vs. laser energy for –300/150 μm powder

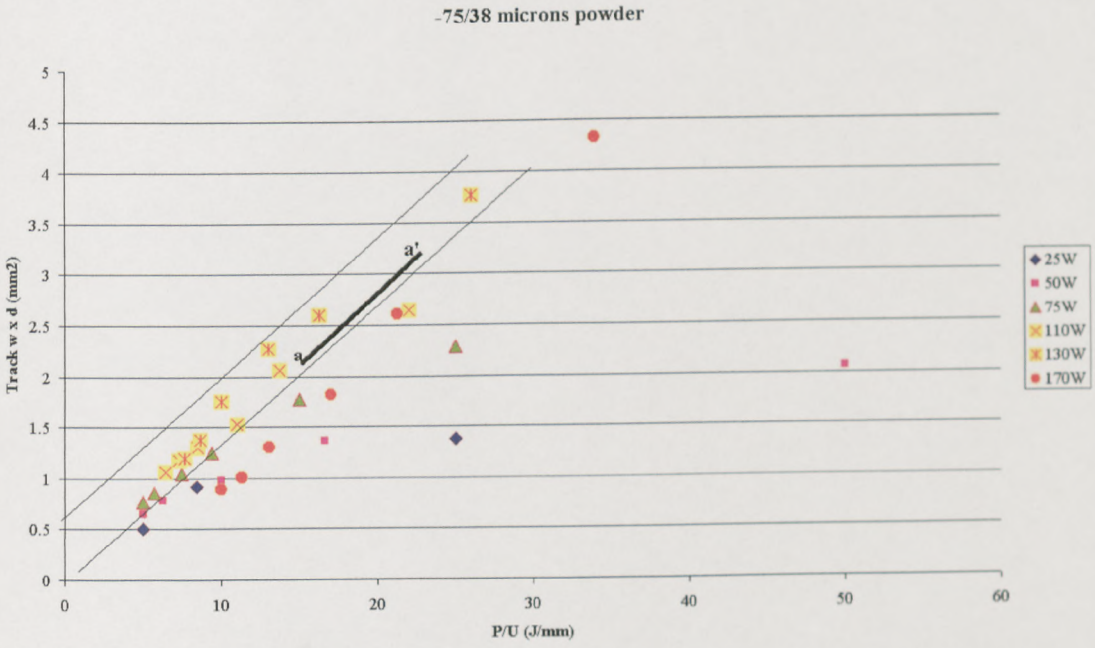

3.27 (b) Track w x d vs. laser energy for –75/38 μm powder

Figure 3.27 (a) and (b) plots similar information to that in figure 3.26 (a) and (b) but shows the product of track width and depths against P/U. Width times depth is a measure of track cross-section area. The pattern of behaviour is almost identical to that in figure 3.26. The main difference, in figure 3.27 (a), is that the data points at P=25W are not separated from the reminder of the results. The track densities can be estimated from the ratio of weight /length to area/length. This, with other aspects of the results, will be considered further in the discussion, Chapter 5.

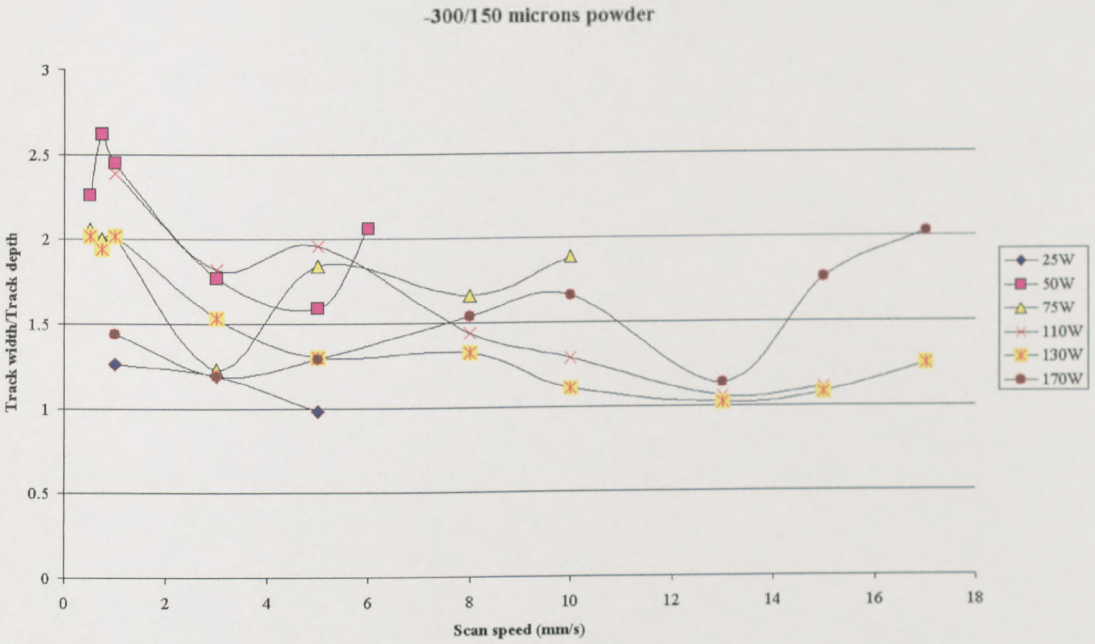

3.28 (a) Track w/d vs. laser energy for –300/150 μm powder

The track aspect ratios, width/depth (w/d) are considered in figure 3.28 (a) and (b) in this case on a linear scale. The results for the –75/38μm powder give a more consistent picture then for –300/150μm powder batch. Figure 3.28 (b) shows that (w/d) at first decreases at any power level, as soon scan speed is increased, and then increases again. Comparing this figure with figure 3.22, it can be seen that the line a-a' in figure 3.28 (b) that passes through the minimum of the (w/d) versus scan speed curves, represents approximately the same power/speed combinations as the boundary c-b in figure 3.22. The same could be written in the case of figure 3.20, except that at the power of 120W, the minimum (w/d) occurs at an unexpectedly low scan speed.

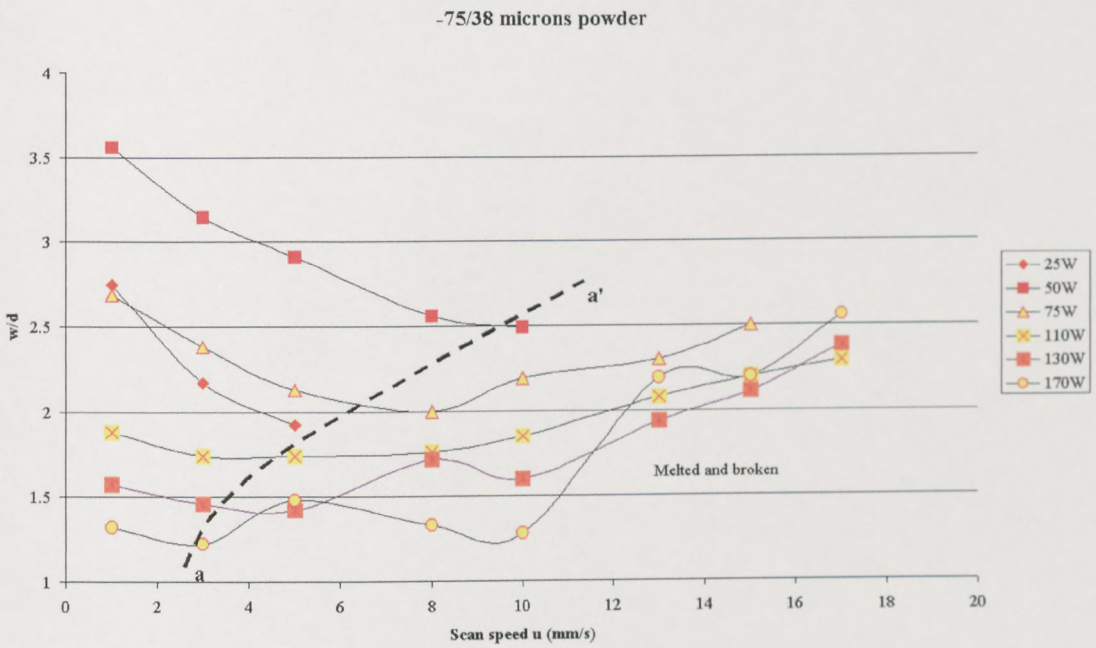

3.28 (b) Track w/d vs. laser energy for –75/38 μm powder

Finally figure 3.29 shows (a) a log-log plot of the mass of a 20mm scan against P/U and (b) (w/d) against scan speed, for the powder mixture 75%, -300/150μm powder with

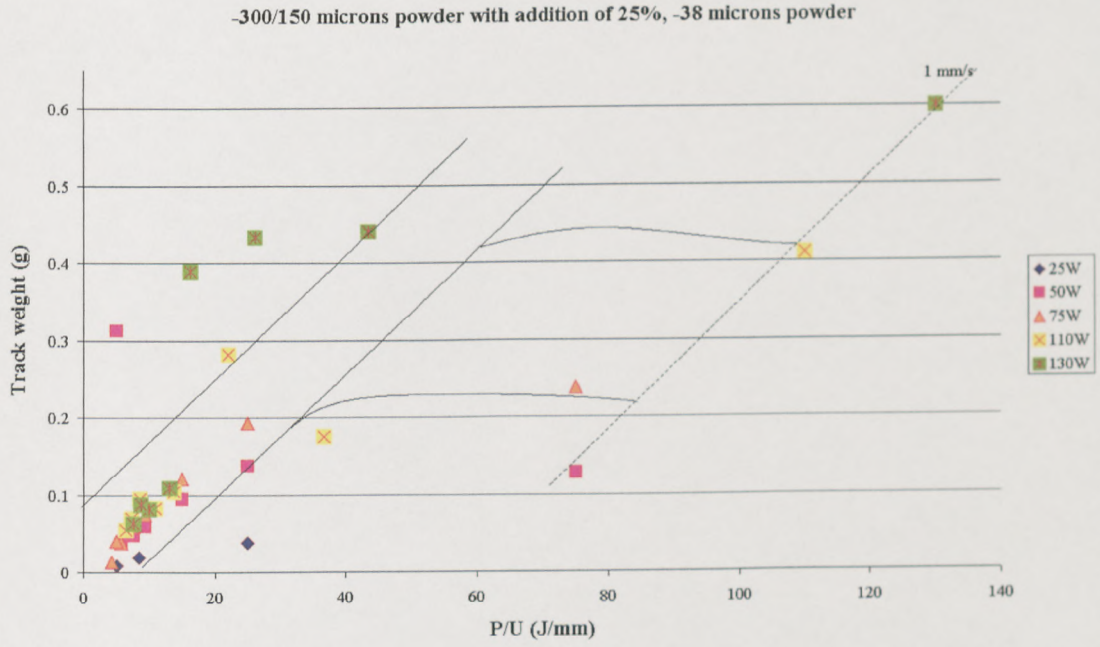

3.29 (a) Track weight vs. laser energy for –300/150 with addition of 25%, -38 μm powder addition of 25%, -30μm powder.

Comparing figure 3.20 (a) with figure 3.26 (a), it is seen that the band of data is at a higher mass per 20 mm length at a given P/U, similar in fact to that in figure 3.26 (b). The (w/d) data shows minima in the range 5 mm/s (25w) to 13mm/s (130W).

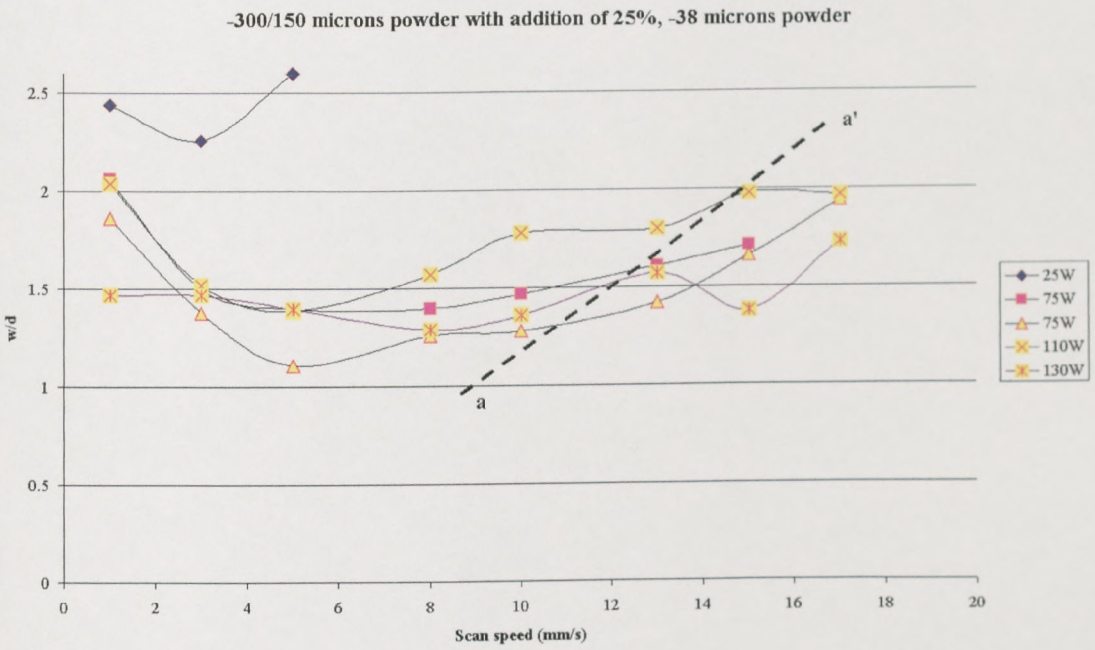

3.29 (b) Track w/d vs. laser energy for –300/150 with addition of 25%, -38 μm powder

3.6 Microscopy studies

The first step in the preparation of the specimens consists of sectioning the single sintered tracks. This operation was carried out using an abrasive disc cooled with water. To remove any cutting debris from the pores thorough rinsing with water had to be carried out.

The specimens were then mounted in Bakelite under pressure and under a high temperature of (140-160C^0). The specimens were then lapped using a series of different grit papers until the majority of the scratches were removed. The final operation was then a polishing treatment which was carried out with 6 and 3 μm diamond polishing paste.

First physical observation regarding the track cross-section shape was a transition area that exists between the transformation of the half-moon shape into full-

moon shape. Referring to figure 3.20, for –300/150 microns powder, the region 20-120W,1 to 5 mm/s is one of the changing track stage. Therefore tracks in this region have been chosen for sectioning. Figure 3.30 shows two sets, one at 75W, the other at 110W, both for scan speeds of 1, 3, 5 mm/s. There are low magnifications, to show track section shape. They are all the same magnification. Figure 3.31 is similar but for mixed powder. These show the changing section shape. In the area of 3mm/s the cross section shape was found to be triangular for all tracks analysed. The triangular shape exists at scan speeds of 3mm/s and on a range of scan speed between 65W up to 120W. Figure 3.30and 3.31 emphasis the transition area that has been found to exist at a scan speed of 3mm/s. Figure 3.30 shows the tracks cross section for –300/150μm powder at different scan speeds and laser powers.

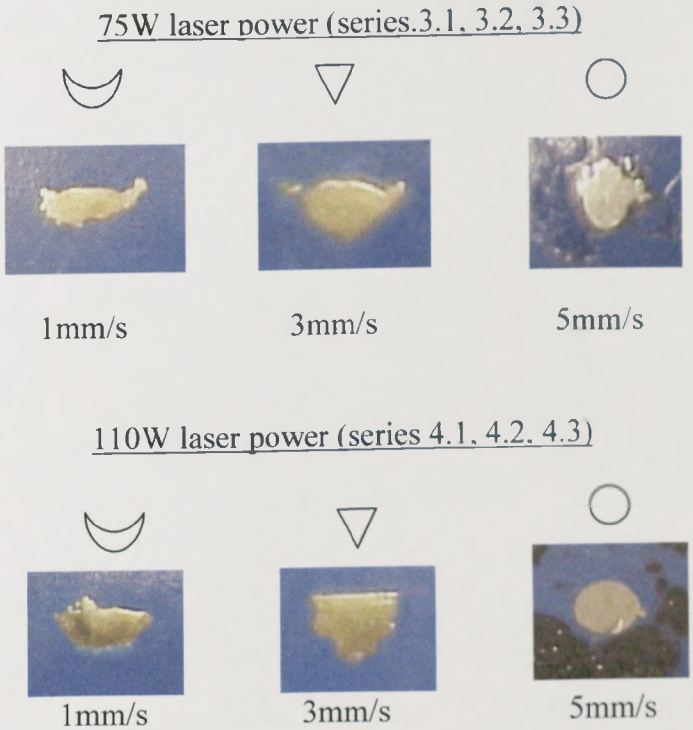

Figure 3.30 Track cross sections of the mixed –300/150μm powder

75 W laser power (series 23.1, 23.2, 22.3)

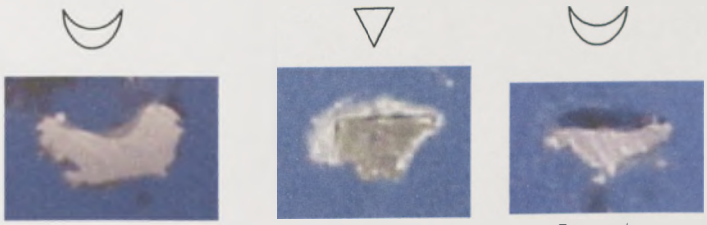

1 mm/s 3 mm/s 5mm/s

Figure 3.31 Track cross sections of the mixed –300/150μm powder with addition of –38μm

It was observed and can be seen in figure 3.30 and 3.31 the cross section shape became deeper by increasing the scan speed. It can be seen above that for a scan speed of 1mm/s both figures indicate a spread of the melting front at the surface of the powder bed. Contrary, for the case where the tracks had a "half-moon" shape but there were situated in the partial sintering area of the sintering maps these were considered not suitable to be used for our goal of building multi-layers because of the poor quality of the particle bonding.

Figure 3.32 (a) and (b) (pages 117 and 118) displays a melted track sintered at 75W laser power and 1mm/s scan speed using one single size fractions -300/150μm powder, and one mixed fraction 75%, -300/150μm with addition of 25%, -38μm powder. It can be easily observed that after the laser source moved on the resolidification process started from the coarse area upwards. Moreover, it was noticed a large dendritic area at the bottom of the sintered track, suggesting that the laser power was not high enough to penetrate and melt the entire track.

At the beginning, the gas atomise 314 HC powder consists of spherical particles characterised by the occurrence of a dendritic microstructure with the increase of the laser power (low power). As the sintering process started the particles are melted and the powder microstructure will become coarse grained.

The solid phase is still present at this early stage. However, the speed factor (heating/cooling) is so rapid that it is not enough time for induce atom migration and the powder particles are still singular.

A further increase of the laser power will induce an increase of the particle temperatures and liquid phase begin to occur. The presence of the liquid action starts to cause regions of liquid among the dendrites. Furthermore, an increase of the laser power will cause a growth of the liquid regions and more liquid become available. At this stage, the dendritic skeleton starts to coarsen and becomes spherical because the coarsening rate increases.

Finally, the dendritic skeleton starts to break and with a further increase of the laser power the temperature gets high enough above the liquidus. The result will be a fully liquid phase.

On the other hand, a different morphological behaviour has been noticed within the melted track if the laser power was not very high. If only partial re-melting is achieved before the laser source passes, the solid phase starts to re-grow from the solid nucleus that are present within the melted track. These solid nuclei represent ideal points for resolidification. Furthermore, if the tracks are fully melted then there are no nuclei to start the re-solidification process within the melt and so solidification must start from the nearest solid particles within the powder bed.

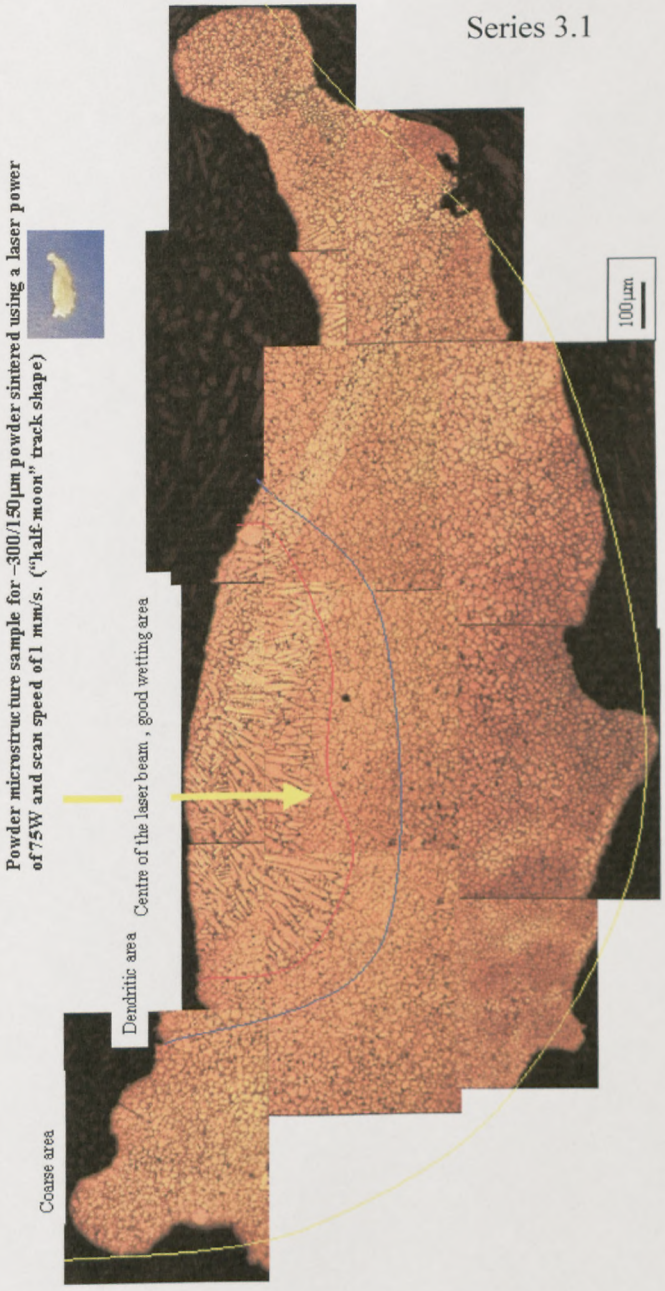

Figure 3.32 (a) Track cross-section, microscopic view for –300/150 microns powder

It was noticed that at a low scan speed (1mm/s) the track was not fully melted (figures 3.32 a and b). Wetting phenomenon was recorded only in the hottest area, middle of the laser beam, and as the laser moved on the molten metal started to re-solidify creating

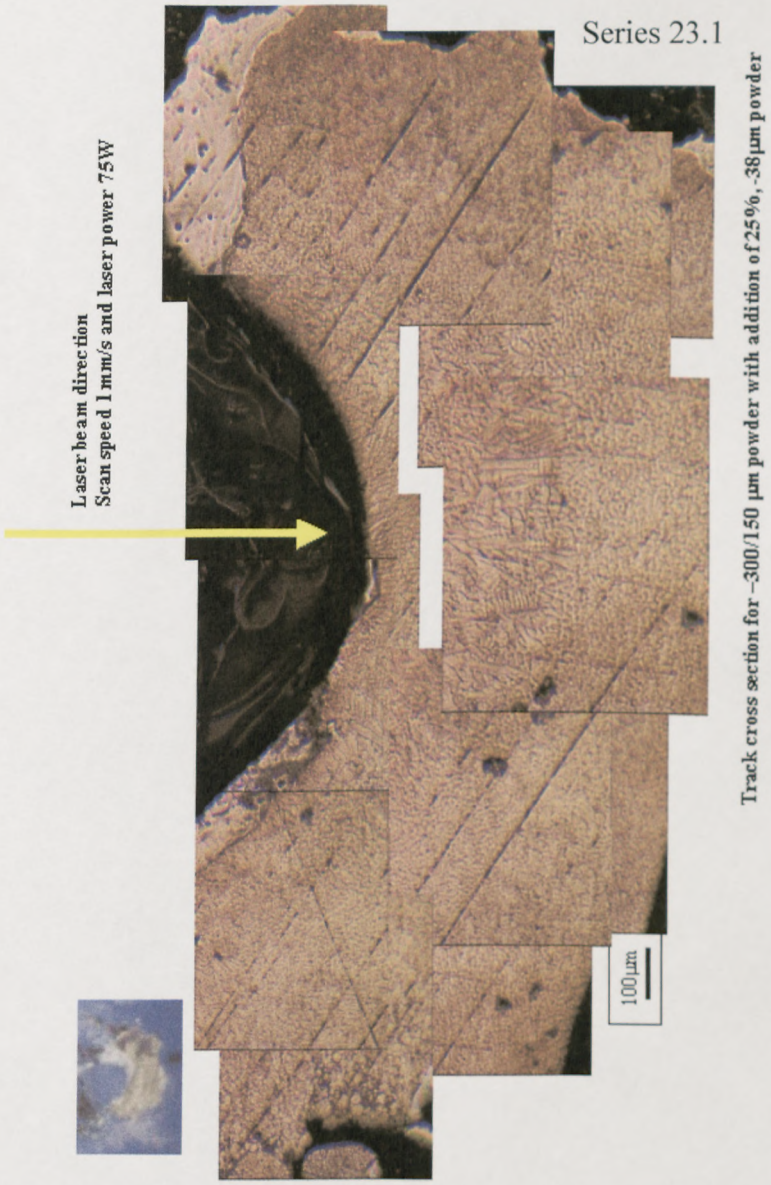

Figure 3.32 (b) Track cross-section microscopic view for –300/150µm powder with addition of 25%, -38µm powder, (1mm/s scan speed)

columnar shapes. These columnar shapes can be seen at the top of the melted track. Bottom of the track was not fully melted even if the powders particles were bonded together. A big trench was also noticed in the middle of the melted track. In addition, the un-mixed –300/150µm powder has a very similar metalographic structure (figure 3.32 a).

The only noticeable difference was the trench in the middle of the track. This trench was not observed for the un-mixed powder.

Furthermore, increasing the scan speed (3mm/s) for the same 75W laser power the track cross-section started to change and became triangular shape. At the same time the

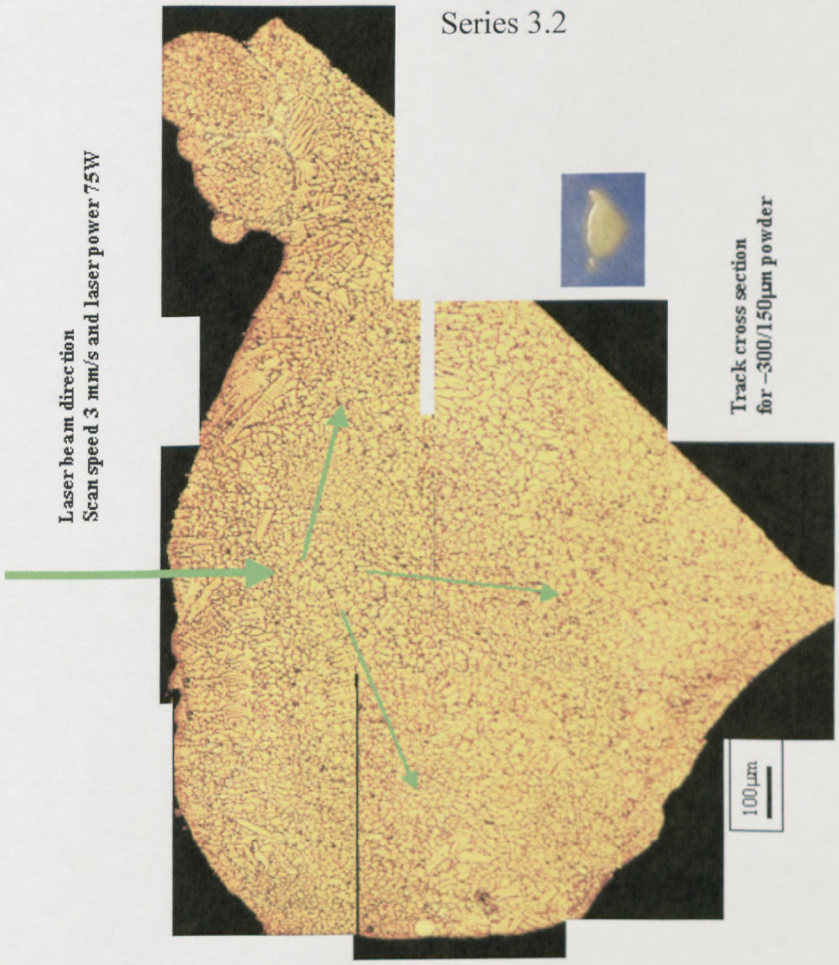

Figure 3.33 (a) Track cross-section microscopic view for –300/150µm powder batch (3mm/s scan speed)

metalographic structure of the track started to change. The wetting phenomenon was found within the entire melted track and the columnar shapes were observed in different parts of the picture not only at the top of the track (figure 3.33 a and b). At this early stage it is thought that the metal liquid was pushed by the gravitational force downwards and at the same time stirred by the melt pool internal forces.

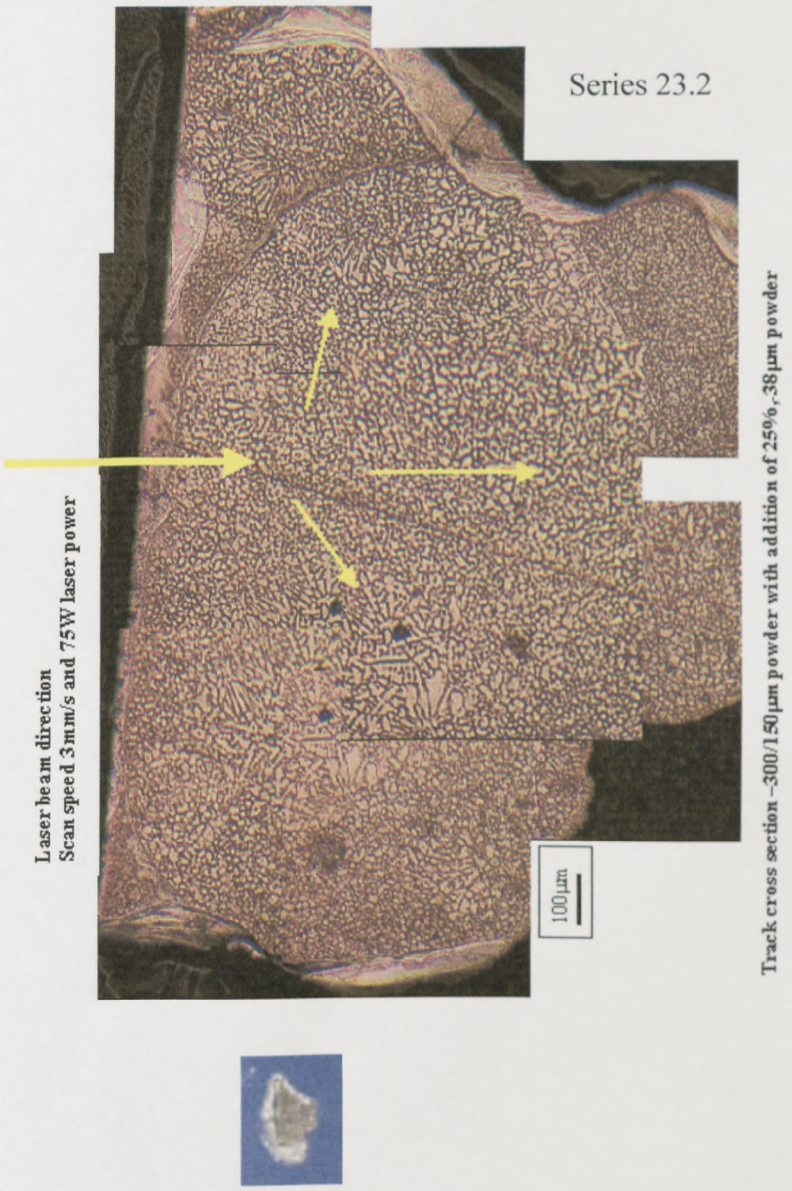

Figure 3.33 (b) Track cross-section microscopic view for –300/150µm with addition of 25%, -38 µm powder (3mm/s scan speed)

A further increase of the scan speed (5mm/s) for the same laser power (75W) had resulted in full melting behaviour for the mixed –300/150 µm powder with addition of 25%, -38µm powder and in a coarsing structure for single size –300/150µm powder. It can be seen in picture 3.34 (a) the columnar grains were visible through out all the cross section of the melted track. Compared to this, figure 3.34 (b) shows a grain structure with only very small areas of columnar shapes.

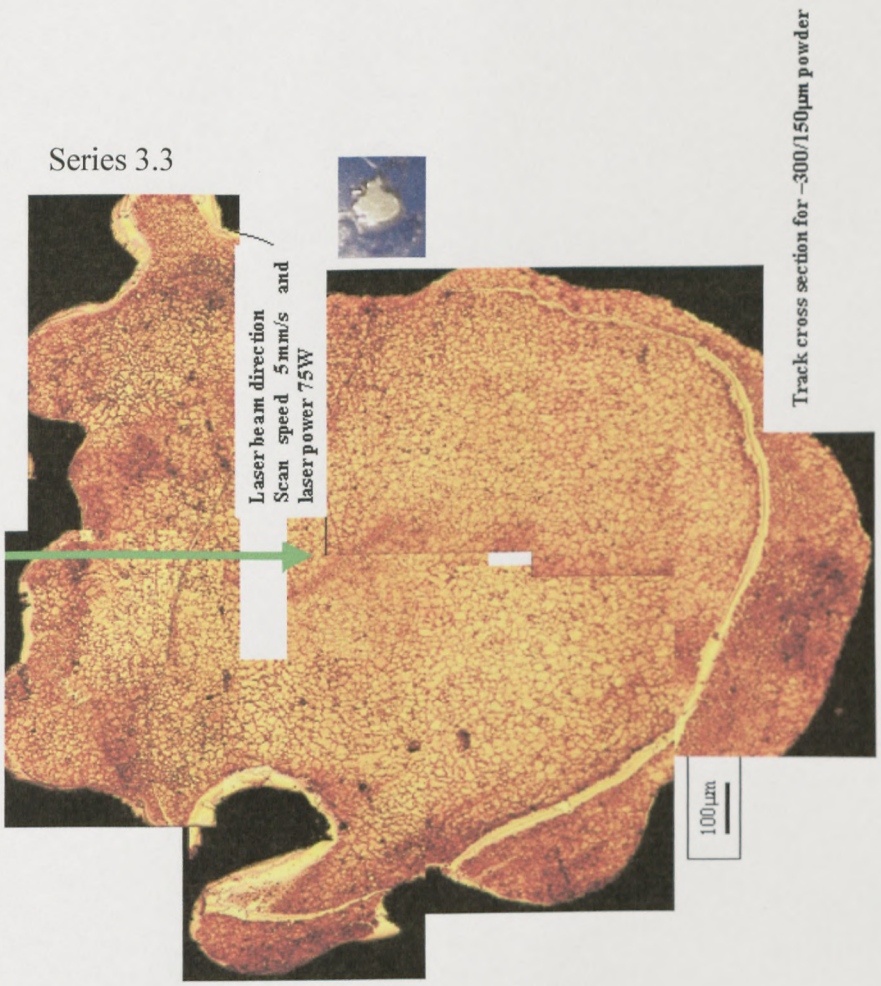

Figure 3.34 (a) Track cross-section microscopic view for –300/150μm (5mm/s scan speed)

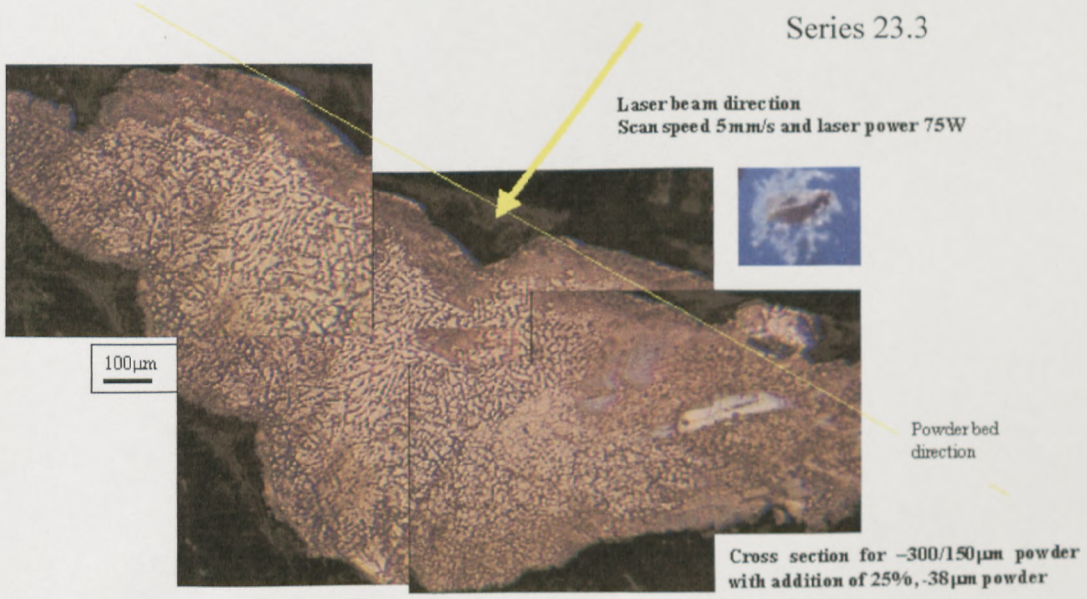

Figure 3.34 (a) Track cross-section microscopic view for –300/150μm with addition of 25%, -38μm powder (5mm/s scan speed)

Figure 3.34 (a) shows a deep line across the section. For a better clarification of this line formation an energy dispersive X-ray (EDX) analysis was performed to detect the components of the sample and their approximate percentage compositions. The EDX results and corresponding quantitative analysis are shown in Figure 3.36. In addition, the sample was observed through a Scanning Electron Microscope (SEM) to help understand the resolidification process and the appearance of the line.

Figure 3.35 shows the SEM view of the track cross-section from figure 3.34 (a).

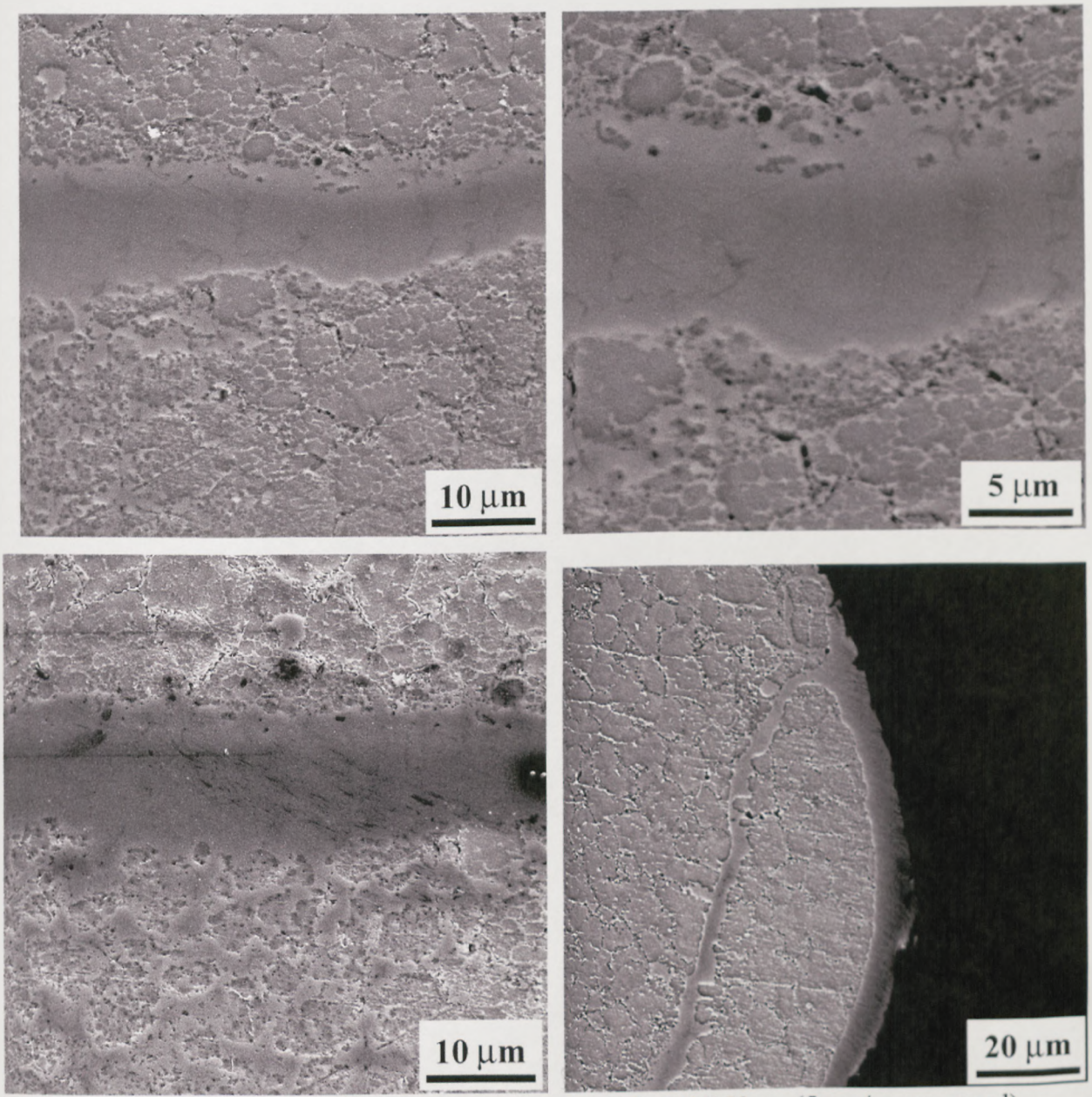

Figure 3.35 SEM images of the track cross-section of –300/150μm (5mm/s scan speed)

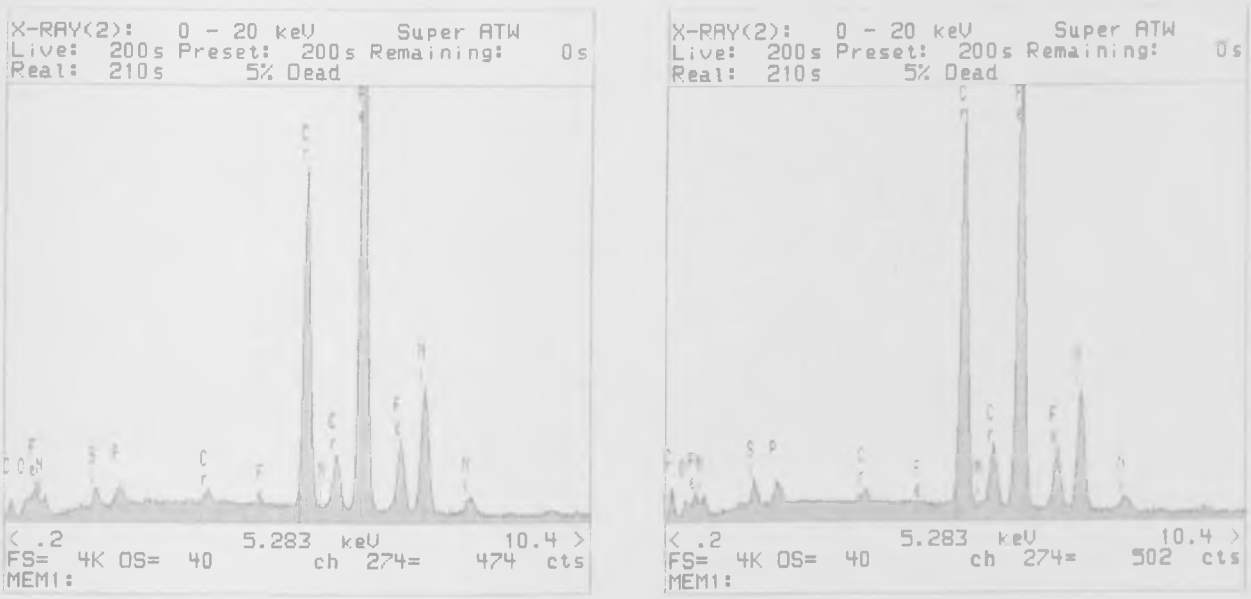

Figure 3.36 Energy dispersive X-ray (EDX) spectrum of analysed sample

(See figure 3.34(a))

The results proved that the samples quality has been altered during preparation process. An early conclusion that can be drawn is that the laser scan speed affects the track cross-section, melt pool structure and behaviour in a strong manner. A different behaviour was observed for the two batches of powder presented as an example. An improvement on powder sinterability was noticed for the mixed powders compared to un-mixed powders.

3.5 Summary

This chapter investigated the powder properties as well as the powder sinterability. At the beginning, the powder density was measured for all four batches of powder. Furthermore, the powders were mixed together in different percentage and the result showed an improvement in the powder density by introducing a small particle size powder into a big particle size powder. The second sets of test were carried out for measuring powder flow rates. The results showed a drop in powder flow rate after 15 minutes of mixing time. The flow rate of a small particle size powder had a big influence over the powder spreading. The third sets of measurements were carried out for measuring

the powder thermal conductivity. The results suggested that the thermal conductivity increases by increasing the powder particle size.

In the final part of this chapter sintering tests were carried out with all four un-mixed batches of powder and with two mixed batches of powder. The results showed an improvement in powder sinterability for the mixed powders. The microscopy studies showed full melting behaviour in the mixed powders for scan speeds over 3mm/s but below 8mm/s. The results also suggested that an increase in the scan speed induces a better heat absorption into the powder bed and a decrease of the heat spread through the powder bed. This suggestion is based on the results obtained during the trial tests and presented in figurers 3.30 and 3.31. it can be observed a deeper penetration of the powder bed for scan speeds between 1 and 5 mm/s.

CHAPTER 4
LAYER AND MULTIPLE LAYER SINTERING OF 314HC POWDER

4.1 Introduction

This chapter extends the laser sintering observations from single tracks to single layers and then to multiple layers. At each stage, new issues become important. For example, single layer's new issues, compared to single tracks, are layer flatness as well as the scan spacing between the consecutive tracks. So, in section 4.2 background testing relating to scanning strategies is first described.

The structure of chapter four sets out first the scanning strategies adopted during layer and multiple layer sintering. This chapter also sets out the results obtained from the sintering tests in an argon atmosphere, using four batches of powder. This is followed by a layer and multiple layer microscopy investigation. Because the layer depth plays an important role during multiple layer sintering, sintering maps were also created focused on layer depth.

In chapter 3, observations were made of powers and scan speeds that resulted in full melting without breakage. The sintering tests with –75/38μm and -38μm powders showed small regions of full melting without breakage. For this reason, these powders were not chosen for the layer and multiple layer sintering tests. As an example, figure 4.1 shows single layer melt tests, using the -38μm powder. The area of each layer was 30mm x 30mm and created at laser powers of 75W to 130W and at a scan spacing of 0.5mm. Although, teach layer was well fused, they were not in fact flat. This phenomena is considered in the next section.

Scan speed 5 mm/s

75W laser power 100W laser power 130W laser power

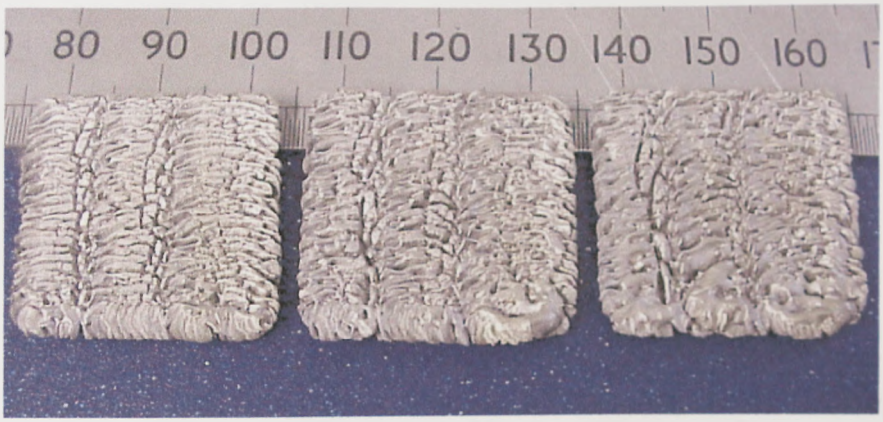

Figure 4.1 Sintered layer scanned using -38μm powder

Besides, the area of half-moon track shape was found to be very limited for –75/38μm and -38μm powders compared to other batches of powder.

4.2 Scanning strategies

Figure 4.2 shows and compares the sintered layers created using a -38μm powder and a -300/150μm powder with addition of 25%, -30μm powder, sintered at the same conditions. These two layers are presented for comparisons only. Both were sintered using 75W of laser power and 3 mm/s scan speed. It can be easily observed that the layer flatness of the -38μm powder is much worse than that of the other.

This warped surface affects the quality of the spread powder when creating the next sintered layer. The non-flatness shown here makes it impossible for the V-hopper to spread the next layer of powder without moving the current layer.

-38μm powder

75W , 3mm/s

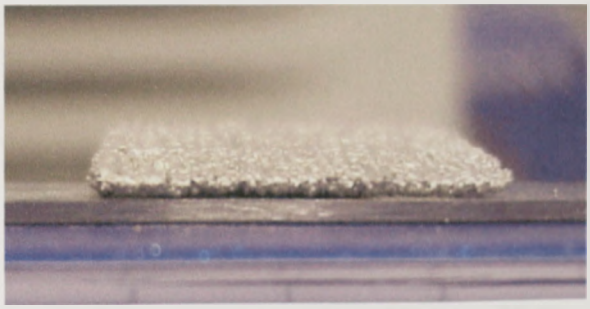

-300/150μm powder with addition of 25%, -30μm powder

75W, 3mm/s

Figure 4.2 Sintered layers scanned using -38μm powder and a mixed powder – side views

Two methods were considered to avoid warping. Published work suggests warping is reduced by heating up the powder bed to at least half its melting temperature. In the present case, half of the melting temperature is about 600^0C - 700^0C. Overall heating to this level is not practical. The second method relates to the dependence of the warping on the scanned length of each track. It is known that a shorter track length reduces layer warping. This second solution has been adopted here. Figure 4.3 shows the strategy. Large areas have been built by fusing together smaller layers (figure 4.13 and 4.14). Preliminary tests show that a scan length of 10mm or less always prevents warping of layers, when using larger powder sizes of –300/150μm or –150/75μm powder and when using mixtures containing 25% of -38μm powder.

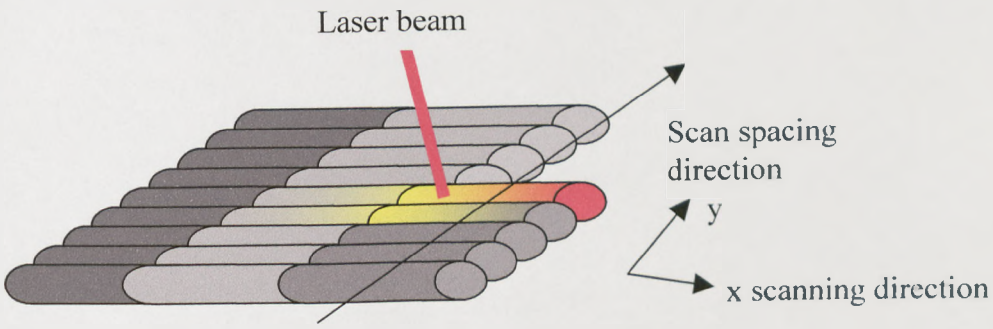

Figure 4.3 Schematic view of a long layer obtained by sintering together small layers

The scan spacing between tracks was also investigated in prelimary tests. Layers were sintered using 0.25mm, 0.5mm and 0.75 mm scan spacing (see fig 4.4).

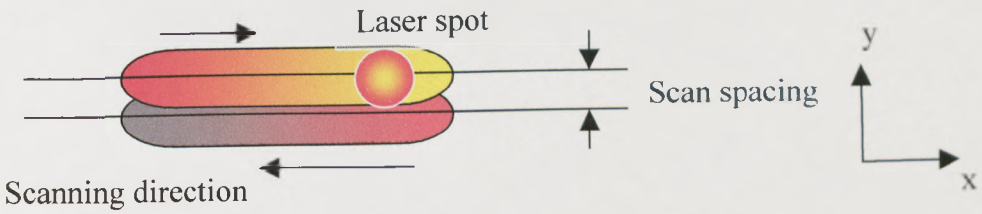

Figure 4.4 Schematic top view of two consecutive tracks

During the initial layer trials, a further issue was notticed, which was defined as first line defect (FLD). FLD is characterized by a first track which is much larger than

subsequent tracks within the same layer. Figure 4.5 shows the FLD at the beginning of the layer, where track diameter H_2 is much larger than track diameter, H_1. It is thought that the FLD phenomenon is caused byabsorbitivity losses as more tracks are produced. Imediately after the first track has been sintered and the second track is melted the first track within that layer acts as an "arrester" for the heat because its heat conductivity is much higher then the loose powder (15.3 W/mK compared to 0.31±0,3 W/mk). In consequence, the first track absorbs more heat than the next tracks.

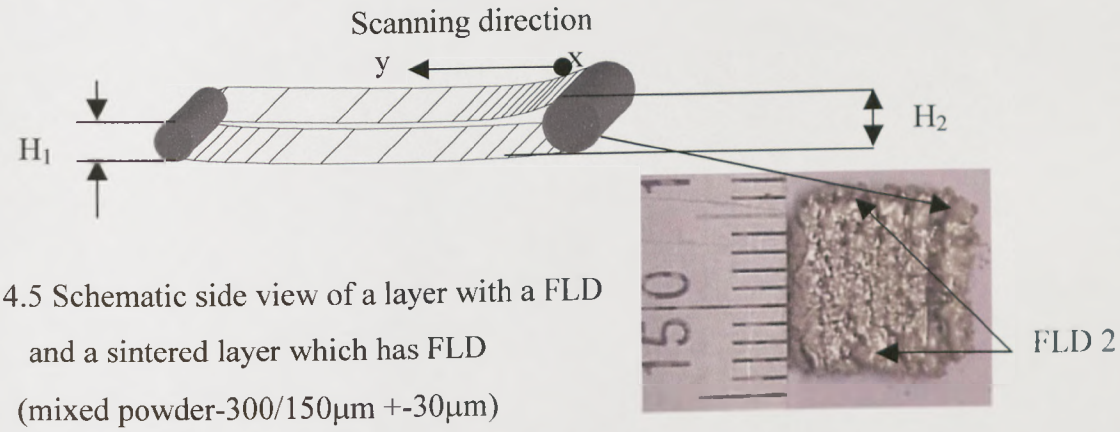

Figure 4.5 Schematic side view of a layer with a FLD and a sintered layer which has FLD (mixed powder-300/150μm +-30μm) Layer scanned at 130W laser power and 3mm/s scan speed

During the first track scan it was observed that the melted pool tends to form the same cross section track shape as those presented in chapter 3 of this thesis for all six batches of powder analysed. As rastering continues subsequent sintered tracks within the layer tend to have a cross section similar to tracks produced at lower energy densities than the actual scanning parameters. Moreover, a second type of defect was recorded, FLD2, at the beginning of each sintered track (picture 4.5 – FLD 2). One possible reason for this second FLD formation is the delay of the mirror before reaching full speed. This delay allows longer exposure of the powder bed in the respective area.

4.3 Single layer scanning

This section follows the same development as section 3.5 on single track observations. First, qualitative observations and mapping are described (4.3.1). Then more quantitative aspects, in this case relating to layer density, layer flatness and extension to large area scanning are reported (4.3.2). Finally, the results of optical microscopy of track sections are reported (4.3.3). The single track observations indicate that the power ranges from 50W to 110W and scan speed ranges from 1 mm/s to 8 mm/s create fully melted track regions without breakage for all these powders (though the low power/high speed combination for –300/150μm powder ranges on the partially melted region). These powers and scan speed combinations are therefore concentrated here.

The qualitative classifications of the sintered parts are listed as follow:

Full-melting with a *poor layer surface quality* (figure 4.6 a)– a focussed, moving back and forwards Gaussian beam pounding on the surface of the powder layer causes a full melting over a delimited powder surface. The outcome is a sintered layer with a surface which is characterised by a violent behaviour of the layer internal forces during the sintering process. A pronounced FLD was also observed for each sintered layer in this category. A high porosity was also observed within the layer in this category.

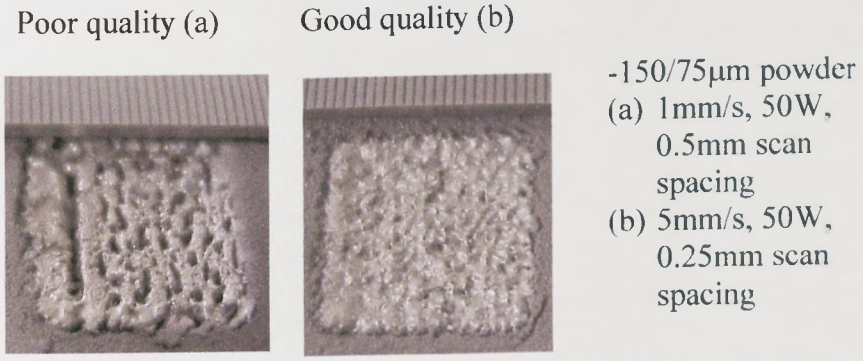

Figure 4.6 Quality characterisation of the sintered layers

Full-melting with a *good layer surface quality* (figure 4.6 b)– a focussed, moving backing and forwards Gaussian beam pounding on the surface of the powder layer causes a full melting over a delimited powder surface. The outcome is a sintered layer which has a top surface characterised by a limited behaviour of internal forces during the sintering process.

FLD phenomenon was limited. A low porosity was also observed within the layer in this category.

4.3.1 Layer qualitative and semi-qualitative observations

Figures 4.7 to 4.10 show the surface appearance of 10mm x 10 mm single layer squares, scanned with both 0.25 and 0.5 mm scan spacing. As already reported, larger spacing gives a lower surface finish. A number of different qualitative behaviours can be seen. The main difference between one and the other concerns surface roughness. In some cases (for example figure 4.7 (a), 75W, 1mm/s), the layer surface solidified relatively smooth and glazed. But in others (figure 4.7 (a), 75W, 3mm/s), the layer surface had solidified rough.

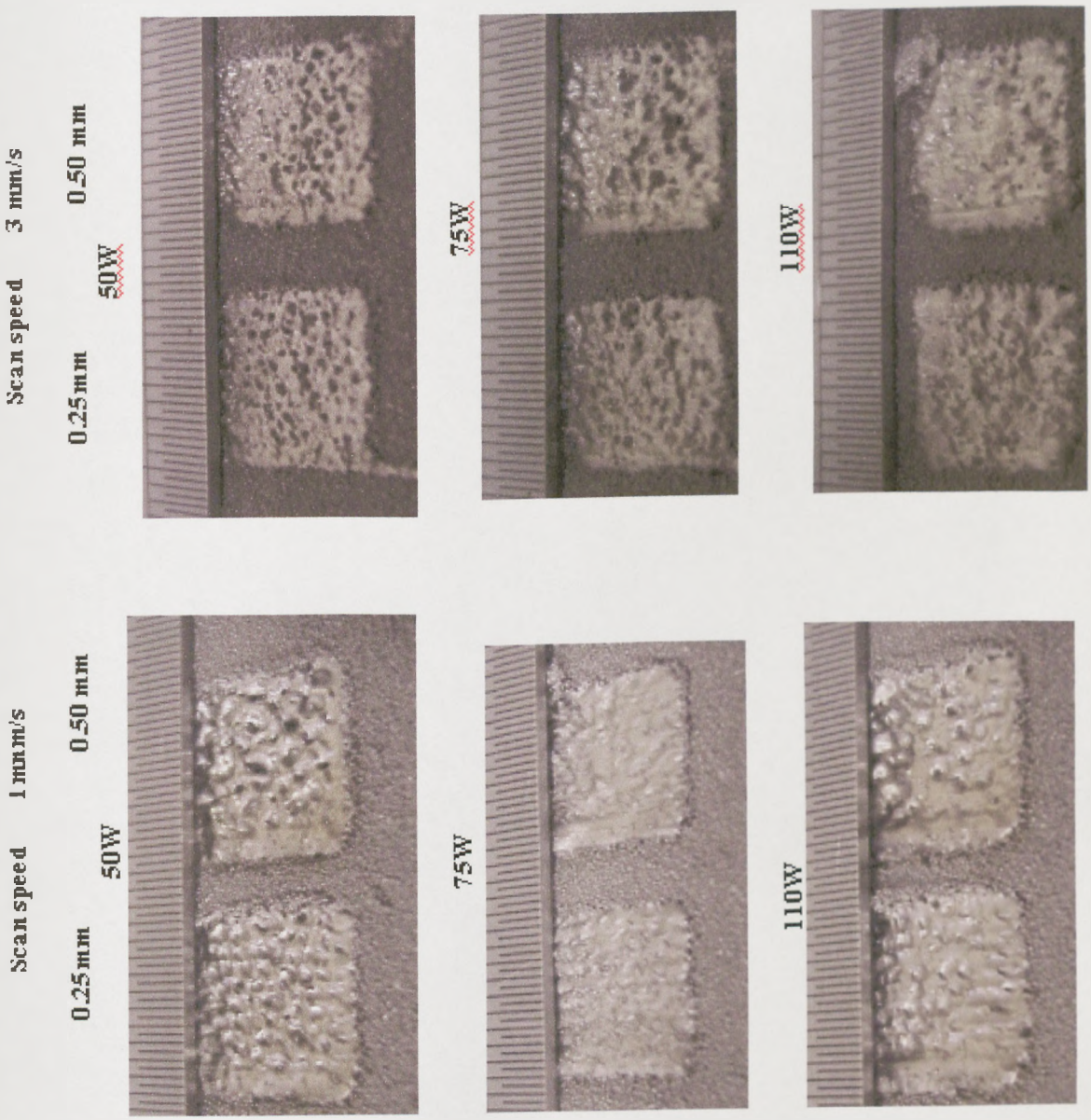

Figure 4.7 (a) Sintered layers scanned using –300/150μm powder batch

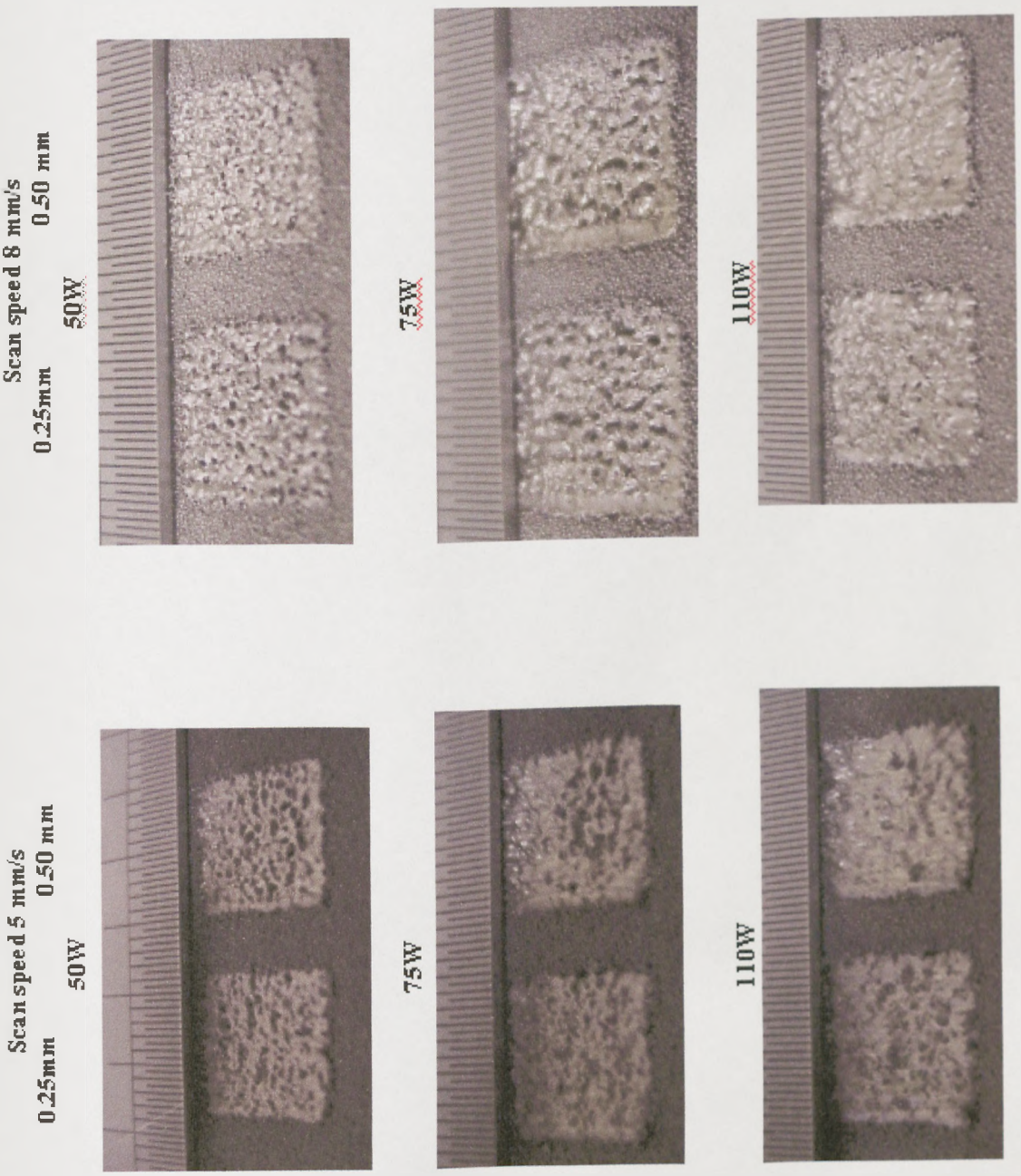

Figure 4.7 (b) Sintered layers scanned using –300/150μm powder batch

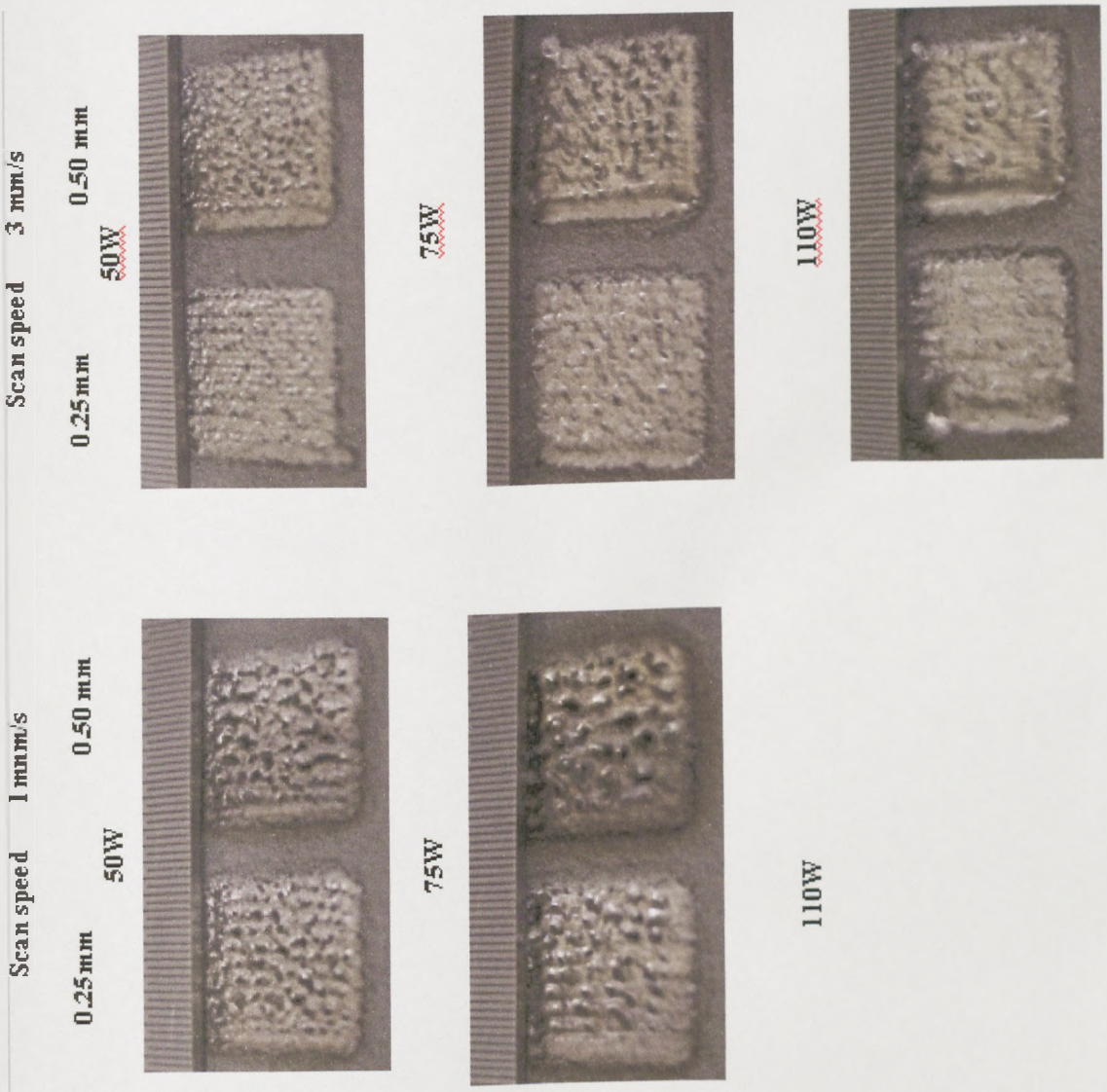

Figure 4.8 (a) Sintered layers scanned using –150/75μm powder batch

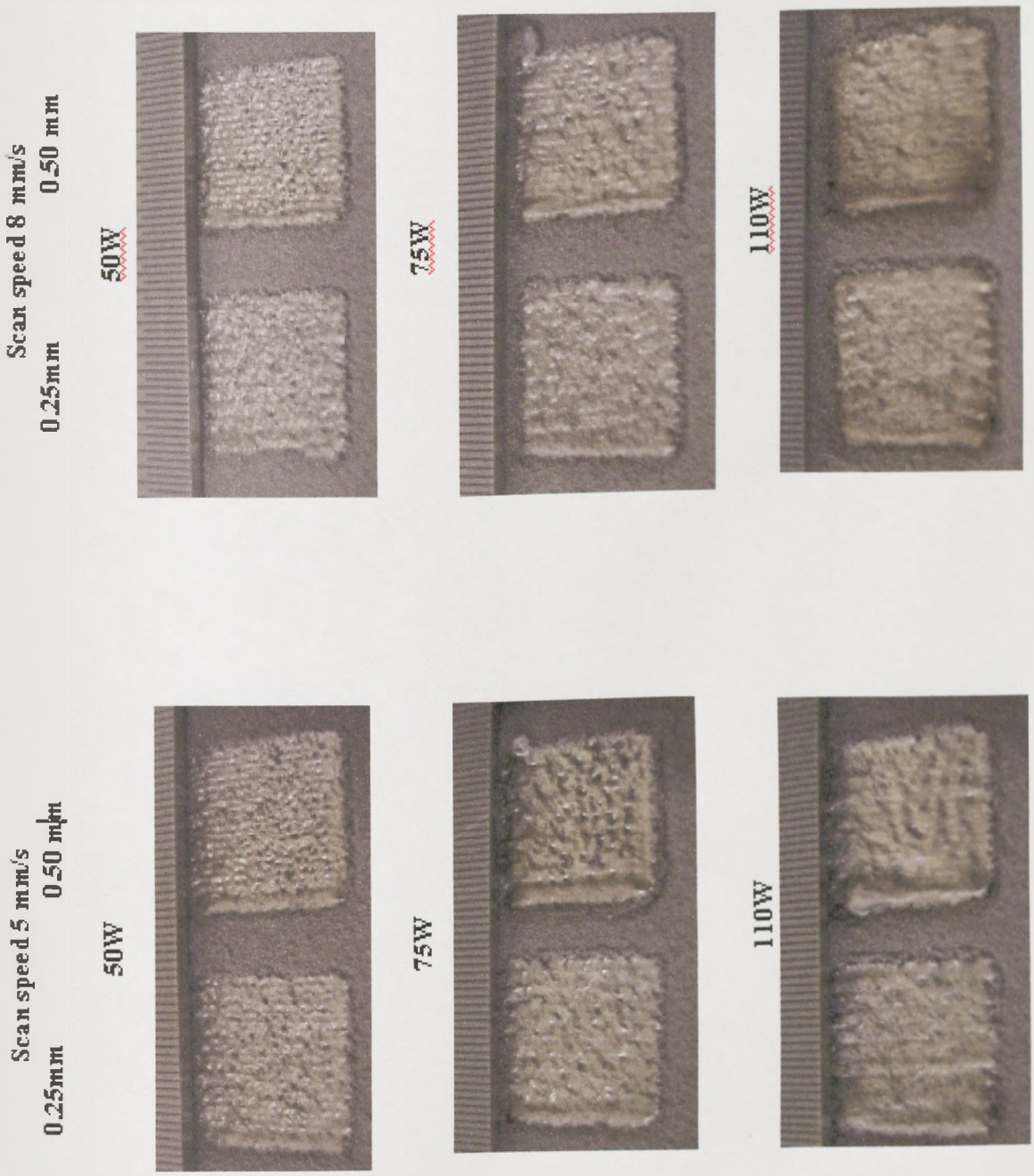

Figure 4.8 (b) Sintered layers scanned using –150/75μm powder batch

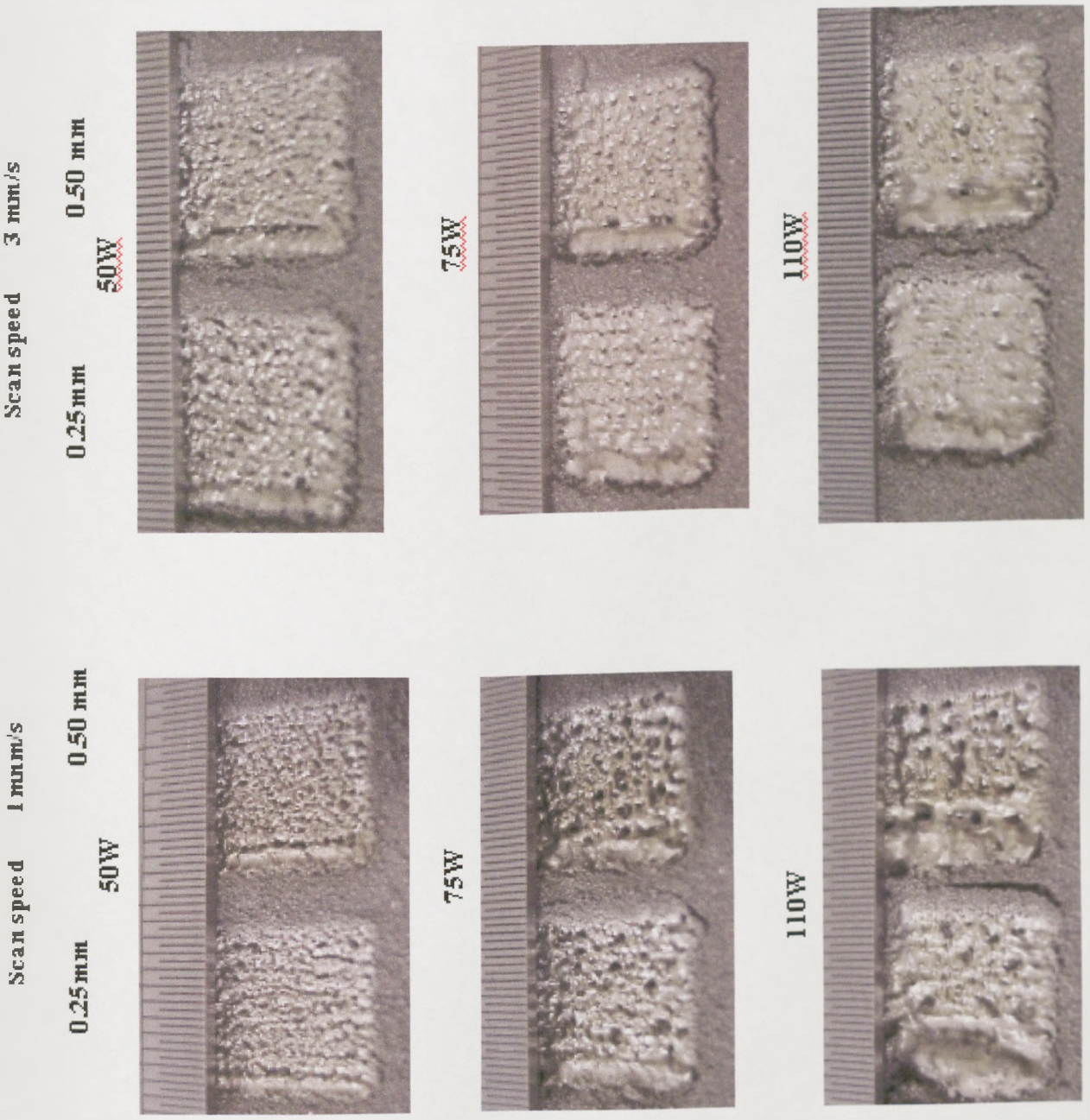

Figure 4.9 (a) Sintered layers scanned using 75%, –300/150μm with addition of 25%, -38μm powder

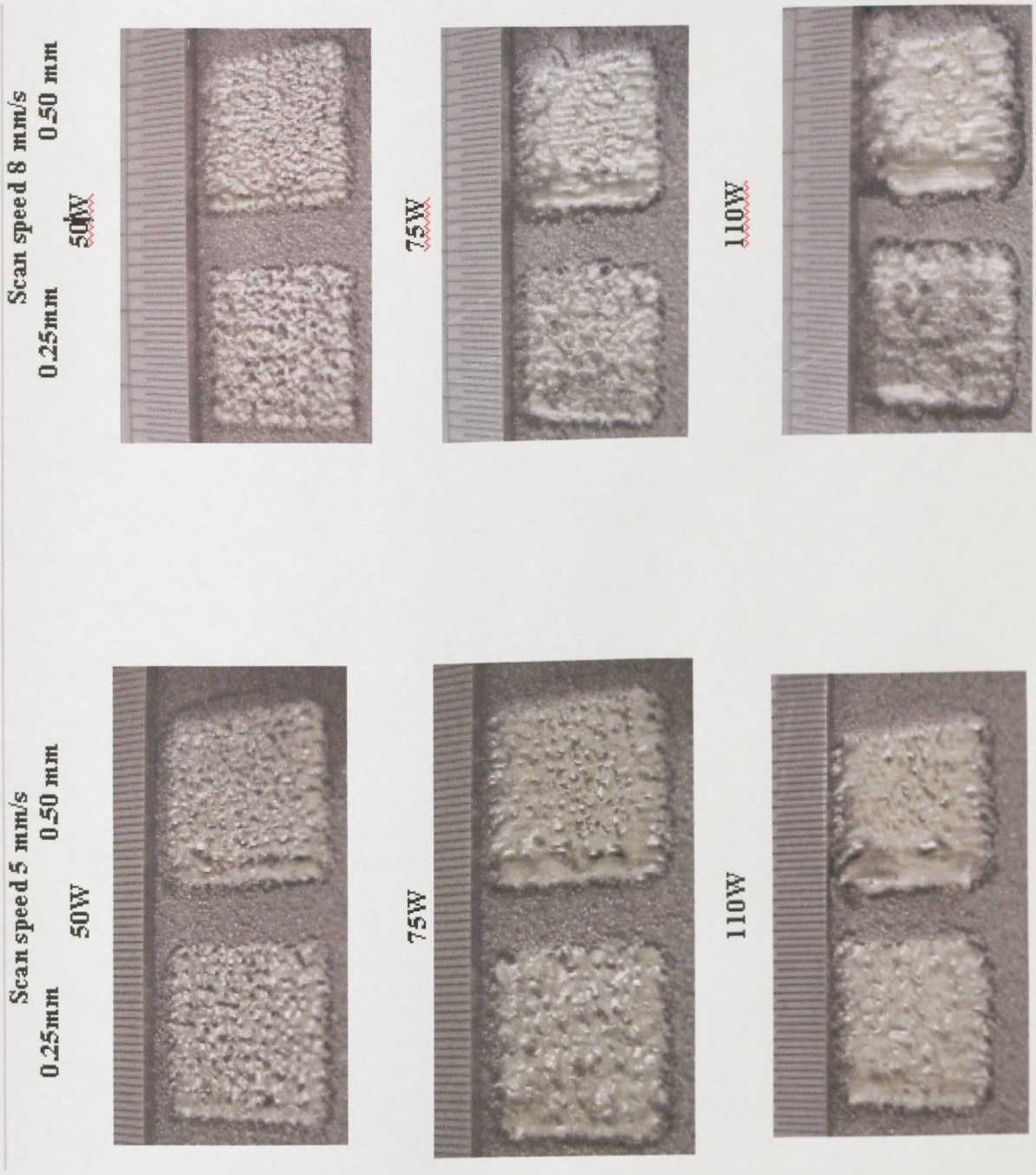

Figure 4.9 (b) Sintered layers scanned using 75%, –300/150μm with addition of 25%, -38μm powder

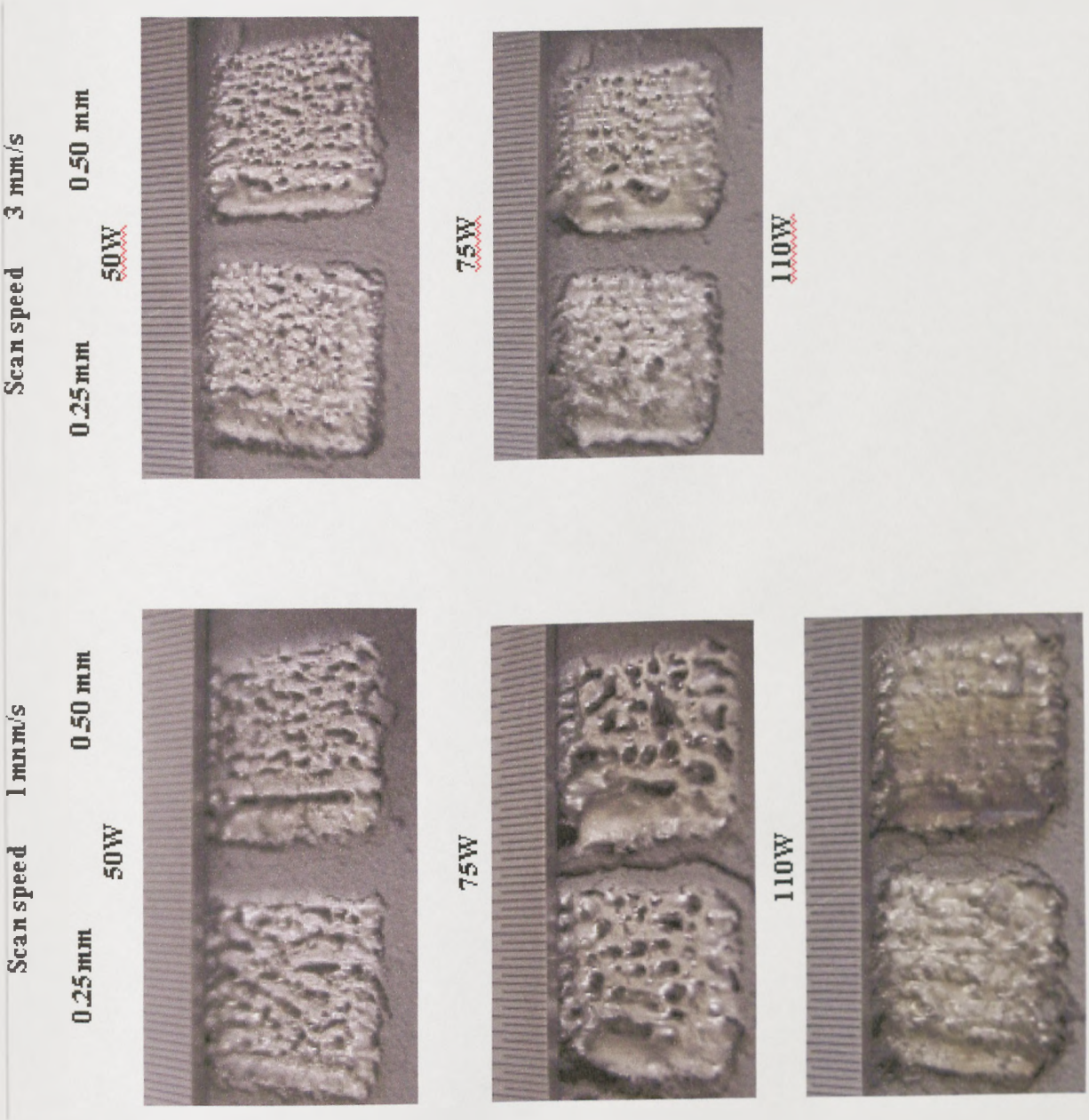

Figure 4.10 (a) Sintered layers scanned using 75%, –150/75μm with addition of 25%, -38μm powder

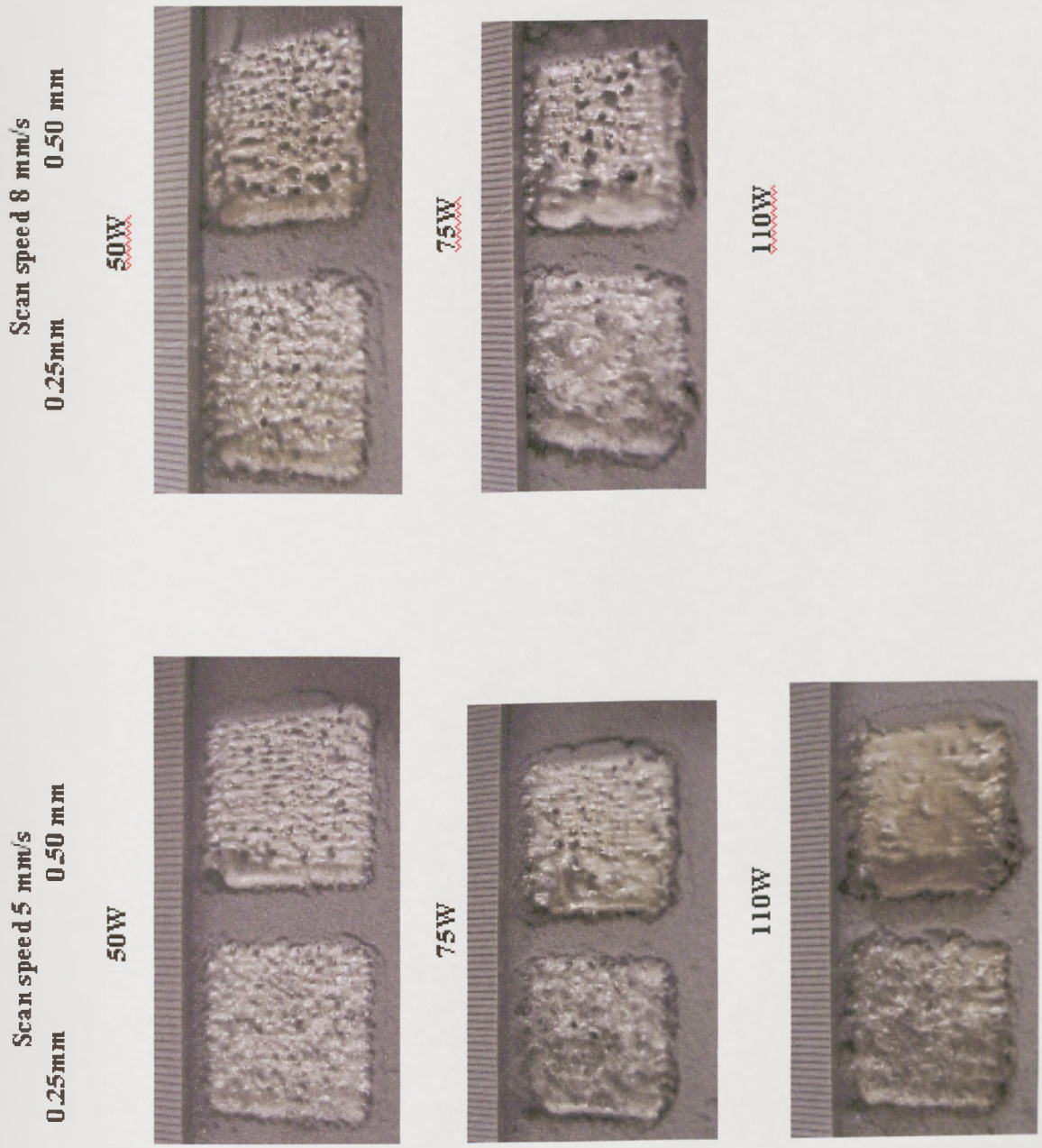

Figure 4.10 (b) Sintered layers scanned using 75%, –150/75μm with addition of 25%, -38μm powder

The occurrence of rough and smooth surfaces has been plotted on power/scan speed maps, in figures 4.11 to 4.14. Figure 4.11 shows the layer process map obtained by joining the information obtained from single track tests for –150/75μm powder with the results from single layer tests for –150/75μm powder. The dashed heavy lines (d-e and e-j) visible on the map defines the area where the single layer tests were carried out.

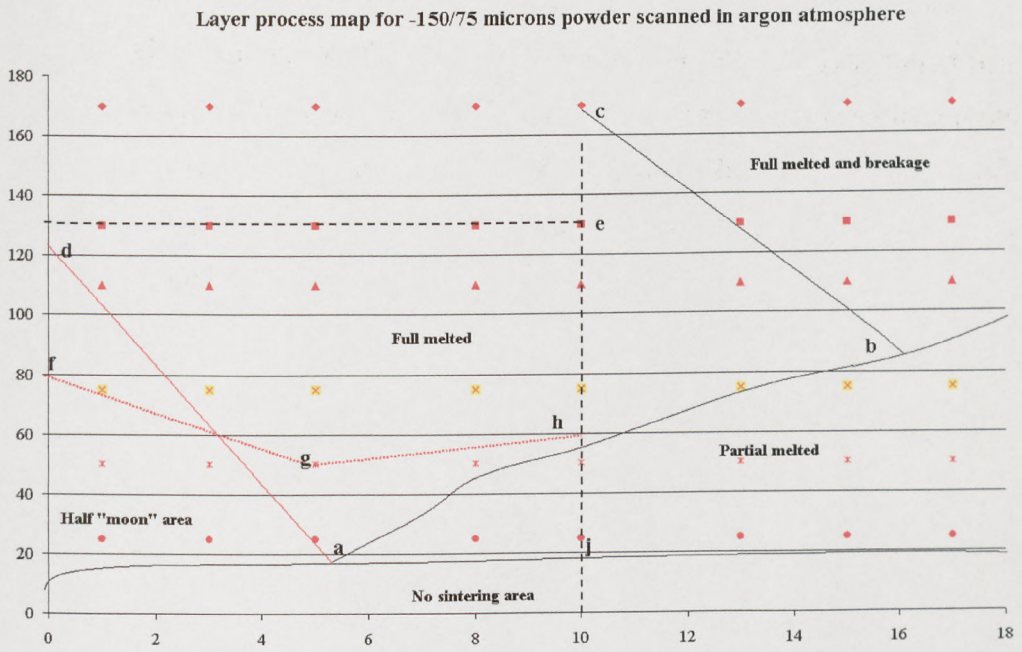

Figure 4.11 Layer process map for –150/75μm powder, 0.5mm scan spacing

Experimental tests were carried out for scan speeds higher than 15 mm/s and 17 mm/s, but the sintered layers of –150/75μm powder could not be handheld. For a scan speed of 13 mm/s and different laser powers the layer sample showed very high internal forces behaviour as well as warping phenomenon and were considered not suitable for multiple layer sintering.

The line (f-g-h) is the boundary between regions that produce rough (figure 4.6 a) and smooth (figure 4.6 b) surfaces. The smooth surfaces occurred above line (f-g-h). At very low scan speeds (<2mm/s) was recorded that a laser power over 75W is necessary for obtaining a good quality of the sintered layer for –150/75μm powder (f-g). A further increase of the scan speed drops the boundary down to 50W laser power(g-h). In general it can be seen in figure 4.11 all good quality layers were obtained above the "half-moon" boundary for single tracks. Also, it was observed that the tracks within the sintered layer

obtained for –150/75μm powder had a "half-moon" shape for values of the scan speed and laser power close to the "half-moon" area boundary. Except for the first track within the sintered layer all other tracks were recorded to have a "half-moon" shape. An explanation of this could be the loss of heat during the sintering process and implicit the dropping of the density energy.

Further increases in laser power and variations in scan speed did not show any big improvements in sintered layer quality. It was observed that scan spacing had a big influence over the sintered layer. A scan spacing higher than 0.5mm showed a dropping in layer quality. At a scan spacing of 0.25mm the sintered tracks within the layer were found to be very distinctive. The shape of the tracks within the sintered layer for a scan spacing of 0.25mm were similar to those presented in chapter 3 of this thesis for –150/75μm powder. Moreover, FLD phenomenon was observed to be more acute for scan spacing below 0.75mm/s.

Figure 4.12 shows the layer process map obtained by joining the information obtained from single track tests for –300/150μm powder with the results from single layer tests for –300/150μm powder. The dash lines visible on the map define the area where the single layer tests were carried out (d-e and h-j)

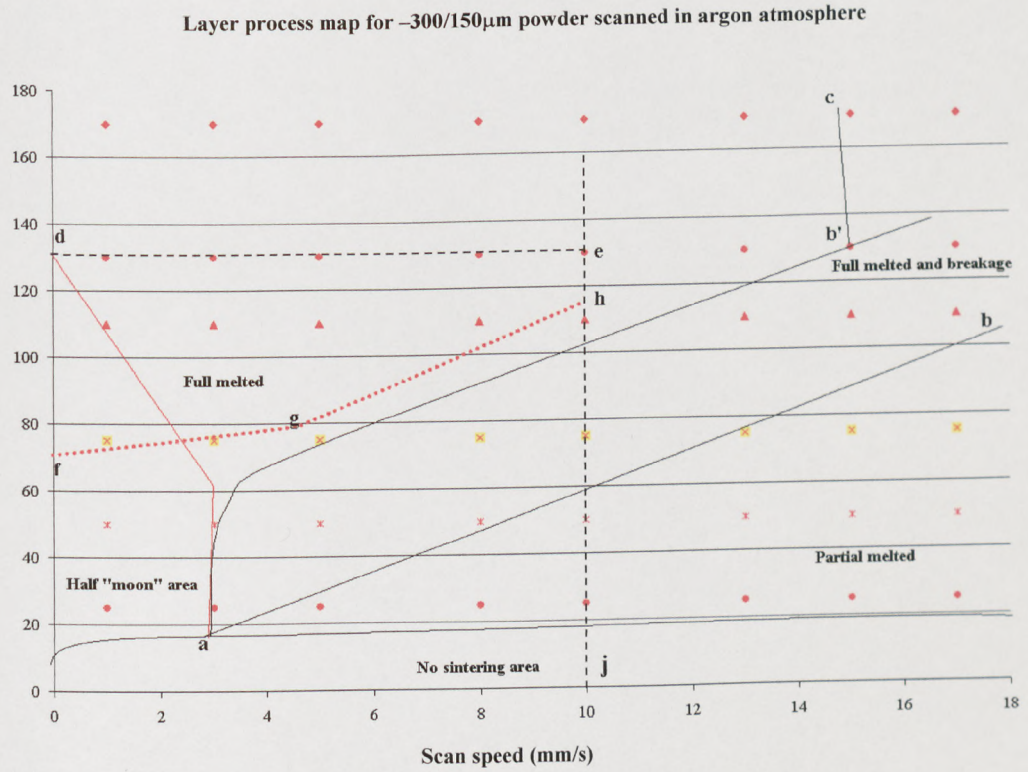

Figure 4.12 Layer process map for –300/150μm powder, 0.5 mm scan spacing

It was recorded for the –300/150μm batch powder that at very low scan speeds (<4mm/s) and laser powers over 75W was necessary for obtaining a good quality of the sintered layer(f-g). A further increase in scan speed caused the boundary of good quality layers to rise above 120W laser power for a scan speed of 10mm/s (g-h). In general, the good quality layer boundary followed the boundary between *full-melting* area and *full-melting and breakage area* for single tracks.

Also, the scan spacing had a high influence over the sintered layer for the –300/150μm powder batch. A decrease of the scan spacing below 0.75mm improved the layer quality.

Large area tests

The scanning tests were extended to sinter larger areas of the powder bed. For this research conditions were based on the information given in figure 4.11 which were gained from the –150/75μm powder layer processing map, using scan speeds of 3-5 mm/s and laser powers of 75-110W. Figure 4.13 shows the result obtained for irradiating –150/75 μm powder in argon atmosphere for different scan speeds. The laser power was (75W) and for a constant 0.5mm scan spacing.

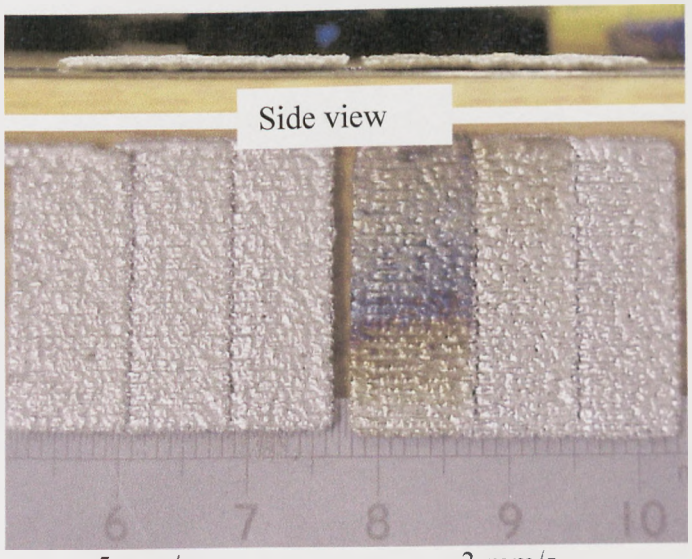

5 mm/s 3 mm/s

Figure 4.13 –150/75μm powder layer irradiated in argon, using a 75W laser power

A first observation can be made regarding the flatness of the layers. It can be seen at the top of figure 4.13 that both layers were completely flat. The influence of the FLD had reduced, but on figure 4.13 the first track is still distinct. The quality of the layer surface is good but the boundary between two consecutive long layer stripes are still visible.

Attempts to assess the layer density were also carried out. Because of the task difficulty, with a very non-regular surface, the solution adopted was the placement of a light source at the back of the sintered layer. Figure 4.14 shows the result of this test.

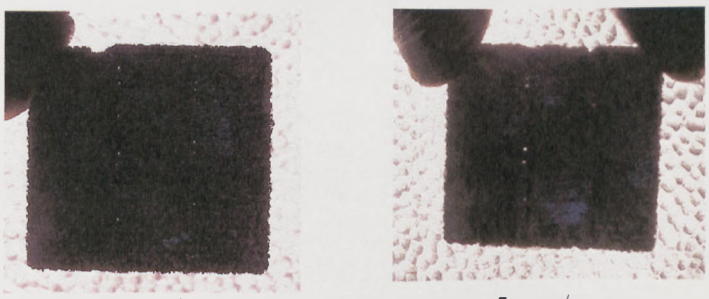

3mm/s 5mm/s

Figure 4.14 Layer density test for –150/75μm powder

Sintering tests were carried out for the –300/150μm powder using different conditions to the –150/75μm powder batch. There were carried out for scan speeds of 1mm/s besides 3mm/s and 5mm/s. The laser power used was between 75W and 110W. Figure 4.15 shows the results obtained for irradiating –300/150 μm powder in argon atmosphere for different scan speeds, laser power (75W) and a constant 0.5mm scan spacing.

5 mm/s 3 mm/s

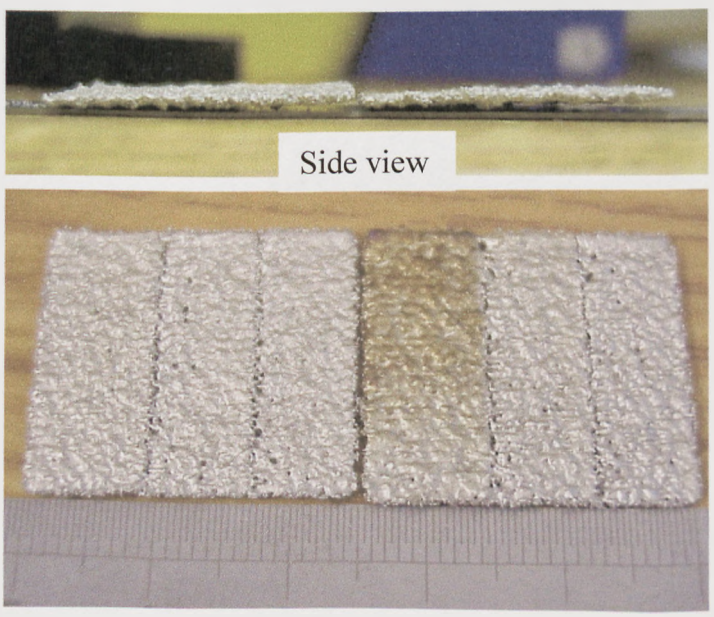

Figure 4.15 –300/150μm layer irradiated in argon, using a 75W laser power

It can be seen at the top of figure 4.15 that the layer flatness is fairly good for this batch of powder even if the layer bottom has more irregularities then –150/75μm layer. The quality of the layer surface is good but a high activity of the internal forces can be seen on the boundary between the two long layers bonded together. These internal forces contributed to the appearance of a number of gaps between the boundaries neighbourhood (figure 4.15).

Mix powder sizes

This section of the thesis is focused on the significance of mixed powder effects during the formation and growth of the stainless steel powder melt pool. Two powder mixes were used; -300/150μm with addition of 25%, -38μm powder and –150/75μm powder with addition of 25%, -38μm powder. The layer sintering maps were produced overlapping the information obtained during single track sintering tests for these two batches of powder. Figure 4.16 shows the layer sintering map for the –150/75μm powder with the addition of 25%, -38μm powder. The dashed lines (j-e-f) define the area where the sintering tests were carried out. The thick line on the map separates the area between a good quality layer surface (above) and a poor surface layer quality (below). The topside of the map has also a thick line which has the same role of delimiting the poor sintering area (above) and the good sinter area (below this second line). As a result, during layer sintering tests for this batch of powder shrinkage of the good sinterability area was recorded (see figure 4.16 above the bottom thick line and below the top thick line).

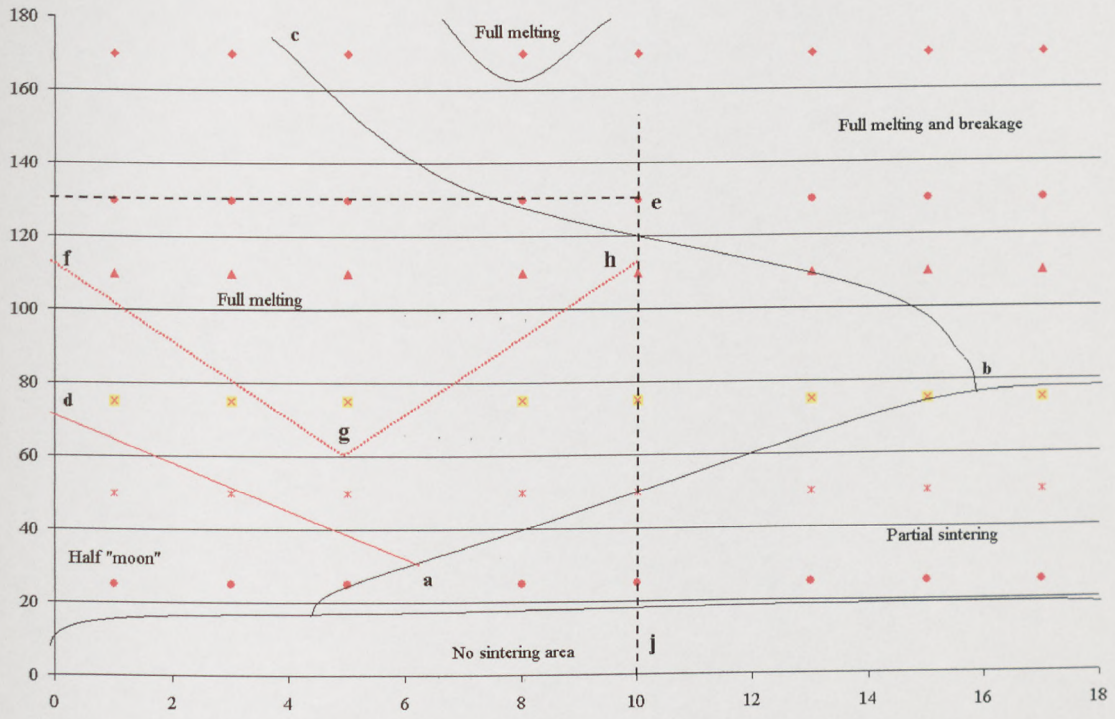

Figure 4.16 Layer process map for –150/75μm powder with the addition of 25% -38μm powder, 0.5 mm scan spacing

Figure 4.17 shows the layer-sintering map for the –300/150μm powder with addition of 25%, -38μm powder. The dashed line (j-e-f) again defines the area where the sintering tests were carried out for this batch of powder. Within this area the thick line is the boundary between good quality layer (above the line) and bad quality layer (below the line).

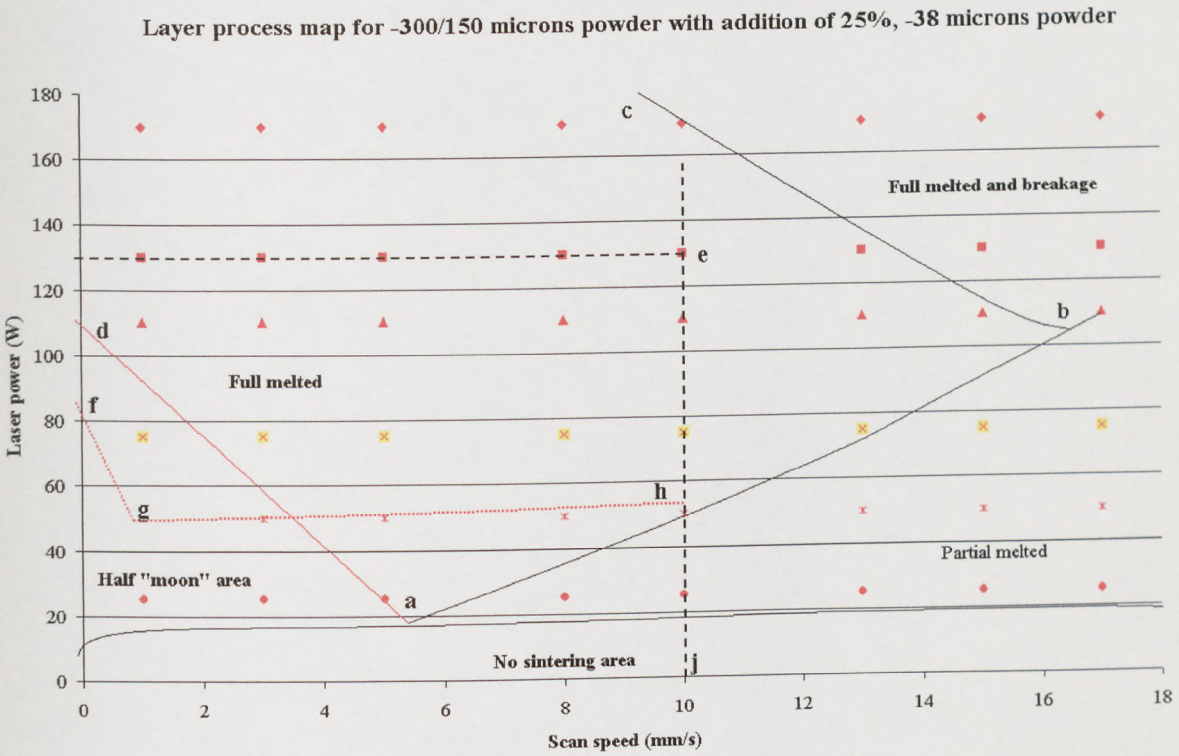

Figure 4.17 Layer process map for –300/150μm powder with addition of 25% -38μm powder, 0.5 mm scan spacing

For this batch of powder a small variation of the layer surface quality line (f-g) was recorded only for small scan speeds (<2mm/s).

As a conclusion, for all four batches of powder analysed during these sintering tests, it was observed that in fact the dashed lines (f-g and g-h) which separated the two areas on the layer sintering maps approximately follows the trend of the boundary of full melting and breakage area recorded during single track sintering tests experiments.

Figure 4.18 shows large area sintering results for –300/150μm powder with addition of 25%, -38μm powder. The sintered layers are flat as can be seen at the top of the picture. The boundaries between the three long stripes which are sintered together are still visible.

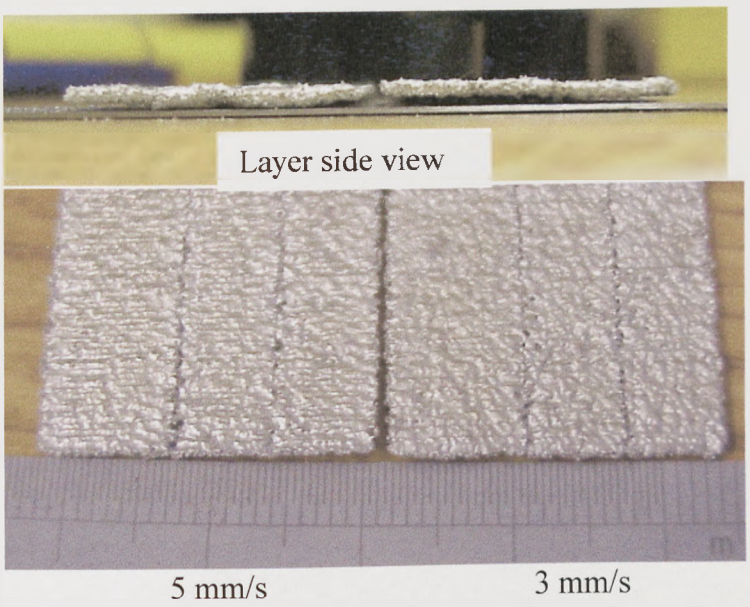

Figure 4.18 –300/150μm powder with addition of 25%, -38μm powder - large layer irradiated in argon and using a 75W laser power, 0.5mm scan spacing

A viable solution has been found to eliminate the visible boundary between the sintered stripes within the layer. Taking advantage of the mirror delay mentioned before to reach the full scan speed, the overlap between two long sintered stripes within a layer was decreased from 0.5mm to 0.25mm. In this way, the powder bed along the edge of first sintered strip was exposed for longer to the laser beam and implicitly more heat was absorbed. Compered to the 0.5mm overlap, where all heat was absorbed by the sintered strip and only a fraction of it reached the loose powder resulting in a visible boundary between two strips. The results can be seen in figure 4.15. During these tests it was also tried to sinter larger areas of the powder bed then it was tried before. The results were sintered layers of 60 mm long and 30 mm wide. It can be easily seen from figure 4.15 that by decreasing the overlap value the sintered layer flatness was much higher (figure 4.15, 1 compared to 2). There was also a recorded improvement in part density along the overlap boundary within the respective layer for an overlap of 0.25mm. FLD effect was also diminished.

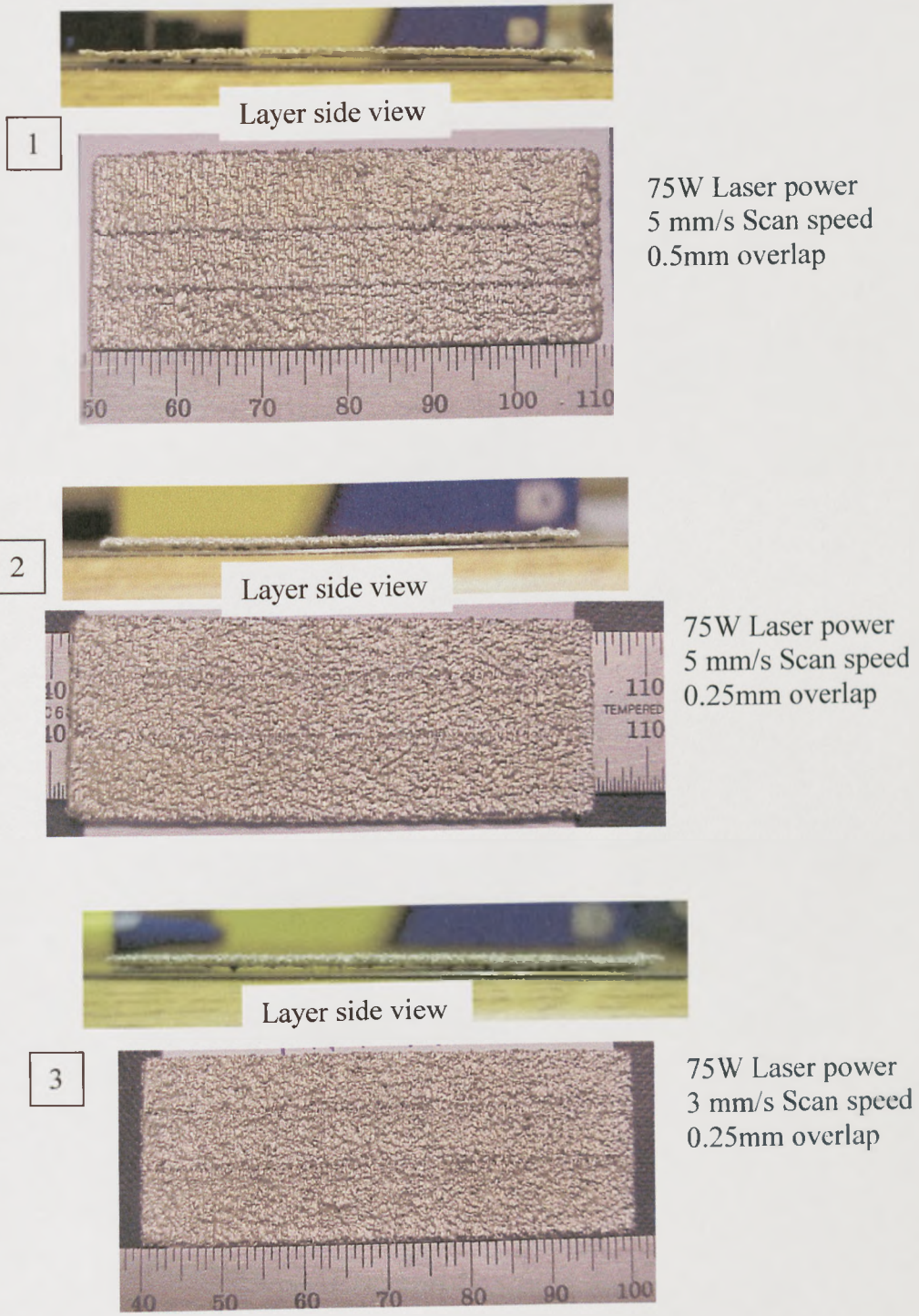

Figure 4.19 Morphological changes of the layer quality by decreasing the overlap size between the long sintered stripes, -300/150μm powder with addition of 25%, -38 μm powder

4.3.3 Microscopy studies

Test samples of single layer scans sintered using 314HC stainless steel powder were sectioned and polished for metalographic inspection. The samples were etched using "marbles reagent" and the microstructure was examined. The melting and re-solidification process of sintered SS powder has been explained in chapter 3 of this thesis for single track tests.

Two examples considered representative for each batch of powder analysed have been chosen to be presented in this part of the thesis. No examples are given for the –150/75μm mixed powder because the experimental tests showed them not suitable for multiple layer sintering. Anticipating a little bit based on the information gained from multiple layer sintering tests it was considered that a 75W laser power and 3 –5 mm/s scan speeds would be taken as representative conditions for layer sintering tests. Moreover, the influence of the scan spacing over the sintering part was considered. A spacing value of 0.5mm was chosen to be presented. Figure 4.16 shows one of these examples for the –300/150μm powder batch.

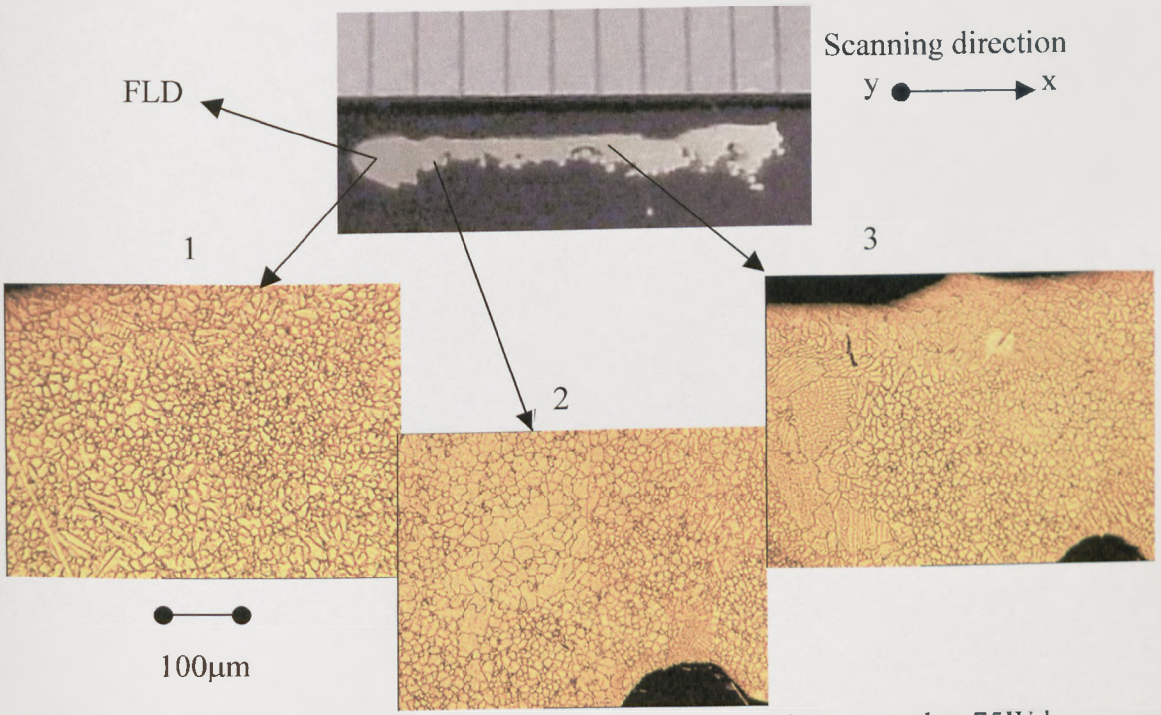

Figure 4.20 Layer cross section for –300/150μm powder scanned at 75W laser power and 3 mm/s scan speed in argon atmosphere for 0.5mm scan spacing

Firstly, in figure 4.20 – 1, an irregular distribution of the wetting front has been observed (liquid phase). It can be suggested that a stirring occurred during the sintering test for 3mm/s scan speed. This confirms the phenomenon observed during the single track experiments where 3mm/s scan speed induces a stirring phenomenon within the track (see Chapter 3). Secondly, figure 4.20 -2 and 3, an increase of the powder grain size during the melting process has been observed. This fact suggests that a higher temperature was recorded in that specific area than in the neighbour areas. This area where a higher temperature was recorded corresponds to the overlapping area between two consecutive tracks.

Moreover, a higher powder volume has been observed that was melted and started to be fully sintered in area 3 of figure 4.20 than in area 2 of the same figure. This fact suggests that the heat absorbed by the previous sintered track was higher in area 3 than in area 2 (the area with FLD). An explanation of this fact could be the semnificative difference between cross section diameters of these two tracks.

Figure 4.21 shows the microscopy test result for –300/150μm powder scanned at 75Wlaser power and 5mm/s scan speed.

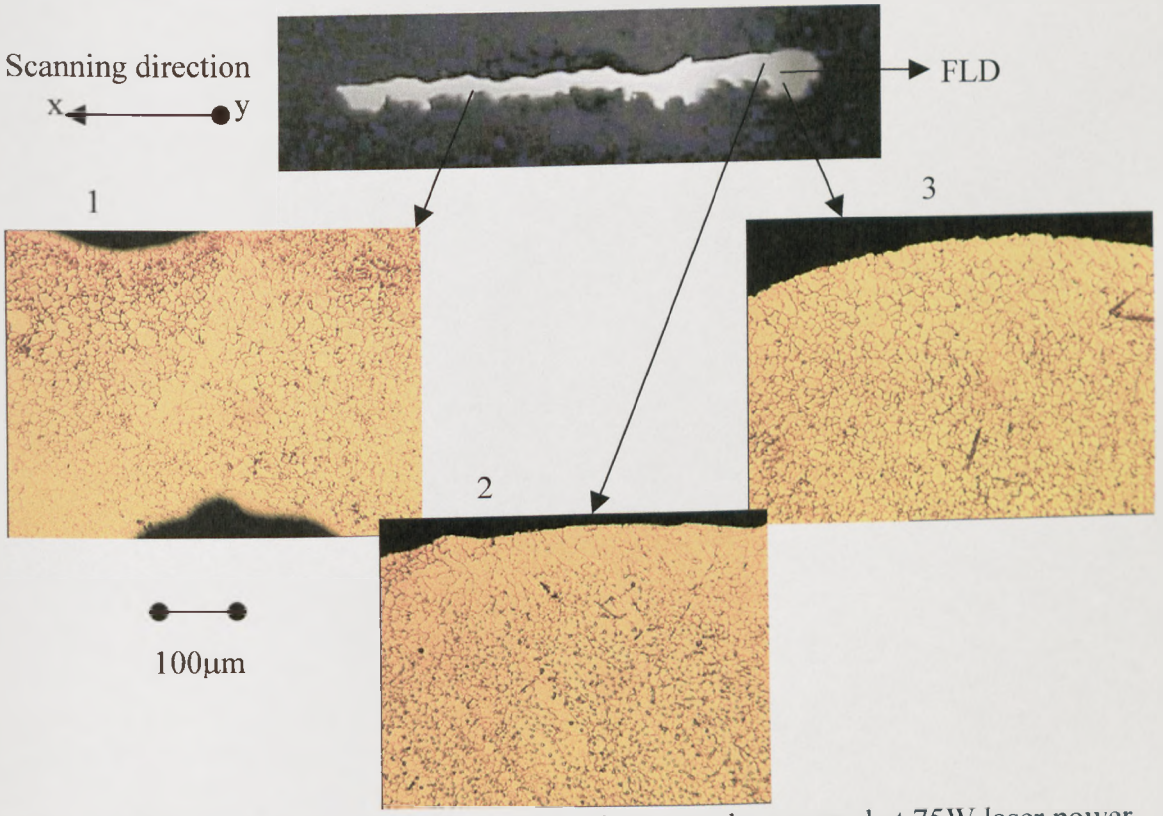

Figure 4.21 Layer cross section for –300/150μm powder scanned at 75W laser power and 5 mm/s scan speed in argon atmosphere for 0.5mm scan spacing

Regarding the sintered layer showed in figure 4.21 the internal structure presents the same patterns as those presented for the same batch of powder but scanned at 3mm/s. Figure 4.17 –1 shows the microstructure of the first line track where there was no stirring and no signs of wetting. These facts are similar to those presented in chapter 3 for single track tests for this batch of powder. A different metalographic structure has been found for the layer section where the overlap between two tracks took place (see 4.21 –2 and 3). A higher temperature due to a longer exposure of the layer to the heat source fully melted the powder in that region and the wetting areas (liquid phase) formed compared to the surrounding dendritic areas. The layer microstructure shows clearly in areas 2 and 3, growth of the grain's diameter.

Figure 4.22 shows the cross section of –300/150μm powder with addition of 25%, -38μm powder scanned at 75W laser power and 3mm/s, for a constant scan spacing of 0.5mm.

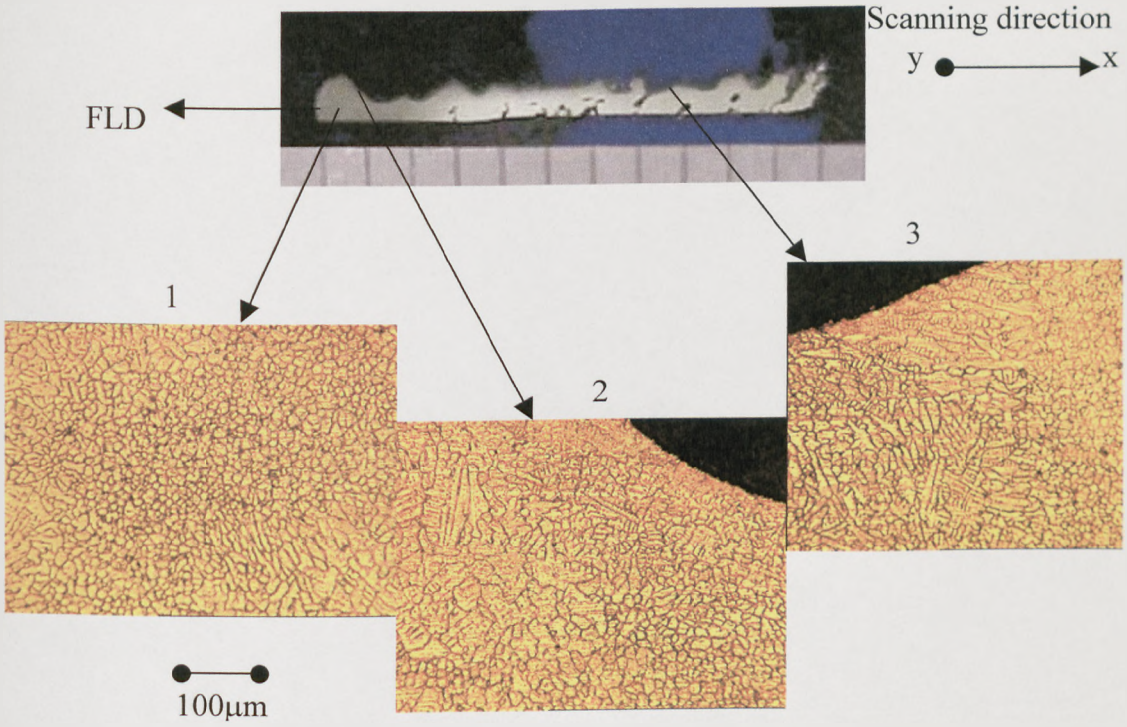

Figure 4.22 Layer cross section for –300/150μm powder with addition of 25%, -38μm powder scanned at 75W laser power and 3 mm/s scan speed in argon atmosphere for 0.5mm scan spacing

As has been mentioned for all the samples scanned using 3mm/s scan speed, the stirring phenomenon was recorded for this layer as well (see figure 4.22 – 1). Moreover, the microstructure recorded for this batch of powder was not very different from that recorded for –300/150μm powder (see figure 4.12). The only noticeable difference was recorded for the wetting front which was larger for the mixed powder (see figure 4.22 – 2and 3) then for the un-mixed powder (see figure 4.21 – 2 and 3). Figure 4.23 shows the cross section of –300/150μm powder with addition of 25%, -38μm powder scanned at 75W laser power and 5mm/s, for a constant scan spacing of 0.5mm.

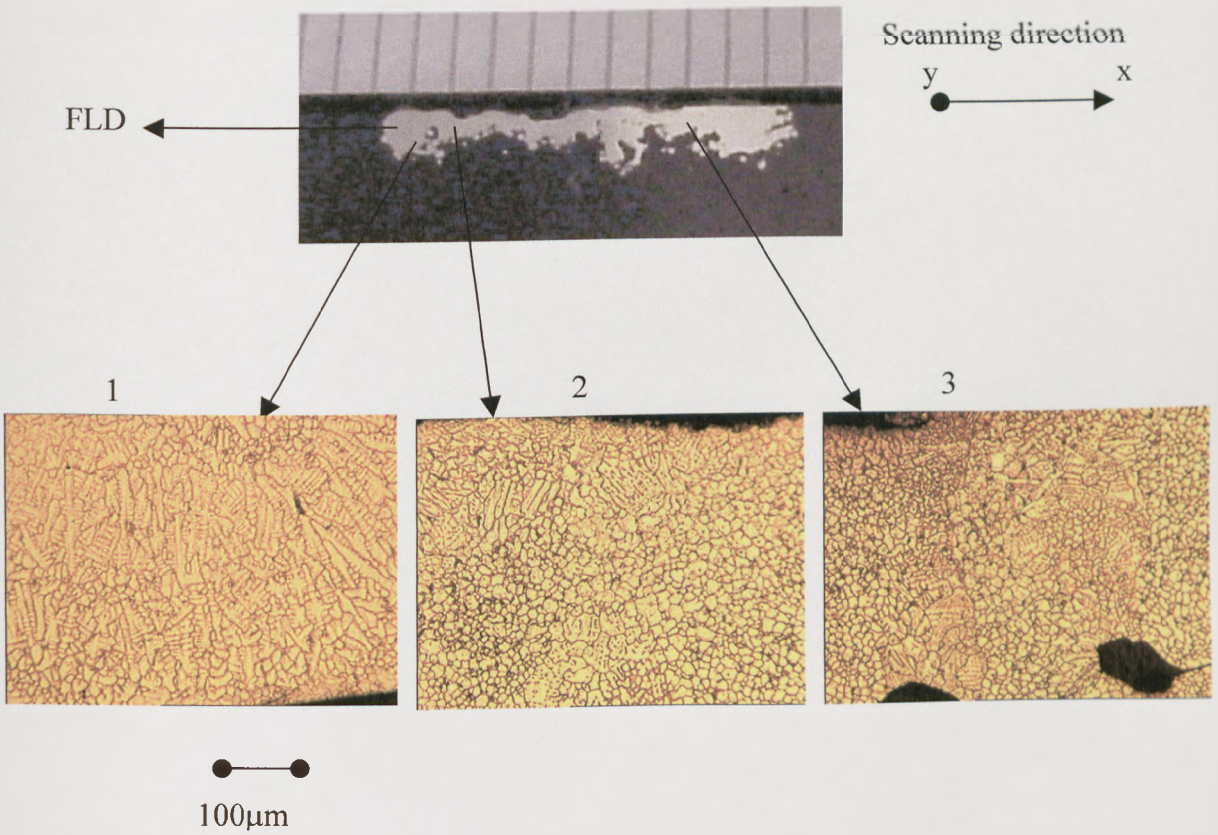

Figure 4.23 Layer cross section for –300/150μm powder with addition of 25%, -38μm powder scanned at 75W laser power and 5 mm/s scan speed in argon atmosphere for 0.5mm scan spacing

Contrary to the result obtained for single tracks at the same scanning conditions for this batch of powder and although wetting area (liquid phase) was recorded to be wide spread within the layer, the layer was not fully melted. As can be seen in figure 4.23 – 2 and 3 there are still areas where the particles are still distinctive even if the diameter of these particles were measured to be 12±0.5μm. The exception is made by the first track area (1) where the liquid phase was recorded through out the first track. It is thought that the small particles in the mix were fully melted and started to flow (liquid phase) compared to large particles which were just melted and started to have a dendritic structure. However, the layer bottom side showed an irregular shape compared to the top surface. This fact could be a bonus during multiple layer sintering because this batch of powder showed a deeper penetration of the powder bed and implicitly a better penetration of the underneath layer. And at the same time it had a flat top surface which helps the spreading of the next layer of powder. Figure 4.24 shows the cross section of –150/75μm powder scanned at 75W laser power and 3mm/s, for a constant scan spacing of 0.5mm.

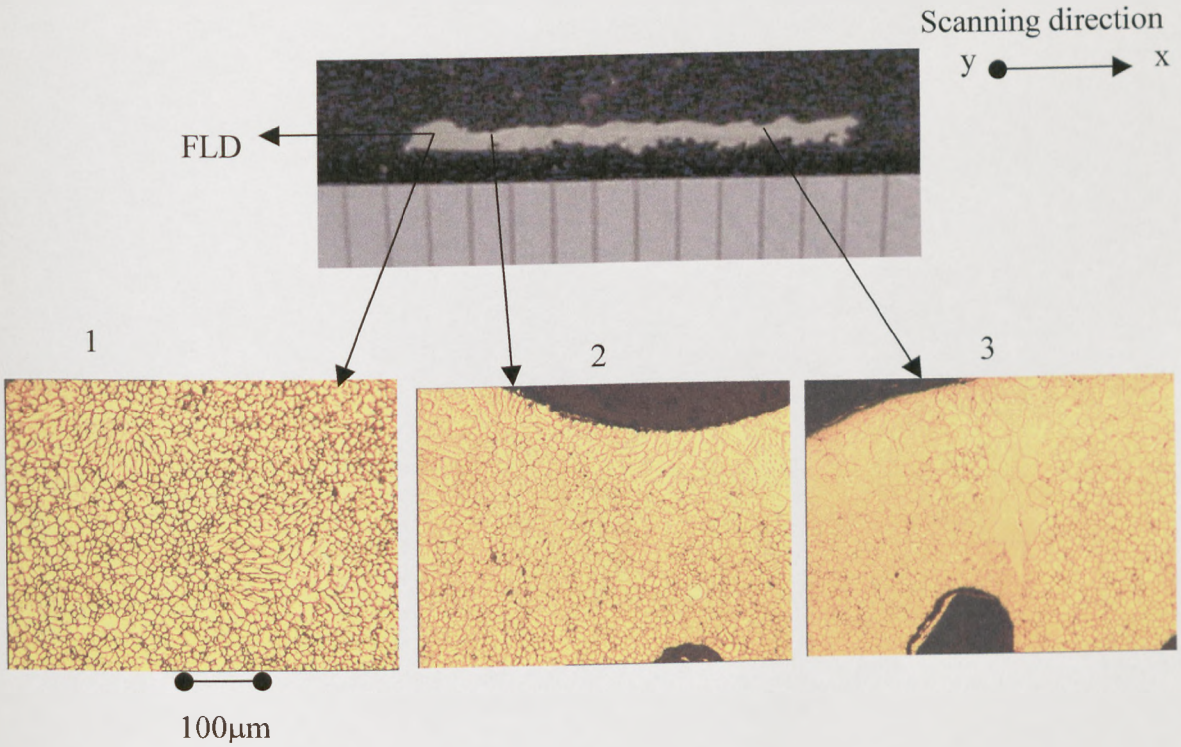

Figure 4.24 Layer cross section for –150/75μm powder scanned at 75W laser power and 3 mm/s scan speed in argon atmosphere for 0.5mm scan spacing

As can be seen in figure 4.24 the stirring phenomenon occurred for the first track within the respective layer (see figure 4.15 –1). Moreover, figure 4.24-2 and 3 present a dendritic structure only where the overlap occurred.

Figure 4.25 shows the cross section of –150μm powder with addition of 25%, -38μm powder scanned at 75W laser power and 5mm/s, for a constant scan spacing of 0.5mm.

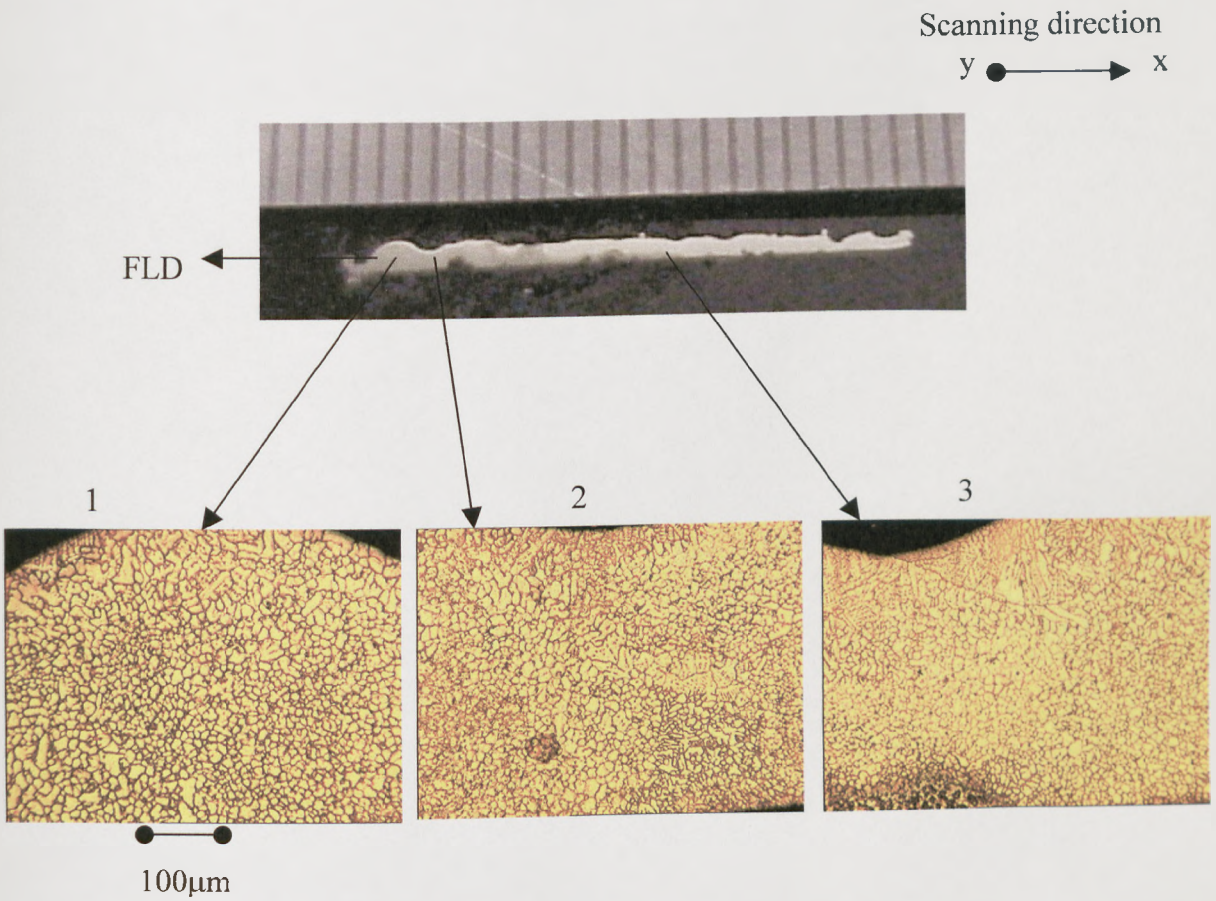

Figure 4.25 Layer cross section for –150μm powder scanned at 75W laser power and 5 mm/s scan speed in argon atmosphere for 0.5mm scan spacing

By increasing the scan speed (figure 4.25), the scanned layer showed a microscopy structure without liquid phase. A very limited liquid phase can be observed only where the overlap took place (see figure 4.25 – 2 and 3).

4.4 Multiple layer scanning

There are two mechanism of layer movement within the powder bed during the spreading process, that of displacement and rotation. Layer movement is caused by the motion of the powder as the hopper passes over the previous sintered layer. Contributory causes are debris that forms on the layer surface or imperfections of layer flatness which interact with the hopper blades as it passes. The occurrence of surface debris is random, but can be decreased through a careful selection of the scanning conditions as has been shown during the first part of chapter 4. An advantage of the new design slot feeder mechanism (SFM) over the roller spreading mechanism is the total elimination of layer rotation and a limitation of layer displacement. It was observed during the experimental tests that the layer displacement depends very much on surface layer flatness.

During these multiple layer sintering tests, all four batches of powder were used even if –150/75μm powder with addition of 25%, -38μm powder was considered not suitable because of the poor results obtained during single layer sintering tests.

An important issue during multiple layer sintering process is the layer depth. Figure 4.26 shows two multiple layers scanned at different layer depth. A better penetration of the heat through a smaller layer depth (<0.5mm) was observed than a larger one. However, a better penetration did not show an improvement of the layer top surface quality but it did show better surrounding surfaces. The gaps between the layers caused by layer curl phenomenon were diminished by decreasing the layer depth.

1 mm layer depth 0.5 mm layer depth

Figure 4.26 Two multiple layer parts (3 layers) scanned using, mix –300/150μm powder with addition of 25%, -38 μm powder, 75W laser power and 3 mm/s scan speed at different layer depth

In subsequent tests, the layer depth was chosen to be 0.5mm.

2 layers test

Furthermore, the next issue which affects the sintered part is the balling phenomenon which occurred during multiple layer sintering tests for one of the next sintered layers of powder. This balling phenomenon of the next layers of powder occurred due to the temperature dropping for the first sintered layer. Time measured for a powder layer spreading was around 30 seconds. It is considered that 30 seconds are not enough for the previous sintered layer to cool down but an increase of this time will conduct to an important temperature drop and implicit the next sintered layer to be sintered on a colder solid layer. A drop of the energy is taking place as the previous sintered layer absorb part of the heat and other part is dissipated because of the sintered layer reflectivity. In the end, the total heat remained for the next sintered layers are not enough and the balling phenomenon occurred. To prevent this, there were considered two possibilities: the first was to speed up the entire process and the second one was to decrease the laser power in such manner that the layers to have a shine-less top surface. There were made some experimental trial tests with a lower laser power (60W) and the result are presented in. It was chosen a laser power close to the boundary between good and poor layer quality. The layer depth during these tests has been limited by the SFM mechanism to 0.5mm. An observation can be made regarding the parts flatness which it showed an improvement by increasing the scan speed. Figure 4.27 shows a side view of all three sintered parts.

60W laser power

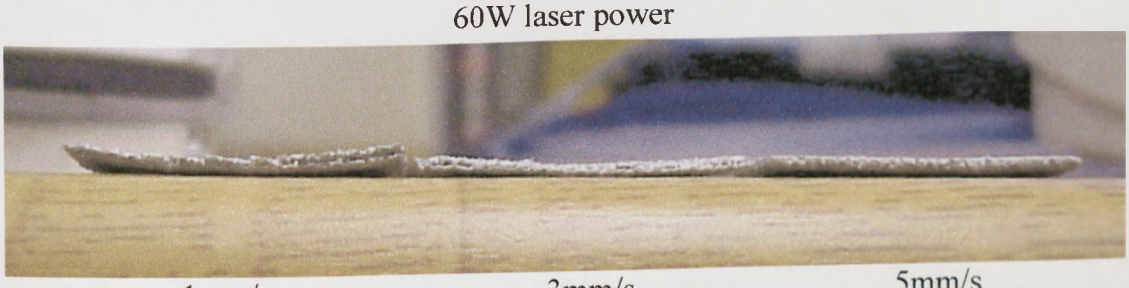

1mm/s 3mm/s 5mm/s

Figure 4.27 Multiple layers side view (2 layers) scanned for different scan speed and 60W laser power using mixed powder

(-300/150μm powder with addition of 25%, -38μm powder)

An increase of the laser power (75W) for the same batch of powder

(-300/150μm powder with addition of 25%, -38μm) and a scan speed of 3 mm/s result in a multiple layer shape where the warping phenomenon occurred as well as the balling phenomenon for the second sintered layer (see figure 4.28). It was observed besides balling phenomenon a full-melting and breakage area on the second layer top surface.

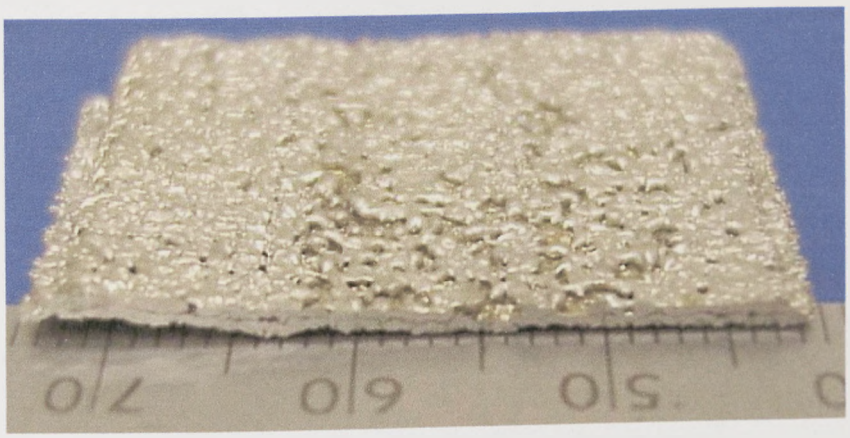

Figure 4.28 Multiple layer sintered using -300/150μm powder with addition of 25%, -38μm powder at 75W laser power and 3 mm/s scan speed

A further increase of the scan speed (5mm/s) did reduced the balling phenomenon and eliminated the layer warping. Figure 4.29 shows a multiple layer scanned using the same batch of powder and a scan speed of 5 mm/s.

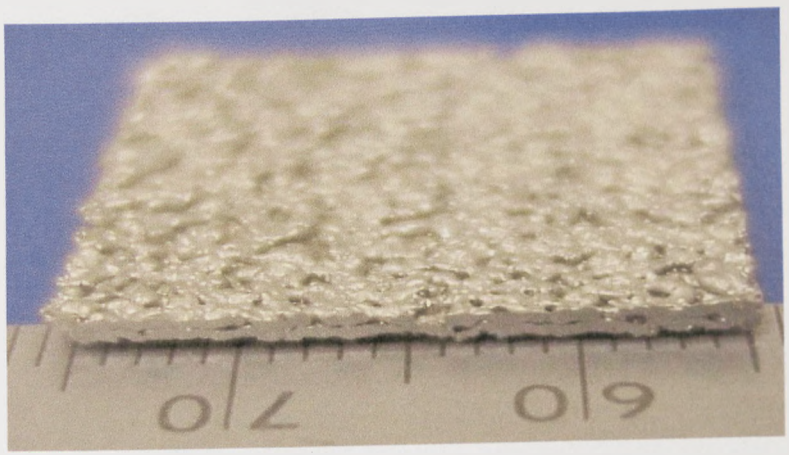

Figure 4.29 Multiple layer sintered using -300/150μm powder with addition of 25%, -38μm powder at 75W laser power and 5 mm/s scan speed

3 layers sintered tests

During multiple layer the main problem was not bonding two layers together. This task was achieved for all four batches of powder in the sintering map areas of good layer quality. The main problem was the achievement of a good layer flatness to enable the spreading of the third layer of powder. Furthermore, the next issue observed during the experimental tests was the third layer's tendency to bond with the previous sintered layers only along the first sintered track (along FLD). Figure 4.30 shows the effect of the FLD over the third scanned layer within the respective sintered sample. Higher heat conductivity enables FLD to absorb more heat and the result is a better penetration.

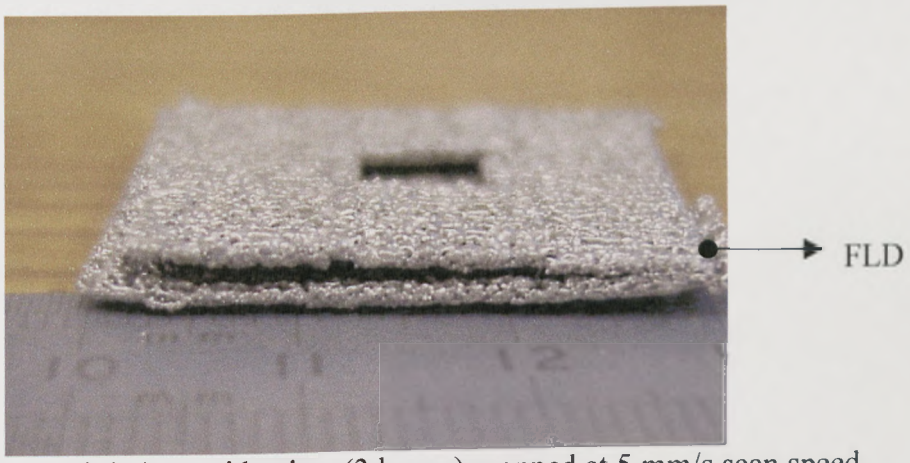

Figure 4.30 Multiple layer side view (3 layers) scanned at 5 mm/s scan speed and 60W laser power, using -150/75μm powder batch

It is thought that the first track layer bonding phenomenon was helped by the slight rotation of the layer as the hopper passed.

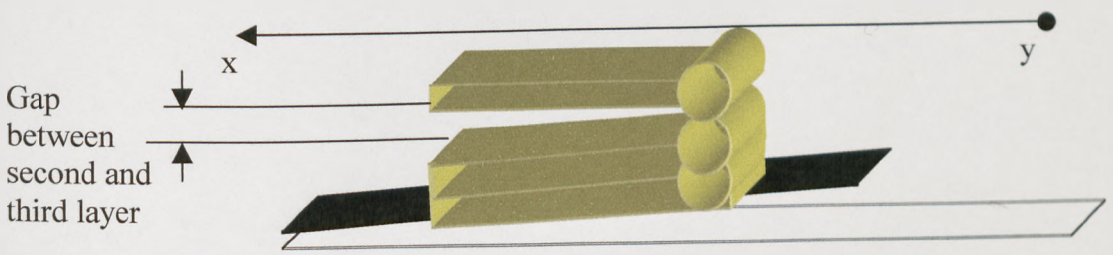

Figure 4.31 Schematic view of layer rotation

4 layers sintering tests

Sintering trial tests were extended and more layers (>2 layers) were sintered together. An example of four layers bonded together are shown in figure 4.32. The -300/150μm powder with addition of 25%, -38μm powder scanned at 75W laser power and 5 mm/s scan speed was used. It can be observed that the layers are bonded together but there are gaps between them. Each particular sintered layer can be clearly seen. This fact suggest that in fact the layers were not melted together.

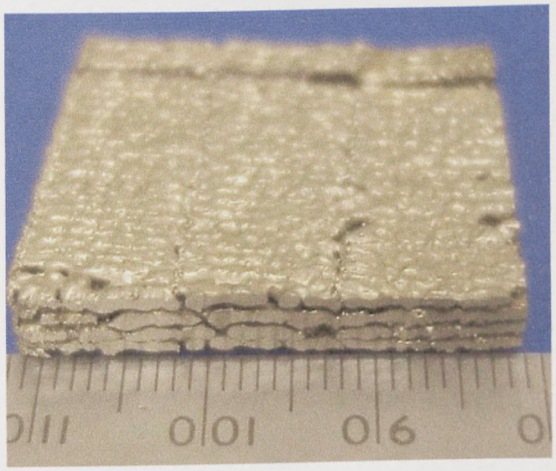

Figure 4.32 Four layers sintered together scanned using -300/150μm powder with addition of 25%, -38μm powder in argon atmosphere

Figure 4.33 shows a multiple layer part sintered using –150/75μm powder at 5 mm/s scan speed and 75W laser power. The same features those presented for figure 4.32 were observed. The sintered layers are distinctive and are only partial bonded together.

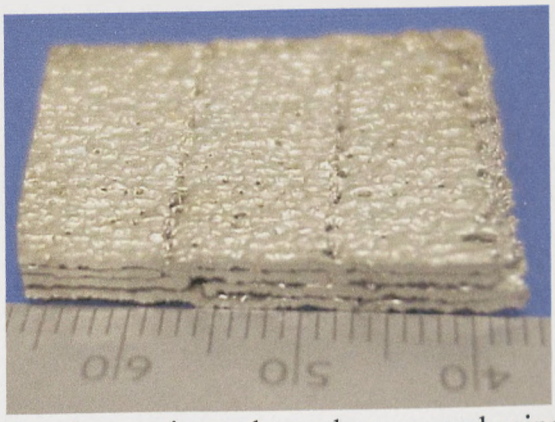

Figure 4.33 Four layers sintered together scanned using –150/75μm powder in argon atmosphere

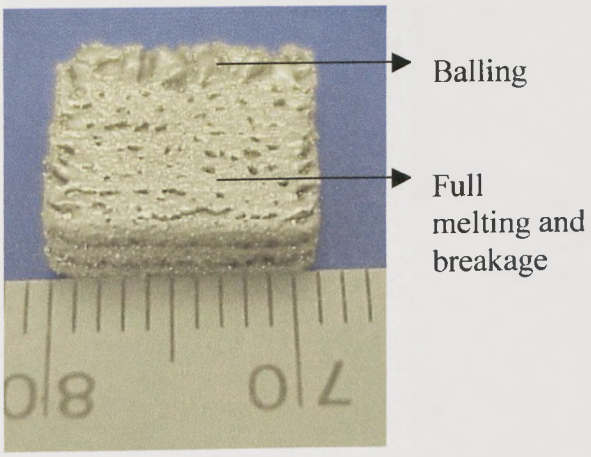

Figure 4.34 Multiple layer part scanned using –300/150 μm powder in argon atmosphere

Figure 4.34 shows the multiple sintered part obtained during –300/150μm powder sintering tests. The result was a sintered three layers block. The effect of balling was recorded at the edges of the block. In the middle, the full-melting and breakage area has been recorded. The apparent density of the part was measured to be around 68%.

10 layer sintering tests - The next step of the research was the building of a sintered part with more then 4 layers. The result is shown in picture 4.35 and a top view of the part can be seen in figure 4.36. The part was scanned using 75W laser power and 5mm/s scan speed. The apparent density of the part was measured to be around 70%.

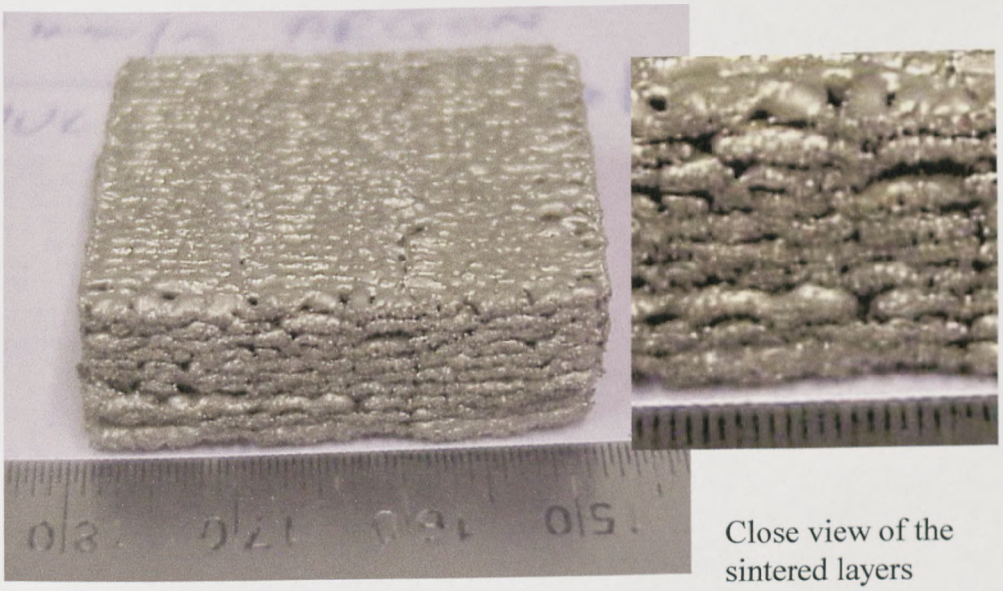

Close view of the sintered layers

Figure 4.35 Multiple layer part (10 layers) scanned using –300/150μm powder with addition of 25%, -38μm powder in argon atmosphere

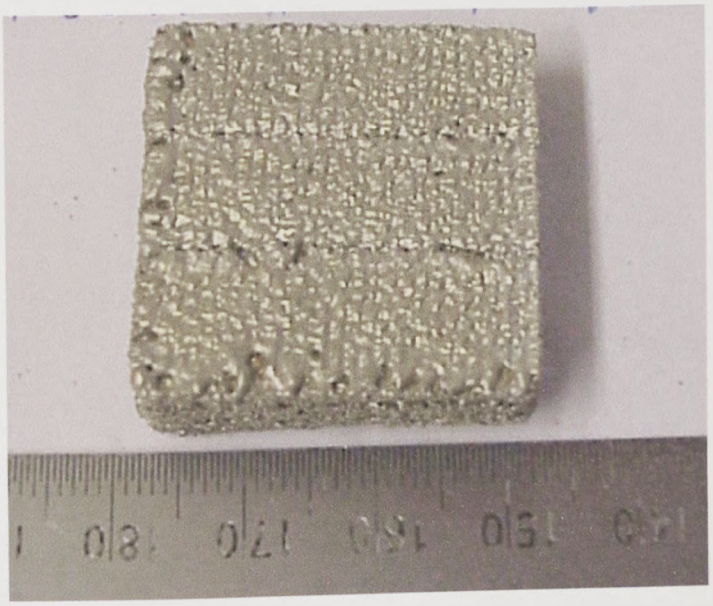

Figure 4.36 Top view of multiple layer part (10 layers) scanned using –300/150μm powder with addition of 25%, -38μm powder

The 10 layer sintered block was scanned using a 75W laser power and a 5mm/s scan speed. The layer depth used was 0.5 mm, a scan spacing of 0.5mm for the long sintered strips and 0.5 mm scan spacing between the long sintered stripes. As can be seen in figure 4.35 the balling phenomenon and the full melting and breakage regime were totally eliminated. The block was sintered using scanning parameters found in the good quality area on the sintering map of this batch of powder.

4.4.1 Multiple layer microscopy studies

Test samples of multiple layer scans sintered using 314HC stainless steel powder were sectioned and polished for metalographic inspection. The samples were etched using "marbles reagent" and the microstructure was examined. This section starts by presenting Figure 4.37 that shows an example of two layers sintered together. The first observation is regarding the large black gaps that are visible between the layers. It is thought that these gaps appeared because of the round bottom track shape. The second observation is regarding the visible boundary between the two sintered layers. This

boundary appeared due to the lack of heat necessary to penetrate and melt the underlying layer.

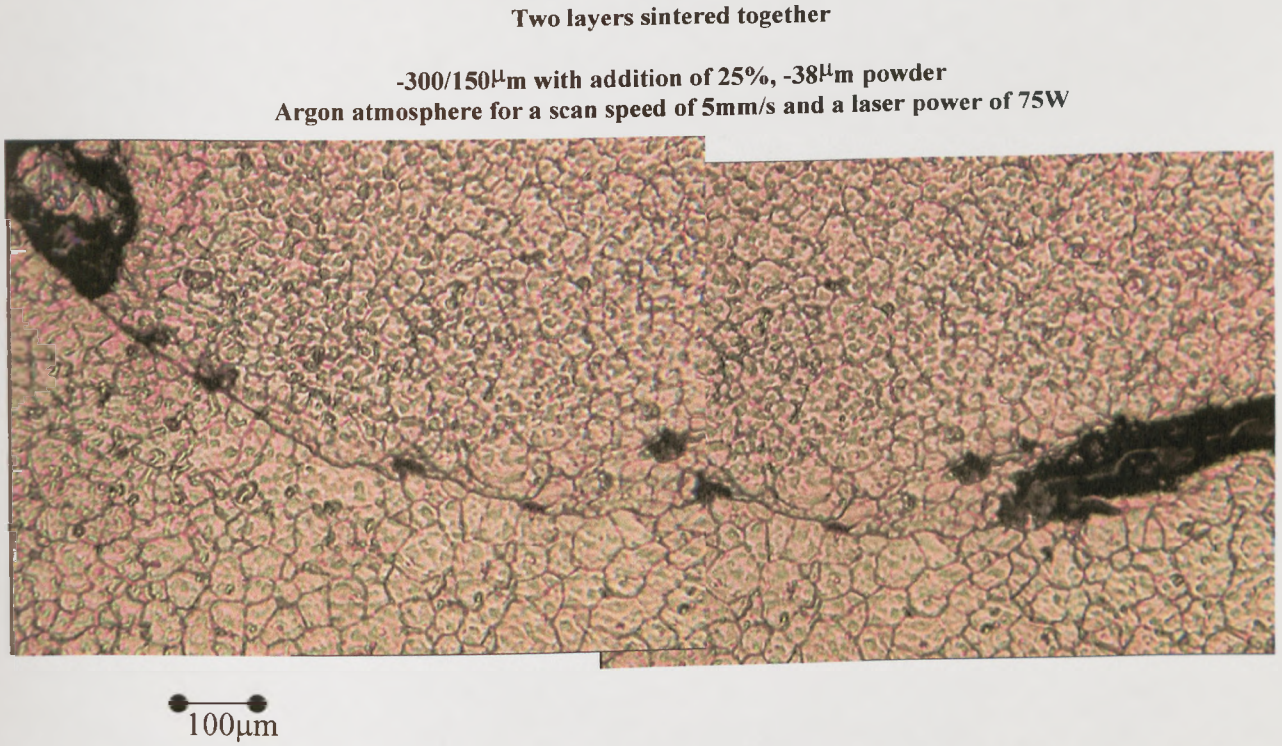

Figure 4.37 Microscopic cross section view of two sintered layers using mix powder

Two layer samples from each batch of powder except –150/75μm with addition of 25%, -38μm powder have been analysed. The second layer of –150/75μm with

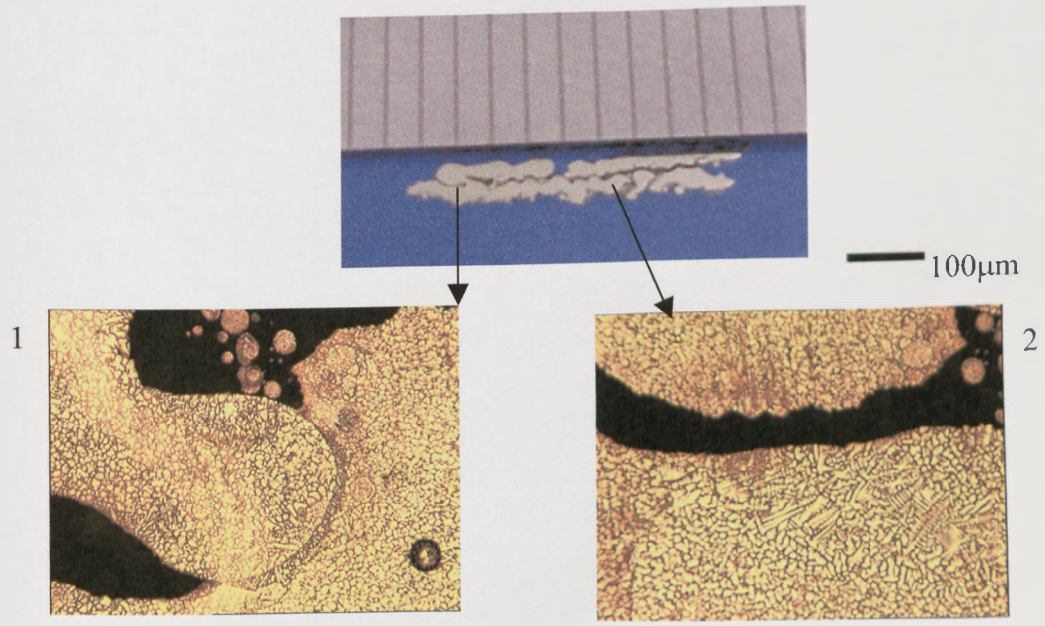

Figure 4.38 Multiple layer cross section for –300/150μm powder batch

addition of 25%, -38μm powder batch had a very pronounced balling phenomenon and it could not be analysed.

Figure 4.38 shows the multiple layer (2 layers) cross section obtained using –300/150 μm powder. The sintered part was scanned using a 75W laser power and a 3 mm/s scan speed. A displaced layer movement as well as a full-melting and breakage phenomenon can be observed. Figure 4.38 – 1 shows the bonding mechanism between these two layers. The layers are bonded together only by small metal molten drops with big gaps between them.

Figure 4.39 shows the multiple layer (2 layers) cross section obtained using –150/75 μm powder. The part was sintered using a 75W laser power and a 3mm/s scan speed. The full melting and breakage phenomenon was found to be very wide spread within the second sintered layer. A slight displacement of the second layer can also be observed. Like in the previous example the layers are bonded together by small metallic droplets.

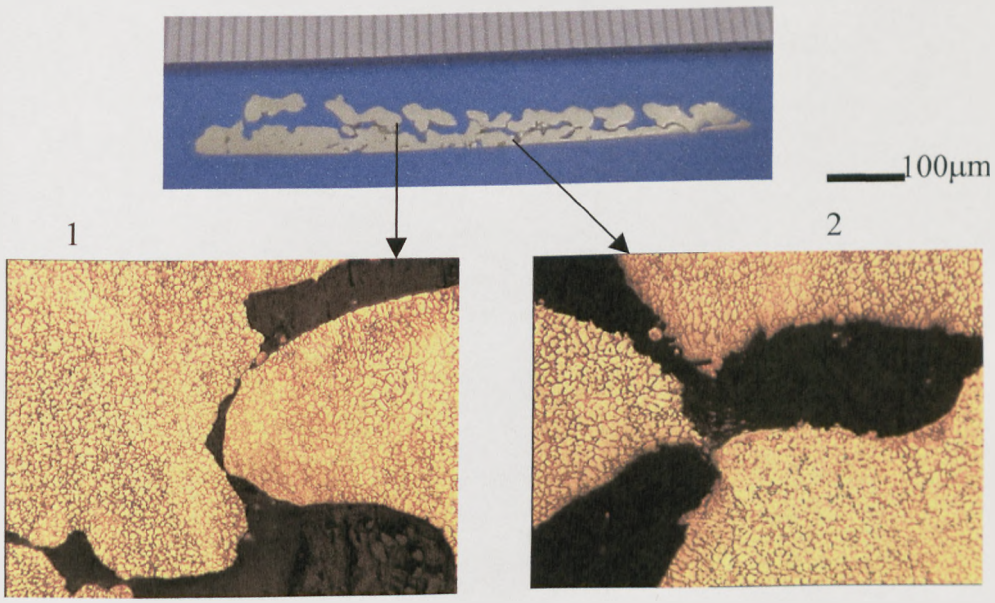

Figure 4.39 Multiple layer cross section for –150/75μm powder batch

Finally in the –300/150μm with addition of 25%, -38μm powder batch case, figure 4.40 shows the multiple layer (2 layers) cross section obtained. In this case a wide

spread fullmelting and breakage area for the second sintered layer was also recorded No displacement of the second layer during powder spreading process was recorded. Even if the second layer had a pronounced full-melting and breakage behaviour the gaps between the two layers were not very big.

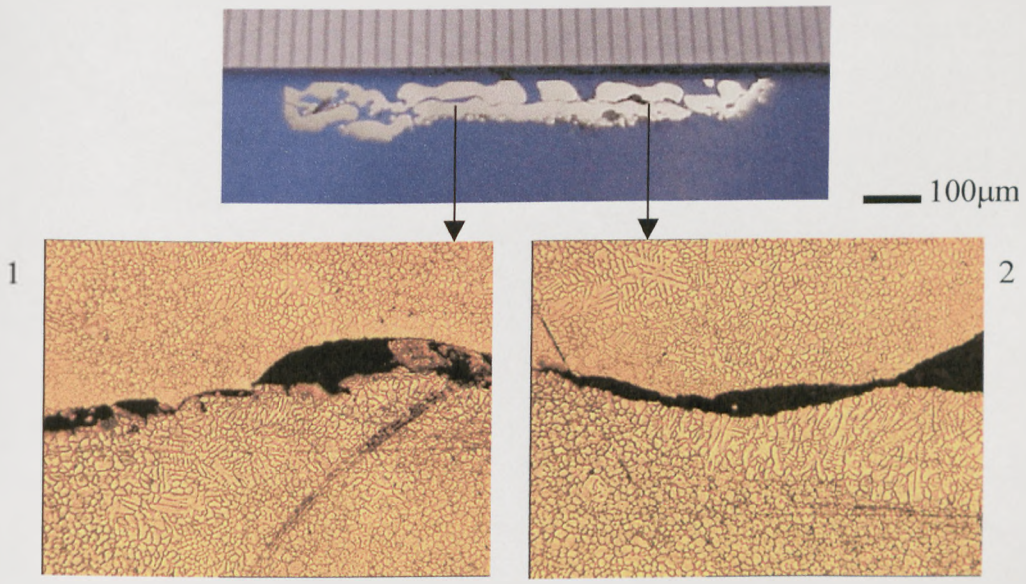

Figure 4.40 Multiple layer cross section for –300/150μm
with addition of 25%, -38μm powder scanned at 3 mm/s scan speed and 75W laser power

4.5 Summary

This chapter investigated possibilities of single layer sintering and furthermore the possibilities of scanning multiple layers.

The first part of this chapter reported on sintering tests for four batches of powder, two un-mixed, -300/150μm powder and –150/75μm powder, and two mixed batches, -300/150μm with addition of 25%, -38μm powder and –150/75μm powder with addition of 25%, -38μm powder. The results were recorded and mapped on to sintering maps by overlapping the information obtained from single tracks sintering tests with those from single layers sintering tests. Microscopy investigations were carried out for each batch of powder. Furthermore, based on this information, multiple layer sintering tests were carried out. This part of the thesis, regarding multiple layer scanning, starts by presenting some usual problems that had to be eliminated during the sintering tests. The

results are shown in figures 4.28 – 4.32. Chapter 4 ends with a microscopy investigation regarding multiple layers for different batches of power scanned with different parameters.

CHAPTER 5
DISCUSSION AND CONCLUSIONS

5.1 Introduction

Chapter 1 stated the mains objectives of this thesis to be reduction of porosity of as-sintered parts, the creation of sintering maps and sintering strategies to guide processing conditions and reduction of balling, warping and curling. The following has been achieved. Powder mixing to increase powder density has created powders that can be sintered without balling over a larger range of laser powers and scan speeds than unmixed powders (chapter 3). Dense single layers as judged by absorption of light, have been achieved (fig 4.14). The creation of sintering maps has been extended from single scan to multi-layer conditions. The power/speed conditions for successful processing are more limited for multiple layers than for single scans. Warping has been avoided by restricting sintered strips to an area of 10 mm width. Larger areas have been created without warping by sintering strips next to each other. An important factor for success has been found to be the overlap between strips. The tests have shown that the sintering map boundary depends on powder size. But it has not been determined definitively what is the cause of these powder size effects. It might be the influence of powder size on its flowability, or it might be different interactions (absorption) with the laser beam, or it might be different surface areas leading to different oxide levels and surface tension in the melt. These and other aspects are considered in later sections.

5.2 Preliminary tests

Mixing the powders for 15, 30, 45 and 60 minutes, as described in section 3.2, resulted in an increase of powder density. Furthermore, the powders were mixed together in different size fractions. The peak density was reached after 15 minutes for all batches of powder except –38 μm powder. -38μm powder peaked after 30 minutes. The powder flow rate was also measured and a poor flow rate was recorded for small particle size powders compared to big particle size powder. The -38μm powder batch did not flow at all in spite of using both flowmeters available. The poor flowability affects the powder sinterability

for this batch of powder, how this happens will be seen later in this chapter. By mixing the powders together in different size fractions the powder flow rate dropped for big particle sizes. A drop from 17g/s to 3g/s was recorded for Carney's flowmeter tests. An improvement of -38μm powder batch flow rate was also recorded for a size fraction of this powder less than 40% in the mix. A poor flow rate resulted in poor powder bed flatness during spreading tests. System vibration recorded during spreading tests had an influence over the spreading process. The spreading tests showed that an increase of powder particle size results in a more flat powder bed surface. In addition, the mixed powder showed good powder bed flatness for mixes where the small particle size powder was less then 40% in the mix. An increase of the small particle size over 40% resulted in a poor powder bed flatness, compared to the results obtained for un-mixed -38μm powder.

Moreover, thermal conductivity tests carried out for all batches of powder suggested a slight increase of thermal conductivity by increasing the powder particle size except the –300/150μm powder which showed a slightly smaller thermal conductivity value. On average the thermal conductivity for all batches was recorded to be 0.31 W/mK. The conductivity rig check has shown a poor quality of data readings for the last thermocouple (R6) and a loss of heat at the rig bottom.

5.3 Single tracks

Single track sintering tests identified four types of melting behaviour. All the qualitative track information was mapped. Each sintering map shows these four melting behaviour types as follows: no sintering, partial sintering area, fully melted area and fully melted and breakage area. Each boundary determined was identified alphabetically (figures 3.20-3.25).

A first observation from the sintering maps is the movement of the c-b boundary (figures 3.20-3.25). The c-b (c-b' for –300/150μm) line was found to move towards the left side of the map by decreasing the powder particle size. A possible reason could be the poor flow rate of the fine powders. Figure 3.4, section 3.3.1 shows the decrease of the flow rate with the decrease of the powder particle size. Powder density may have an influence as well.

However, there are other differences between the powder batches as well. During the sintering tests the sintered tracks physical proprieties such as, track depth, track width and track mass were also measured. The dimensional measurements were taken for all batches of powder but the mass measurements were carried out only for three batches of powder: -75μm, -300μm and –300/150+25%, -38μm powder. Constants of proportionality for the scanned single tracks have been calculated and are shown in table 5.1. The last column of the table is the second column divided by the third column and is presented as a density check on the measurements.

Table 5.1 Constants of proportionality

Powder size (μm)	mass/length /P/U (10^{-3}g/J)	w x d / P/U (mm^3/J)	mass/length/ w x d (ρ) kg/m^3
-300/150 μm	0.3±0.1	0.08±0.02	3,750
-75/38 μm	0.65±0.1	0.14±0.04	4,650
75%,-300/150+ 25%, -38μm	0.45±0.1	0.11±0.08	4,090

It is seen from table 5.1 that the –300/150 μm powder track is lighter per unit length than is the –75/38μm one and it also has a smaller cross-section area for a given P/U value. The final row is intermediate between these two.

Why the different powder size tracks should have different mass/unit length and area, when their densities and conductivities are not so different, merits further discussion. Perhaps they absorb the laser energy by different amounts. The following is an estimate of the absorptivity α, based on an energy balance. If a fraction α of the laser power P is absorbed, then in 1s, an energy αP Joules is absorbed. If the track mass per unit length is m', the track mass in 1s is m' x U. If the energy required to melt unit mass, heating it from room temperature, T_0, to the melting temperature, T_m, is [C (T_m -T_0) +L], where L is the latent heat,

$$\alpha P = m' U [C (T_m - T_0) + L] \qquad (5.1)$$

In the present case C=650 J/kg K, T_m= 1400^{0}C and L=280kJ/kg.

From Table 5.1, for –300/150μm powder tracks we also have:

$$m'/(P/U) = (0.3\pm0.1)\ 10^{-3}\ \ (g/J) \qquad (5.2)$$

We therefore have an estimate for α as:

$$\alpha = (0.3\pm0.1)\ 10^{-6}\ [650 \times 1380 + 280{,}000] \qquad (5.3)$$

$$\alpha_{-300/150\mu m} = 0.353\pm0.1 \qquad (5.4)$$

Similarly, using –75/38μm and 75%-300/150 + 25%,-38μm powders, we have an estimate for α as:

$$\alpha_{-75/38\mu m} = 0.765\pm0.1 \qquad (5.5)$$

$$\alpha_{-300/150+-38\mu m} = 0.529\pm0.1 \qquad (5.6)$$

Thus, it is suggested from equations (5.4 and 5.5) that –75/38μm powder absorptivity rate is twice as high as –300/150μm powder absorptivity. And, the mixed powder shows an absorptivity rate between the small and large particle size powders absorptivity values (equation 5.6). Assuming an effective absorptivity of 0.35 and 0.76 results in an absorbed power of 26.6W and 57W for a 75W laser power used to sinter –300/150μm powder and –75/38μm powder respectively. The power absorbed by the mix powder is 39.6W for a delivered laser power of 75W. In conclusion, these calculations suggest a small powder particle size absorbs more heat from the heat source than a big powder particle size.

This suggestion is also supported by the physical measurements of the sintered tracks and also by powder thermal conductivity tests. Small particle size powder produced larger and heavier sintered tracks thanbig particle size powder. The density (ρ) of the track-melted material may be estimated from the mass/J and mm^3/J constants in table 5.1. If the track cross-section is rectangular, elliptical or triangular, the three relationships between track area and w x d are, respectively:

$$A = w \times d \qquad (5.6)$$

$$A = (\pi/4)\ w \times d \qquad (5.7)$$

$$A = 0.5\ w \times d \qquad (5.8)$$

In general,

$$A = c\ (w \times d) \qquad (5.9)$$

with c typically between 0.5 and 1.0. The calculated densities of the tracks are tabulated in table 5.1, based on a value of c equal to 0.75. The stainless steel density is 7652 kg/m^3. The results show a 60% dense track for –75/38μm powder, a 53% dense track for mixed powder and a 49% dense track for –300/150μm powder.

But if c equal to 0.5 is used, the densities will be as follow:

-75/38μm powder – 7500 kg/m^3

-300/150μm powder - 9300 kg/m^3

75%, -300/150μm + 25%,-38μm - 8180 kg/m^3

It can be concluded that the calculated values are in a range of acceptability. Due to the very difficult task and the complex shape of the tracks these values are only an estimate. The answer why small powder size absorbs more heat then big particle size is a question for future work.

Another observation from the single tracks tests was the changing cross sectional shape of the sintered track as scan speed increases. Three different cross sectioned shapes, crescent-shape triangular shape and elliptical shape were recorded. These shape characteristics were used for c values during the absorptivity calculation. A possible explanation for the formation of the crescent or half-moon track shape was found to be the evaporation or expulsion of the melted powder from the interaction area during the sintering process. Figure 5.1 shows the powder bed reactions during sintering tests at different scan speeds. The pictures were taken using a SONY digital camera.

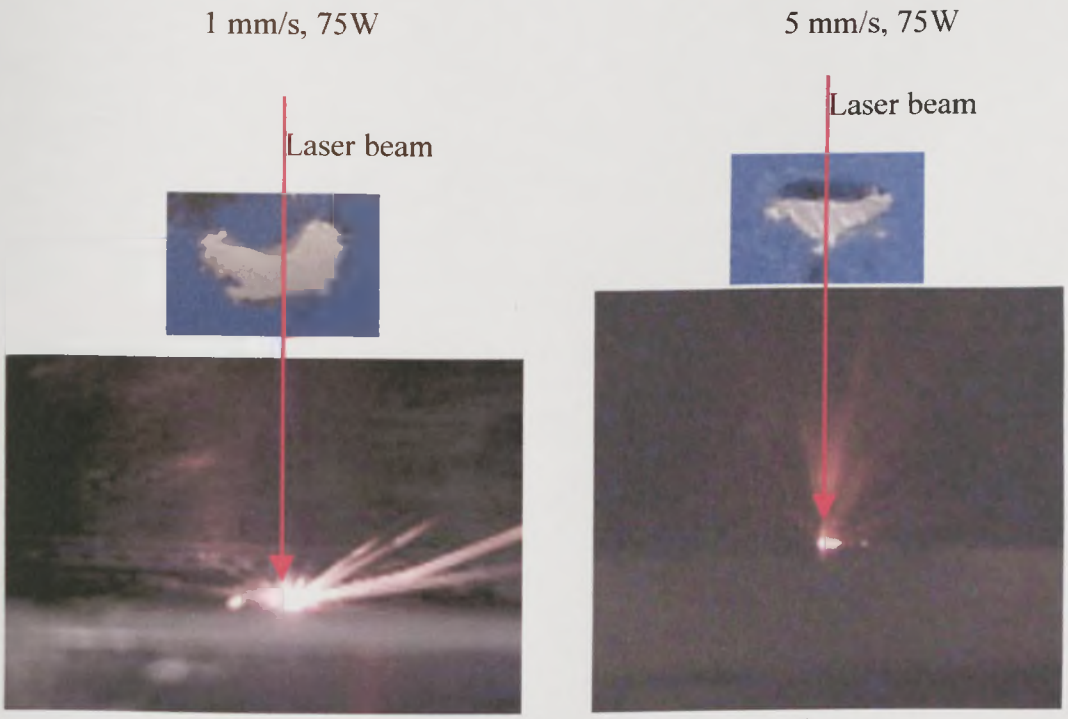

Figure 5.1 Powder bed reactions during scanning tests in argon atmosphere

It can be easily seen from picture 5.1 (left picture) the 'violent' reaction of the powder during the scanning process at low scan speeds (≈1mm/s) compared with the powder reaction on the right side of figure 5.1 at 5 mm/s.

The influence of the half-moon shape over the full melting and breakage area is definitely correlated. A small half-moon area resulted in a bigger full-melting and breakage area on the sintering map. Besides, the boundary of the half-moon area (d-a) is parallel to the full melted and breakage area (c-b). By correlating these two pieces of information a conclusion could be drawn that a poor powder flow rate results in a small half-moon area for that powder and corresponds to large full melted and breakage area on the sintering map.

Furthermore, the sintered tests were carried out for scan speeds below 1mm/s for some of the powder batches. The results recorded for U≤1 mm/s differ from those recorded for U≥1mm/s. A possible explanation of this fact can be based on the following explanation: from conductivity measurements (k≈0.31 W/mK), powder bed density (e≈5000Kg/m^3) and the average specific heat of steel in the range 20^{0}C to 1000^{0}C (C≈650

J/kgK), the diffusivity of the powder bed K/e x C ≈ 0.1 mm^2/s. The Peclet number Ua/2k associated with the scan speed, U, and the laser beam diameter, 2a≈1mm, is therefore 2.5 when U= 1mm/s. Speed dropping below 1mm/s is associated with Peclet number approaching 1.0. It is well-known that this is the borderline between a high-speed moving heat source temperature distribution and a slow-speed ones. High-speed is associated with heat having a long time to diffuse away from absorption region in the time the laser beam passes by. Slow-speed means heat has enough time to diffuse away in the time the laser beam passes by. So, the lower weight per length at a given P/U as the scan speed drops below 1mm/s can be interpreted as being due to less constrained heating in these cases.

5.4 Single layers

The sintering tests were carried out using four batches of powder. Two of the initial six batches of powder were eliminated due to a very narrow full melted area obtained during single track tests. By joining the information obtained from single tracks tests with the information for single layers tests, shrinkage of the *full melted* area for all four batches of powder was noticed. The boundary between good quality and poor quality areas (f-g and g-h) moved upwards relative to the single-track boundary in the area where the tests were carried out. Also, the tendency of the boundary g-h to follow the boundary a-b was noticed except for –300/150 μm with addition of 25%, 38μm powder. The layers' physical properties were measured such as layer weight. The results are plotted on a P/U scale and are presented in figures 5.2 and 5.3.

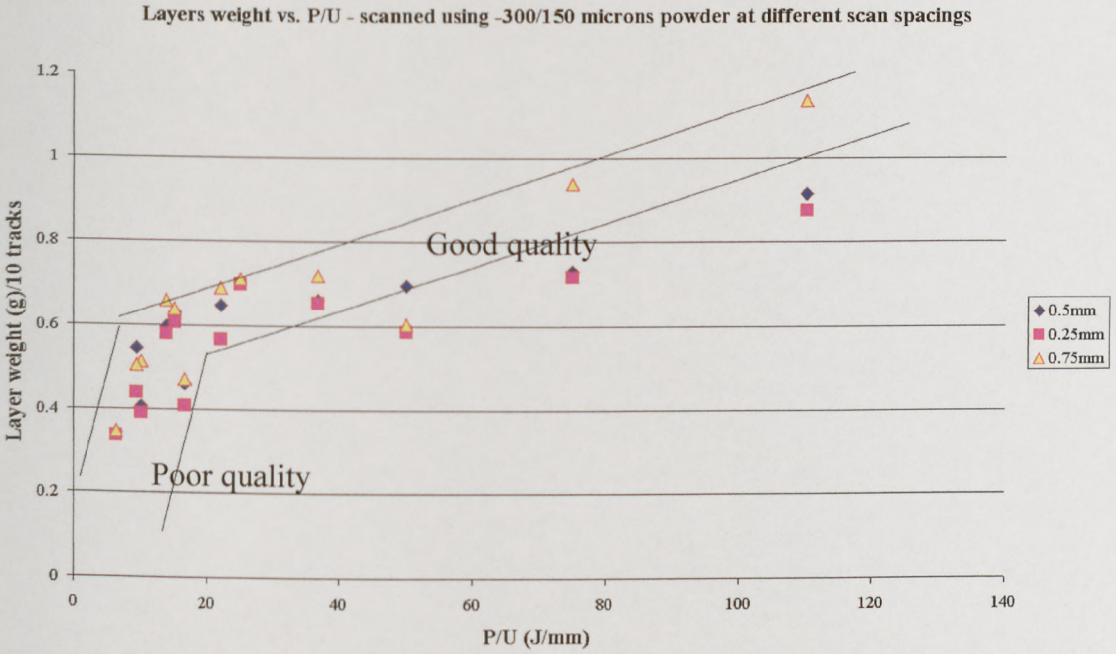

Figure 5.2 Layer weight vs. energy (-300/150μm powder)

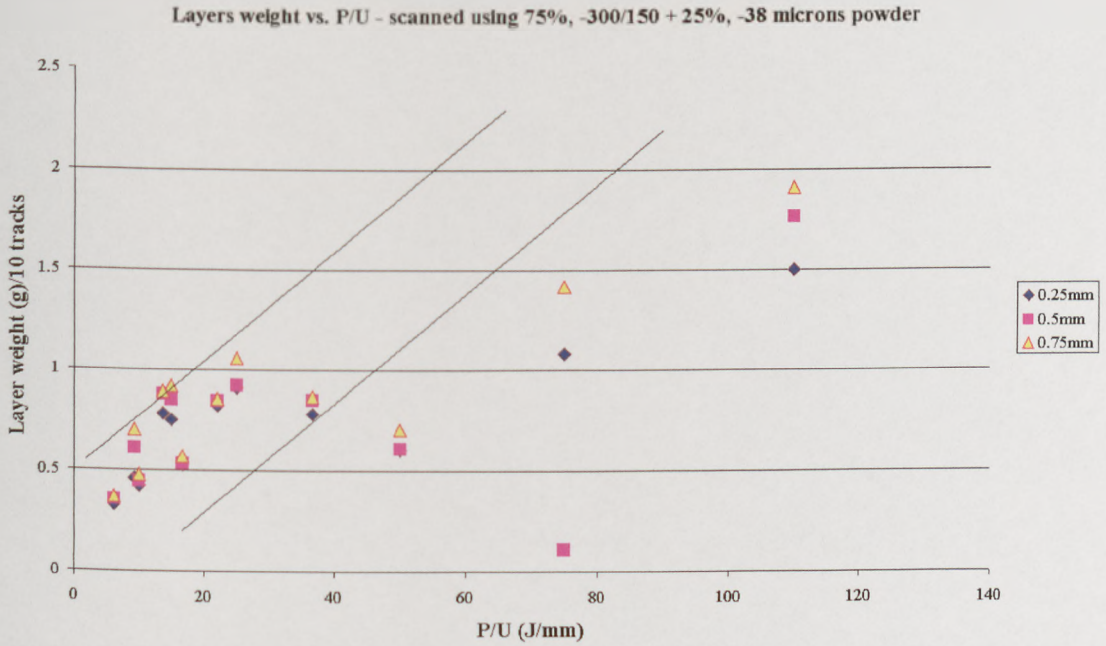

Figure 5.3 Layer weight vs. energy (75%, -300/150μm powder with addition of 25%, -38μm powder)

By comparing figures 5.2 and 5.3 with the data obtained for single tracks using the same batches of powder (see chapter 3, figures 3.27(a) and 3.30(a)) the results are very similar. For a very low energy (<25J/mm) the –300/150μm powder batch shows the same characteristics of full melted area as those for single tracks. Dividing the layer weight of 10 tracks will result in a track weight for any scan spacing on average of 0.05±00.1g. But, if the FLD phenomenon is considered, the real track weight within the layer is 0.04g. Then, the influence of the FLD phenomenon does not have a big influence over the sintered part for low energies (<25J/mm). A similar observation can be made for the mixed powder batch.

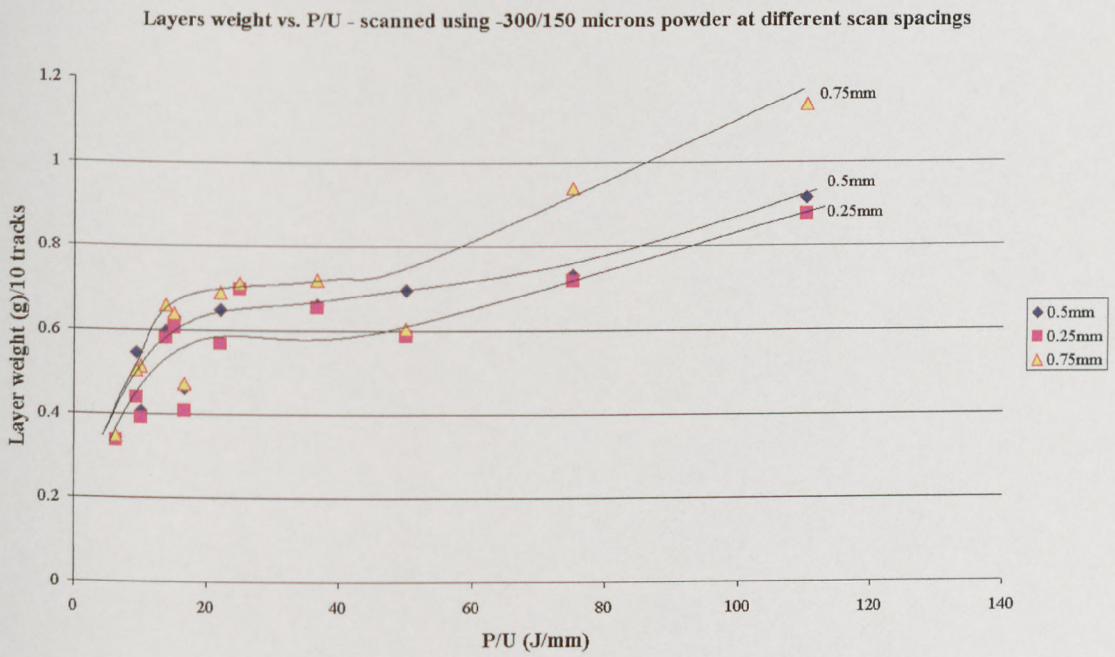

Figure 5.4 Layer weight vs. energy density (-300/150μm powder)

Figure 5.4 and 5.5 show layer weight versus energy. Layers were scanned at different scan spacing. A visible gain in weight was obtained by mixing the powders together. The influence of the scan spacing over the sintering part weight has a big impact. By comparing these two figures, the measured weight for a scan spacing of 0.25mm in the mixed powder case is higher than with a scan spacing of 0.75mm for the unmixed powder. Also, a significant difference in coupon weight for coupons scanned using 0.5mm scan

spacing and 0.75 mm for the –300/150μm powder batch was recorded. In comparison, the mixed powder showed a difference only for a scan spacing below 0.3mm.

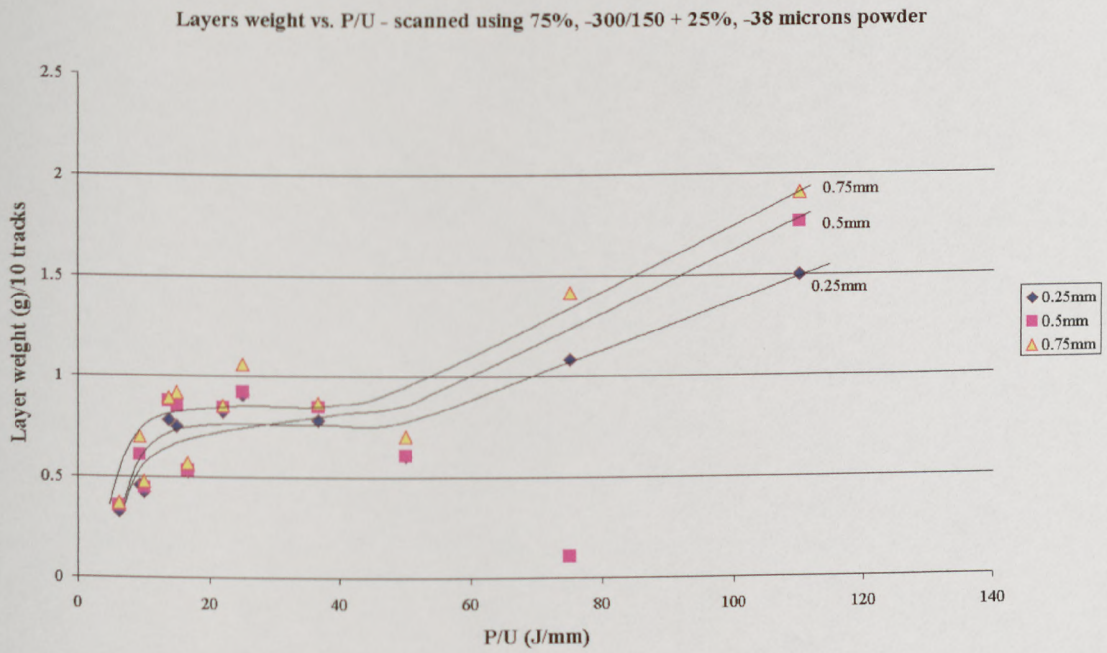

Figure 5.5 Layer weight vs. energy (75%, -300/150μm powder with addition of 25%, -38μm powder)

The density of the layer of melted material (ρ_{layer}) might be estimated from the weight /area /layer depth constants. It was considered that all the tracks within the layer have the same depth. If the layer area is rectangular, A_{layer} = length x width =100 mm^2.

Then, $$\rho_{layer} = weight_{layer} / area_{layer} / layer_{depth} \quad (kg/m^3) \quad (5.10)$$

The estimated layer densities obtained for a laser power of 75W and three scan spacings using the mixed powder are shown in table 5.2. The layer area was considered a constant of 100mm^2.

Laser power(W)	Scan speed (mm/s)	Scan spacing (mm)	ρ layer (kg/m3)
75	1	0.25	9.008
75	1	0.5	9.216
75	1	0.75	11.118
75	3	0.25	6.327
75	3	0.5	6.43
75	3	0.75	7.375
75	5	0.25	7.663
75	5	0.5	8.693
75	5	0.75	9.367
75	8	0.25	5.191
75	8	0.5	6.842
75	8	0.75	7.876

Table5.2 Estimated layer density for mixed powder

The calculated values suggested an increase of the layer density by increasing the scan spacing. The calculated values are estimates only. If the FLD effect and not totally flat surfaces are considered the results would be slightly different. For example, for a layer scanned at 75W laser power, 0.5 mm scan spacing and 5mm/s scan speed, the calculated density taking into account the FLD effect would be:

Layer depth – with first track (FT) – 0.98mm

Layer depth – without first track (WFT) – 0.8mm

Then, $\rho_{layer\ WFT} = 6.5875\ kg/m^3$ compared to $\rho_{layer\ FT} = 8.693\ kg/m^3$. In conclusion, the real value of layer density could only be estimated to an average value of 7.640 kg/m^3. This value corresponds to 99% layer density. This value could drop by a few percent for large layers duo to the existing gaps between additional small layers.

For comparison, the calculated value of –300/150μm layer density, for the same scanning conditions, showed an estimated layer density of $\rho_{layer\ FT} = 7.987\ kg/m^3$ and $\rho_{layer\ WFT} = 6.642\ kg/m^3$. The average value is 7.314 kg/m^3. This value corresponds to 95% layer density.

5.5 Multiple layers

For the trial all four batches of powder tests were used. The layer thickness importance during the tests was proven. A newly designed slot feed mechanism enabled layers to be spread with less then 0.5mm thickness. The layer-warping phenomenon was

diminished by using short (<12mm) raster scanning. A new scanning strategy was developed. By adding small layers (10mm by 10mm) together large areas could be scanned (60mm x 30mm) without layer warping. Taking advantage of the mirror delay and decreasing the overlap down to 0.25mm from 0.5mm between two consecutive long stripes the boundary visible within the long layers was totally eliminated.

During multiple layer scanning tests two characteristics were determined for the second sintered layer: the balling phenomenon and melt and breakage. These are believed to be influenced by the cold previous layer underneath. The cold layer acts in the same way as the FLD phenomenon by absorbing part of the heat from the heat source.

5.6 Conclusion

Powder physical properties were found to have an influence over the sintering process along with process parameters. It was found out that by mixing the powders for 15 minutes the powder density and therefore the powder bed density increases. The influence of powder flow rate proved to be decisive during the spreading tests. It is believed that powder flow affects the shape of track cross-sections. The poorer the flow rate, the deeper is the track trench. In addition, a poor flow rate stops the fresh powder to flow in the sintering area and the existing melted powder is over heated and evaporation occurs. There were observed large gaps into the powder bed along the sintered tracks for those batches of powder with poor flow rate. The tests for powder thermal conductivity showed no important differences between all batches of powder.

A conclusion that can be drawn based on the physical measurement of the tracks is the suggestion that the melt pool diameter (D) is smaller then the laser spot for energies less than 10 J/mm. The smaller size occurs because of high scan speeds and implies a reduced net power absorbed in the powder bed. Moreover, track measurements showed a deeper penetration for 3mm/s scan speed even if the track width value is smaller then at 1mm/s scan speed for example. The microscopy studies suggested a stirring phenomenon takes place for this particular scan speed of 3mm/s. At this moment any plausible explanation could not be presented for this phenomenon. A further investigation as is suggested will be seen in next section (section 5.7).

The next conclusion is based on the absorptivity calculations which showed a low powder absorptivity for big particle size powders (0.35) and a high powder absorptivity for small particle size powders (0.76). An improvement of powder absorptivity was obtained for mixed powders. An insertion of 25% of -38μm powder in the mix with –300/150μm powder showed an improved powder absorptivity rate (0.52). Also, it was determined that the big particle size powders spread better than the small particle size powders. By combining this information it can be said that using a mixed powder the chances of obtaining a good quality layer are higher.

Layer sintering tests showed an improvement of large layer quality by using small layers attached one to another. The warping phenomenon due to thermal gradients that existed was totally eliminated. The tests also showed that a full melted and good quality track does not necessary mean a good quality layer. The area on the sintering maps where good quality layers were obtained proved to be smaller then the full melted area on the track sintering maps. The influence of the FLD phenomenon is considered to be very important. By mixing the powders together and careful control of the sintering parameters the FLD phenomenon was almost eliminated.

In the end, the sintering tests showed that it is possible to sinter large areas and to bond the layers together in a block (10 layers in our case, chapter 4).

5.7 Future work

The aim of RP technologies is to reduce cost and lead time required for the production cycle of different parts. A successful RP technique using direct selective laser sintering of SS powders should take into account several conditions. Besides the influence of processing parameters, the laser type and powder characteristics are a main concern. It was reported (Kruth et al 1999) that an Nd:YAG laser gives better results then the CO_2 laser used in this research. A main bonus from using an Nd:YAG laser is the better penetration of the powder bed and implicitly an increase of the melted pool size. Moreover, the better penetration is a big bonus during multiple layer sintering. These advantages make the Nd:YAG laser at the moment the optimal laser for direct laser sintering of SS powders. Additionally, an improvement of the sintered parts could be obtained, using a CO_2 laser, only by decreasing the laser spot diameter (the actual spot diameter is 1.1mm).

The actual work focused on direct SLS of stainless steel powders and has identified the effects of powder mechanical properties, and determined the optimal parameters for obtaining good quality layers and proved the possibility of building multiple layers.

References

Abe F., Osakada K., "A study of Laser Prototyping for direct manufacturing of dies from metallic powders" Osaka University, 1995

Agarwala M., Bourell D.L., Beaman J.J, Marcus H. and Barlow J., "Direct Selective Laser Sintering of Metals," Rapid Prototyping Journal, Vol. 1 No. 1, pp. 26-36, 1995 a.

Agarwala M. K., Bourell D.L., Benny Wu, and Beaman J.J., "An Evaluation of the Mechanical Behavior of Bronze-NI Composites Produced by Selective Laser Sintering," Proceeding of the Solid Freeform Fabrication Symposium, The University of Texas at Austin, Austin, Texas, pp. 193-203, 1993.

Agarwala M., Bourell D.L., Beaman J.J, Marcus H. and Barlow J., "Post-Processing of Selective Laser Sintered Metal Parts," Rapid Prototyping Journal, Vol. 1 No. 2, pp. 36-44, 1995 b.

Badrinarayan B., and Barlow J. W., "Effect of Processing Parameters in SLS of Metal-Polymer Powders," Proceeding of the Solid Freeform Fabrication Symposium, The University of Texas at Austin, Austin, Texas, pp. 55-63, 1995.

Badrinarayan B., and Barlow J. W., "Metal Parts From Selective Laser Sintering of Metal-Polymer Powders," Proceeding of the Solid Freeform Fabrication Symposium, The University of Texas at Austin, Austin, Texas, pp. 141-146, 1992.

Beaman J. J., Barlow J. W., Bourell D. L., Crawford R. H., Marcus H. L., and McAlea K. P., "Solid Freeform Fabrication: A New Direction in Manufacturing," Kluwer Academic Publishers Group, 1997.

Boivie Klas, "SLS Application of the Fe-Cu-C System for Liquid Phase Sintering," Proceeding of the Solid Freeform Fabrication Symposium, The University of Texas at Austin, Austin, Texas, pp. 141-149, 2000.

Bunnell D. E., Bourell D. L., and Murcus H. L., " Fundamentals of Liquid Phase Sintering Related to Selective Laser Sintering", Proceeding of the Solid Freeform Fabrication Symposium, The University of Texas at Austin, Austin, Texas, pp. 379-385, 1994.

Bunnell D. E., "Fundamentals of SLS of metals", Dissertation, University of Texas at Austin, 1995

Carter William T., and Jones M. G., "Direct Laser Sintering of Metals", Proceeding of the Solid Freeform Fabrication Symposium, The University of Texas at Austin, Austin, Texas, pp. 51-59, 1993.

Childs T. H. C., Ryder G. R., and Berzins M., "Experimental and Theoretical Studies of Selective Laser Sintering," Proceeding of the Solid Freeform Fabrication Symposium, The University of Texas at Austin, Austin, Texas, pp. 132-141, 1997.

Chua C. K., and Leong Kah Fai, "Rapid Prototyping: Principles and Applications in Manufacturing," John Wiley & Sons (Asia) Pte Ltd., Singapore, 1997.

Cubital Homepage: http://www.cubital.com/cubital, 2001.

Dalgarno K. W., "Production Grade Tooling Via Layer Manufacture," Rapid Prototyping Journal, Vol. 7 No.4, pp. 203-206, 2001.

Dalgarno K. W., Stewart T. D., and Childs T. H. C., "Production Tooling for Polymer Components Via the DTM RapidSteel Process," Proceeding of the Solid Freeform Fabrication Symposium, The University of Texas at Austin, Austin, Texas, pp. 559-566, 2000.

Dalgarno K. W., Stewart T. D., "Production Tooling for Polymer Moulding Using the RapidSteel Process," Rapid Prototype Journal, Vol. 7, No, 3, pp. 173-179, 2001.

Das S., Wohlert M., Beaman J.J. and Bourell D.L. "Direct Selective Laser Sintering and Containerless Hot Isostatic Pressing for High Performance Metal Components," Solid Freeform Fabrication Proceedings, The University of Texas, Austin, pp. 81-90, 1997.

Dawidar M. A. D., PhD Thesis, "Direct and indirect selective laser sintering of metals", University of Leeds, 2002

Dawidar M. A. D, Dalgarno K.W., Childs T.H.C, "Direct selective laser sintering of HSS processed using room temperature powder beds", 2002

DTM, Homepage: www.dtm.com , 2002

DTM. 'Guide to Materials: RapidSteel™ 2.0 Used to Produce Rapid Tool LR Mold Inserts' DTM Corporation, DCN: 8002-10001, August, 1998.

DTM. 'SinterStation 2000 System User's Guide: Part and Build Profile Parameter Definitions' DTM Corporation, DCN: 8010-00000-006, March, 1996.

DTM. http://www.dtm-corp.com/products/slssystems/Hi_res/LASERF100High.pdf, 2002.

EOS GmbH, Homepage : www.eos.com, 2002

Eric Radstok, "Rapid Tooling," Rapid Prototyping Journal, Vol. 5 No.4, pp. 164-168, 1999.

Petzoldt F., Greul M., and Loffer H., "Direct Metal Laser Sintering-Different Applications/Different Material Concepts," Advances in Powder Metallurgy & Particulate Materials Vol. 5 pp 71-77, 1999.

Gedda H., "Laser surface cladding, a literature survey" Lulea Tekniska University, 2000

German R. M., "Liquid Phase Sintering," Plenum Press, New York 1985.

German, R. M., "Sintering Theory and Practice," John Wiley & Sons, Inc., 1996.

Gopalakrishna B. Prabhu and Bourell D.L., "Supersolidus Liquid Phase Selective Laser Sintering of Prealloyed Bronze Powder," Proceeding of the Solid Freeform Fabrication Symposium, The University of Texas at Austin, Austin, Texas, pp. 317-324, 1993.

Griffith M. "Process maps for laser deposition of thin-walled structures" Sandia National Laboratories, Proceeding of the Solid Freeform Fabrication Symposium, The University of Texas at Austin, Austin, Texas, 1996.

GSI (General Scanning Inc.) XY Scan Head Series: X-Y Scan Head User Manual. GSI PN 12P-XY, Rev. B, 1991.

A - Hauser C, Childs T. H. C., Dalgarno K. W., and Eane R. B., "Atmospheric Control During Selective Laser Sintering of Stainless Steel 314S Powder," Proceeding of the Solid Freeform Fabrication Symposium, The University of Texas at Austin, Austin, Texas, pp. 265-272, 1999.

B - Hauser C., "Selective Laser Sintering of a Stainless Steel Powder," PhD Thesis, School of Mechanical Engineering, The University of Leeds, UK, 2002.

C - Hauser C., Childs T. H. C., and Dalgarno K. W., "Selective Laser Sintering of Stainless Steel 314S HC Processed Using Room Temperature Powder Beds," Proceeding of the Solid Freeform Fabrication Symposium, The University of Texas at Austin, Austin, Texas, pp. 273-280, 1999.

Helysis, Inc. Homepage: http://helisys.com, 2001.

Karapatis N. P., Guidoux Y., Gygax P. E., and Glardon R., "Thermal Behavior of Parts Made Direct Metal Laser Sintering", Proceeding of the Solid Freeform Fabrication Symposium, The University of Texas at Austin, Austin, Texas, pp. 79-87, 1998.

Karunakaran K. P., Vivekananda Shanmuganathan P., Sanjay J.J., Prashant B., and Ashish P., "Rapid Prototyping of Metallic Parts and Moulds," Journal of Materials Processing Technology, Vol. 105, pp. 371-381, 2000.

Klocke F., and Wirtz H., "Direct of Metal Prototypes and Prototype Tools," Proceeding of the Solid Freeform Fabrication Symposium, The University of Texas at Austin, Austin, Texas, pp. 141-147, 1996.

Klocke F., Celiker T., and Song Y.-A., "Rapid Metal Tooling," Rapid Prototyping Journal, Vol. 1 No. 3, pp. 32-42, 1995.

Kruth J. P., Peeters P., Smolderen T., Bonse J., Laoui T., and Froyen L., "Comparison between CO_2 and Nd:YAG lasers for use with selective laser sintering of Steel- Copper

powders," Photonics applied to Mechanics and Environmental Testing Engineering European, Proceeding of the Workshop on Rapid Prototyping, 24-26 November, 1999.

Kruth J. P., Peeters P., "Smolderen T., Bonse, J., Laoui T., & Froyen L., The Performance of CO_2 and Nd:YAG Lasers in the Selective Laser Sintering of Steel-Copper Powders," Proc. of the 7th Assises Européennes du prototypage Rapide, Paris, pp 15-27, 1998.

Kruth J. P., Van der Schuren B., Bonse J., and Morren B., "Basic Powder Metallurgical Aspects in Selective Metal Powder Sintering", Annals of the CIRP, Vol. 45, No. 1, pp.183-186, 1996.

Longtin J.P., Ogawa K., "Laser-induced surface tension driven flows in liquids" State University of New York and Tokyo Institute of Technology, 1998

Mazumder J., Koch J., Chio J. "Rapid manufacturing by laser aided direct deposition of metals" Centre for Laser Aided Materials Processing, University of Illinois

Marcus H. L., Beaman J. J., Barlow J. W., and Bourell D. L., " Solid Freeform Fabrication: Powder Processing," Ceramic Bulletin Vol. 69, No. 6, pp. 1030-1031, 1990 b.

Metal Powder Industries Federation, "Standard Test Methods for Metal Powders and Powder Metallurgy Products," Metal Powder Industries Federation, 1991.

Morgan R., Sutcliffe C. F., and O'Neill W., "Experimental Investigation of Nanosecond Pulsed Nd:YAG Laser Re-melted Pre-placed Powder Beds," Rapid Prototyping Journal, Vol. 7 No.3, pp. 159-172, 2001.

Nelson C., McAlea K., and Gray D., "Improvement in SLS Part Accuracy," Proceeding of the Solid Freeform Fabrication Symposium, The University of Texas at Austin, Austin, Texas, pp. 159-169, 1995.

Niu H. J., and Chang I. T. H., "Instability of Scan Tracks Selective Laser Sintering of High Speed Steel Powder", Scripta Materialia, Vol. 41, No. 11, pp. 1229-1234, 1999 a.

Niu H. J., and Chang I. T. H., "Liquid Phase Sintering of M3/2 High Speed Steel by Selective Laser Sintering", Scripta Materialia, Vol. 39, No. 1, pp. 67-72, 1998.

Niu H. J., and Chang I. T. H., "Selective Laser Sintering of Gas Atomized M2 High Speed Steel Powder", Journal of Materials Science, Vol. 35, No. 1, pp. 31-38, 2000.

Niu H. J., and Chang I. T. H., "Selective Laser Sintering of Gas and Water Atomized High Speed Steel Powders", Scripta Materialia, Vol. 41, No. 1, pp. 25-30, 1999 b.

Olli Nyrhila, Juha Kotila, Jan-Erik Lind, and Tatu Syvanen, " Industrial Use of Direct Metal Laser Sintering", Proceeding of the Solid Freeform Fabrication Symposium, The University of Texas at Austain, Austin, Texas, pp. 487-493, 1998.

O'Neill W., Sutcliffe C. J., Morgan R., and B Hon K. K., "Investigation of Short Pulse Nd:YAG Laser Interaction with Stainless Steel Powder Beds," Proceeding of the Solid Freeform Fabrication Symposium, The University of Texas at Austain, Austin, Texas, pp. 147-159, 1998.

O'Neill W., Sutcliffe C. J., Morgan R., Landsborough A., and B Hon K. K., "Investigation on Multi-Layer Direct Metal Laser Sintering of 316L Stainless Steel Powder Beds," Annals of the CIRP Vol. 48/1, pp 151-154, 1999.

Orbital, Homepage: www.orbital.com, 2001

Pham D. T., and Dimov S., "Rapid Manufacturing the Technologies and Applications of Rapid Prototyping and Rapid Tooling," Springer-Verlag London Limited, 2001.

Pham D. T., and Gault R. S. " A Comparison of Rapid Prototyping Technologies", International Journal of Machine Tools & Manufacture, Vol. 38, pp. 1257-1287, 1998.

Pham D. T. and Wang X., "Prediction and Reduction of Build Times for the Selective Laser Sintering Process," Proc Instn Mech Engrs Vol. 214 Part B, pp. 425, 2000.

Sachs Emanuel, Samuel Allen, Michael Cima, Edward Wylonis, Honglin Guo, "Production of Injection Molding Tooling with Conformal Cooling Channels using The Three Dimensional Printing Process," Solid Freeform Fabrication Proceedings, pp 448-467, 1995.

Sih, S.S. and Barlow, J. W., "The Measurement of the Thermal Properties and Absorbtances of Powders Near Their Melting Temperatures," Solid Freeform Fabrication Proceedings, The University of Texas, Austin, pp. 131-140, 1992.

Sontea S., "Powder metallurgy", Ed. Universitaria, Romania, 1999

Steen, W. M., "Laser surface treatment. Laser Processing: Surface Treatment and Film Deposition,". Proceedings of the NATO Advanced Study Institute on Laser Processing. Kluwer Academic Press. Netherlands. pp. 1-19, 1996.

Steen, W. M., "Laser material processing," Second Edition. Springer - Verlag, London, 1998.

Stratasys, Inc., "Fast, Precise, Safe Prototypes with FDM", Proceedings of the 1991 Solid Freeform Fabrication Symposium, The University of Texas at Austin, Austin, Texas, August, pp. 115-122, 1991.

Stratasys, Inc., Homepage : www.strarasys.com , 2000.

Suh, Y.S. and Wozny, M.J. 'Adaptive Slicing of Solid Freeform Fabrication Processes' Solid Freeform Fabrication Proceedings, The University of Texas, Austin, Texas, pp. 404-411, 1994.

Taylor C.M., Childs T.H.C, " Thermal experiments in direct metal laser sintering", EURO RP, 10th European Conference on Rapid prototyping and Manufacturing, 2001

Thummler F., and Oberacker R., "An Introduction to Powder Metallurgy," The institute of Materials, 1 Carlton House Terrace London SW1Y 5DB, 1993.

Tobin J. R., Badrinaraya B., Barlow J. W., Beaman J. J., and Bourell D. L., "Indirect Metal Composite Part Manufacture Using the SLS Process," Proceeding of the Solid Freeform Fabrication Symposium, The University of Texas at Austin, Austin, Texas, pp. 303-307, 1993.

Tontowi A.E., Childs T.H.C. and Gopinathan N. "Study of a Powder Bed Structure of Stainless Steel 314-HC for Selective Laser Sintering Application, University of Leeds

Tolochko, N.K., Laoui, T., Khlopkov, Y.V., Mozzharov, S.E., Titov, V.I and Ignatiev, M.B., "Absorbtance of powder materials suitable for laser sintering," Rapid Prototyping Journal, Vol.6, No.3, pp. 155-160, 2000.

Hejmadi U., and McAlea K., "Selective Laser Sintering of Metal Moulds: The RapidTool™ Process," Proceeding of the Solid Freeform Fabrication Symposium, The University of Texas at Austin, Austin, Texas, pp. 97-104, 1996.

Volpato N., "Time-Saving and Accuracy Issues in Rapid Tooling by Selective Laser Sintering". PhD Thesis, School of Mechanical Engineering, The University of Leeds, UK, 2001.

Westin L., "Mechanical Properties of PM High-Speed Steels Related to Heat Treatment and Hardness," M.P.R. pp. 768-773 1989.

Wiedemann B., Jantzen S.K., " Strategies and applications for rapid product and process development in Daimler-Benz AG" Daimler-Benz Research Centre, Germany, 1999

Wilkening, C. 'Fast Production of Technical Prototypes Using Direct Laser Sintering of Metals and Foundry Sand'. Solid Freeform Fabrication Proceedings, The University of Texas, Austin, pp. 133-140, 1996.

Williams John D., and Deckard C. R., "Advances in Modelling the Effects of Selected Parameters on the SLS Process," Rapid Prototyping Journal, Vol. 4 No.2, pp. 90-100, 1998.

Wright C. S., and Ogel B., "Super-solidus Liquid Phase Sintering of High Speed Steels, Part 1: Sintering of Molybdenum Based Alloys", Powder Metallurgy Vol. 36, No.2, pp. 213-217 1993.

Wright C. S., Youseffi M., Wronski A. S., Ansara I., Durand-Charre M., Mascarenhas J., Oliveira M. M., Lemoisson F., and Bienvenu Y., "Super-solidus Liquid Phase Sintering of High Speed Steels, Part 3: Computer Aided Design of Sinterable Alloys", Powder Metallurgy Vol. 42, No.2, pp. 131-146, 1999.

Wohlert, M., Das, S., Beaman, J. J. & Bourell, D. L. "Direct laser fabrication of high performance metal components via SLS/HIP". Proceeding of the Solid Freeform Fabrication Symposium. The University of Texas at Austin. Austin Texas. pp. 281-288, 1999.

Yevko V., Park C. B., Zak G., Coyle T. W., and Benhabib B., "Cladding Formation in Laser-Beam Fusion of Metal Powder," Rapid Prototyping Journal, Vol. 4 No.4, pp. 168-184, 1998.

Zong G., Beaman D.L., Tran Y., " Direct selective laser sintering of high temperatures material" Proc. Solid freeform Fabrication Symposium, University of Texas, Austin, pp. 72-85, 1992.

3D System web page, 3D Systems Inc/ 2002

Web page: www.manufacturingtalk.com/2002

Appendix A

Hall's Flowmeter – (ϕ 2.5 mm)

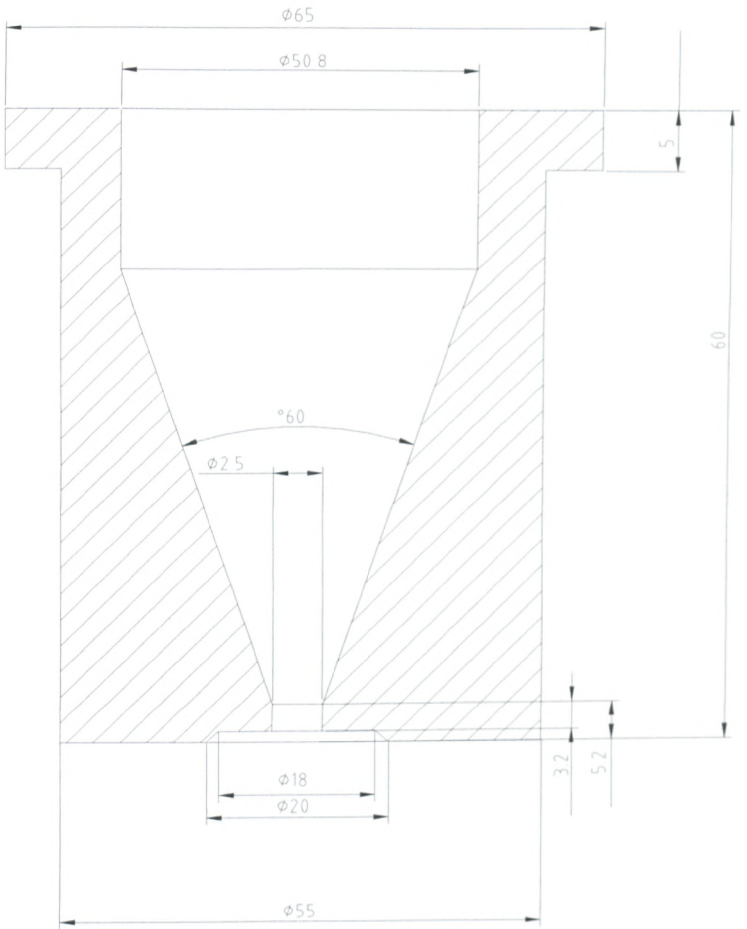

Appendix B - Pascal program used for Slot Feeder Mechanism (SFM)

```
PROGRAM StepperController;    {written by Radu Eane}
uses crt;

VAR
 steps,dly : integer;
 key : char;
 pos : byte;
 dir,hsteps : string[5];

procedure SendSignal;
var count : integer;
begin
count:=steps;
gotoxy(1,23);writeln ('Start to move Motor       ');
port[888]:=$00;
if (hsteps='yes') then
 begin
  if (dir='right') then while (count>0) do begin
   if (pos=8) then begin port[888]:=$09;pos:=9;gotoxy(1,24);writeln('/');end
    else if (pos=9) then begin port[888]:=$01;pos:=1;gotoxy(1,24);writeln('-');end
     else if (pos=1) then begin port[888]:=$03;pos:=3;gotoxy(1,24);writeln('\');end
      else if (pos=3) then begin port[888]:=$02;pos:=2;gotoxy(1,24);writeln('|');end
       else if (pos=2) then begin port[888]:=$06;pos:=6;gotoxy(1,24);writeln('/');end
        else if (pos=6) then begin port[888]:=$04;pos:=4;gotoxy(1,24);writeln('-');end
         else if (pos=4) then begin port[888]:=$0C;pos:=12;gotoxy(1,24);writeln('\');end
          else if (pos=12) then begin port[888]:=$08;pos:=8;gotoxy(1,24);writeln('|');end;
  delay(dly);
  count:=count-1;
  end;
 if (dir='left') then while (count>0) do begin
  if (pos=8) then begin port[888]:=$1C;pos:=12;gotoxy(1,24);writeln('\');end
   else if (pos=12) then begin port[888]:=$04;pos:=4;gotoxy(1,24);writeln('-');end
    else if (pos=4) then begin port[888]:=$06;pos:=6;gotoxy(1,24);writeln('/');end
     else if (pos=6) then begin port[888]:=$02;pos:=2;gotoxy(1,24);writeln('|');end
      else if (pos=2) then begin port[888]:=$03;pos:=3;gotoxy(1,24);writeln('\');end
       else if (pos=3) then begin port[888]:=$01;pos:=1;gotoxy(1,24);writeln('-');end
        else if (pos=1) then begin port[888]:=$09;pos:=9;gotoxy(1,24);writeln('/');end
         else if (pos=9) then begin port[888]:=$08;pos:=8;gotoxy(1,24);writeln('|');end;
   delay(dly);
   count:=count-1;
  end;
 end
else
```

```
begin
 if (dir='right') then while (count>0) do begin
 if (pos=8) then begin port[888]:=$01;pos:=1;gotoxy(1,24);writeln('-');end
  else if (pos=4) then begin port[888]:=$08;pos:=8;gotoxy(1,24);writeln('|');end
      else if (pos=2) then begin port[888]:=$04;pos:=4;gotoxy(1,24);writeln('-');end
          else if (pos=1) then begin port[888]:=$02;pos:=2;gotoxy(1,24);writeln('|');end;
 delay(dly);
 count:=count-1;
 end;
 if (dir='left') then while(count>0) do begin
 if (pos=1) then begin port[888]:=$08;pos:=8;gotoxy(1,24);writeln('|');end
 else if (pos=2) then begin port[888]:=$01;pos:=1;gotoxy(1,24);writeln('-');end
     else if (pos=4) then begin port[888]:=$02;pos:=2;gotoxy(1,24);writeln('|');end
         else if (pos=8) then begin port[888]:=$04;pos:=4;gotoxy(1,24);writeln('-');end;
 delay(dly);
 count:=count-1;
 end;
port[888]:=$00;
end;
gotoxy(1,23);
writeln('Finished              ');
end;

BEGIN
dir:='right';steps:=40;dly:=4000;pos:=1;hsteps:='no';
ClrScr;
writeln ('StepperMotor-Controller 1.0');
writeln ('     written by Radu EANE');
writeln;
writeln ('1  Longer Delay');
writeln ('2  Shorter Delay');
writeln ('3  Change Direction');
writeln ('4  More Steps');
writeln ('5  Less Steps');
writeln ('6  Enable/Disable Half Steps');
writeln ('7  Run Motor');
writeln ('8  Exit');
writeln;
writeln('Please select number ...');
repeat
gotoxy(1,15);
writeln('Direction : ',dir,'   ');
writeln('Steps : ',steps,'    ');
writeln('Half Steps : ',hsteps,'   ');
writeln('Delay : ',dly,' ms      ');
 key:=readkey;
```

```
if (key='4') then begin steps:=steps+1;if steps=32000 then steps:=29999;end;
 if (key='6') then if (hsteps='no') then hsteps:='yes' else begin hsteps:='no';pos:=1;end;
 if (key='5') then begin steps:=steps-1;if steps=0 then steps:=1;end;
 if (key='7') then SendSignal;
 if (key='3') then if (dir='left') then dir:='right' else dir:='left';
 if (key='1') then begin dly:=dly+100;if dly>32000 then dly:=29995;end;
 if (key='2') then begin dly:=dly-100;if dly<1 then dly:=0;end;
until (key='8');

END.
```

Appendix C – Packed powder density, experimental test results

(a) –150/75μm powder with addition of –75/38μm powder

Powder type	Mass (g)	Mass (g)	Mass (g)	Avg. mass (g)	Powder Density Kg/m3	Mixing time (min)
80%,150 + 20%,-75/38	43.9752	44.0125	44.1128	44.0035	4875	15
75%,150 + 25%,-75/38	44.6122	44.0258	44.1132	44.2504	4906	15
60%,150 + 40%,-75/38	43.4521	43.5217	43.413	43.4622	4807	15
40%,150 + 60%,-75/38	43.1128	43.2258	43.4501	43.2627	4782	15
20%,150 + 80%,-75/38	42.1121	42.9917	42.1692	42.4243	4678	15

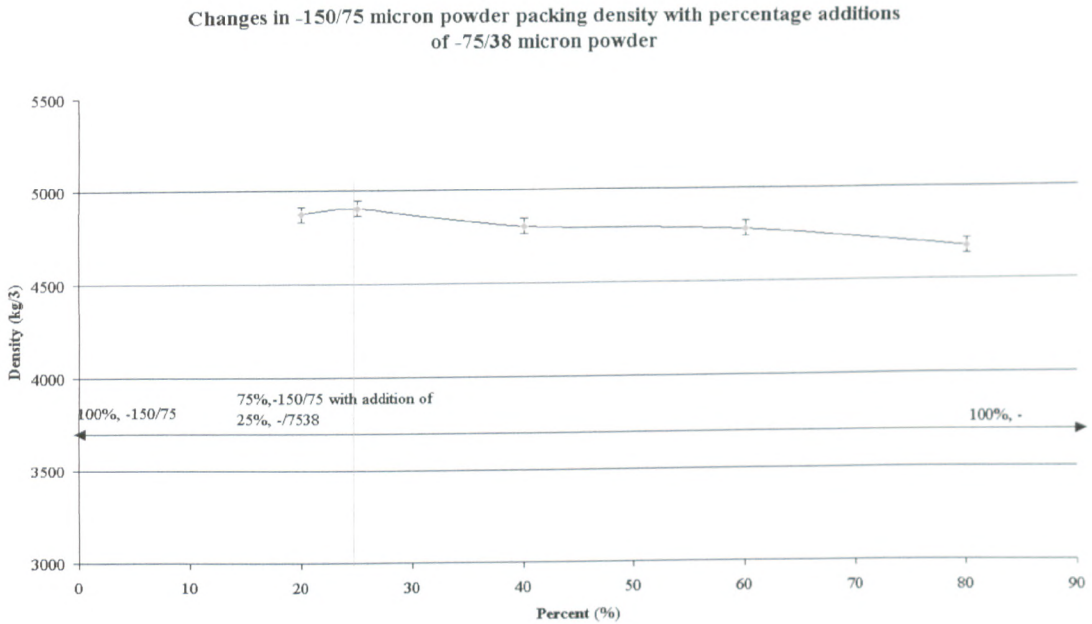

(b) –75/38μm powder with addition of -38μm powder

Powder type	Mass (g)	Mass (g)	Mass (g)	Avg. mass (g)	Powder Density Kg/m3	Mixing time (min)
80%,-75/38 + 20%,38	43.5214	43.258	43.0253	43.2682	4782	15
75%,-75/38 + 25%,38	43.8675	43.6985	43.9587	43.8415	4855	15
60%,-75/38 + 40%,38	42.0028	43.0258	43.1857	42.7381	4717	15
40%,-75/38 + 60%,38	43.3187	43.1089	43.9865	43.4713	4808	15
20%,-75/38 + 80%,38	42.2014	41.987	42.4425	42.2103	4651	15

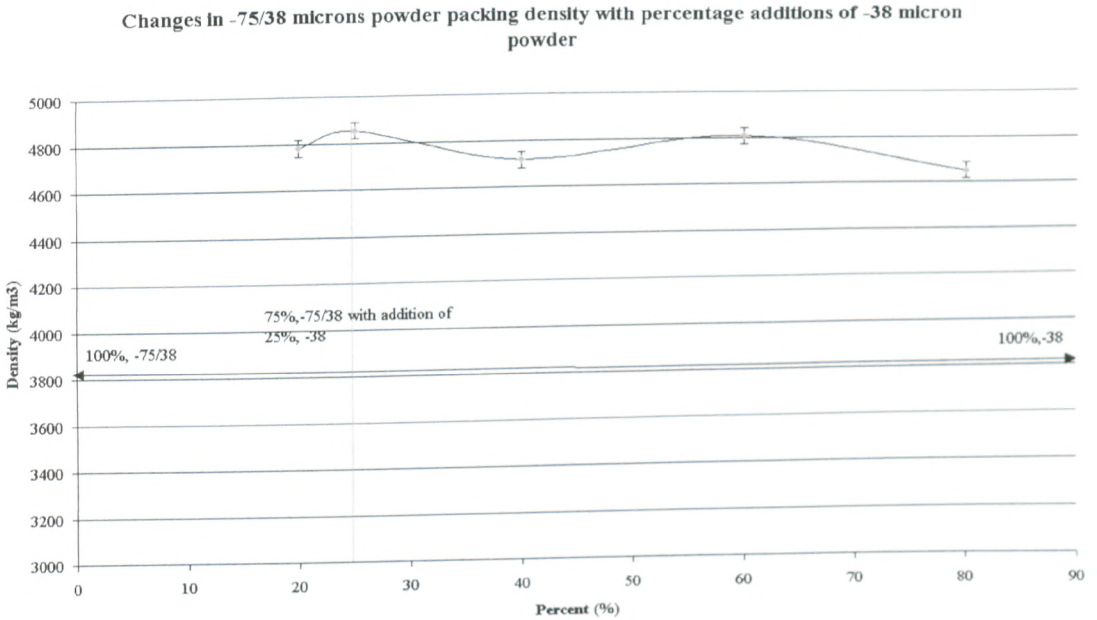

Appendix D – Powder flow rates (grams/ second)

Powder size 1	%1	Powder size 2	%2	Time (s)	Mass (g)	Flow rate (s/g)	Mixing time
38	20	300	80	11	55	5	60
38	40	300	60	23	51	2.21	60
38	60	300	40	Not flow	50	Not flow	60
38	80	300	20	Not flow	48	Not flow	60
150	20	300	80	16	50	3.12	60
150	40	300	60	21	51	2.42	60
150	60	300	40	22	55	2.5	60
150	80	300	20	19	50	2.63	60
75	20	300	80	20	55	2.75	60
75	40	300	60	21	50	2.38	60
75	60	300	40	23	49	2.13	60
75	80	300	20	20	48	2.4	60
38	20	150	80	14	52	3.71	60
38	40	150	60	18	51	2.83	60
38	60	150	40	Not flow	50	Not flow	60
38	80	150	20	Not flow	54	Not flow	60
38	20	75	80	26	52	2	60
38	40	75	60	26	51	1.96	60
38	60	75	40	Not flow	54	Not flow	60
38	80	75	20	Not flow	55	Not flow	60
75	20	150	80	18	52	2.88	60
75	40	150	60	17	51	3	60
75	60	150	40	19	53	2.78	60
75	80	150	20	22	50	2.27	60

Powder size 1	%1	Powder size 2	%2	Time (s)	Mass (g)	Flow rate (s/g)	Mixing time
38	20	300	80	12	48	4	45
38	40	300	60	23	53	2.3	45
38	60	300	40	Not flow	50	Not flow	45
38	80	300	20	Not flow	51	Not flow	45
150	20	300	80	17	55	3.23	45
150	40	300	60	21	48	2.28	45
150	60	300	40	22	52	2.36	45
150	80	300	20	18	50	2.77	45
75	20	300	80	17	51	3	45
75	40	300	60	19	50	2.63	45
75	60	300	40	21	51	2.42	45
75	80	300	20	21	52	2.47	45
38	20	150	80	17	51	3	45
38	40	150	60	20	50	2.5	45
38	60	150	40	Not flow	54	Not flow	45
38	80	150	20	Not flow	50	Not flow	45
38	20	75	80	24	51	2.12	45
38	40	75	60	27	53	1.96	45
38	60	75	40	Not flow	51	Not flow	45
38	80	75	20	Not flow	55	Not flow	45
75	20	150	80	18	52	2.88	45
75	40	150	60	15	51	3.4	45
75	60	150	40	19	50	2.63	45
75	80	150	20	23	55	2.39	45

Powder size 1	%1	Powder size 2	%2	Time (s)	Mass (g)	Flow rate (s/g)	Mixing time
38	20	300	80	11	52	4.72	30
38	40	300	60	20	50	2.5	30
38	60	300	40	Not flow	50	Not flow	30
38	80	300	20	Not flow	51	Not flow	30
150	20	300	80	18	53	2.94	30
150	40	300	60	19	51	2.68	30
150	60	300	40	22	54	2.45	30
150	80	300	20	19	52	2.73	30
75	20	300	80	18	55	3.05	30
75	40	300	60	19	50	2.63	30
75	60	300	40	22	49	2.22	30
75	80	300	20	23	50	2.17	30
38	20	150	80	17	53	3.11	30
38	40	150	60	19	57	3	30
38	60	150	40	Not flow	48	Not flow	30
38	80	150	20	Not flow	51	Not flow	30
38	20	75	80	26	51	1.96	30
38	40	75	60	25	50	2	30
38	60	75	40	Not flow	55	Not flow	30
38	80	75	20	Not flow	54	Not flow	30
75	20	150	80	20	55	2.75	30
75	40	150	60	17	51	3	30
75	60	150	40	19	50	2.63	30
75	80	150	20	23	51	2.21	30

Powder size 1	%1	Powder size 2	%2	Time (s)	Mass (g)	Flow rate (s/g)	Mixing time
38	20	300	80	10	51	5.1	15
38	40	300	60	22	52	2.36	15
38	60	300	40	Not flow	51	Not flow	15
38	80	300	20	Not flow	55	Not flow	15
150	20	300	80	17	54	3.17	15
150	40	300	60	20	56	2.8	15
150	60	300	40	21	56	2.66	15
150	80	300	20	18	55	3.05	15
75	20	300	80	18	52	2.88	15
75	40	300	60	20	55	2.75	15
75	60	300	40	22	52	2.36	15
75	80	300	20	21	53	2.52	15
38	20	150	80	15	51	3.4	15
38	40	150	60	18	50	2.77	15
38	60	150	40	Not flow	52	Not flow	15
38	80	150	20	Not flow	55	Not flow	15
38	20	75	80	25	55	2.2	15
38	40	75	60	25	53	2.12	15
38	60	75	40	Not flow	51	Not flow	15
38	80	75	20	Not flow	50	Not flow	15
75	20	150	80	19	49	2.57	15
75	40	150	60	16	54	3.375	15
75	60	150	40	20	52	2.6	15
75	80	150	20	24	51	2.12	15

Appendix E – Thermal conductivity recorded data

-150+75 batch powder heated at 150 C degrees (steady state)

15620	42.38	41.19	45.57	63.9	69.23	112.4	117.32	4.92	5.33	4.38
15650	36.58	41.19	45.69	64.14	69.23	112.4	117.32	4.92	5.09	4.5
15680	35.87	41.08	45.69	64.14	69.23	112.28	117.32	5.04	5.09	4.61
15710	37.64	41.19	45.69	64.14	69.23	112.28	117.44	5.16	5.09	4.5
15740	35.99	41.08	45.69	64.02	69.11	112.28	117.44	5.16	5.09	4.61
15770	44.03	41.19	45.69	64.14	69.11	112.28	117.44	5.16	4.97	4.5
15800	36.58	41.08	45.69	64.02	69.11	112.28	117.44	5.16	5.09	4.61
15830	36.1	41.31	45.69	64.02	69.11	112.4	117.32	4.92	5.09	4.38
15860	37.88	41.19	45.69	64.02	69.11	112.28	117.32	5.04	5.09	4.5
15890	36.1	41.43	45.69	64.02	69.11	112.52	117.32	4.8	5.09	4.26
15920	41.9	41.43	45.69	64.02	69.11	112.52	117.32	4.8	5.09	4.26
15950	36.46	41.43	45.69	64.02	69.35	112.4	117.32	4.92	5.33	4.26
15980	36.1	41.31	45.69	64.02	69.47	112.4	117.32	4.92	5.45	4.38
15010	37.64	41.43	45.69	64.02	69.35	112.4	117.32	4.92	5.33	4.26
15040	36.22	41.31	45.81	64.14	69.47	112.28	117.32	5.04	5.33	4.5
15070	42.02	41.31	45.69	64.02	69.47	112.4	117.32	4.92	5.45	4.38
15100	36.34	41.31	45.92	64.38	69.35	112.28	117.32	5.04	4.97	4.61
15130	35.99	41.31	45.92	64.38	69.35	112.28	117.44	5.16	4.97	4.61
15160	37.17	41.43	45.92	64.38	69.35	112.28	117.32	5.04	4.97	4.49
15190	36.1	41.43	45.92	64.26	69.35	112.28	117.32	5.04	5.09	4.49
15220	40.37	41.43	45.92	64.49	69.35	112.28	117.32	5.04	4.86	4.49
15250	36.46	41.43	45.92	64.38	69.35	112.28	117.32	5.04	4.97	4.49
15280	36.22	41.43	45.92	64.14	69.23	112.28	117.32	5.04	5.09	4.49
15310	36.93	41.31	45.92	64.26	69.35	112.16	117.44	5.28	5.09	4.61
15340	36.34	41.55	45.81	64.26	69.35	112.4	117.32	4.92	5.09	4.26
15370	39.54	41.43	45.92	64.26	69.23	112.28	117.32	5.04	4.97	4.49
15400	36.58	41.67	45.81	64.14	69.35	112.4	117.2	4.8	5.21	4.14
	R7	**R6**	**R5**	**R4**	**R3**	**R2**	**R1**	**Δ12**	**Δ34**	**Δ56**

-300+150 batch powder heated at 150 C degrees (steady state)

14830	33.5	40.72	44.39	62.48	66.98	116.12	111.32	4.8	4.5	3.67
14860	35.87	40.84	44.15	62.13	67.1	116.12	111.32	4.8	4.97	3.31
14890	33.85	40.84	44.39	62.48	67.1	116.12	111.32	4.8	4.62	3.55
14920	33.5	40.84	44.39	62.6	67.1	116.12	111.32	4.8	4.5	3.55
14950	34.8	40.84	44.39	62.36	67.1	116.12	111.44	4.68	4.74	3.55
14980	33.74	40.84	44.39	62.6	67.1	116.12	111.32	4.8	4.5	3.55
15010	37.64	40.96	44.39	62.48	67.22	116.12	111.44	4.68	4.74	3.43
15040	34.09	40.96	44.5	62.72	67.22	116.12	111.44	4.68	4.5	3.54
15070	33.62	40.96	44.5	62.6	67.22	116.24	111.32	4.92	4.62	3.54
15100	35.51	40.96	44.5	62.72	67.22	116.24	111.44	4.8	4.5	3.54
15130	33.85	40.96	44.5	62.72	67.22	116.24	111.44	4.8	4.5	3.54
15160	43.32	41.08	44.5	62.6	67.34	116.12	111.44	4.68	4.74	3.42
15190	34.45	40.96	44.62	62.72	67.22	116.24	111.44	4.8	4.5	3.66
15220	33.85	40.96	44.5	62.6	67.22	116.36	111.44	4.92	4.62	3.54
15250	36.58	41.08	44.62	62.72	67.34	116.36	111.56	4.8	4.62	3.54
15280	34.09	41.08	44.62	62.72	67.34	116.24	111.56	4.68	4.62	3.54
15310	34.09	41.19	44.62	62.6	67.34	116.36	111.8	4.56	4.74	3.43
15340	34.92	41.08	44.62	62.72	67.34	116.24	111.68	4.56	4.62	3.54
15370	34.21	41.31	44.62	62.6	67.34	116.24	111.8	4.44	4.74	3.31
15400	41.43	41.19	44.62	62.72	67.34	116.24	111.68	4.56	4.62	3.43
15430	34.57	41.43	44.62	62.72	67.34	116.24	111.92	4.32	4.62	3.19
15460	34.09	41.31	44.74	62.72	67.46	116.12	111.8	4.32	4.74	3.43
15490	36.22	41.43	44.74	62.72	67.34	116.24	111.8	4.44	4.62	3.31
15520	34.21	41.43	44.74	62.72	67.46	116.24	111.8	4.44	4.74	3.31
15550	34.09	41.43	44.74	62.72	67.69	116.24	111.8	4.44	4.97	3.31
15580	34.8	41.43	44.86	62.72	67.46	116.24	111.92	4.32	4.74	3.43
15610	34.21	41.55	44.86	62.84	67.69	116.24	111.92	4.32	4.85	3.31
15640	39.54	41.55	44.86	62.84	67.57	116.24	111.92	4.32	4.73	3.31
15670	34.57	41.55	44.86	62.84	67.69	116.24	111.8	4.44	4.85	3.31
15700	34.21	41.55	44.98	62.96	67.81	116.24	111.8	4.44	4.85	3.43
	R7	**R6**	**R5**	**R4**	**R3**	**R2**	**R1**	**Δ12**	**Δ34**	**Δ56**

-75+38 batch powder heated at 150 C degrees (steady state)

14910	31.72	34.09	36.82	49.71	52.78	82.53	85.98	3.45	3.07	2.73
14940	30.3	34.09	36.7	49.59	52.78	82.65	85.86	3.21	3.19	2.61
14970	36.82	34.09	36.7	49.71	52.78	82.65	85.86	3.21	3.07	2.61
15000	30.77	34.21	36.82	49.71	52.66	82.65	85.86	3.21	2.95	2.61
15030	30.3	34.33	36.82	49.71	52.66	82.89	85.86	2.97	2.95	2.49
15060	33.26	34.21	36.82	49.71	52.78	82.77	85.98	3.21	3.07	2.61
15090	30.42	34.33	36.82	49.71	52.78	82.89	85.86	2.97	3.07	2.49
15120	30.3	34.45	36.82	49.83	53.02	82.89	85.98	3.09	3.19	2.37
15150	31.96	34.33	36.82	49.71	52.9	83.01	85.98	2.97	3.19	2.49
15180	30.3	34.33	36.93	49.94	53.14	82.77	85.98	3.21	3.2	2.6
15210	39.42	34.33	36.93	49.83	53.14	82.89	85.98	3.09	3.31	2.6
15240	30.77	34.33	37.05	50.06	53.02	82.77	85.98	3.21	2.96	2.72
15270	30.18	34.21	36.93	50.06	52.9	82.77	85.98	3.21	2.84	2.72
15300	33.62	34.21	36.93	50.06	53.02	82.65	86.1	3.45	2.96	2.72
15330	30.42	34.33	36.93	49.94	52.9	82.77	86.1	3.33	2.96	2.6
15360	30.3	34.33	36.93	49.94	52.9	82.77	85.98	3.21	2.96	2.6
15390	31.72	34.33	36.93	49.83	52.9	82.77	86.1	3.33	3.07	2.6
15420	30.42	34.57	36.93	49.83	52.9	83.01	85.98	2.97	3.07	2.36
15450	36.58	34.33	36.93	49.83	52.9	82.77	85.98	3.21	3.07	2.6
15480	30.89	34.57	36.93	49.83	52.9	83.01	85.98	2.97	3.07	2.36
15510	30.3	34.45	36.93	49.94	53.14	82.89	85.98	3.09	3.2	2.48
15540	33.5	34.57	36.93	49.83	53.14	82.89	85.98	3.09	3.31	2.36
15570	30.42	34.45	37.05	50.06	53.14	82.77	85.98	3.21	3.08	2.6
15600	30.18	34.45	37.05	50.06	53.14	82.77	86.1	3.33	3.08	2.6
15630	31.25	34.45	37.17	50.18	53.14	82.77	85.98	3.21	2.96	2.72
15660	30.42	34.33	37.05	50.18	53.02	82.77	86.1	3.33	2.84	2.72
15690	37.41	34.45	37.17	50.18	53.14	82.77	86.1	3.33	2.96	2.72
15720	30.89	34.45	37.17	50.06	53.14	82.77	86.1	3.33	3.08	2.72
15750	30.54	34.57	37.05	49.94	53.14	82.89	85.98	3.09	3.2	2.48
15780	33.26	34.45	37.17	50.06	53.14	82.77	85.98	3.21	3.08	2.72
15810	30.77	34.8	37.05	50.06	53.14	83.01	86.1	3.09	3.08	2.25
15840	30.42	34.68	37.17	50.06	53.37	83.01	85.98	2.97	3.31	2.49
15870	31.72	34.8	37.17	50.06	53.14	83.12	86.1	2.98	3.08	2.37
	R7	**R6**	**R5**	**R4**	**R3**	**R2**	**R1**	**Δ12**	**Δ34**	**Δ56**

-38 batch powder heated at 150 C degrees (steady state)

14980	40.48	37.41	40.48	57.99	61.89	103.05	107.24	4.19	3.9	3.07
15010	34.21	37.29	40.48	57.87	61.89	103.17	107.24	4.07	4.02	3.19
15040	33.5	37.29	40.72	57.75	61.89	103.29	107.24	3.95	4.14	3.43
15070	37.05	37.29	40.6	57.87	62.01	103.29	107.12	3.83	4.14	3.31
15100	33.74	37.29	40.48	57.99	61.89	103.17	107.24	4.07	3.9	3.19
15130	33.5	37.29	40.72	57.75	61.77	103.29	107.12	3.83	4.02	3.43
15160	35.04	37.29	40.72	57.75	62.01	103.29	107.12	3.83	4.26	3.43
15190	33.5	37.41	40.6	58.1	62.01	103.05	107.24	4.19	3.91	3.19
15220	43.56	37.41	40.48	58.1	62.01	103.05	107.24	4.19	3.91	3.07
15250	34.21	37.29	40.72	57.87	61.89	103.29	107.24	3.95	4.02	3.43
15280	33.62	37.41	40.6	57.87	62.13	103.29	107.24	3.95	4.26	3.19
15310	36.46	37.41	40.6	57.99	62.13	103.17	107.24	4.07	4.14	3.19
15340	33.62	37.41	40.6	58.1	62.01	103.17	107.24	4.07	3.91	3.19
15370	33.62	37.41	40.72	57.87	61.89	103.29	107.24	3.95	4.02	3.31
15400	35.39	37.41	40.72	57.87	62.01	103.29	107.24	3.95	4.14	3.31
15430	33.5	37.53	40.6	58.22	62.13	103.05	107.24	4.19	3.91	3.07
15460	42.85	37.53	40.6	58.22	62.13	103.17	107.24	4.07	3.91	3.07
15490	34.21	37.41	40.6	57.99	62.01	103.17	107.24	4.07	4.02	3.19
15520	33.5	37.41	40.72	57.87	62.25	103.29	107.12	3.83	4.38	3.31
15550	36.58	37.41	40.72	57.99	62.13	103.29	107.24	3.95	4.14	3.31
15580	33.74	37.53	40.6	58.1	62.01	103.17	107.24	4.07	3.91	3.07
15610	33.62	37.41	40.72	57.99	62.01	103.41	107.24	3.83	4.02	3.31
15640	34.92	37.41	40.84	57.99	62.13	103.41	107.24	3.83	4.14	3.43
15670	33.62	37.53	40.72	58.22	62.13	103.17	107.24	4.07	3.91	3.19
	R7	**R6**	**R5**	**R4**	**R3**	**R2**	**R1**	**Δ12**	**Δ34**	**Δ56**

Appendix E – Thermal conductivity

Temperature difference within the reference disk for –38 microns powder and temperature vs. time for -38μm powder heated at 150^0C

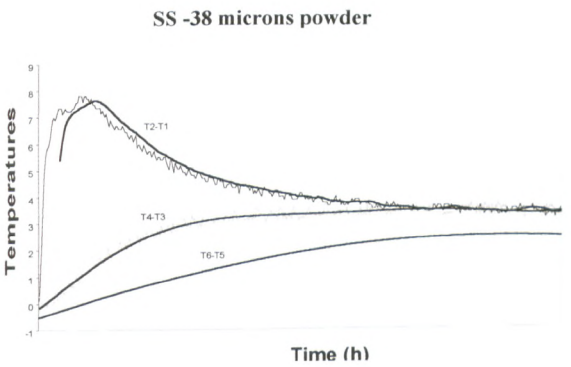

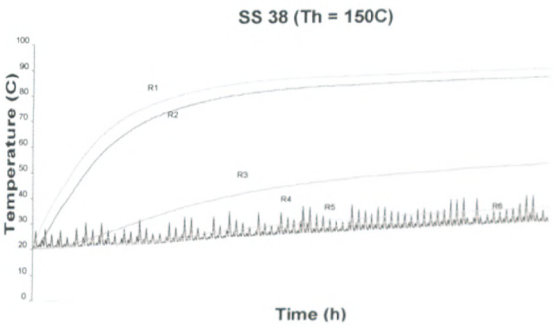

Temperature difference within the reference disk for –75+38 microns powder and temperature vs. time for –75+38μm powder heated at 150^0C

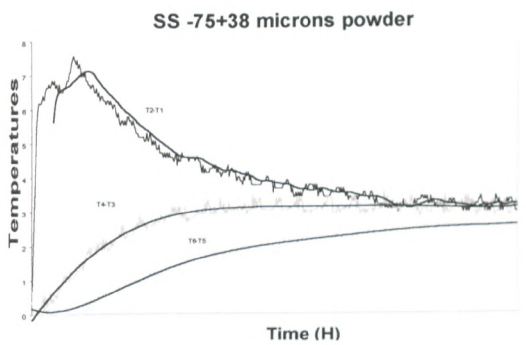

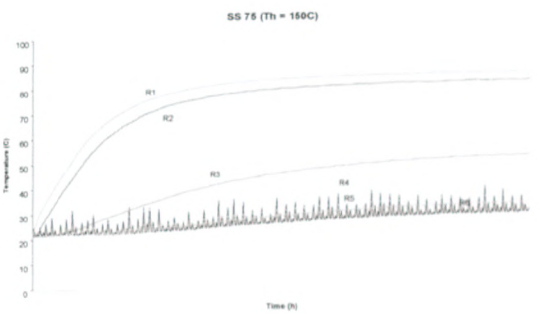

Appendix F – Test serial numbers for all sintering experimental tests

Test serial numbers	Powder size	Type of sintering	Laser power range (W)	Scan speed range (mm/s)
Series 1.1	-300/150	Track	25w	1
1.2	-300/150	Track	25w	3
1.3	-300/150	Track	25w	5
1.4	-300/150	Track	25w	8
1.5	-300/150	Track	25w	10
1.6	-300/150	Track	25w	13
1.7	-300/150	Track	25w	15
1.8	-300/150	Track	25w	17
Series 2.1	-300/150	Track	50w	1
2.2	-300/150	Track	50w	3
2.3	-300/150	Track	50w	5
2.4	-300/150	Track	50w	8
2.5	-300/150	Track	50w	10
2.6	-300/150	Track	50w	13
2.7	-300/150	Track	50w	15
2.8	-300/150	Track	50w	17
Series 3.1	-300/150	Track	75w	1
3.2	-300/150	Track	75w	3
3.3	-300/150	Track	75w	5
3.4	-300/150	Track	75w	8
3.5	-300/150	Track	75w	10
3.6	-300/150	Track	75w	13
3.7	-300/150	Track	75w	15
3.8	-300/150	Track	75w	17
Series 4.1	-300/150	Track	110w	1
4.2	-300/150	Track	110w	3
4.3	-300/150	Track	110w	5
4.4	-300/150	Track	110w	8
4.5	-300/150	Track	110w	10
4.6	-300/150	Track	110w	13
4.7	-300/150	Track	110w	15
4.8	-300/150	Track	110w	17
Series 5.1	-300/150	Track	170w	1
5.2	-300/150	Track	170w	3
5.3	-300/150	Track	170w	5
5.4	-300/150	Track	170w	8
5.5	-300/150	Track	170w	10
5.6	-300/150	Track	170w	13
5.7	-300/150	Track	170w	15
5.8	-300/150	Track	170w	17

Test serial numbers	Powder size	Type of sintering	Laser power range (W)	Scan speed range (mm/s)
Series 6.1	-38	Track	25w	1
6.2	-38	Track	25w	3
6.3	-38	Track	25w	5
6.4	-38	Track	25w	8
6.5	-38	Track	25w	10
6.6	-38	Track	25w	13
6.7	-38	Track	25w	15
6.8	-38	Track	25w	17
Series 7.1	-38	Track	50w	1
7.2	-38	Track	50w	3
7.3	-38	Track	50w	5
7.4	-38	Track	50w	8
7.5	-38	Track	50w	10
7.6	-38	Track	50w	13
7.7	-38	Track	50w	15
7.8	-38	Track	50w	17
Series 8.1	-38	Track	75w	1
8.2	-38	Track	75w	3
8.3	-38	Track	75w	5
8.4	-38	Track	75w	8
8.5	-38	Track	75w	10
8.6	-38	Track	75w	13
8.7	-38	Track	75w	15
8.8	-38	Track	75w	17
Series 9.1	-38	Track	110w	1
9.2	-38	Track	110w	3
9.3	-38	Track	110w	5
9.4	-38	Track	110w	8
9.5	-38	Track	110w	10
9.6	-38	Track	110w	13
9.7	-38	Track	110w	15
9.8	-38	Track	110w	17
Series 10.1	-38	Track	170w	1
10.2	-38	Track	170w	3
10.3	-38	Track	170w	5
10.4	-38	Track	170w	8
10.5	-38	Track	170w	10
10.6	-38	Track	170w	13
10.7	-38	Track	170w	15
10.8	-38	Track	170w	17

Test serial numbers	Powder size	Type of sintering	Laser power range (W)	Scan speed range (mm/s)
Series 11.1	-150/75	Track	25w	1
11.2	-150/75	Track	25w	3
11.3	-150/75	Track	25w	5
11.4	-150/75	Track	25w	8
11.5	-150/75	Track	25w	10
11.6	-150/75	Track	25w	13
11.7	-150/75	Track	25w	15
11.8	-150/75	Track	25w	17
Series 12.1	-150/75	Track	50w	1
12.2	-150/75	Track	50w	3
12.3	-150/75	Track	50w	5
12.4	-150/75	Track	50w	8
12.5	-150/75	Track	50w	10
12.6	-150/75	Track	50w	13
12.7	-150/75	Track	50w	15
12.8	-150/75	Track	50w	17
Series 13.1	-150/75	Track	75w	1
13.2	-150/75	Track	75w	3
13.3	-150/75	Track	75w	5
13.4	-150/75	Track	75w	8
13.5	-150/75	Track	75w	10
13.6	-150/75	Track	75w	13
13.7	-150/75	Track	75w	15
13.8	-150/75	Track	75w	17
Series 14.1	-150/75	Track	110w	1
14.2	-150/75	Track	110w	3
14.3	-150/75	Track	110w	5
14.4	-150/75	Track	110w	8
14.5	-150/75	Track	110w	10
14.6	-150/75	Track	110w	13
14.7	-150/75	Track	110w	15
14.8	-150/75	Track	110w	17
Series 15.1	-150/75	Track	170w	1
15.2	-150/75	Track	170w	3
15.3	-150/75	Track	170w	5
15.4	-150/75	Track	170w	8
15.5	-150/75	Track	170w	10
15.6	-150/75	Track	170w	13
15.7	-150/75	Track	170w	15
15.8	-150/75	Track	170w	17

Test serial numbers	Powder size	Type of sintering	Laser power range (W)	Scan speed range (mm/s)
Series 16.1	-75/38	Track	25w	1
16.2	-75/38	Track	25w	3
16.3	-75/38	Track	25w	5
16.4	-75/38	Track	25w	8
16.5	-75/38	Track	25w	10
16.6	-75/38	Track	25w	13
16.7	-75/38	Track	25w	15
16.8	-75/38	Track	25w	17
Series 17.1	-75/38	Track	50w	1
17.2	-75/38	Track	50w	3
17.3	-75/38	Track	50w	5
17.4	-75/38	Track	50w	8
17.5	-75/38	Track	50w	10
17.6	-75/38	Track	50w	13
17.7	-75/38	Track	50w	15
17.8	-75/38	Track	50w	17
Series 18.1	-75/38	Track	75w	1
18.2	-75/38	Track	75w	3
18.3	-75/38	Track	75w	5
18.4	-75/38	Track	75w	8
18.5	-75/38	Track	75w	10
18.6	-75/38	Track	75w	13
18.7	-75/38	Track	75w	15
18.8	-75/38	Track	75w	17
Series 19.1	-75/38	Track	110w	1
19.2	-75/38	Track	110w	3
19.3	-75/38	Track	110w	5
19.4	-75/38	Track	110w	8
19.5	-75/38	Track	110w	10
19.6	-75/38	Track	110w	13
19.7	-75/38	Track	110w	15
19.8	-75/38	Track	110w	17
Series 20.1	-75/38	Track	170w	1
20.2	-75/38	Track	170w	3
20.3	-75/38	Track	170w	5
20.4	-75/38	Track	170w	8
20.5	-75/38	Track	170w	10
20.6	-75/38	Track	170w	13
20.7	-75/38	Track	170w	15
20.8	-75/38	Track	170w	17

Test serial numbers	Powder size	Type of sintering	Laser power range (W)	Scan speed range (mm/s)
Series 21.1	-300 + -38	Track	25w	1
21.2	-300 + -38	Track	25w	3
21.3	-300 + -38	Track	25w	5
21.4	-300 + -38	Track	25w	8
21.5	-300+ -38	Track	25w	10
21.6	-300 + -38	Track	25w	13
21.7	-300 + -38	Track	25w	15
21.8	-300 + -38	Track	25w	17
Series 22.1	-300 + -38	Track	50w	1
22.2	-300 + -38	Track	50w	3
22.3	-300 + -38	Track	50w	5
22.4	-300 + -38	Track	50w	8
22.5	-300+ -38	Track	50w	10
22.6	-300 + -38	Track	50w	13
22.7	-300 + -38	Track	50w	15
22.8	-300 + -38	Track	50w	17
Series 23.1	-300 + -38	Track	75w	1
23.2	-300 + -38	Track	75w	3
23.3	-300 + -38	Track	75w	5
23.4	-300 + -38	Track	75w	8
23.5	-300+ -38	Track	75w	10
23.6	-300 + -38	Track	75w	13
23.7	-300 + -38	Track	75w	15
23.8	-300 + -38	Track	75w	17
Series 24.1	-300 + -38	Track	110w	1
24.2	-300 + -38	Track	110w	3
24.3	-300 + -38	Track	110w	5
24.4	-300 + -38	Track	110w	8
24.5	-300+ -38	Track	110w	10
24.6	-300 + -38	Track	110w	13
24.7	-300 + -38	Track	110w	15
24.8	-300 + -38	Track	110w	17
Series 25.1	-300 + -38	Track	170w	1
25.2	-300 + -38	Track	170w	3
25.3	-300 + -38	Track	170w	5
25.4	-300 + -38	Track	170w	8
25.5	-300+ -38	Track	170w	10
25.6	-300 + -38	Track	170w	13
25.7	-300 + -38	Track	170w	15
25.8	-300 + -38	Track	170w	17

Test serial numbers	Powder size	Type of sintering	Laser power range (W)	Scan speed range (mm/s)
Series 26.1	-150 + -38	Track	25w	1
26.2	-150 + -38	Track	25w	3
26.3	-150 + -38	Track	25w	5
26.4	-150 + -38	Track	25w	8
26.5	-150+ -38	Track	25w	10
26.6	-150 + -38	Track	25w	13
26.7	-150 + -38	Track	25w	15
26.8	-150 + -38	Track	25w	17
Series 27.1	-150 + -38	Track	50w	1
27.2	-150 + -38	Track	50w	3
27.3	-150 + -38	Track	50w	5
27.4	-150 + -38	Track	50w	8
27.5	-150+ -38	Track	50w	10
27.6	-150 + -38	Track	50w	13
27.7	-150 + -38	Track	50w	15
27.8	-150 + -38	Track	50w	17
Series 28.1	-150 + -38	Track	75w	1
28.2	-150 + -38	Track	75w	3
28.3	-150 + -38	Track	75w	5
28.4	-150 + -38	Track	75w	8
28.5	-150+ -38	Track	75w	10
28.6	-150 + -38	Track	75w	13
28.7	-150 + -38	Track	75w	15
28.8	-150 + -38	Track	75w	17
Series 29.1	-150 + -38	Track	110w	1
29.2	-150 + -38	Track	110w	3
29.3	-150 + -38	Track	110w	5
29.4	-150 + -38	Track	110w	8
29.5	-150+ -38	Track	110w	10
29.6	-150 + -38	Track	110w	13
29.7	-150 + -38	Track	110w	15
29.8	-150 + -38	Track	110w	17
Series 30.1	-150 + -38	Track	170w	1
30.2	-150 + -38	Track	170w	3
30.3	-150 + -38	Track	170w	5
30.4	-150 + -38	Track	170w	8
30.5	-150+ -38	Track	170w	10
30.6	-150 + -38	Track	170w	13
30.7	-150 + -38	Track	170w	15
30.8	-150 + -38	Track	170w	17

Test serial numbers	Powder size	Type of sintering	Laser power range (W)	Scan speed range (mm/s)
Series 31.1	300	Layer	25w	1
31.2	300	Layer	25w	3
31.3	300	Layer	25w	5
31.4	300	Layer	25w	8
31.5	300	Layer	25w	10
31.6	300	Layer	25w	13
31.7	300	Layer	25w	15
31.8	300	Layer	25w	17
Series 32.1	300	Layer	50w	1
32.2	300	Layer	50w	3
32.3	300	Layer	50w	5
32.4	300	Layer	50w	8
32.5	300	Layer	50w	10
32.6	300	Layer	50w	13
32.7	300	Layer	50w	15
32.8	300	Layer	50w	17
Series 33.1	300	Layer	75w	1
33.2	300	Layer	75w	3
33.3	300	Layer	75w	5
33.4	300	Layer	75w	8
33.5	300	Layer	75w	10
33.6	300	Layer	75w	13
33.7	300	Layer	75w	15
33.8	300	Layer	75w	17
Series 34.1	300	Layer	110w	1
34.2	300	Layer	110w	3
34.3	300	Layer	110w	5
34.4	300	Layer	110w	8
34.5	300	Layer	110w	10
34.6	300	Layer	110w	13
34.7	300	Layer	110w	15
34.8	300	Layer	110w	17
Series 35.1	300	Layer	130w	1
35.2	300	Layer	130w	3
35.3	300	Layer	130w	5
35.4	300	Layer	130w	8
35.5	300	Layer	130w	10
35.6	300	Layer	130w	13
35.7	300	Layer	130w	15
35.8	300	Layer	130w	17

Test serial numbers	Powder size	Type of sintering	Laser power range (W)	Scan speed range (mm/s)
Series 36.1	150	Layer	25w	1
36.2	150	Layer	25w	3
36.3	150	Layer	25w	5
36.4	150	Layer	25w	8
36.5	150	Layer	25w	10
36.6	150	Layer	25w	13
36.7	150	Layer	25w	15
36.8	150	Layer	25w	17
Series 37.1	150	Layer	50w	1
37.2	150	Layer	50w	3
37.3	150	Layer	50w	5
37.4	150	Layer	50w	8
37.5	150	Layer	50w	10
37.6	150	Layer	50w	13
37.7	150	Layer	50w	15
37.8	150	Layer	50w	17
Series 38.1	150	Layer	75w	1
38.2	150	Layer	75w	3
38.3	150	Layer	75w	5
38.4	150	Layer	75w	8
38.5	150	Layer	75w	10
38.6	150	Layer	75w	13
38.7	150	Layer	75w	15
38.8	150	Layer	75w	17
Series 39.1	150	Layer	110w	1
39.2	150	Layer	110w	3
39.3	150	Layer	110w	5
39.4	150	Layer	110w	8
39.5	150	Layer	110w	10
39.6	150	Layer	110w	13
39.7	150	Layer	110w	15
39.8	150	Layer	110w	17
Series 40.1	150	Layer	130w	1
40.2	150	Layer	130w	3
40.3	150	Layer	130w	5
40.4	150	Layer	130w	8
40.5	150	Layer	130w	10
40.6	150	Layer	130w	13
40.7	150	Layer	130w	15
40.8	150	Layer	130w	17

Appendix G - Melt track dimensional measurements

Argon atmosphere track physical measurement results for –300+150 microns powder

Experimental results for -300/150 microns powder with argon atmosphere								
Experment 1		Experiment 2		Av. D	Av. width	Scan speed	Laser power	Weight
Depth	Width	Depth	Width	(mm)	(mm)	(mm/s2)	(W)	(g)
1.22	1.45	1.16	1.55	1.19	1.5	1	25	0.0299
0.97	1.35	1.05	1.05	1.01	1.2	3	25	0.0128
0.95	1.01	0.87	0.79	0.91	0.9	5	25	0.0071
0	0	0	0	0	0	8	25	0
0	0	0	0	0	0	10	25	0
0	0	0	0	0	0	13	25	0
0	0	0	0	0	0	15	25	0
0	0	0	0	0	0	17	25	0

Experimental results for -300/150 microns powder with argon atmosphere								
Experment 1		Experiment 2		Av. D	Av. width	Scan speed	Laser power	Weight
Depth	Width	Depth	Width	(mm)	(mm)	(mm/s2)	(W)	(g)
1.14	2.83	1.42	2.97	1.28	2.9	0.5	50	0.0289
1.21	3.14	1.15	3.06	1.18	3.1	0.75	50	0.0223
0.99	2.55	1.11	2.61	1.05	2.58	1	50	0.0298
0.85	1.56	0.93	1.6	0.89	1.58	3	50	0.0125
0.61	0.79	0.51	0.99	0.56	0.89	5	50	0.0098
0	0	0	0	0	0	8	50	0
0	0	0	0	0	0	10	50	0
0	0	0	0	0	0	13	50	0
0	0	0	0	0	0	15	50	0
0	0	0	0	0	0	17	50	0

Experimental results for -300/150 microns powder with argon atmosphere								
Experment 1		Experiment 2		Av. D	Av. width	Scan speed	Laser power	Weight
Depth	Width	Depth	Width	(mm)	(mm)	(mm/s2)	(W)	(g)
1.02	2.17	1.1	2.21	1.06	2.19	0.5	75	0.2108
1.15	2.3	1.11	2.22	1.13	2.26	0.75	75	0.23
1.2	2.31	1.12	2.35	1.16	2.33	1	75	0.2
0.81	1.61	0.97	1.51	0.89	1.56	3	75	0.1282
0.77	1.44	0.81	1.46	0.79	1.45	5	75	0.0581
0.65	0.95	0.57	1.07	0.61	1.01	8	75	0.0125
0.41	0.91	0.49	0.79	0.45	0.85	10	75	0.0089
0	0	0	0	0	0	13	75	0
0	0	0	0	0	0	15	75	0
0	0	0	0	0	0	17	75	0

Experimental results for -300/150 microns powder with argon atmosphere								
Experment 1		Experiment 2		Av. D	Av. width	Scan speed	Laser power	Weight
Depth	Width	Depth	Width	(mm)	(mm)	(mm/s2)	(W)	(g)
1.54	3.69	1.62	3.87	1.58	3.78	1	110	0.2897
1.43	2.75	1	2.67	1.45	2.71	3	110	0.21
1.05	1.89	1.47	2.07	1.01	1.98	5	110	0.1567
0.91	1.27	0.87	1.29	0.89	1.28	8	110	0.1354
0.82	0.95	0.72	1.03	0.77	0.99	10	110	0.0942
0.61	0.71	0.67	0.65	0.64	0.68	13	110	0.0248
0.44	0.53	0.48	0.49	0.46	0.51	15	110	0.0098
0	0	0	0	0	0	17	110	0

Experimental results for -300/150 microns powder with argon atmosphere								
Experment 1		Experiment 2		Av. D	Av. width	Scan speed	Laser power	Weight
Depth	Width	Depth	Width	(mm)	(mm)	(mm/s2)	(W)	(g)
1.41	2.99	1.51	3.05	1.46	3.02	0.5	130	0.3434
1.35	2.8	1.45	2.64	1.4	2.72	0.75	130	0.3709
1.51	3.12	1.45	3.02	1.48	3.07	1	130	0.4643
1.28	2.08	1.34	1.94	1.31	2.01	3	130	0.2105
1.12	1.48	1.08	1.42	1.1	1.45	5	130	0.1193
1.02	1.29	0.96	1.33	0.99	1.31	8	130	0.0946
0.98	1.05	0.84	0.97	0.91	1.01	10	130	0.0658
0.91	0.87	0.83	0.91	0.87	0.89	13	130	0.0584
0.68	0.81	0.74	0.73	0.71	0.77	15	130	0.0512
0.49	0.67	0.61	0.71	0.55	0.69	17	130	0.0158

Experimental results for -300/150 microns powder with argon atmosphere								
Experment 1		Experiment 2		Av. D	Av. width	Scan speed	Laser power	Weight
Depth	Width	Depth	Width	(mm)	(mm)	(mm/s2)	(W)	(g)
2.98	4.3	3.04	4.38	3.01	4.34	1	170	0.8966
1.95	2.38	2.01	2.32	1.98	2.35	3	170	0.4466
1.31	1.57	1.21	1.67	1.26	1.62	5	170	0.2389
0.98	1.58	1.04	1.54	1.01	1.56	8	170	0.1329
0.91	1.4	0.79	1.42	0.85	1.41	10	170	0.1109
1.15	1.38	1.23	1.34	1.19	1.36	13	170	0.088
0.81	1.55	0.91	1.49	0.86	1.52	15	170	0.0742
0.63	1.37	0.73	1.39	0.68	1.38	17	170	0.0641

Width/Depth	WidthxDepth	Power (P)/Scan speed (u)	Scan speed	Laser power
1	mm2	W/mm/s	mm/s	W
1.26	1.28	25	1	25
1.19	1.08	8	3	25
0.98	0.81	5	5	25
2.26	3.77	100	0.5	50
2.62	3.66	66	0.75	50
2.45	2.21	50	1	50
1.77	1.41	12	3	50
1.59	0.9	10	5	50
2.06	2.32	150	0.5	75
2	2.55	100	0.75	75
2.01	2.2	75	1	75
1.23	1.39	25	3	75
1.84	1.15	15	5	75
1.66	0.62	9.4	8	75
1.89	0.38	7.5	10	75
2.39	5.92	110	1	110
1.82	3.93	37	3	110
1.96	2	22	5	110
1.44	1.14	14	8	110
1.29	0.26	11	10	110
1.06	0.44	8.5	13	110
1.11	0.23	7.3	15	110
2.02	4.4	260	0.5	130
1.94	3.81	173	0.75	130
2.02	4.54	130	1	130
1.53	2.63	43	3	130
1.3	1.6	26	5	130
1.32	1.3	16	8	130
1.11	0.92	13	10	130
1.02	0.77	10	13	130
1.08	0.55	8.8	15	130
1.25	0.38	7.6	17	130
1.44	13.06	170	1	170
1.19	4.65	55	3	170
1.29	2.04	34	5	170
1.54	1.58	21	8	170
1.66	1.2	17	10	170
1.14	1.62	13	13	170
1.76	1.31	11	15	170
2.03	0.94	10	17	170

Appendix G -Melt track dimensional measurements

Argon atmosphere track physical measurement results for 75%, –300+150 microns powder with addition of 25%, -38 microns powder

Experimental results for -300/150 microns powder with addition of -38 microns powder								
Experment 1		Experiment 2		Av. D	Av. width	Scan speed	Laser power	Weight
Depth	Width	Depth	Width	(mm)	(mm)	(mm/s2)	(W)	(g)
0.47	1.1	0.51	1.3	0.49	1.2	1	25	0.0378
0.32	0.83	0.38	0.75	0.35	0.79	3	25	0.0187
0.28	0.76	0.26	0.64	0.27	0.7	5	25	0.0084
0	0	0	0	0	0	8	25	0
0	0	0	0	0	0	10	25	0
0	0	0	0	0	0	13	25	0
0	0	0	0	0	0	15	25	0
0	0	0	0	0	0	17	25	0

Experimental results for -300/150 microns powder with addition of -38 microns powder								
Experment 1		Experiment 2		Av. D	Av. width	Scan speed	Laser power	Weight
Depth	Width	Depth	Width	(mm)	(mm)	(mm/s2)	(W)	(g)
0.99	2.05	1.13	2.31	1.06	2.18	1	50	0.128
1.3	1.95	1.36	2.05	1.33	2	3	50	0.1376
1	1.39	1.06	1.49	1.03	1.44	5	50	0.0951
0.82	1.19	0.96	1.31	0.89	1.25	8	50	0.0589
0.69	1.08	0.87	1.22	0.78	1.15	10	50	0.0479
0.7	1.2	0.74	1.12	0.72	1.16	13	50	0.037
0.61	1.17	0.71	1.09	0.66	1.13	15	50	0.312
0	0	0	0	0	0	17	50	0

Experimental results for -300/150 microns powder with addition of -38 microns powder								
Experment 1		Experiment 2		Av. D	Av. width	Scan speed	Laser power	Weight
Depth	Width	Depth	Width	(mm)	(mm)	(mm/s2)	(W)	(g)
1.28	2.19	1.12	2.27	1.2	2.23	1	75	0.2379
1.47	2.05	1.41	1.91	1.44	1.98	3	75	0.1925
0.96	1.04	1	1.14	0.98	1.09	5	75	0.1211
0.9	1.17	0.88	1.07	0.89	1.12	8	75	0.075
0.87	1	0.75	1.08	0.81	1.04	10	75	0.0595
0.71	0.95	0.65	1.05	0.68	1	13	75	0.0382
0.6	1.2	0.7	0.96	0.65	1.08	15	75	0.0408
0.31	0.59	0.37	0.73	0.34	0.66	17	75	0.0134

Experimental results for -300/150 microns powder with addition of -38 microns powder								
Experment 1		Experiment 2		Av. D	Av. width	Scan speed	Laser power	Weight
Depth	Width	Depth	Width	(mm)	(mm)	(mm/s2)	(W)	(g)
1.28	2.7	1.42	2.8	1.35	2.75	1	110	0.4109
1.6	2.45	1.54	2.75	1.57	2.46	3	110	0.175
1.25	1.8	1.29	1.74	1.27	1.77	5	110	0.2821
0.93	1.61	1.07	1.53	1	1.57	8	110	0.1037
0.82	1.39	0.78	1.45	0.8	1.42	10	110	0.0829
0.47	0.85	0.51	0.91	0.49	0.88	13	110	0.0944
0.39	0.78	0.41	0.8	0.4	0.79	15	110	0.0701
0.37	0.65	0.33	0.73	0.35	0.69	17	110	0.0542

Experimental results for -300/150 microns powder with addition of -38 microns powder								
Experment 1		Experiment 2		Av. D	Av. width	Scan speed	Laser power	Weight
Depth	Width	Depth	Width	(mm)	(mm)	(mm/s2)	(W)	(g)
1.98	3.15	2.22	3.01	2.1	3.08	1	130	0.6003
2.05	2.71	1.75	2.89	1.9	2.8	3	130	0.4401
1.83	2.53	1.79	2.55	1.81	2.54	5	130	0.4329
1.61	2.08	1.51	1.96	1.56	2.02	8	130	0.389
1.05	1.48	1.15	1.52	1.1	1.5	10	130	0.1089
0.73	1.13	0.67	1.07	0.7	1.1	13	130	0.0814
0.63	0.75	0.53	0.85	0.58	0.8	15	130	0.0879
0.38	0.69	0.44	0.73	0.41	0.71	17	130	0.0625

Appendix G - Melt track dimensional measurements

Argon atmosphere results for –75+38 microns powder

Experimental results for -75/38 microns powder with argon atmosphere								
Experment 1		Experiment 2		Av. D	Av. width	Scan speed	Laser power	Weight
Depth	Width	Depth	Width	(mm)	(mm)	(mm/s2)	(W)	(g)
0.68	1.97	0.74	1.93	0.71	1.95	1	25	0.1487
0.67	1.4	0.63	1.42	0.65	1.41	3	25	0.1062
0.55	0.99	0.47	0.97	0.51	0.98	5	25	0.713
0	0	0	0	0	0	8	25	0
0	0	0	0	0	0	10	25	0
0	0	0	0	0	0	13	25	0
0	0	0	0	0	0	15	25	0
0	0	0	0	0	0	17	25	0

Experimental results for -75/38 microns powder with argon atmosphere								
Experment 1		Experiment 2		Av. D	Av. width	Scan speed	Laser power	Weight
Depth	Width	Depth	Width	(mm)	(mm)	(mm/s2)	(W)	(g)
0.77	2.73	0.75	2.69	0.76	2.71	1	50	0.1787
0.61	2.06	0.71	2.1	0.66	2.08	3	50	0.1375
0.59	1.66	0.57	1.72	0.58	1.69	5	50	0.0869
0.53	1.44	0.57	1.38	0.55	1.41	8	50	0.0596
0.53	1.29	0.49	1.25	0.51	1.27	10	50	0.514
0	0	0	0	0	0	13	50	0
0	0	0	0	0	0	15	50	0
0	0	0	0	0	0	17	50	0

Experimental results for -75/38 microns powder with argon atmosphere								
Experment 1		Experiment 2		Av. D	Av. width	Scan speed	Laser power	Weight
Depth	Width	Depth	Width	(mm)	(mm)	(mm/s2)	(W)	(g)
1.07	2.94	1.09	2.88	1.08	2.91	1	75	0.1876
1.01	2.3	0.95	2.36	0.98	2.33	3	75	0.1976
0.93	1.91	0.89	1.97	0.91	1.94	5	75	0.1069
0.77	1.61	0.81	1.55	0.79	1.58	8	75	0.0709
0.67	1.53	0.71	1.49	0.69	1.51	10	75	0.0588
0.63	1.39	0.59	1.41	0.61	1.4	13	75	0.0437
0.57	1.36	0.53	1.4	0.55	1.38	15	75	0.0391
0	0	0	0	0	0	17	75	0

Experimental results for -75/38 microns powder with argon atmosphere								
Experment 1		Experiment 2		Av. D	Av. width	Scan speed	Laser power	Weight
Depth	Width	Depth	Width	(mm)	(mm)	(mm/s2)	(W)	(g)
2.09	3.78	1.93	3.76	2.01	3.77	1	110	1.0373
1.68	3.01	1.74	2.95	1.71	2.98	3	110	0.4192
1.25	2.2	1.21	2.1	1.23	2.15	5	110	0.2733
1.11	1.93	1.05	1.89	1.08	1.91	8	110	0.1762
0.93	1.67	0.89	1.69	0.91	1.68	10	110	0.1784
0.77	1.66	0.81	1.62	0.79	1.64	13	110	0.1226
0.75	1.63	0.71	1.59	0.73	1.61	15	110	0.1157
0.66	1.56	0.7	1.56	0.68	1.56	17	110	0.1074

Experimental results for -75/38 microns powder with argon atmosphere								
Experment 1		Experiment 2		Av. D	Av. width	Scan speed	Laser power	Weight
Depth	Width	Depth	Width	(mm)	(mm)	(mm/s2)	(W)	(g)
2.64	4.15	2.58	4.07	2.61	4.11	1	130	1.089
2.01	1.91	2.07	3.05	2.04	2.98	3	130	0.5772
1.64	2.35	1.62	2.27	1.63	2.31	5	130	0.4875
1.25	2.13	1.21	2.09	1.23	2.11	8	130	0.2354
1.18	1.88	1.2	1.94	1.19	1.91	10	130	0.1258
0.97	1.87	0.93	1.81	0.95	1.84	13	130	0.1287
0.83	1.75	0.79	1.67	0.81	1.71	15	130	0.1187
0.69	1.72	0.73	1.66	0.71	1.69	17	130	0.1002

Experimental results for -75/38 microns powder with argon atmosphere								
Experment 1		Experiment 2		Av. D	Av. width	Scan speed	Laser power	Weight
Depth	Width	Depth	Width	(mm)	(mm)	(mm/s2)	(W)	(g)
3.15	4.04	3.07	4.14	3.11	4.09	1	170	1.1
2.35	2.87	2.41	2.95	2.38	2.91	3	170	0.687
1.68	2.55	1.74	2.51	1.71	2.53	5	170	0.654
1.27	2.09	1.33	1.93	1.3	2.01	8	170	0.2879
1.06	1.94	0.96	1.66	1.01	1.8	10	170	0.1957
0.81	1.71	0.73	1.67	0.77	1.69	13	170	0.1687
0.63	1.69	0.59	1.61	0.61	1.65	15	170	0.1351
0.61	1.58	0.57	1.44	0.59	1.51	17	170	0.1128

Width/Depth	WidthxDepth	Power (P)/Scan speed (u)	Scan speed	Laser power
w/d	w x d (mm2)	W/mm/s	mm/s	W
2.75	1.38	25	1	25
2.17	0.92	8.4	3	25
1.92	0.5	5	5	25
3.56	2.06	50	1	50
3.15	1.37	16.6	3	50
2.91	0.98	10	5	50
2.56	0.78	6.25	8	50
2.49	0.65	5	10	50
2.69	2.36	75	1	75
2.38	2.28	25	3	75
2.13	1.77	15	5	75
2	1.25	9.4	8	75
2.19	1.04	7.5	10	75
2.3	0.85	5.7	13	75
2.5	0.76	5	15	75
1.88	7.57	110	1	110
1.74	5.1	36.6	3	110
1.74	2.64	22	5	110
1.76	2.06	13.7	8	110
1.85	1.53	11	10	110
2.08	1.3	8.5	13	110
2.2	1.18	7.3	15	110
2.29	1.06	6.4	17	110
1.57	10.73	130	1	130
1.46	6.08	43.3	3	130
1.42	3.77	26	5	130
1.72	2.6	16.25	8	130
1.6	2.27	13	10	130
1.94	1.75	10	13	130
2.11	1.38	8.66	15	130
2.38	1.2	7.64	17	130
1.32	12.7	170	1	170
1.22	6.93	56.6	3	170
1.48	4.33	34	5	170
1.33	2.61	21.25	8	170
1.28	1.82	17	10	170
2.19	1.3	13.07	13	170
2.2	1.01	11.33	15	170
2.56	0.89	10	17	170

APPENDIX H – TWO LAYERS SINTERED TOGETHER USING DIFFERENT SCANNING CONDITIONS IN AN ARGON ATMOSPHERE

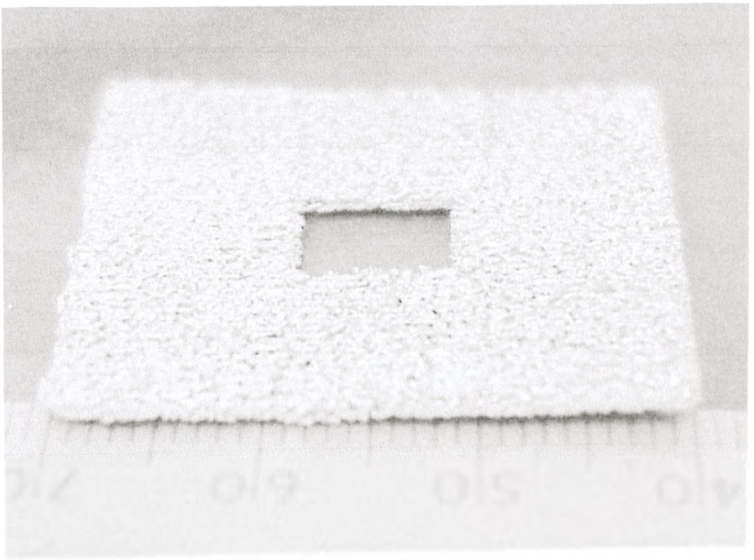

Two layer sintered together using –300/150μm powder with addition of 25%, -38μm powder scanned at 55W laser power and 1 mm/s scan speed in argon atmosphere

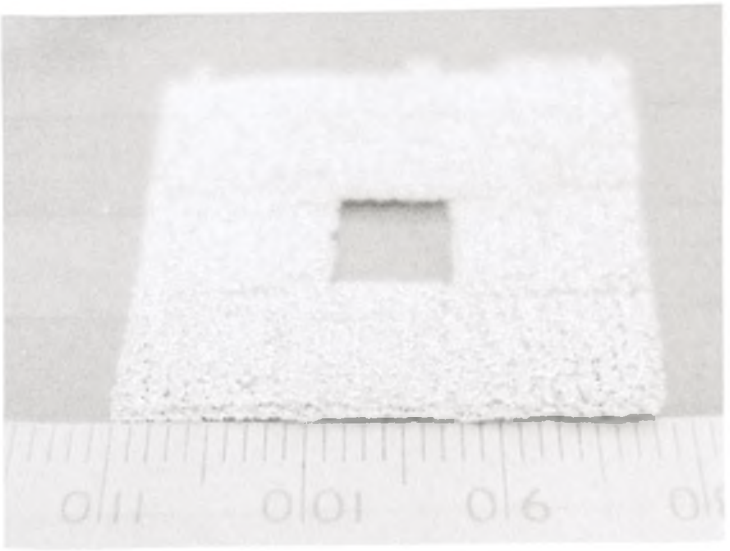

Two layer sintered together using –300/150μm powder with addition of 25%, -38μm powder scanned at 55W laser power and 3 mm/s scan speed in argon atmosphere

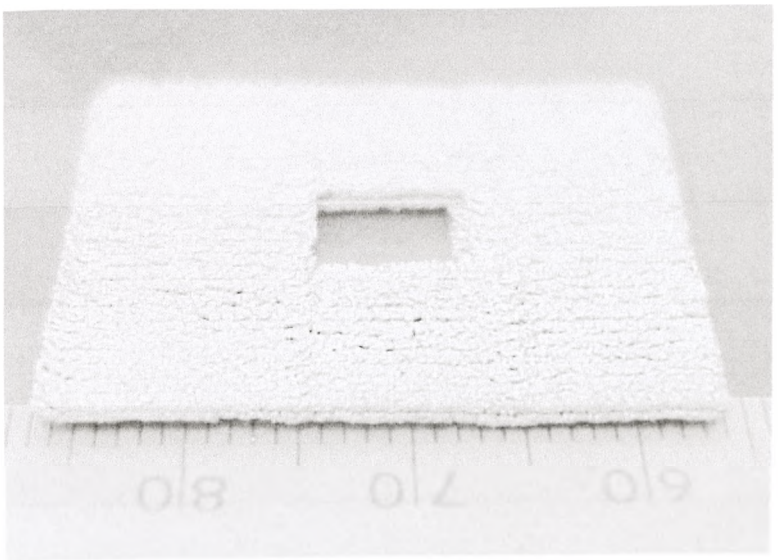

Two layer sintered together using –300/150μm powder with addition of 25%, -38μm powder scanned at 55W laser power and 5 mm/s scan speed in argon atmosphere

Appendix I – Single layer measurements

Single layers	Mix 300 + 38 powder		Mass	Energy
P	U	S		
(W)	(mm/s)	(mm)	(g)	(J/mm)
50	1	0.25	0.607	50
50	1	0.5	0.61	50
50	1	0.75	0.704	50
50	3	0.25	0.528	16.6
50	3	0.5	0.531	16.6
50	3	0.75	0.569	16.6
50	5	0.25	0.424	10
50	5	0.5	0.445	10
50	5	0.75	0.478	10
50	8	0.25	0.327	6.25
50	8	0.5	0.357	6.25
50	8	0.75	0.367	6.25
75	1	0.25	1.085	75
75	1	0.5	0.109	75
75	1	0.75	1.417	75
75	3	0.25	0.911	25
75	3	0.5	0.926	25
75	3	0.75	1.062	25
75	5	0.25	0.751	15
75	5	0.5	0.852	15
75	5	0.75	0.918	15
75	8	0.25	0.462	9.37
75	8	0.5	0.609	9.37
75	8	0.75	0.701	9.37
110	1	0.25	1.498	110
110	1	0.5	1.763	110
110	1	0.75	1.906	110
110	3	0.25	0.781	36.6
110	3	0.5	0.85	36.6
110	3	0.75	0.871	36.6
110	5	0.25	0.824	22
110	5	0.5	0.848	22
110	5	0.75	0.854	22
110	8	0.25	0.785	13.75
110	8	0.5	0.881	13.75
110	8	0.75	0.891	13.75

Single layers	-300/150 microns powder		Mass	Energy
P	U	S		
(W)	(mm/s)	(mm)	(g)	(J/mm)
50	1	0.25	0.588	50
50	1	0.5	0.697	50
50	1	0.75	0.604	50
50	3	0.25	0.409	16.6
50	3	0.5	0.461	16.6
50	3	0.75	0.471	16.6
50	5	0.25	0.39	10
50	5	0.5	0.406	10
50	5	0.75	0.513	10
50	8	0.25	0.335	6.25
50	8	0.5	0.342	6.25
50	8	0.75	0.346	6.25
75	1	0.25	0.718	75
75	1	0.5	0.732	75
75	1	0.75	0.938	75
75	3	0.25	0.699	25
75	3	0.5	0.701	25
75	3	0.75	0.711	25
75	5	0.25	0.607	15
75	5	0.5	0.631	15
75	5	0.75	0.639	15
75	8	0.25	0.439	9.37
75	8	0.5	0.545	9.37
75	8	0.75	0.505	9.37
110	1	0.25	0.876	110
110	1	0.5	0.914	110
110	1	0.75	1.136	110
110	3	0.25	0.654	36.6
110	3	0.5	0.661	36.6
110	3	0.75	0.72	36.6
110	5	0.25	0.568	22
110	5	0.5	0.649	22
110	5	0.75	0.69	22
110	8	0.25	0.581	13.75
110	8	0.5	0.598	13.75
110	8	0.75	0.66	13.75